UNIVERSITY OF NOVA GORICA
GRADUATE SCHOOL

MODELLING OF MICROSTRUCTURE FORMATION IN METALS BY A NOVEL POINT AUTOMATA METHOD

DISSERTATION

M.Sc. Agnieszka Zuzanna Lorbiecka

Mentor: Prof. Dr. Božidar Šarler

Nova Gorica, 2011

Acknowledgements

Writing a dissertation is like setting off on a long journey, lasting many years, before it comes to a successful end. I have taken such a journey ... Today, when I reached the destination, I would like to thank all the people who accompanied me on the way.

First of all I would like to thank my supervisor Prof. Bozidar Šarler, for being a great advisor. I will never find the words to thank him for his time spent helping me. Without his ideas and tremendous support the dissertation would never be finished.

Many thanks to the Inspire Marie Curie Program for giving me the possibility of work and study at the University of Nova Gorica in Slovenia and Štore Steel company for giving me all necessary data, relevant for developing the numerical model.

Special thanks to my parents for their love and for having always stayed behind me, especially when I was losing the point in continuing the dissertation. Special thanks to my father for his time spent with me and his valuable advices. Without his help it would not be possible to finish the dissertation.

Thanks to my boyfriend Dorijan for his persistence and patience during the time when I worked on the dissertation. Thanks to you Slovenia becoming my second home.

Additionally I would like to thank Prof. Polonca Trebše, all my colleagues from the Laboratory of Multiphase Processes, and all the people who supported me and contributed to a greater or lesser degree in writing this dissertation.

Napisanie pracy doktorskiej to jakby udanie się w długą i meczącą podroż, która trwa lata żeby mogła być udanie zakończona. Ja się w taka podroż wybrałam, nie byłam jednak sama. Dziś, kiedy dotarłam do celu, pragnę w tych kilku słowach, podziękować współtowarzyszom mojej wędrówki.

Dziękuję mojemu Promotorowi, prof. Božidarowi Šarlerowi za poświęcony czas oraz cenne uwagi przekazywane w trakcie przygotowania niniejszej pracy. Bez Pan profesora pomocy merytorycznej i wyrozumiałości powstanie tej pracy byłoby niemożliwe.

Dziękuję moim rodzicom za Waszą miłość i wsparcie szczególnie wtedy kiedy traciłam wiarę i sens w kontynuowanie tej pracy. Przede wszystkim dziękuję mojemu Tacie za poświecony czas i cenne wskazówki, bez których nie byłabym w stanie dokończyć tego doktoratu.

Dziękuje mojemu chłopakowi Dorijanowi za wytrwałość i cierpliwości, gdy pisałem pracę. Dzięki Tobie Słowenia stała się moim drugim domem.

Dziękuję Prof. Polonci Trebše, moim współpracownikom i wszystkim którzy w mniejszym lub większym stopniu przyczyniły się do ułatwienia mi napisania pracy doktorskiej.

Modelling of Microstructure Formation in Metals by a Novel Point Automata Method.

Abstract

The research described in this dissertation is focused on the numerical simulation and analysis of the mesoscopic and microscopic models coupled with the heat transfer calculations which are able to predict the grain structure formation and the dendritic growth occurring during solidification of metals. The grain structure formation model is applied to Equiaxed to Columnar Transition (ECT) and Columnar to Equiaxed Transition (CET) of steel billet in Continuous Casting (CC). The dendritic growth model is applied to simulation of thermally driven dendritic structures in pure aluminium.

First a 2D meso-macroscopic model was described and developed to predict the grain structure ((ECT) and (CET)) in the CC steel billets. The model predicts well the temperature field in the Štore Steel CC machine. The macroscopic model is designed to be able to calculate the steady temperature distribution in the continuously cast billet as a function of the following process parameters: billet dimension, steel grade, casting temperature, casting velocity, primary, and two secondary cooling systems flows, pressures, temperatures, type and quantity of the casting powder, and the (non)application of the radiation shield and electromagnetic stirring. The Bennon-Incropera mixture continuum formulation is used for the physical model, solved by the recently developed LRBFCM. The macroscopic heat transfer model is solved by the meshless technique by using Local Radial Basis Function Collocation Method (LRBFCM).

The Cellular Automata (CA) and novel Point Automata (PA) techniques are used to solve the mesoscopic model. In the CA method the calculations are done on the regular cell distribution. The nucleation is modelled through a continuous dependency of the nucleation density on temperature by the Gaussian distribution. Different nucleation parameters are used at the boundary and in the bulk region of the billet. The growth and impingement stages are modelled by the Kurz, Giovanola, Trivedi (KGT) model. The CA method is based on the Nastac's definition of neighbourhood and newly introduced four different neighbourhood configurations. A novel neighbourhood configuration of the PA method has been chosen which contains random points within circle with radius of neighbourhood centred around the reference point. In the novel approach the CA cells have been replaced by the nodes randomly located on the domain. The irregular node arrangement is achieved in practice as a random selection of points from the centres of CA cells. It is constructed from the regular CA cell distributions by randomly taking away certain percentage of the points. The differences in numerical implementation of the classical LRBFCM-CA and the

novel LRBFCM-PA are compared. The ECT/CET model parameters were adjusted in order to obtain the experimentally determined actual 140 mm x 140 mm billet ECT and CET positions of the heat 46352 with the alloy 51CrMoV4 in the Štore Steel company. A systematic procedure is outlined for adjusting of the model data with the industrial experiment. The influence of the variation of different parameters on calculated grain structure is demonstrated. Calculations are done for the square billets of the dimension 140 mm (and 180 mm x 180 mm). Fixed input parameter of the model represents the macroscopic temperature field. All other grain structure physical model parameters are varied, such as: the surface and the bulk area, mean nucleation undercooling, standard deviation of undercooling, maximum density of nuclei, Gibbs-Thomson coefficient, diffusion coefficient in the liquid, slope of the liquidus line, initial carbon concentration. The computational parameters, such as the node arrangement size and the time step are constant.

Simulations have been carried out for nominal casting conditions, reduced casting temperature, reduced casting speed, for different dimensions of the square billet 140 mm x 140 mm (and 180 mm x 180 mm) and steel grades (51MoCr4, 51CrV4 and 25MoCr4). The dimensions of the three characteristic zones: chill, columnar and equiaxed, measured in the industry were compared to the simulated results for five heats with different casting speeds and four different casting temperatures. The simulated positions of ECT/CET compare well to Baumann prints. Proper response of the multiscale model with respect to the experimentally observed grain structure from the industrial process is proved.

In this dissertation, a novel LRBFCM-PA approach is for the first time demonstrated for prediction of the grain structure which occurs during the CC of steel by coupling the macro and mesoscopic models. It is shown that the PA method offers a simple and powerful approach of cellular simulations. It is shown that both methods are able to qualitatively and quantitatively model a diverse range of solidification phenomena.

The second 2D microscopic model was described and developed for the prediction of dendritic grain structures formed during the solidification of pure metals. It is physically described by the heat conduction and phase change kinetics. The deterministic heat transfer model is solved by the Finite Difference Method (FDM). The governing microstructure equations are solved by the stochastic CA and PA methods. The stochastic model receives temperatures from the deterministic model and the deterministic model receives the solid fraction for the stochastic model. The solid fraction calculations are performed on the regular CA or random PA nodes and then fed back to the FDM nodes in order to update the temperature field. The stochastic model includes calculations of the interface temperature, curvature, Gibbs-Thomson coefficient and crystal growth velocity. The models account for two anisotropies: thermodynamic anisotropy related to the crystal orientation calculated through the Gibbs-Thomson coefficient and the kinetic anisotropy which takes into the consideration the crystal growth direction and the preferential orientation. The CA approach is established on quadratic cells and Neumann neighbourhood. The PA approach is established on randomly distributed points and neighbourhood configuration, similar as appears in meshless methods. The random node arrangement is in the dissertation generated from the regular CA mesh. In order to construct the irregular node arrangement the CA cell centres are displaced to quasi-random positions on the computational domain.

The potentiality of the FDM-CA and FDM-PA models are demonstrated through the predictions of the typical dendritic forms. Numerical examples are done for the square domain of dimension 350 μm with Neumann boundary conditions. Fixed input parameters of the dendritic model represent the material properties for the pure aluminium, cell size, average Gibbs-Thomson coefficient and anisotropy coefficients for the CA/PA methods.

In the CA method the numerical results are prepared for the following varied input parameters: thermal fluctuations, curvature calculation radius and Gibbs-Thomson coefficient. Subsequently, we present simulation of the growth process simulated by the CA method for seven four branched dendrites growing simultaneously at orientations 0° and 45°.

In the PA method the dendritic growth is simulated with the same and different types of random node arrangements. Several cases are prepared for ten different orientations and with three different more or less random node arrangements. Next, dendritic growth is simulated by including the randomness growth correction factor responsible for the correction in lengths of the primary branches as compared with the CA method. Finally, we present the growth process simulated by the PA method for seven dendrites growing simultaneously at the same orientations as for the CA model and at random orientations.

It is shown that the random grid computing appears to be a promising way for solving problems that can not be achieved by applying the conventional CA method. The developed numerical LRBFCM-PA method is found to be applicable for simulating more proper dimensions of chill, columnar and equiaxed zones. The different density of nucleuses across the domain of interest allows to model the appropriate dimensions of the central region which is usually difficult to predict. For the FDM-CA method, the significant problem exists in the Cartesian grid structures. It is well know that the classical CA methods have a tendency to deform the results by introducing the anisotropy associated with the network of cells. Consequences are that dendrites tend to grow only in the grid direction. A successful solution for this problems is presented. A novel FDM-PA method is able to resolve the preferred crystallographic orientation-mesh orientation problem. It is shown that by using the random node arrangement the dendrites are able to grow in any direction.

Keywords

grain growth, dendritic growth, solidification, recrystallization, continuous casting of steel, equiaxed to columnar transition, columnar to equiaxed transition, Gaussian nucleation model, KGT growth model, cellular automata method, point automata method, local radial basis function collocation method, finite difference method.

Modeliranje formiranja mikrostrukture v kovinah z novo točkovno metodo celičnih avtomatov.

Povzetek

Raziskava, opisana v tej disertaciji, je usmerjena v numerično simuliranje in analizo mezoskopskih in mikroskopskih modelov sklopljenih z izračuni prenosa toplote. Modeli omogočajo napoved formiranja strukture zrn in dendritov med strjevanjem kovin. Model tvorbe zrn je uporabljen za izračun prehodov iz enakoosnih v stebričaste (Equiaxed to Columnar Transition ECT) in iz stebričastih v enakoosne strukture (Columnar to Equiaxed Transition CET) v jeklenih gredicah pri kontinuiranem litju (Continuous Casting CC). Model rasti dendritov je uporabljen pri simulaciji toplotno gnanih dendritskih struktur v čistem aluminiju.

Dvodimenzionalni mezo-makroskopski model je najprej opisan in razvit za napoved strukture zrn (ECT in CET) v kontinuirano litih jeklenih gredicah. Model dobro napove temperaturno polje v primeru naprave za kontinuirno litje podjetja Štore Steel. Makroskopski model je narejen tako, da lahko izračuna ustaljeno temperaturno porazdelitev v kontinuirno liti gredici v odvisnosti od naslednjih procesnih parametrov: dimenzij gredice, kvalitete jekla, začetne temperature ulivanja, hitrosti ulivanja, primarnega in sekundarnega hladilnega toka, tlaka, temperature, tipa in količine livnega praška ter uporabe oziroma neuporabe radiacijskega ščita in elektromagnetnega mešanja. Kot fizikalni model je uporabljen model kontinumske mešanice Bennona in Incropere, ki je bil rešen z uporabo pred kratkim razvite metode radialnih baznih funkcij z lokalno kolokacijo (Local Radial Basis Function Collocation Method, LRBFCM). Makroskopski model je bil rešen z brezmrežno tehniko z uporabo lokalne kolokacije na podlagi radialnih baznih fukncij. Pri reševanju mezoskopskega modela sta bili uporabljeni tehnika celičnih avtomatov (Cellular Automata CA) in nova tehnika točkovnih avtomatov (Point Automata PA). Pri CA metodi izračuni potekajo na regularni distribuciji celic. Nukleacija je modelirana z zvezno odvisnostjo nukleacijske gostote od temperature po Gaussovi porazdelitvi. Različni nukleacijski parametri so uporabljeni na robu in v notranjem območja gredice. Faza rasti in zadevanje mej sta modelirani z modelom Kurz, Giovanola, Trivedi (KGT).

Metoda CA je osnovana na Nastacovi definiciji soseščine in na novo vpeljanih štirih različnih konfiguracijah soseščin. Izbrana je nova konfiguracija soseščin metode točkovnih avtomatov. Ta vsebuje naključne točke znotraj kroga z radiem soseščine, centriranega okoli referenčne točke. V novem pristopu so bile CA celice zamenjane z naključno porazdeljenimi točkami v domeni. Neregularna porazdelitev točk je v praksi ustvarjena z naključno izbiro točk iz centralnih celic metode CA. Konstruirana je iz regularne celice z naključnim izključevanjem

določenega deleža točk. Narejena je primerjava numeričnih implementacij klasične LRBFCM-CA in nove LBRFCM-PA. Modelski parametri ECT/CET so nastavljeni tako, da dobimo eksperimentalno določene položaje ECT in CET za gredice 140 mm x 140 mm šarže 46352 jekla s podjetja Štore steel. Zasnovan je sistematični postopek prilagoditve modelskih podatkov glede na industrijske eksperimente. Predstavljen je vpliv variacije različnih parametrov na izračunane strukture zrn. Izračuni so narejeni za gredici kvadratnega profila dimenzij 140 mm x 140 mm in 180 mm x 180 mm. Fiksni vhodni parameter je makroskopsko temperaturno polje. Vsi ostali fizikalni parametri strukture zrn se spreminjajo: površinsko in notranje območje, povprečna nukleacija, podhladitev, standardna deviacija podhladitve, največja gostota jeder, Gibbs-Thomsonov koeficient, difuzijski koeficient kapljevine, naklon likvidus linije, začetna koncentracija ogljika). Numerični parametri, kot sta porazdelitev točk in časovni korak, so konstantni.

Simulacije so bile narejene pri nominalnih pogojih ulivanja, zmanjšani temperaturi ulivanja, zmanjšani hitrosti ulivanja, za različne dimenzije gredic 140 mm x 140 mm and (180 mm x 180 mm) in različne kvalitete jekel (51MoCr4, 51CrV4 in 25MoCr4). Dimenzije treh karakterističnih con: gašena, stebričasta in enakoosna, izmerjene v industrijskem procesu so primerjane z izračuni simulacij za pet šarž pri različnih hitrostih ulivanja in štirih različnih temperaturah ulivanja.

Simulirani položaji ECT/CET dobro sovpadajo z Baumannovimi odtisi. Potrjen je pravilen odziv večnivojskega modela v povezavi z eksperimentalno določenimi strukturami zrn v industriji.

V tej disertaciji je nov LRBFCM-PA pristop prvič uporabljen za napoved strukture zrn, ki nastanejo pri CC jekla preko sklopitve makro in mezoskopskega modela. Prikazano je, da je PA metoda preprosto in močno orodje za celične simulacije. Prikazano je, da sta obe metodi sposobni kvalitativno in kvantitativno modelirati raznolik spekter pojavov strjevanja.

Dvodimenzionalen mikroskopski model je opisan in razvit za napoved dendritskih struktur zrn, ki nastanejo pri strjevanju čistih kovin. Fizikalno je opisan s prevajanjem toplote in s kinetiko fazne preobrazbe. Deterministični model prenosa toplote je rešen z uporabo metode končnih razlik (Finite Difference Method, FDM). Enačbe za opis mikrostrukture so rešene s povezanima stohastičnima metodama celičnih in točkovnih avtomatov. Stohastični model dobi temperaturno polje iz determinističnega modela, deterministični model pa dobi delež trdne faze iz stohastičnega modela. Izračuni stohastičnega modela so izdelani na regularni porazdelitvi točk v modelu celičnih avtomatov, oziroma naključni porazdelitvi točk v modelu točkovnih avtomatov ter prevedeni nazaj na točke v modelu končnih razlik v skladu z izračunanim temperaturnim poljem. Stohastični model vsebuje izračune mejne temperature, ukrivljenosti, Gibss-Thomsonovega koeficienta in hitrosti rasti kristalov. Model vključuje dve vrst anizotropije. Termodinamična anizotropija je povezana s kristalno orientacijo izračunano preko Gibbs-Thomsonovega koeficienta. Kinetična anizotropija upošteva smer rasti kristala in preferenčno smer. CA pristop je vzpostavljen na kvadratnih celicah in Neumannovih soseščinah. PA pristop je vzpostavljen na naključni porazdelitvi točk in soseščin, podobno kot se pojavlja v brezmrežnih metodah. Naključna porazdelitev točk je v tej disertaciji generirana iz regularne CA mreže, tako da so CA centri premaknjeni na kvazi-naključne pozicije na računski domeni. Potencial modelov FDM-CA in FDM-PA je prikazan z napovedjo tipičnih dendritskih oblik. Numerični primeri so izvedeni na kvadratnih domenah dimenzij 350 μm z Neumannovimi robnimi pogoji. Fiksni vhodni parametri dendritskih modelov predstavljajo snovne lastnostni za čisti aluminij, velikost celic, povprečen Gibbs-Thomsonov koeficient in koeficiente anizotropije za metodi CA/PA. Pri metodi CA so numerični izračuni narejeni za kombinacijo naslednjih različnih vhodnih podatkov: termičnie fluktuacije, radij ukrivljenosti in Gibbs-Thomsonov koeficient. Na koncu je predstavljena simulacija procesa rasti z metodo CA za sedem dendritov s štirimi primarnimi vejami, ki rastejo vzporedno med 0° in 45°.

Pri metodi PA je dendritska rast simulirana z enakim in različnimi tipi naključno generiranih distribucij točk. Več testov je pripravljenih za deset različnih orientacij in s tremi različnimi bolj ali manj naključnimi porazdelitvami točk. Dendritska rast je simulirana z upoštevanjem korekcijskega faktorja dolžin primarnih vej, ki je odgovoren za pravilno dolžino primarnih vej glede na izračunane z metodo CA. Na koncu so predstavljeni rezultati procesa rasti z metodo PA za primer sedmih dendritov, ki rastejo vzporedno, najprej z enakima orientacijama kot za model CA in nato pri naključnih orientacijah.

Pokazano je, da je računanje z naključnimi položaji točk obetaven pristop k reševanju problemov, ki jih ni moč rešiti s konvencionalno CA metodo. Na novo razvita metoda LRBFCM-PA je uporabna za izboljšane simulacije dimenzij gašenih, stebričastih in enakoosnih con. Različne gostote nukleacijskih jeder po območju omogočajo natančnejše računanje dimenzij centralnega enakoosnega območja, kar je v splošnem zapleteno napovedati. Pri metodi FDM-CA obstaja velik problem kartezijeva mreža. Znano je, da klasična CA metoda teži k popačenju rezultatov preko anizotropije povezane z usmeritvijo računske mreže. Posledično dendriti rastejo samo v smeri mreže. Predstavljena je uspešna rešitev tega problema. Z novo metodo FDM-PA je možno rešiti problem orientacije kristala glede na mrežo. Predstavlja se, da je z razvito naključno porazdelitvijo računskih točk možno doseči, da dendriti lahko rastejo v vse smeri.

Ključne besede

rast zrn, dendritska rast, strjevanje, rekristalizacija, kontinuirno ulivanje jekla, enakosno-stebričasta tranzicija, stebričasto-enakoosna tranzicija, Gaussov model nukleacije, KGT model rasti, metoda celičnih avtomatov, metoda točkovnih avtomatov, metoda radialnih baznih funkcij z lokalno kolokacijo, metoda končnih razlik.

Contents

List of Figures v

List of Tables xiii

List of Symbols xv

1 Introduction 1

1.1 Modelling of Microstructure 2
1.2 Application of CA to Modelling of Microstructure 5
1.3 Dissertation Goals and Performed Work 8
1.4 Overview of the Dissertation 12

2 Introduction to the Solidification Theory 13

2.1 Nucleation Stage 13
2.2 Growth Stage 17
  2.2.1 Growth Kinetics of the Dendritic Tip 19
    2.2.1.1 Hemispherical Needle Approximation 19
    2.2.1.2 Paraboloid of Revolution 22
    2.2.1.3 KGT Model 23

3 Cellular Automata and Point Automata Methods 27

3.1 Literature Review 27
3.2 Definition of CA Method 29
3.3 Typical CA Neighbourhood and PA Neighbourhood Definitions 32

4 Point Automata Advantages 37

4.1 CA Problems 37

4.2 An Overview of Modelling the Recrystallization by the CA and PA Methods 39
4.3 CA Method for Recrystallization 40
  4.3.1 Modelling of the Nucleation Rate 40
    4.3.1.1 Initial Microstructure 40
  4.3.2 Modelling of the Grain Growth Kinetics 41
    4.3.2.1 Neighbourhood Configuration 41
    4.3.2.2 Grain Boundary Migration 42
  4.3.3 Transition Rules 43
4.4 PA Method for Recrystallization 44
  4.4.1 Initial Microstructure 44
  4.4.2 Neighbourhood Configuration 45
  4.4.3 Grain Transition Rules and Grain Boundary Movements 46

5 Mesoscopic Model of ECT/CET 47

5.1 Characteristic Zones of CC 48
5.2 CC Process 50
5.3 Macroscopic Model 53
  5.3.1 Governing Equations of Macroscopic Model 53
  5.3.2 Spatial Discretization 55
  5.3.3 Boundary Conditions 57
5.4 Coupling of the Mesoscopic and the Macroscopic Models 57
  5.4.1 LRBFCM-CA and LRBFCM-PA Transfer of Temperature ... 59
5.5 Mesoscopic Model 60
  5.5.1 Nucleation Process 60
  5.5.2 Growth Process 62
    5.5.2.1 Numerical Treatment of the KGT Model 62
  5.5.3 Impingement Process 63
5.6 Solution of the Mesoscopic Model by the CA 63
  5.6.1 LRBFCM-CA 63
    5.6.1.1 Neighbourhood Configuration and Mesh in the CA Method 66
  5.6.2 LRBFCM-PA 66
    5.6.2.1 Neighbourhood Configuration and Node Arrangement in the PA Method 68

6 Dendritic Growth Model 69

6.1 Governing Equations 69
  6.1.1 Temperature Field 70
6.2 Phase Change Kinetics 71
  6.2.1 Interface Undercooling 71

- 6.2.2 Dendritic Growth Kinetics 71
- 6.2.3 Thermodynamic Anisotropy 71
- 6.2.4 Kinetic Anisotropy 72
- 6.3 Coupling Scheme 72
- 6.4 Solution of the Temperature Field 73
- 6.5 Solution of the Solid Fraction Field 74
  - 6.5.1 Definition of Mesh and Neighbourhood Configuration 74
  - 6.5.2 Mesh and Neighbourhood in the CA Method 74
  - 6.5.3 Mesh and Neighbourhood in the PA Method 76
- 6.6 Curvature Calculations 77
  - 6.6.1 Calculation of Curvature in the CA Method 77
  - 6.6.2 Calculation of Curvature in the PA Method 77
- 6.7 Phase Change 80
- 6.8 FDM-PA-FDM Transfer of Temperature and Solid Fraction 81
  - 6.8.1 FDM-CA/PA Transfer of Temperature 81
  - 6.8.2 CA/PA-FDM Transfer of Solid Fraction 82

7 Numerical Results 83

- 7.1 Numerical Results of the ECT/CET by the CA Method 83
  - 7.1.1 Mesoscopic Model Input Parameters 85
    - 7.1.1.1 Nucleation Parameters Sensitivity Study 85
    - 7.1.1.2 Neighbourhood Configuration Sensitivity Study 85
  - 7.1.2 Macroscopic Model Input Parameters 90
    - 7.1.2.1 Simulated Results for Variable Casting Parameters ..95
- 7.2 Numerical Results of the ECT/CET by the PA Method 96
  - 7.2.1 A Sensitivity Study of Meso Input Parameters 97
- 7.3 Numerical Results of the Dendritic Growth 100
  - 7.3.1 Problem Definition and Discretization 101
  - 7.3.2 Simulated Results by the CA Method 103
    - 7.3.2.1 Discussion of the Results 105
  - 7.3.3 Simulated Results by the PA Method 113
    - 7.3.3.1 Discussion of the Results 115

8 Summary and Conclusions 141

- 8.1 Summary of the Main Contributions 141
  - 8.1.1 ECT/CET Macro-Mesoscopic Model 141
  - 8.1.2 Dendritic Growth Model 143
- 8.2 Technological Relevance 144
- 8.3 Conclusions and Future Work 144

Appendix A 147

A.1 Database of Measurements from Štore Steel Company 147
A.2 Meshless Solution Procedure of the Macroscopic Heat Transfer Model 166
Bibliography **169**

List of Figures

1.1 Schematics of the ECT and CET occurring during the CC of steel with three characteristic zones (chill, columnar and equiaxed one). 9
1.2 Dendritic structures. Left: single dendrite, right: several dendrites growing simultaneously. 11
2.1 Graphical representation of the continuous nucleation model. 15
2.2 Graphical representation of the instantaneous nucleation model. 15
2.3 Schematics of the growth morphologies. Left: view from the front, right: view from the side. 18
2.4 Concentration field for the dendrite having a parabolic shape. 19
2.5 Dendrite having a parabolic shape. 20
3.1 Conventional CA model discretization. 30
3.2 Random PA model discretization. 31
3.3 The von Neumann neighbourhood configuration with 4 neighboring cells. 32
3.4 The Moore neighbourhood configuration with 8 neighboring cells. 32
3.5 The modified Moore neighbourhood configuration with 6 neighboring cells 33
3.6 The modified Moore neighbourhood configuration with 6 neighboring cells 33
3.7 A newly introduced neighbourhood configurations to model the grain growth evolution. 34
3.8 Example of 2D PA neighbourhood configuration. 35
3.9 Example of 3D CA neighbourhood configurations. Left: Moore, right: von Neumann. 35
3.10 Example of 3D PA neighbourhood configuration. 35
4.1 Example of a 2D distribution of grains and CA cells. Different colors represent different grains with different orientations, respectively. 41
4.2 A definition of the neighbourhood configuration for the CA method. 41
4.3 Calculation of the grain boundary displacement in the boundary CA cell. 42
4.4 Example of irregular CA distribution of cells based on the Voronoi

tessellation computed from the random distribution of points. Different colours represent different grains with different orientations... 45
4.5 A definition of the neighbourhood configuration for the irregular CA method. ... 46
5.1 Grain structure occurring during CC of steel (Štore Steel company). Billet of dimension 180 mm, 25MoCr4, $T_{cast} = 1545\,\mathrm{K}$ and $V_{cast} = 1.12\,\mathrm{m/min}$. ... 49
5.2 Scheme of the CC of steel. ... 51
5.3 CC of steel: the ladle (Štore Steel company). ... 52
5.4 CC of steel: the tundish (Štore Steel company). ... 52
5.5 CC of steel: the billet (Štore Steel company). ... 52
5.6 Macro heat transfer simulator. ... 54
5.7 Slice traveling schematics of the billet. ... 56
5.8 Flowchart of the ECT/CET model. ... 58
5.9 Scheme of the transfer of temperature from the macroscopic to mezoscopic discretisation (circles represent the macro nodes, black square represents the CA cell). ... 59
5.10 Left: Relationship between the macro node arrangement and, right: meso CA mesh. Solid circles in the macro node arrangement represent schematics of the corner, surface and bulk 5-noded domains of influence of the meshless method. ... 60
5.11 Surface and bulk area. ... 61
5.12 Nucleation curves for the surface and bulk area. ... 61
5.13 The explanation of growth stage, see also Table 5.1. ... 64
5.14 Left: growth front will not reach the closest neighbour $c_{i,j} = \left\{ c_{i+1,j+1} \right\}$ - the cell will not be trapped $d < 1$, right: growth front will reach the closest neighbour $c_{i,j} = \left\{ c_{i+1,j+1} \right\}$ -the cell will be trapped $d \geq 1$ and becomes solid. ... 65
5.15 Left: growth front will not reach the closest neighbour $c_{i,j} = \left\{ c_{i+1,j} \right\}$. The cell will not be trapped $d < 1$, right: growth front will reach the closest neighbour $c_{i,j} = \left\{ c_{i+1,j} \right\}$. The cell will be trapped $d \geq 1$ and becomes solid. ... 65
5.16 Growth front will not reach the closest neighbour. The point will not be trapped $d < 1$ ... 67
5.17 Growth front will reach the closest neighbour. The point will be trapped $d \geq 1$ and becomes solid. ... 67
5.18 Left: Relationship between macro field and, right: PA node arrangement. Solid circles in the macro field represent schematics of

the corner, surface and bulk 5-noded domains of influence of the meshless method. 68
6.1 Calculation domain of the dendritic growth. 72
6.2 Flowchart of the thermal field and solid fraction calculations. 73
6.3 Schematics of space discretization. Top: FDM nodes with $N_{xy} = 21$, middle: CA cells with $n_{xy} = 20$, bottom: PA nodes for $n_{xy} = 20$. 75
6.4 Schematic representation of the relationship between FDM nodes (4 corners), CA cell (centre) and the random PA node 76
6.5 Scheme showing a circle sample with $R_c = 2a$ for calculating the curvature in the conventional CA method (example: $N_{s\,CA} = 8$ and $N_{t\,CA} = 12$). 78
6.6 Scheme showing a circle sample with $R_c = 2a$ for calculating the curvature in the random PA method (example: $N_{s\,PA} = 7$ and $N_{t\,PA} = 11$). 78
6.7 Scheme of the area used to compare the curvature calculations by the CA and PA methods. $R = 10\,\mu$m and $a = 1\,\mu$m. Green area represents solid, white area represents liquid. 79
6.8 Calculated curvature with the CA method and PA-(A) method $(\varepsilon = 0.49)$ for $R_c = 1\,\mu$m and $a = \overline{a} = 1\,\mu$m with respect to the data depicted in Figure 6.7. The node arrangement of CA and PA is given in Table 7.6. 79
6.9 Calculated curvature with the CA method and PA-(A) method $(\varepsilon = 0.49)$ for $R_c = 5\,\mu$m and $a = \overline{a} = 1\,\mu$m with respect to the data depicted in Figure 6.7. The node arrangement of CA and PA is given in Table 7.6. 80
6.10 Schematic representation of the shape function (parameters see Table 7.3). 80
6.11 Relationship between four FDM nodes and a CA cell (left) and PA node (right) for calculation of the temperature. 81
6.12 Relationship between FDM node and four neighbouring PA nodes or CA cells for transfer of the solid fraction. 82
7.1 Centerline temperatures along the casting direction (reference case).
7.2 Corner temperatures along the casting direction (reference case). 87
7.3 Centerline temperatures along the casting direction (reduced casting temperature) 87
7.4 Corner temperatures along the casting direction (reduced casting temperature). 87

7.5 Centerline temperatures along the casting direction (reduced casting speed). 88
7.6 Corner temperatures along the casting direction (reduced casting speed). 89
7.7 Input data to the ECT/CET model. 89
7.8 Calculated billet microstructures as a function of the changeable micro parameters (see Table 7.1 and 7.2) for the Nastac's neighbourhood configuration (see Figures 3.3-3.6), heat 46352 with dimension 140 mm x 140 mm. 91
7.9 Calculated billet microstructures as a function of the changeable micro parameters for the simplified neighbourhood configuration (see Figure 3.7), heat 46352 with dimension 140 mm x 140 mm. 92
7.10 Comparison of two different neighbourhood configurations. Left: Nastac's neighbourhood, right: simplified one for the same nucleation and growth parameters (CASE VI). 93
7.11 Baumann print of the 51CrMoV4 spring steel (see Table A.2), ECT between chill and columnar (dashed line) and CET transition between columnar and central zone (dotted line). 93
7.12 Characteristic mesostructure of the heat 46352 after some periods of time for the following casting parameters. Left: T_{cast} = 1500 K, V_{cast} = 1.75 m/min (periods of time: 1 min, 2 min, 3 min, 4 min, 5 min, 5 min 33 s from the top to the bottom), middle: T_{cast} =1530 °C, V_{cast} = 1.75 m/min (periods of time: 1 min, 2 min, 3 min, 4 min, 5 min, 5 min 55 s from the top to the bottom), right: T_{cast} = 1530 °C, V_{cast} = 1.00 m/min (periods of time: 1 min, 2 min, 3 min, 4 min, 4 min 36 s from the top to the bottom). 94
7.13 Left: Baumann print of the 51CrMoV4 spring steel (see Table A.2), T_{cast} = 1525 K, V_{cast} = 0.95 m/min, dimension 180 mm, right: simulated result. 95
7.14 Left: Baumann print of the 51CrMoV4 spring steel (see Table A.2), T_{cast} = 1529 K, V_{cast} = 1.15 m/min, dimension 180 mm, right: simulated example. 95
7.15 Left: Baumann print of the 51CrMoV4 spring steel (see Table A.2), T_{cast} = 1550 K, V_{cast} = 1.10 m/min, dimension 180 mm, right: simulated example. 96
7.16 Left: Baumann print, right: simulated result with the PA method. Black circle represents approximate position of CET (51CrMoV4). 97
7.17 Simulated grain structure ECT and CET of the billet by PA method, $R_H = 1.2\text{x}10^{-3}$ m, node density 90 % of CA grid. 98

7.18 Simulated grain structure ECT and CET of the billet by PA method, $R_H = 3.0\text{x}10^{-3}$ m, node density 90 % of CA grid. 98
7.19 Simulated grain structure ECT and CET of the billet by PA method, $R_H = 1.2\text{x}10^{-3}$ m, node density 70 % of the CA grid. 99
7.20 Simulated grain structure ECT and CET of the billet by PA method, $R_H = 3.0\text{x}10^{-3}$ m, node density 70 % of CA grid. 100
7.21 Simulated results. Left: conventional CA method, right: PA method. Black circle represents approximate position of CET. 100
7.22 Geometry and initial conditions. 102
7.23 Structure of the dendritic growth model. 103
7.24 Simulated dendritic growth for a single dendrite at orientation $\theta_{def} = 0^\circ$ by the CA method with different fluctuations. 108
7.25 Vertical cross section of the temperature field for Case 2 at y =175 μm. 108
7.26 Simulated dendritic growth for a single dendrite at orientation $\theta_{def} = 45^\circ$ by the CA method. 109
7.27 Effect of different curvature calculation radius $R_c = 4$ and $R_c = 12$ cell size (from the top to the bottom). 110
7.28 Effect of different values of the average Gibbs-Thomson coefficient $\overline{\Gamma} = 1.6\text{x}10^{-5}$ Km and $\overline{\Gamma} = 1.6\text{x}10^{-6}$ Km (from the top to the bottom)......111
7.29 Seven dendrites growing simultaneously at orientations 0° and 45° after (1) 350, (2) 700, (3) 1500 and (4) 2500 time steps of the length $6.82\text{x}10^{-10}$ s. FDM-CA solution procedure, see Table 7.5. 112
7.30 Simulated dendrites with different orientations by the PA method for the same PA-(A) random node arrangement. 122
7.31 The lengths of the dendritic branches in x and y directions for ten orientations, random node arrangement PA-(A), (see Figure 7.30). 123
7.32 The lengths of the dendrite branches in x and y directions at different orientations $\theta_{def} = 5^\circ, \theta_{def} = 15^\circ$ and $\theta_{def} = 30^\circ$ (from the top to the bottom), for the random node arrangements (see Figures 7.33-7.35). 124
7.33 Simulated dendritic growth at orientation 5° with different random node arrangements: PA-(B), PA-(C), PA-(D). 127
7.34 Simulated dendritic growth at orientation 15° with different random node arrangements: PA-(B), PA-(C), PA-(D). 128
7.35 Simulated dendritic growth at orientation 30° with different random node arrangements: PA-(B), PA-(C), PA-(D). 130
7.36 Simulated dendritic growth at orientation $\theta_{def} = 5°$ for the different node arrangements randomness $\varepsilon = 0.1$, $\varepsilon = 0.25$, $\varepsilon = 0.49$ 132

7.37 Simulated dendritic growth at orientation $\theta_{def} = 30°$ for different node arrangement randomness $\varepsilon = 0.1$, $\varepsilon = 0.25$, $\varepsilon = 0.49$ 133
7.38 Simulated dendritic growth by the PA method with randomness growth correction factor 1.25 for PA-(B)-F, PA-(C)-F, PA-(D)-F node arrangements (from the top to the bottom). 135
7.39 Simulated dendritic growth by the CA method, PA method and PA method with randomness growth correction factor (from the top to the bottom). 137
7.40 Seven dendrites growing simultaneously at orientations 0° and 45° (see Tables 7.3 and 7.8) after (1) 350, (2) 700, (3) 1500 and (4) 2500 time steps of the length $6.82\text{x}10^{-10}$ s by the FDM-PA method (such a simulation is not possible with the FDM-CA method). 138
7.41 Seven dendrites growing simultaneously at different orientations (see Table 7.7) after (1) 350, (2) 700, (3) 1500 and (4) 2500 time steps of the length $6.82\text{x}10^{-10}$ s by the FDM-PA method. 139
A.1 Left: Baumann print, right: simulated result for steel 51CrMoV4, dimension 140 mm, $T_{cast} = 1530\,\text{K}$ and $V_{cast} = 1.75\,\text{m/min}$ (Reference case, heat 46352). 149
A.2 Centerline and corner temperatures along the casting direction (heat 46352). 150
A.3 Left: Baumann print, right: simulated result for steel 51CrV4+Mo, dimension 180 mm, T_{cast} = 1522 K and V_{cast} = 0.95 m/min. 151
A.4 Centerline and corner temperatures along the casting direction (heat 48807 3/II). 152
A.5 Left: Baumann print, right: simulated result for steel 51CrV4+Mo, dimension 180 mm, T_{cast} = 1520 K and V_{cast} = 1.15 m/min 153
A.6 Centerline and corner temperatures along the casting direction (heat 48807 3/IV). 154
A.7 Left: Baumann print, right: simulated result for steel 51CrV4+Mo, dimension 180 mm, $T_{cast} = 1524\,\text{K}$ and $V_{cast} = 0.95\,\text{m/min}$. 155
A.8 Centerline and corner temperatures along the casting direction (heat of 48695 3/I). 156
A.9 Left: Baumann print, right: simulated result for steel 51CrV4+Mo, dimension 180 mm, T_{cast} = 1525 K and V_{cast} = 1.15 m/min. 157
A.10 Centerline and corner temperatures along the casting direction (heat 48695 3/III). 158
A.11 Left: Baumann print, right: simulated result for steel 52CrMoV4o, dimension 180 mm, T_{cast} = 1522 K and V_{cast} = 1.05 m/min. 159
A.12 Centerline and corner temperatures along the casting direction (heat 46484/1). 160

A.13 Left: Baumann print, right: simulated result for steel 25MoCr4, dimension 180 mm, T_{cast} = 1545 K and V_{cast} = 1.12 m/min......................161
A.14 Centerline and corner temperatures along the casting direction (heat 46693/1)..162
A.15 Left: Baumann print, right: simulated result for steel 25MoCr4, dimension 180 mm, T_{cast} = 1550 K and V_{cast} = 1.12 m/min......................163
A.16 Centerline and corner temperatures along the casting direction (heat 46693/3)..164
A.17 Baumann print for steel 51CrV4, dimension 180 mm, with EMS. 165
A.18 Baumann pront for steel 51CrV4, dimension 180 mm, without EMS. ...165

List of Tables

5.1 Selection of neighbourhood configuration based on probabilistic calculation of θ for Nastac configurations. 66
7.1 Growth model parameters (heat 46352). 84
7.2 Variable parameters of Gaussian distribution for the Nastac's configuration and simplified configuration of the meso model (Figures 7.8 and 7.9). 90
7.3 Nominal parameters used in simulations. 104
7.4 Parameters varied in the calculations with FDM-CA method. 105
7.5 Initial positions and orientations of nucleuses for simulation with the FDM-CA method (see Figure 7.29). 105
7.6 Parameters varied in the calculations with PA method. 114
7.7 Initial positions and orientations of nucleuses for simulation with the FDM-PA method (see Figure 7.40). 115
7.8 Initial positions and orientations of nucleuses for simulation with the FDM-PA method (see Figure 7.41). 115
7.9 The lengths of dendritic branches in x and y directions with respect to the random node arrangements. 125
A.1 Database of measurements from Štore Steel company. 148
A.2 Material properties - compositions 148

List of Symbols

Latin symbols

a	cell size in CA and PA methods
$\bar{a}$	average node distance in PA method
a_i	length between two random points
a_c	experimental constant (Stefanescu nucleation model)
A_p	cross section of the cylinder (KGT model)
A_h	surface area of the cap (KGT model)
b_c	experimental constant (Stefanescu nucleation model)
c_0	initial concentration (KGT model)
c_l	concentration in the liquid
c_1	constant determined from the boundary condition (KGT model)
c_2	constant determined from the boundary condition (KGT model)
c_s	concentration in the solid
c	constant from derivation (KGT model)
c_p	specific heat
d	distance between two CA cells
D	diffusion coefficient in liquid
$E_1(x)$	exponential integral function
$\mathrm{erfc}(x)$	complementary error function
f_s	solid fraction
f_l	liquid fraction
f_{s0}	function for determination of solid fraction
$f_{s\,PA\,i,j}$	solid fraction in the PA node i, j
$f_{s\,CA\,i,j}$	solid fraction in the CA node i, j
$f_{s\,i,j}$	solid fraction in the FDM node
f_l^V	liquid volume fraction
f_s^V	solid volume fraction
$f_\wp^V$	volume fraction of the phase $\wp$
F	function for definition of Neumann boundary conditions
G	mean temperature gradient at the interface (KGT model)
G_c	concentration gradient in liquid at the interface (KGT model)

h	specific enthalpy
$Iv(\mathrm{x})$	Ivantsov function
$\mathbf{i}$	base vector
J_1	solute rejection flux in hemispherical needle approximation (KGT model)
J_2	flux due to the diffusion in the liquid in hemispherical needle approximation (KGT model)
k	partition coefficient
K	curvature
l	length of the computational domain (dendritic growth)
l_i	distances to the nearest nodes
L	latent heat
m	slope of the liquidus line
m_b	boundary mobility
n_{xy}	number of CA cells in x and y directions
N	number of nucleuses
N_i	number of nucleuses that nucleate at time t_i
N_{xy}	number of FDM points in x and y directions
$N_{s\,tot}$	total number of nucleated crystals
$N_{s\,CA}$	number of solid CA cells inside the circle in curvature calculations
$N_{s\,PA}$	number of solid PA points inside the circle in curvature calculations
$N_{t\,CA}$	total number of CA cells inside the circle in curvature calculations
$N_{t\,PA}$	total number of PA nodes inside the circle in curvature calculations
$\mathbf{n}$	normal on $\partial\Omega$
p	probability
p_d	driving force
Pe	Peclet number
$\mathbf{p}$	position vector
r	radius of nuclei
r_c	equivalent radius
$rand$	random number
R	radius
$R_{\max}$	maximum grain size
$R_{\min}$	minimum grain size
R_H	radius of neighbourhood
R_c	curvature calculation radius
s	fitting parameter (Oldfield nucleation model)
S	factor controlling the number of preferential directions
t	time
t_0	initial time

T	temperature
$\dot{T}$	cooling rate
$T_{i,j}$	temperature in the FDM node i,j
$T_{CA\,i,j}$	temperature in the CA cell i,j
$T_{PA\,i,j}$	temperature in the PA node i,j
T_0	function for definition of initial temperature
T_f	interface undercooling
T_L	liquidus temperature
T_M	melting temperature
T_{macro}	macrostructure temperature from the thermal model
T_N	nucleation temperature (Hunt's nucleation model)
T_p	the nucleation periodic temperature
T_{ref}	reference temperature
T_S	solidus temperature
$w(x)$	the function of contact angle in nucleation model
x	Cartesian coordinate x
y	Cartesian coordinate y
$x_{CA\ i,j}$	x coordinate of CA cell
$y_{CA\ i,j}$	y coordinate of CA cell
$x_{PA\,i,j}$	x coordinate of PA point
$y_{PA\,i,j}$	y coordinate of PA point
$x_{FDM\ i,j}$	x coordinate of FDM node
$y_{FDM\ i,j}$	y coordinate of FDM node
z	z coordinate
v	fitting parameter (Oldfield nucleation model)
V	velocity (rate of interface movement)
V_g^*	the interface growth velocity

Greek symbols

α	thermal diffusivity
γ_1	calculated coefficient (KGT model)
γ_2	calculated coefficient (KGT model)
γ_3	calculated coefficient (KGT model)
δ_t	thermodynamic anisotropy
δ_k	kinetic anisotropy
ΔT	undercooling temperature
$\overline{\Delta T}$	average undercooling temperature
ΔT_c	thermal undercooling (KGT model)
ΔT_r	curvature undercooling

ΔT_{macro}	undercooling temperature in macro nodes
ΔT_{micro}	interpolated undercooling temperature for the CA cells
$\Delta T_{\max}$	mean nucleation undercooling in Gaussian model
ΔT_{σ}	standard deviation in Gaussian model
Δt	time step
Δt_{CA}	time step of CA method
Δt_{PA}	time step of PA method
Δt_{FDM}	time step of FDM method
Δx	distance between nodes in x direction
Δx_b	grain boundary displacement
Δy	distance between nodes in y direction
ε	scaling factor (dendritic growth)
ζ_1	coefficient (KGT model)
ζ_2	coefficient (KGT model)
ζ_3	coefficient (KGT model)
ς_c	stability parameter
η	positive constant in time step calculation
θ	crystallographic angle
θ_{def}	preferential crystallographic orientation
θ_1	contact angle
Γ	Gibbs-Thomson coefficient
$\overline{\Gamma}$	average Gibbs-Thomson coefficient
$\Gamma_{s,l}$	solid/liquid interface
λ	thermal conductivity
λ_i	critical wavelength of the solid-liquid interface
λ^*	scaling value for fluctuations
μ_2	nucleation frequency
μ_3	Dirac delta function
μ_K	interface kinetic coefficient
ρ	density
σ	standard deviation of the length of primary dendritic branches
ψ	thermal fluctuations
Ω_1	solutal supersaturation (KGT model)
Ω	domain
$\partial\Omega$	boundary
$\wp$	phase

Subscripts

CA	cellular automata method
FDM	finite difference method
H	neighbourhood
i, j, k	counters
l	liquid
L	liquidus
max	maximum value
min	minimum value
M	melting
PA	point automata method
s	solid
S	solidus
0	known initial value
x	x direction
y	y direction

Acronyms

CA	Cellular Automata Method
CET	Columnar to Equiaxed Transition
ECT	Equiaxed to Columnar Transition
FDM	Finite Difference Method
PA	Point Automata Method
PFM	Phase Field Method
MC	Monte Carlo Method
RW	Random Walker
rand	random number
surface	surface area
bulk	bulk area
2D	two-dimensions
3D	three-dimensions

1 Introduction

Manufacturing processes such as ingot casting, Continuous Casting (CC), atomization, welding, soldering, etc. involve melting and solidification as an important stage of the process [Flemings, 1974; Beckermann, 2002; Dantzig and Rappaz, 2009; Fredriksson and Akerlind, 2010; Oldfield, 1966]. The thermal and solutal conditions that prevail during the process and the thermodynamic and kinetic constraints of the material determine the final microstructure of the product. The mechanical or functional properties and the microstructure of various phases in turn dictate the performance of the final component. Prediction of microstructure evolution in solidification is an important key factor in controlling solidification structures. However, it is difficult to predict the structure features because they are determined through the complicated solidification mechanisms. Solidification phenomena involve many physical phenomena such as heat and mass diffusion, dendritic morphology, capillary effects, etc. These phenomena interact with each other and predominate at different length scales [Stefanescu, 2009]. It is well known that in order to control this formation in practise means understanding the connection between process parameters and microstructure evolution. The understanding of such physical relation can only be complete in case it can be explained mathematically and this mathematical representation of the process is called a model. Numerical modelling of the solidification in metallic alloys received a great interest with the development of computing technology and algorithms.

- The macroscale. This scale is of the order of millimeter to meter and the macro-features of castings such as shrinkage cavities, macrosegregation due to fluid flow, cracks and casting dimensions are predicted.
- The microscale. This scale is of the order of micrometer to millimeter. The features predicted in this scale include the grain size distribution, dendritic features, phase distribution, microsegregation and porosity. The mechanical properties of final product are directly influenced by these micro level features.
- The nano scale. This scale is of the order of nanometers. Nanoscale processing of materials includes techniques such as rapid solidification, plasma processing, chemical vapor deposition.

There is a growing interest in computational modelling of the microstructure level in order to be able to predict the properties of the product and optimize its production with respect to productivity, quality and environmental impact. The properties of the product can be calculated through a combination of the macroscopic and microscopic models. The macroscopic models calculate the relations between the process parameters and the macroscopic variables, such as temperatures, concentrations, and velocities on the scale of the process (casting, rolling, heat treatment,…). The microscopic models calculate the relations between the macroscopic variables and the microstructure (grain size, grain concentration, grain stresses and strains,…). In general, solidification growth morphologies of metals can be divided into two primary groups: single-phase primary structures, which may be globular, cellular, and/or dendritic and poly-phase morphologies, such as eutectics. These morphologies, alone or in combination, comprise most solidification microstructures, and have been in the focus of numerous numerical and theoretical studies.

In the dissertation we first give an overview and literature survey of computational modelling of solidification processes at a macro/meso and micro levels. Further chapters are focused on modelling microstructure evolutions.

1.1 Modelling of Microstructure

Researchers have observed, analyzed, and modelled microstructural evolution for over a century [Asta *et al.*, 2009]. The advances in computer technology and numerical methods have made it possible to analyze transport phenomena to a high level of details.

In the past two decades, the fundamental understanding of solidification microstructures has vastly improved mainly due to: development of mathematical models and simulation techniques, aided by powerful computers, and development of refined experimental techniques with better visualization and characterization of microstructural development, thereby providing useful data to validate the models. The experimental techniques, analytical models and numerical models have been developed to help understand the evolution of grain growth in solidification of alloys. A lot of experimental work has been reported on the grain morphology of transparent materials [Bruncko *et al.*, 2003; Mathiesen and Arnberg, 2006; Haghighat and Taheri, 2007; Atamanenko *et al.*, 2007]. Many complex models have been developed to predict texture, misorientation distribution and grain size distribution of a final rolled or extruded product [Raabe *et.al.*, 2004]. But there are still many difficulties remaining. Microstructural evolution is a many variable and a multiscale problem and even simple phenomena are still not well understood. Due to the difficulty of directly incorporating topological features into mathematical models there has been increasing interest in using computer simulation to study and predict the microstructure evolution in a range of technologically important materials. A progress of that knowledge has, in turn, developed various kinds of deterministic and stochastic models to predict the evolution of microstructures in solidification.

Computational simulations of evolving microstructures have been performed for approximately half a century, beginning with Fullman [Fullman, 1952], who simulated grain growth in a polycrystal. He did all his calculations manually and his model is referred to as vertex model. Later Soares *et al*. [Soares *et al*., 1985] and Kawasaki *et al.* [Kawasaki *et al.*, 1989] improved his model by modifying the equation for the velocity of the vertex. Their complete equation of motion states that the vertex does not always move in the direction of the line tension resultant at its position. The most common micro models for microstructural evolution are nowadays: Potts models [Potts, 1952], front tracking models, Vertex models [Weaire and Kermode, 1983], Phase Field Methods (PFM), Monte Carlo (MC) [Anderson *et al.*, 1984; Anderson *et al.*, 1984], Random Walker (RW) [Chorin,1973], and Cellular Automata (CA) [Raabe, 2002]. Unfortunately, each of these models has some advantages and some restrictions as well. In this work only three areas, where the most significant advancements have taken place, are shortly introduced: principles atomistic calculations, deterministic modelling of the temporal microstructure evolution by PFM and stochastic methods by MC and CA. The basic characteristic of these models have been summarized from the article [Chen *et al.*, 2001].

First-principles atomistic calculations. First principles atomistic calculations [Gosalvez *et al.*, 2008], based on density-functional theory, do not rely on empirical input and hence are predictive in nature. These methods yield quantities related to the electronic structure and the total energy of a given system, and may be used to accurately predict zero temperature phase stabilities of alloys and compounds. By combining first-principles techniques with the statistical mechanics methods one opens the possibility of exploring, without any fitting parameters, thermodynamics phenomena such as phase transformation temperatures and phase diagrams. Furthermore, these approaches are applicable to any phases of a given alloy system, not only the equilibrium phases. Hence, first-principles techniques can provide a method to obtain properties of metastable phases, which are often crucial to mechanical properties (e.g., strengthening precipitates) but are difficult to isolate and study experimentally.

Deterministic models. Deterministic models treat space, time and other variables in continua, and the outcome of the calculation is fully determined by the boundary and initial conditions. These models bring an identical solution each time, for a given set of calculation conditions and can be very useful predictive tools. These models are usually based on continuum modelling where partial differential equations are derived. The conservation equations are solved to predict phase motion, solid/liquid interface motion and shrinkage of the casting. Analytical models describing dendrite tip characteristics [Hunt, 1979; Kurz and Fisher, 1981] and eutectics fall into this category.

In this group, recent modelling approach, the PFM, is being used extensively to simulate dendritic, eutectic and peritectic microstructures [Fan and Chen, 1997; Chen, 2002]. PFM are known as one of the most adequate deterministic models for directly simulating the dendritic growth morphology. In this method, two conservation equations - the heat or solute diffusion equation and the PFM diffusion equation are solved to track the phase field variable. The PFM variable represents the solid or liquid phase and the interface is tracked implicitly through the solution of the two parabolic equations. However, PFM are presently limited to qualitative simulation of a single dendrite or a very small calculation domain due to the large computational capacity needed. In order to study the interactions of the dendritic growth in many grains in a solidifying mushy region, a large calculation domain has to be considered, which surely will be a very difficult task in the phase field methods. Some mesoscopic models for dendritic growth are currently under development. Steinbach *et al.* [Steinbach *et al.*, 1998] used a novel mesoscopic simulation technique to describe the non-steady growth of several equiaxed dendritic grains into a supercooled melt of a pure substance. However, it is clear that their model cannot account for the topology and texture evolution of a typical columnar structure.

Deterministic models suffer from several limitations. As the complexity of the physical system increases, the analytical models require many assumptions and are unable to capture the behavior of the real physical system. In the deterministic models the grains are assumed to remain spherical even in the strong thermal gradient, columnar structures and Equiaxed to Columnar Transition (ECT) and Columnar to Equaixed Transition (CET) are usually not accounted for, the competition occurring among grains belonging to the columnar zone and the associated evolution of their crystallographic texture are not described at all [Gandin *et al.*, 1995]. For these reasons the simulations of the grain structure formation has been approached using stochastic models which have been developed over the past several years.

Stochastic models. In stochastic models, the physical phenomena are described by using random numbers. As a consequence, the outcome of a simulation can vary among each simulation. The MC, RW and CA method have been usually applied to the prediction of macroscopic grain structures. The MC method has been used to predict the solid-state transformation such as recrystallization or grain growth, whilst the CA model that accounts for the dendritic growth kinetics has been applied to simulate the solidification grain structures and the CET.

The first MC procedure model was developed by Anderson *et al.* [Anderson *et al.*, 1984] for the prediction of grain growth in solid. This method is based on minimization of the interfacial energy (between liquid/solid or between two different grains) and by allowing transition between two states according to the randomly generated numbers. By using this method, Spittle and Brown [Spittle and Brown, 1989] were able to produce computed two-dimensional solidification grain structures, in particular the selection of grains in columnar zone and the CET transition. The microstructures were similar to the observed experimental microstructures. However, these methods suffer from a lack of physical basis. Although they qualitatively demonstrate some phenomena, such as the effect of solute saturation or melt superheat, they cannot be straightforwardly used for quantitative analysis of the effects of various physical phenomena. In particular they do not account easily for the growth kinetics of dendrite tips and for the preferential growth directions of the dendrite.

CA were first introduced by von Neumann in 1951 [von Neumann, 1951], and later on in 1986 by Wolfram [Wolfram, 2002] to a broader scientific public. CA method is based upon the consideration of physical mechanisms on nucleation, growth kinetics of a dendrite tip, and crystallographic orientations. Furthermore, the mechanisms of competitive dendritic growth, embeded directly in the CA algorithm are still under development. So that the CA model can quantitatively carry out the time-dependent simulation for microstructure evolution, in which the individual grains are identified and their shapes and sizes can be shown graphically. A series of studies using the CA model have been reported by Hong *et al.* [Cho and Hong, 1997; Lee and Hong, 1997] on the simulation of solidification structures in squeeze casting and planar flow casting as well as on the prediction of the deflection behaviour of columnar grains solidified in a flowing melt. A detailed introduction to the CA method is given in Chapter 3.

1.2 Application of CA to Modelling of Microstructure

In the last decade, several numerical models, which can solve complicated transport phenomena and phase transformation under different boundary and initial conditions, were developed to calculate various microstructure features of solidifying materials such as grain growth. Application of the CA models, for simulation of the different phenomena in materials, has been significantly increased these days. This approach is known especially in the fields of solidification [Rappaz, 1989; Rappaz and Gandin, 1993; Raabe, 2004], dynamic and static recrystallization [Hurley and Humphreys, 2003; Kumar *et al.*,1998; Hasselbarth and Gobel, 1991; Raabe, 2001], phase transformation [Spittle and Brown, 1994], grain refinement [Janssens *et al.*, 2007], dendritic growth [Brown *et al.*, 1994; Spittle and Brown, 1995; Gandin and Rappaz, 1997; Gandin, 2001] and micro-shear band and shear band propagation [Kugler and Turk, 2006]. CA method has been successfully used in the simulation of solidification microstructure evolution. The main asset of the CA based methods is their ability for a close correlation between the microstructure and the mechanical properties during both micro- and meso-scale simulations. The advantages are that they combine the simplicity and scalability of a switching model with a physical dynamics model [Raabe, 2002]. They are based on less complicated algorithms, simpler for design, implementation and more useful for visualization when compared to known PFM(s).

Rappaz and Gandin [Rappaz and Gandin, 1993] were the pioneering researchers who developed the CA model for modelling microstructure in which nucleation and growth kinetics could be considered and grain structure with certain shapes and size were predicted. Gandin and Rappaz [Gandin and Rappaz, 1994; Gandin and Rappaz, 1997] simulated the grain structure by coupling the CA technique for the grain growth with the Finite Element Method (FEM) solver for the heat flow (FEM-CA). Later Spittle and Brown [Spittle and Brown, 1995] coupled the CA with a Finite Difference Method (FDM-CA) for solute diffusion during the solidification of casting to predict its structure. In their model, the status of an individual cell has only two states, solid or liquid, giving a stepped motion of the interface. Nastac [Nastac, 1999] applied a continuous variable front tracking technique, allowing a smooth evolution of solid fraction within each growing cell. These models not only allow the resolution of grain envelopes, but also of the detailed dendritic structure and solute interactions at the advancing front. Using the model based on the CA technique, Lee and co-workers [Wang *et al.*, 2003; Dong and Lee, 2005] simulated microstructure evolution during solidification process for many materials. And they even developed a model coupling the nucleation and growth of pores and grains [Atwood and Lee, 2003]. These achievements make it possible to model the microstructure evolution of casting solidification process by combining CA with FDM and CA with FEM [Wang *et al.*, 2003; Dong and Lee, 2005; Atwood and Lee, 2003; Brown, 1998; Jarvis *et al.*, 2000; Gandin *et al.*, 1996; Gandin and Rappaz, 1997]. However, the understanding of solidification process and related microstructures is very complicated. This is because it is affected by many interacting phenomena on different scales [Rettenmayr and Buchmann, 2006]. Experiments that allow direct visualization of microstructure formation are difficult to perform.

Among all of the numerical approaches fos studing the microstructure evolution the CA modelling and the PFM modelling [Qin and Wallach, 2003] are the most popular and widely used. In this dissertation we focus on the CA approach for modelling microstructure formation. A considerable progress on solidification microstructure simulation [Boettinger *et al.*, 2000; Lorbiecka *et al.*, 2009; Lorbiecka and Šarler, 2010a; Miodownik, 2002] has been made by the CA approach. The difficulty in developing the CA growth algorithm is that it has to reflect the specific features of the solidifying material. During the growth processes of grains the crystallographic orientation axes of different grains have different divergence angles with respect to the coordinate system. It is well know that the classical CA methods have a tendency to deform the results by introducing the anisotropy associated with the network of cells. Consequences are that they tend to grow only in the grid direction [Zhan *at al.*, 2008]. It does not matter which orientation will be chosen it will always shift the dendrite with respect to the grid axis. In this case the growth stage is difficult to simulate by the CA method. It is because the configuration of the CA mesh has a direct influence on simulated structure and shape. Anderson [Anderson *et al.*, 1984] and later Spittle and Brown [Spittle and Brown, 1989] used a hexagonal, rather than the standard square 2D lattice in order to better represent the grain anisotropy. But in general even now it is still difficult to properly model the preferred crystallographic orientation.

Rappaz and Gandin solved this crystallographic orientation problem [Gandin and Rappaz, 1997] by employing 2D decentered and 3D decentered octahedron CA growth algorithms, developed and coupled with FE heat flow solver which turns out to be complicated. One of their criteria used to validate the CA dendritic growth algorithm is to reproduce the shape of a single grain envelope. The observation of transparent substances like cyclohexanol or succinonitrile has shown that this envelope has an octahedral shape. Based on this observations the CA growth algorithm for modelling dendritic growth was designed to reproduce such envelopes. The model demonstrates its stability to account for different crystallographic orientations and growth kinetics parameters.

Here a simpler approach to this problem, represented by the novel Point Automata (PA) [Lorbiecka and Šarler, 2009, Lorbiecka and Šarler, 2009, Lorbiecka and Šarler, 2009] method is demonstrated. A novel concept of random cellular grid or irregular cellular grid presented in this dissertation follows the CA concept and is able to solve the mentioned crystallographic orientation problem. A basic feature of this method is to distribute nodes randomly in the domain instead of using regular cells, which leads to different distances between the nodes and different neighbourhood configurations for each of them. The method is described in Chapter 3. Janssens published the first concept of PA to the simulation of recrystalization and grain growth but with very limited numerical examples [Janssens, 2003; Janssens, 2010; Janssens *et al.*, 2007]. In 2003 [Janssens, 2003]. Janssens represented the capability of the irregular CA for modelling the evolution of a microstructure transformation including volume and curvature driving pressures and in 2004 Janssens *et al*. [Janssens *et al.*, 2004] presented a hybrid model combining it within diffusion. Lorbiecka *et al.* [Lorbiecka *et al.*, 2009] were the first who coupled the classical CA method with a meshless method instead of the FEM or FDM. This concept has not been previously used in solidification problems. They successfully predicted the grain structure in CC of steel. Subsequently, they replaced the CA method by the PA method in the same physical system [Lorbiecka and Šarler, 2009] and demonstrated the suitability of the PA method for transitions (ECT, CET) in steel billets and dendritic structures. The preliminary results of the dendritic growth based on the PA approach have been presented in [Lorbiecka and Šarler, 2009].

This approach is explained and evaluated in details in the present dissertation where we numerically discuss a simple physical model which can simulate micro-structure formations. The developed numerical models have the capability to simulate the grain structure ECT/CET on the mesoscale and the dendritic growth on the microscale.

1.3 Dissertation Goals and Performed Work

The principal goal of present dissertation is to develop a simulation tool, based on the classical CA method and a novel PA method for modelling the grain structure [Rappaz *et al.*, 1993; Yamazaki *et al.*, 2006] in solidification by using the coupled stochastic mesoscopic and macroscopic physical models, and validation of the model results with the experimental results. The following two numerical models were developed in order to be able to simulate the microstructure formations:

(**1**) the position of ECT/CET which occur during the CC of steel,

(**2**) thermal dendritic growth of pure metals.

The calculations were in both classes of processes done by the conventional CA method with rectangular polygon mesh structure and by the newly developed PA approach based on the irregular positions of the nodes (see Chapters 5 and 6).

Ad.1: *Mesoscopic model to simulate ECT and CET* (see Chapters 5 and 7). This numerical model was developed for the simulation of the solidification grain structure formation ECT/CET during the CC process of steel billets (Figure 1.1). The mesoscopic model encompasses three theoretical stages occurring during the solidification: nucleation, growth and impingement. The CA microstructure model is combined with the macroscopic heat transfer simulator. The heat transfer model is solved by the meshless technique by using the Local Radial Basis Function Collocation Method (LRBFCM) [Šarler *et al.*, 2006]. Related simulator calculates the temperatures for the steel billet for the selected alloy which need to be transferred to the mesoscopic CA model over the time. The CA model is based on the Nastac's definition of neighbourhood [Nastac, 2004], Gaussian nucleation rules [Lee and Hong, 1997] and Kurz-Giovanola-Trivedi (KGT) growth model [Kurz, Giovanola and Trivedi, 1986; Kurz and Fisher, 1998]. Finally, the CA algorithm for ECT/CET has been replaced by the PA method. The transition rules are described and the numerical results presented.

The numerical results are performed for the classical LRBFCM-CA and the novel LRBFCM-PA approach. For the both methods all numerical results have been carried out for the nominal casting conditions $T_{cast} = 1530\ \mathrm{K}$ and $V_{cast} = 1.75\ \mathrm{m/min}$, for the steel billet of heat 46352 from Štore Steel [http://www.store-steel.si/] with dimension 140 mm x 140 mm and alloy type 51CrMoV4. In the present study the mesoscopic model parameters have been adjusted with respect to the experimental data. The sensitivity study of the microstructure mode, solved by the LRBFCM-CA method has been introduced with respect to the nucleation parameters and simplified neighbourhood configuration, casting temperature and casting speed. Proper response of the multiscale model with respect to the measured grain structures in the Štore Steel company, has been demonstrated.

In Appendix 1 several additional simulations are presented for assessment of the influence of casting parameters on the dimension of three characteristic zones: chill, columnar and equaixed and compare with the database of measurements from the Štore Steel. The Baumann prints of billet with dimension 140 mm and 180 mm, are represented.

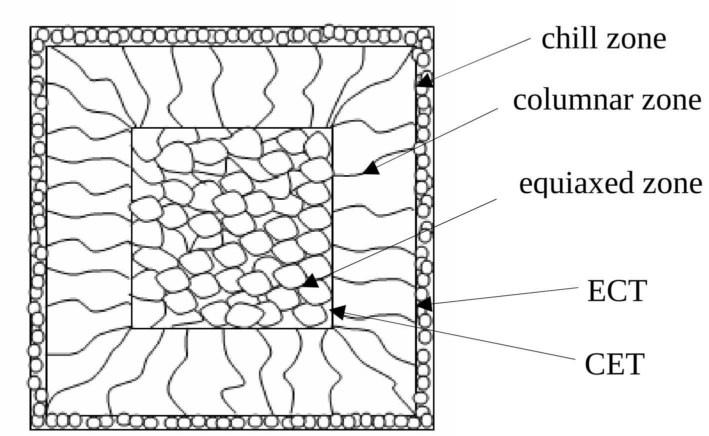

Figure 1.1: Schematics of the ECT and CET occurring during the CC of steel with three characteristic zones (chill, columnar and equiaxed one).

The available measurements casting correspond to speed range from 0.9 m/min to 1.75 m/min and casting temperature range from 1520 K to 1550 K. According to the received samples, the influence of macro input parameters, for the formation of grain structures during the CC of steel, were studied. From the technical reports [Manojlović, 2007; Manojlović, 2008] the following heats were analyzed: 48695 3/I, 48695 3/III, 48807 3/II and 48807 3/IV for the different casting speeds and 46484/1, 46484/3, 46693/1 and 46693/3 for the different casting temperatures. Other measurements (18 out of 32) were rejected because of the bad quality of the samples or not entirely known casting parameters.

For the PA method all numerical results have been carried out for the nominal heat 46352 with dimension alloy 140 mm x 140 mm and alloy (see Table A.1). The sensitivity study has been done for the following two parameters: for the different values of radius of neighbourhood R_H and different structures of random grids. The input parameters have been adjusted with respect to the experimental data. Finally prepared numerical result for the same macro and micro input parameters for the CA and PA method have been compared to the experimental data for the heat 46352.

The results of this part of the dissertation have been published in [Lorbiecka *et al.*, 2009; Lorbiecka and Šarler, 2009; Lorbiecka and Šarler, 2009; Lorbiecka and Šarler, 2010a].

The main goal of this part of this dissertation is a development of the numerical model which predicts the ECT/CET occurring during the CC of steel with respect to the measurements data.

Ad.2: *Microscopic model to simulate thermally driven dendritic growth of pure metals* (see Chapters 6 and 7). The second numerical model represents a simple physical system where one or more thermal dendrites grow from the undercooled melt at a predefined position and orientation (Figure 1.2). In order to predict the dendritic structure, the solution was combined with the deterministic model for calculation of the temperature field. The stochastic model includes calculations of the interface temperature, curvature, Gibbs-Thomson coefficient which takes into account the thermodynamic anisotropy related to the crystal orientation and crystal growth velocity which accounts for the kinetic anisotropy by taking into the consideration the crystal growth direction and the preferential crystallographic orientation. The stochastic model receives temperatures from the deterministic model and the deterministic model receives the solid fraction for the stochastic model. The heat transfer model is solved by the FDM on the regular nodes. The value of the temperature is send to the CA cell which is located exactly in the middle of four FDM nodes. In each time step the nodal values of temperature, based on the status of solid fraction from the CA level of calculations, are updated. The CA method, used to solve the governing equations for dendritic growth, has been in this dissertation replaced by the novel PA method. The differences in implementation are presented and discussed.

The dendritic morphologies were calculated by the classical FDM-CA and the novel FDM-PA approaches. All numerical results were prepared for the same material properties (pure aluminium). The dendritic growth process is simulated by the conventional CA method without and with random fluctuations. For the CA method the thermal fluctuations are included into the calculations of growth velocity. In the PA method, where the calculations are done on the random node arrangement, the random fluctuations replaced by the random positions of the nodes. No other fluctuations are needed. For the FDM-CA method a sensitivity study of radius of neighbourhood, Gibbs-Thomson coefficient and thermal fluctuations, is performed.

For the FDM-PA method the dendritic growth process is first simulated with the same random node arrangement denoted (PA-(A)) for ten crystallographic orientations and then with different random node arrangements (PA-(B), PA-(C), PA-(D)) for three crystallographic orientations. Finally the dendritic growth is simulated with different randomness of the node arrangement $\varepsilon = 0.10$, $\varepsilon = 0.25$ and $\varepsilon = 0.49$.

For the same input parameters the dendritic growth process is simulated by the CA and PA methods at orientation considering to the principal axes of the Cartesian coordinate system. The lengths of x and y branches are different in both cases. This is due to the influence of the random node arrangement in the PA method and subsequent variable distances between the nodes. The growth process is then simulated by including the randomness growth correction factor responsible for the agreement in the lengths of both branches obtained by the CA and PA methods.

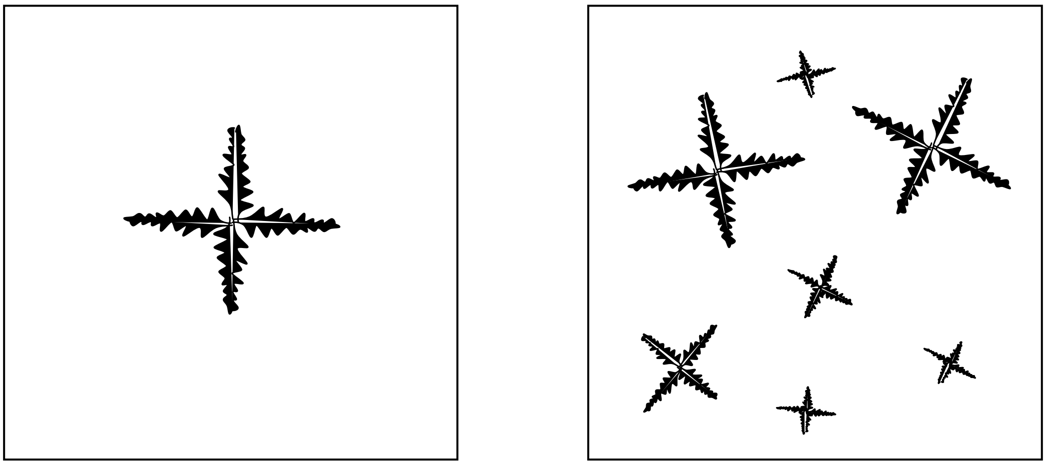

Figure 1.2: Dendritic structures. Left: single dendrite, right: several dendrites growing simultaneously.

The results of this part of the dissertation have been published in [Lorbiecka and Šarler, 2009; Lorbiecka and Šarler, 2009; Lorbiecka and Šarler, 2010b; Lorbiecka and Šarler, 2010c].

The main goal of this part of the dissertation is a development of the numerical model which simulates thermally driven dendritic growth of pure metals from the undercooled melt at a predetermined positions and orientations by the novel PA method.

1.4 Overview of the Dissertation

- In Chapter 2 a review of the main physical phenomena, occurring in solidification of metallic alloys, is presented. In the first part we give an overview of the nucleation models following the description of the growth process. Subsequently, the derivation of the KGT model which is used in the mesoscopic calculations, is presented.
- In Chapter 3 the definition and application of the CA method is presented. In the second part of the chapter we give an introduction to the novel PA method. The comparison of two methods is given in detail.
- In Chapter 4 we first list the common problems occurring during the CA modelling. Next the application of the regular CA and irregular CA method (PA method) for modelling the recrystallization is discussed. The Janssens concept of the PA method to simulation of grain growth is shortly presented. Only his theoretical part of the novel method is given, without any numerical examples.
- In Chapter 5 the development of a new simulation tool for modelling the grain structure in solidification processes is described. In this chapter we present the numerical mesoscopic model which is designed to be able to simulate the positions of the ECT and CET. First the procedures responsible for coupling the macroscopic heat transfer model with the mesoscopic model are demonstrated in details. Then the attention is focused on the governing mesoscopic equations which are solved by the classical CA method and by the novel PA method. The differences in numerical implementation of both approaches are presented.
- In Chapter 6 we give an overview of the numerical model which can simulate the dendritic forms during the solidification of a pure substance from its supercooled melt. The coupling scheme of the explicit FDM with the CA and PA method is presented. In addition the solution of governing equations by the FDM-CA and FDM-PA method is given.
- In Chapter 7 many numerical examples of the two developed models are presented. The calculations are in both cases done by the conventional CA method with rectangular polygon mesh structure and then by the newly developed PA approach, based on the irregular positions of the nodes. Each set of the results is accompanied with a detailed discussion.
- Finally, Chapter 8 represents the summary of the achievements and future directions as well as possible improvements of the models.

2 Introduction to the Solidification Theory

Control of solidification microstructure is an important aspect for the control of the properties and quality of final casting products in modern casting technology. Computational prediction of microstructure evolution in solidification of alloys is a key factor in controlling solidification microstructure. In modelling the microstructure evolution two perspectives can be taken into the consideration: the physical aspect, which means the quantitative understanding of physical phenomena and the practical aspect which is very important application of solidification models into practice.
The basic theories of the solidification process are well described by Flemings [Flemings, 1974], Kurz and Fischer [Kurz and Fischer, 1998], Dantzig and Rappaz [Dantzig and Rappaz, 2009]. Solidification represents a phase transformation where a liquid turns into a solid when it is cold enough. It starts when the melt cools and reaches the liquidus temperature. The rate of this phenomena is mainly determined by the rate of heat extraction from the system, the driving force for nucleation and the growth of crystals from undercooling. The main purpose of this process is in generation of temporal and spatial movement of the liquid/solid interface. In order to model the solidification the attention is on theoretical description of the solidification stages: nucleation and growth. These mechanisms have been the focus of many researchers and many theories were suggested [Gandin *et al.*, 1995]. The theoretical part of this phenomena is reviewed and represented in this chapter.

Nucleation stage (formation of tiny solid nuclei) is described in Chapter 2.1 and growth stage of these nuclei, which finally makes up the final solidified structure, is described in Chapter 2.2.

2.1 Nucleation Stage

Nucleation is the process which initiates the formation of new phases and is a general phenomenon in multiphase system. The fundamental concepts of nucleation are in the focus of such diverse fields as thermodynamics, metallurgy, physical chemistry, solid state physics, surface science, atmospheric physics, geophysics, etc. From the thermodynamics point of view, a necessary condition for formation of the nucleus in the melt is that it must be undercooled, i.e. it needs a temperature that is lower than the melting point T_M or the liquidus temperature T_L. The first step of metal solidification is the formation of tiny, stable, solid nuclei at various positions and orientations in the melt, which in advance start to grow and become crystals (grains). When the temperature of the liquid reaches the assumed undercooling the movements of the atoms in the liquid phase decrease and some small nuclei form (Figures 2.1 and 2.2). Nucleation is an important aspect of microstructure evolution. It affects solidification under-cooling, heat evolution during solidification and the final number of grains. Different types of nuclei available in the melt can be the result of the following processes:

1. Homogeneous nucleation
2. Heterogeneous nucleation
3. Dynamic nucleation

Ad.1
It implies that the growth initiates on substrates having the same chemistry as the solid. It is not common in casting alloys.

Ad.2
It implies that the growth initiates on substrates having different chemistry as the solid. Two distinct models, based on the heterogeneous nucleation theory, have been developed. These are *continuous* and *instantaneous* nucleation models.
The continuous model assumes a continuous dependency of the number of nucleuses N on temperature. Some relations need to be provided to correlate the nucleation velocity $\partial N / \partial t$ with the under-cooling ΔT or with the temperature. A procedure is carried on to determine the final number of nuclei.
The instantaneous model assumes that the new nucleuses generate at the determinate nucleation temperature T_M. Again, in addition the empirical relation needs to be added with respect to the under-cooling temperature or cooling rate, to correlate the final amount of nucleuses. A schematic comparison of these two nucleation models is depicted in Figures 2.1 and 2.2. The equations of heterogeneous nucleation models include many fitting parameters, which need to be assumed or find experimentally.

The most common forms of the *continuous nucleation models* are:

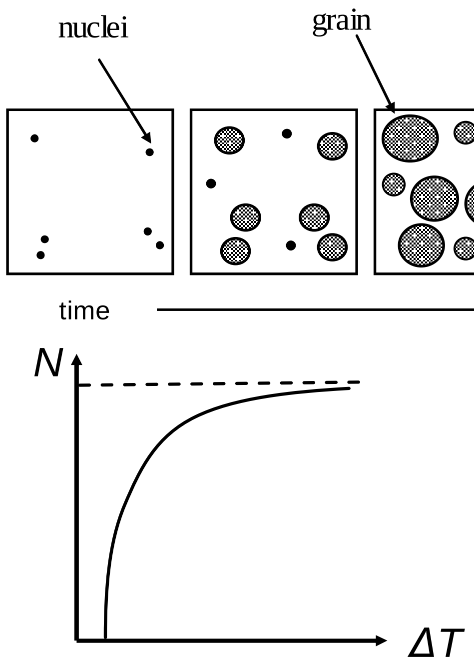

Figure 2.1: Graphical representation of the continuous nucleation model.

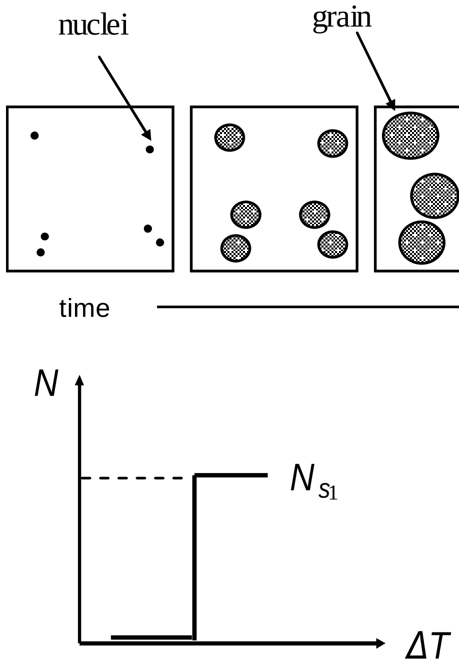

Figure 2.2: Graphical representation of the instantaneous nucleation model.

- Oldfield model [Oldfield, 1966]

$$\frac{\partial N}{\partial t} = -vs\left(\Delta T\right)^{n-1}\frac{\partial T}{\partial t}, \tag{2.1}$$

where v, s, ΔT, T, t, Δt represent the two fitting parameters, the undercooling temperature, temperature, time and time step, respectively.

- Maxwell and Hellawell model [Maxwell and Hellawell, 1975]

$$\frac{\partial N}{\partial t} = \left(N_{stot} - N_i\right)\mu_2 \exp\left[-\frac{w(\theta_1)}{\Delta T^2\left(T_p - \Delta T\right)}\right], \tag{2.2}$$

where N_{stot}, N_i, μ_2, T_p, $w(\theta_1)$, θ_1 represent the total density of nucleated crystals (fitting parameter), the number of nucleuses that have nucleated at time i, the nucleation frequency, the nucleation (periodic) temperature, the classic function of contact angle and the contact angle (fitting parameter), respectively.

- Goettsch and Dantzig (quadratic distribution) model [Goettsch and Dantzig, 1990]

$$N(r) = \frac{3N_{stot}}{\left(R_{\max} - R_{\min}\right)}\left(R_{\max} - r\right)^2, \tag{2.3}$$

where $R_{\max}$, $R_{\min}$, r represent the maximum grain size (fitting parameter), the minimum grain size (fitting parameter) and the given radius of nuclei, respectively.

- Thevoz *et al.* model [Thevoz *et al.*, 1989]

$$\frac{dN}{d\left(\Delta T\right)} = \frac{N_{stot}}{\sqrt{2\pi}\Delta T_\sigma}\exp-\left[\frac{\overline{\Delta T} - \Delta T_{\max}}{\Delta T_\sigma\sqrt{2}}\right]^2, \tag{2.4}$$

where $\overline{\Delta T}$, $\Delta T_{\max}$, ΔT_σ represent the average undercooling temperature, mean nucleation undercooling and the standard deviation, respectively. This model is used in Chapter 5 of this dissertation.

The most common forms for the *instantaneous nucleation models* are:

- Stefanescu *et al.* model [Stefanescu *et al.*,1990]

$$N = a_c + b_c \dot{T}, \tag{2.5}$$

where a_c, b_c, $\dot{T}$ represent the experimental constants and the cooling rate, respectively.

- Hunt model [Hunt, 1984]

$$\frac{\partial N}{\partial t} = N_{stot} \mu_3 \left(T - T_N \right) \tag{2.6}$$

where μ_3 and T_N represent the Dirac delta function and the nucleation temperature, respectively.

Ad.3
The thermosolutal natural convection occuring in front of the columnar mushy zone imposes the dendritic fragmentation in the bulk liquid. It means that the nucleation of the equiaxed grains will depend not only from the heterogeneous substrates, but also on the crystal fragmentation as a result of the dynamic nucleation. This approach is physically more correct than the heterogeneous nucleation, but formulation of these mechanisms would require substantial efforts.

2.2 Growth Stage

The growth of crystals is the second stage of solidification, when the heat is extracted through the solid, and the freezing front is cooled below the equilibrium freezing point. The grain growth simulation encompasses the computation of velocity of solid/liquid interface at dendritic tip. Therefore, the definition of growth velocity at the dendritic tip is important to simulate the grain growth of metal solidification. Solidification growth morphologies can be divided into two primary groups: single-phase primary structures, which may be globular, cellular, and/or dendritic and poly-phase morphologies, such as eutectics [Kurz and Fisher, 1998]. These morphologies comprise most metallic solidification microstructures, and have been in focus of numerous numerical and theoretical studies [Dantzig and Rappaz, 2009]. Three growth forms are usually present in the solidification process: planar, cellular and dendritic (Figure 2.3). For a pure metal, as the driving force for solidification increases, the solidification front undergoes such transitions. When the liquid temperature is higher than the freezing point of the melt and the temperature gradient of the liquid is positive, the solidifying front is known as planar. At higher advance rates, the front develops deep into the liquid and spaces evenly over the front. Ahead of the advancing interface, the liquid develops a negative temperature gradient. This is called cellular growth. At higher velocities still, the cells grow into rapidly advancing (looking like a tree complex) geometry forms called dendritic growth.

The grain growth stage can be presented at least by two analytical models: KGT model and the Lipton-Kurz-Trivedi (LKT) model [Lipton *et al.*, 1987b; Lipton *et al.*, 1987a]. The first one represents the growth process with a positive temperature gradient in the liquid at the solid/liquid interface. LKT mode is able to predict the free dendritic growth into the undercooled melt where the temperature gradient in the liquid ahead of the solid/liquid interface is assumed to be negative.

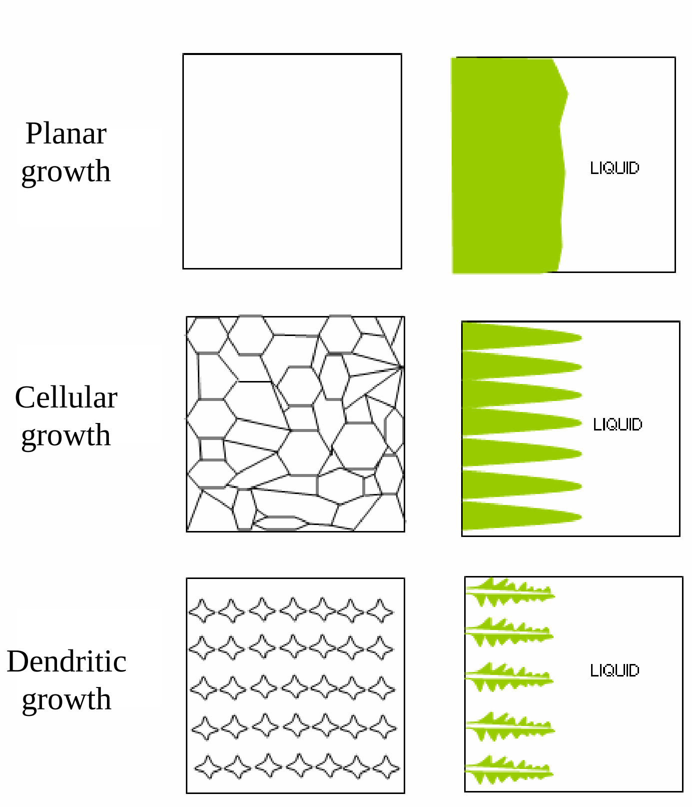

Figure 2.3: Schematics of the growth morphologies. Left: view from the front, right: view from the side.

The growth stage can be described through the analogous theoretical models, which include these two important steps [Stefanescu, 2009]:

1. Derivation of equation which describes the relationship between the scale of microstructure and the undercooling and the growth rate.

2. Choice of the criterion which permits the definition of relationship between the scale of microstructure and the undercooling or the growth rate.

Regarding the first problem it is required to determine the expression for the heat and/or solute distribution. Second step described below can be satisfied by using one of the following two alternative growth criteria:

A. Growth at the extremum, this is the maximum growth rate or the minimum undercooling.
B. Growth at the limit of morphological stability.

In the present dissertation the KGT model was applied (Chapter 5). In the Section 2.2.1 the derivation of the growth velocity equation is presented.

2.2.1 Growth Kinetics of the Dendritic Tip

2.2.1.1 Hemispherical Needle Approximation

A cylinder with a hemispherical tip, growing along the axis, is the simplest approximation which can be made according to cope with the problem of dendritic tip growth. Figure 2.5 presents the cylinder with the cross section $A_p = \pi R^2$ which grows in the time increment dt and which is responsible for the rejection of solute.

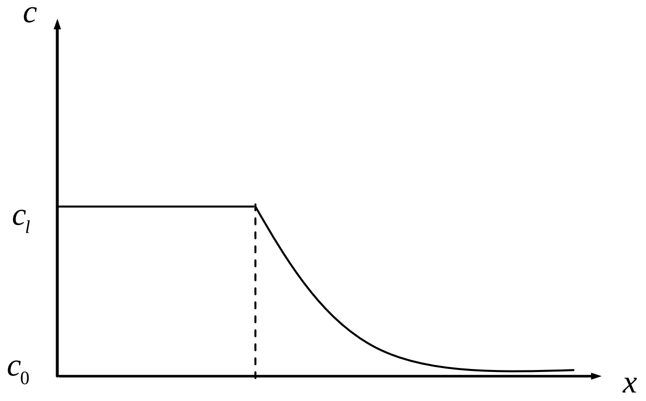

Figure 2.4: Concentration field for the dendrite having a parabolic shape.

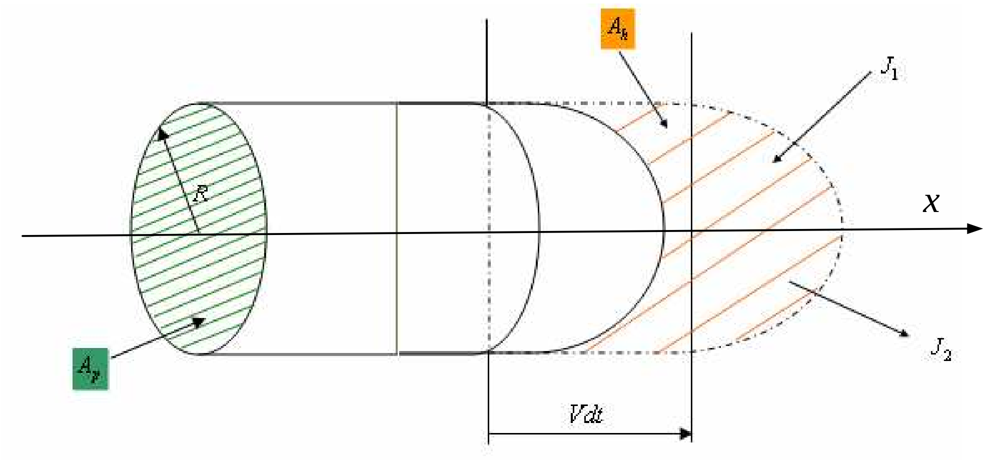

Figure 2.5: Dendrite having a parabolic shape.

The surface area of the cap $A_h = 2\pi R^2$ determines the amount of radial solute diffusion. Fluxes, due to solute rejection J_1 and due to the diffusion in the liquid ahead of the tip J_2, can be identified [Stefanescu, 2009]

$$J_1 = A_p V\left(c_l - c_s\right), \tag{2.7}$$

$$J_2 = -D_l A_h \left(\frac{dc}{dr}\right)_{r=R}, \tag{2.8}$$

where A_p, V, D_l, A_h, c_s represent cross section of the cylinder, velocity (rate of the interface movements), diffusion coefficient in liquid, surface area of the cap and the concentration in the solid, respectively.

Under steady state conditions, both fluxes must be equal, which results in

$$V(c_l - c_s) = -2D_l \left(\frac{dc}{dr}\right)_R, \tag{2.9}$$

with

$$c_s = c_l k, \tag{2.10}$$

where k represents the partition coefficient.

To find the composition gradient at the tip of the grain it is necessary to solve the steady state diffusion equation in radial coordinates with no tangential diffusion

$$\frac{d^2c}{dr^2}+\frac{1}{r}\frac{dc}{dr}=0. \tag{2.11}$$

The general solution of this equation is

$$c=c_1+c_2/r, \tag{2.12}$$

where c_1 and c_2 are constants, determined from the boundary conditions. By appling the following boundary condition

at $r\to\infty$ $c=c_0$ then $c_1=c_0$
at $r=R$ $c=c_l$ then $c_2=R\left(c_l-c_0\right)$

we obtain

$$\left(\frac{dc}{dr}\right)_{r=R}=\left[-\frac{R}{r^2}\left(c_l-c_0\right)\right]=-\frac{c_l-c_0}{R}, \tag{2.13}$$

where c_l, c_0, R represent the concentration in the liquid, initial concentration in the solute and dendritic tip radius, respectively.

Finally, equation (2.9) tip can be rewritten to

$$\frac{VR}{2D_l}=\frac{c_l-c_0}{c_l(1-k)}. \tag{2.14}$$

Since the solutal supersaturation is

$$\Omega_1=\frac{c_l-c_0}{c_l\left(1-k\right)}, \tag{2.15}$$

and the solutal Peclet number is

$$\mathrm{Pe}=\frac{VR}{2D_l}, \tag{2.16}$$

where Ω_1, Pe represent the solutal saturation and the Peclet number, respectively. The solution of the equation (2.9) becomes

$$\mathrm{Pe}=\Omega_1 \tag{2.17}$$

It shows that the velocity depends on tip radius R and on supersaturation Ω_1, which are the driving forces. The solution of this diffusion equation does not specify whether a dendrite will grow fast or slow, but only relates the tip curvature to the dendritic rate of propagation. In addition, the hemispherical cap does not grow only in x - direction, but also in R - direction.

The main task is to calculate the growth rate as a function of the ratio of the change in concentration (or temperature) of the dendritic interface at the tip to the equilibrium concentration (or temperature). The ratio of these quantities is known as the solutal (thermal) supersaturation. The growth rate of the solid phase increases with the increase of the supersaturation. The heat and mass rejection rate, and therefore the growth rate, is influenced by the shape of the tip. At the same time the form of the tip is affected by the distribution of the solute and temperature fields. All these interactions make the development of exact theory for the dendritic growth velocity extremely complex [Kurz and Fisher, 1998]. In order to overcome the complexity arising from the dendritic structure geometry, the dendritic shape is commonly described as the paraboloid of revolution as originally proposed by Papapetrou [Papapetrou, 1935].

2.2.1.2 Paraboloid of Revolution

According to the above presented problem the following solution is derived. To make the calculations simpler the dendritic shape is assumed to have a parabolic shape instead of a circular one. Papapetrou described the form of a dendritic crystal as a paraboloid of revolution with a fixed radius of curvature, growing at a constant velocity. Ivantsov [Ivantsov, 1947] was the first who described the growth of a paraboloid crystal. Ivantsov based his own classical transport analysis on a suggestion made originally by Papapetrou in 1935. He solved the related diffusion equation in co-moving paraboloidal coordinates, scaled by the only obvious length in the problem, the (unknown) tip radius of curvature.

Two stability growth regimes can be defined: pure diffusion regime and the growth in the presence of fluid flow. Under steady state and in pure diffusion regime, the resolution of the temperature field ahead of the moving paraboloid of revolution interface leads to a relation between the supersaturation, the tip radius R and the tip velocity V, according to the equation (2.18)

$$Iv\left(\mathrm{Pe}\right)=\Omega_1. \tag{2.18}$$

Ivantsov assumed that all the energy released by solidification diffuses away from the isothermal paraboloidal crystal-melt interface *via* the melt phase. He obtained the following equation relating the growth for steady-state paraboloidal dendrites

$$Iv(\mathrm{Pe}) = \mathrm{Pe}\exp(\mathrm{Pe})E_1(\mathrm{Pe}), \tag{2.19}$$

where $Iv(\mathrm{Pe})$, $E_1(\mathrm{Pe})$ are the Ivantsov function and the exponential integral function, respectively.

The exponential integral function is defined as

$$E_1(x) = \int_x^{\infty} \frac{\exp(-z)}{z} dz. \tag{2.20}$$

There are several approximations of the integral function that can be used in numerical evaluation. In our calculation for the parabolic cylinder the following solution was applied

$$Iv(\mathrm{Pe}) = \sqrt{\pi \mathrm{Pe}}\exp(\mathrm{Pe})\mathrm{erfc}\left(\sqrt{\mathrm{Pe}}\right), \tag{2.21}$$

where $erfc$ is the complementary error function defined as

$$erfc(x) = \frac{2}{\sqrt{\pi}}\int_x^{\infty} \exp^{\left(-z^2\right)} dz. \tag{2.22}$$

Equation (2.14) establishes the relationship between the tip velocity and radius. Hence, for the constant undercooling the relation RV is then constant and means that either a dendrite with small radius will grow rapidly or one with a large radius will grow slowly. In order to calculate the resulting velocity of the tip radius, additional equation is required accordingly. Experimental work demonstrates that for each undercooling a unique value of tip velocity and radius needs to be obtained.

2.2.1.3 KGT Model

To find the additional equation it is necessary to find additional criteria that define the tip radius [Kurz, Giovanola and Trivedi, 1986; Kurz and Fisher, 1998]:

- the marginal stability criterion
- the extremum criterion

2.2.1.3.1 The Marginal Stability Criterion

Several experiments indicate that the radius of curvature of the dendrite is approximately equal to the lowest wavelength perturbation of the tip. As proposed by Langer and Müller-Krumbhaar [Langer and Müller-Krumbhaar, 1987] the dendritic tip grows with a tip radius equal to the limit of stability which is known as the marginal stability criteria. Langer and Muller-Krumbhaar presented a linear stability analysis for Ivantsov parabola dendritic tip region. Movements of the parabolic shape in the system were caused by the interface energy. It was assumed that the dendritic radius is not stable in the regions smaller than predicted by the extremum criteria or larger than the certain critical value. At such a large radius a tip splitting will occur in order to decrease the radius. This largest radius is selected by the dendrite during the growth stage. Dendrites grow with the tip which size is limited by the marginal stability, following the equation

$$R = \lambda_i, \tag{2.23}$$

where λ_i express the critical wavelength of the solid-liquid interface at the limit of stability.

The wavelength of the marginally stable plane front is given by

$$\omega^2 \Gamma = m G_c \varsigma_c - G, \tag{2.24}$$

with

$$\omega = \frac{2\pi}{\lambda_i}, \tag{2.25}$$

$$\varsigma_c = 1 - \frac{2k}{\left\{1 + \left[4\pi D_l / \left(\lambda_i V\right)\right]^2\right\}^{1/2} - 1 + 2k}, \tag{2.26}$$

$$G_c = \frac{-V c_l \left(1-k\right)}{D_l}, \tag{2.27}$$

where Γ, G_c, G, ς_c represent the Gibbs-Thomson coefficient, interface concentration gradient in the liquid, interface mean temperature gradient and stability parameter, respectively.

At high Peclet numbers equation (2.25) reduces to

$$\varsigma_c = \frac{\pi^2 \Gamma}{\mathrm{Pe} k}. \tag{2.28}$$

By applying liquid concentration

$$c_l = \frac{c_0}{1-(1-k)Iv\left(\mathrm{Pe}\right)}, \tag{2.29}$$

the interface concentration gradient can be rewritten to

$$G_c = \frac{-V(1-k)c_0}{\left[1-\left(1-k\right)Iv\left(\mathrm{Pe}\right)\right]D_l}. \tag{2.30}$$

Finally, substituting this concentration gradient into the equation (2.23), one can obtain

$$R = 2\pi\left(\frac{\Gamma}{m\dfrac{-V(1-k)c_0}{\left[1-\left(1-k\right)Iv\left(\mathrm{Pe}\right)\right]D_l}\varsigma_c - G}\right)^{1/2}. \tag{2.31}$$

Including the definition of Peclet number, according to the equation (2.16) and using Ivantsov's solution for the transport problem, this relation can be expressed as

$$V^2\zeta_1 + V\zeta_2 + \zeta_3 = 0, \tag{2.32}$$

with the following coefficients ζ_1, ζ_2 and ζ_3

$$\zeta_1 = \frac{\pi^2\Gamma}{\mathrm{Pe}^2 D_l^{\,2}}, \tag{2.33}$$

$$\zeta_2 = \frac{mc_0(1-k)\varsigma_c}{D_l\left[1-(1-k)Iv(\mathrm{Pe})\right]}, \tag{2.34}$$

$$\zeta_3 = G. \tag{2.35}$$

In the directional growth the temperature gradient is determined by the external heat flow. Neglecting this effect (at low growth rates) on the diffusion field around the tip, the concentration gradient can be calculated using a flux balance at the dendritic tip. In our calculation it was set to zero ($G = 0$), as proposed by Kurz and Fisher [Kurz and Fisher, 1998; Yamazaki *et al*., 2006], what gives the absolute stability condition. It reduces the equation (2.32) for growth velocity as follows

$$V = -\zeta_2 / \zeta_1. \tag{2.36}$$

2.2.1.3.2 The Extremum Criterion

This criterion implies that growth stage takes place at the maximum possible velocity and at the minimum possible undercooling. These two assumptions are fulfilled by the velocity corresponding to the radius tip of the dendrite R. The expression for rate of interface movement V can be obtained for example for a perturbation driven only by the solutal and the curvature undercooling

$$\Delta T = \Delta T_c + \Delta T_r, \tag{2.37}$$

where ΔT_c, ΔT_r are solutal undercooling and the curvature undercooling, respectively.

$$\Delta T_c = -m\left(c_l - c_0\right), \tag{2.38}$$

$$\Delta T_r = \frac{2\Gamma}{R}, \tag{2.39}$$

where m represents the slope of the liquidus line.

Substituting these two undercooling temperatures into the total undercooling equation (2.37) we receive the following relation

$$\Delta T = m\left(c_0 - c_l\right) + \frac{2\Gamma}{R}. \tag{2.40}$$

This equation transforms into

$$\Delta T = m\left(c_0 - \frac{c_0}{1-(1-k)Iv\left(\mathrm{Pe}\right)}\right) + \frac{2\Gamma}{R}, \tag{2.41}$$

by assuming the equation (2.29).

Presented KGT model was used in our calculations for modeling the ECT/CET transitions.

3 Cellular Automata and Point Automata Methods

3.1 Literature Review

The increasing importance of computers has lead to a new way of looking at the world. This point of view shows nature as a form of computation. Computers follow some rules. At each step the rules determine exactly what type of computation will be performed next. This behavior is an example of the automata system. Another type of the automata, that received a lot of attention during the last years, is CA. From one side it is a collection of colorful cells located in a grid which show us pretty pictures, but from another side this is an excellent tool which can be related to exciting new ideas and can solve many problems. By building appropriate rules for the cellular system we are able to simulate many kinds of complex behavior from any of the scientific and engineering fields. CA represents a discrete dynamical system with a long and illustrious history of study.

First work in this field was done by the John von Neumann in 1951 [von Neumann, 1951], who was interested in the problem of machines (or automata) which are able to produce copies of themselves. He started considering how physical automata should be constructed to be able to produce the copies of themselves. The details of such construction were very complicated, and so following discussions with Stanislaw Ulam, von Neumann began to study a logical model of self-reproducing automata. His approach was a design for a Turing Machine implementation as a concept of CA using 29 states per cell and 5 cells (often referred to now as von Neumann, see Figure 3.3) neighbourhood. His work was edited and published by his colleague Arthur Burks [von Neumann, 1966]. This simple discovery proves that CAs are able to simulate many phenomena. In the early 1970’s two dimensional CA named Game of Life was also able to perform any computation [Wainwright, 1974]. This algorithm, invented by John Conway became widely known. It actually employs very simple rules. It was proven that it can be also used to emulate a universal Turing Machine what was achieved by identifying propagating structures or configurations of cell states. The discovery that a CA with only 2 states and 8 transition rules could perform any computation was truly remarkable.

During the early 1980's Stephen Wolfram began a systematic investigation into these simplest CA approaches, one-dimensional CA with 3 neighbourhood size and two possible states. The lattice in this 1D version represents a line where the cells are updated based on their own state and their direct neighbors to the left and right side. As the neighbourhood size is 3, and the number of states is 2, there are $2^8 = 256$ such CAs possibilities. In 1983 Stefan Wolfran published the first in a series of papers dating from the 1980's [Wolfram, 2002], systematically investigating very basic classes of CA which he named 'elementary CA'. He described several other simple computational models which can be divided into four classes depending on their behavior. Wolfram's classification was the first attempt to classify the rules themselves. In order of complexity these classes are:

- **Class 1** - limit points.
- **Class 2** - limit cycle.
- **Class 3** - chaotic - "strange" attractor.
- **Class 4** - more complex behaviour, but capable of universal computation.

Class 1

CAs of Class 1 evolve to a uniform configuration of cell states, from almost any initial configuration. This state can be thought of in dynamical systems terms as a 'point attractor', or 'limit point'. As one would suspect, the rules for Class 1 CAs map from most or all possible neighbourhood configurations to the same new state. Initial lattice configurations do exist for some Class 1 CAs that lead to non-trivial cycles, but these are very rare.

Class 2

CAs of Class 2 evolve to produce simple stable or periodic configurations on the lattice, according to the initial lattice configuration. Changes of cell state in the initial configuration will only affect final cell states that are nearby (in comparison to the neighbourhood size). Class 2 CAs can be thought of as 'filters' acting on the initial lattice configuration. The evolution of class 2 CAs to periodic configurations can be thought of as analogous to 'limit cycles' in dynamical systems terms.

Class 3

CAs of Class 3 evolve to a periodic, or chaotic, configurations from almost all initial lattice configurations. Over sufficient time, from any of initial states the statistical properties of the resulting configuration, such as proportion of non-zero cells, converge to some value. Small changes in initial lattice configuration lead to larger and larger changes in resulting configuration as time progresses, as is the case for chaotic dynamical systems.

Class 4

CAs of Class 4 evolve into propagating structures. In some sense Class 4 is ‘between’ the purely chaotic behavior of Class 3, and the static behavior of Class 2. Some authors [Waldrop, 1993] have made strong but vague arguments that complex systems are those ‘posed at the edge of order and chaos’. However there may be something in this view as, more concretely, some CAs in Class 4 have been demonstrated to have a very special property, described in the next paragraph.

It can be assumed that the CA method represents a new approach of modelling. The theory of CA is very rich, with simple rules and structures being capable of producing a great variety of unexpected behaviour. During the last years, this method has been studied in many scientific fields as in the computability theory, mathematics, theoretical biology, psychology and metallurgy.

It must be emphasized that the subject of this dissertation is the application of the CA method to solve the mesoscopic evolution equations to be able to model the following transitions: ECT/CET and the dendritic formations during the growth stage. It is comprehensively described in the forthcoming chapters.

3.2 Definition of CA Method

This section presents the basic features of the CA method. What follows are the basic elements of the CA method:

- n-D (n=1, 2, 3) space is divided into a discrete number of n-dimensional elements which are named cells (polygons and polyhedrons).
- a state is assigned to each CA cell,
- the neighbourhood configuration is defined deterministic or stochastic for each CA cell,
- transition rules are defined which create a new state of the cell as a function of the states(s) of the cell(s) consisting of the previously defined local neighbourhood of the cell.

Let’s take a look at these general descriptions in more details. In the vast majority of all previous science and engineering applications of CA, a regular 2D rectangular cell structure (Figure 3.1) has been often used in the calculations with respect to the represented definition. These cells are defined by the finite number of states (different phase fraction, temperature, velocity). CA discretisation is based on polygons and transition rules between polygons. A neighbourhood relationship is defined on this lattice which is divided into the square (or hexagonal) CA cells. Each cell can have its own neighbourhood configuration which is chosen during the evaluation. The state of a cell at time t is a function of the states of a finite number of cells (called its *neighbourhood*) at time t_0. At each time step, every cell updates its state using a transition rule based on the values in its neighbourhood. The initial state of the CA is defined, but then repeated synchronous application of the deterministic or stochastic transition rules (functions) to all cells in the lattice will lead to the evolution of the CA system while the new conditions are created. Many variations of the system exist.

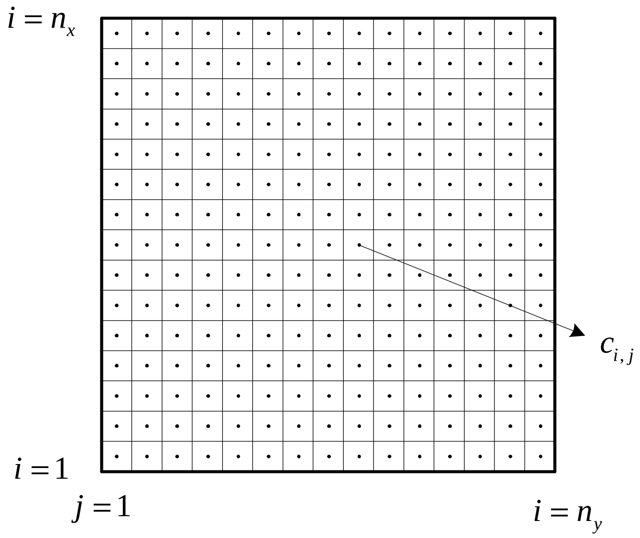

Figure 3.1: Conventional CA model discretization.

The above presented basic features of the CA system are commonly implemented in the literature. In the present work an alternative solution to a common CA method is introduced. First the partitioning is not required to be a regular grid, in other words not all cells need to have the same shape or dimensions. The number of possible states does have to be finite. Finally, the neighbourhood definition could vary from cell to cell and from time to time. The state change rule does not necessarily need to be deterministic, what allows for the probabilistic CA application. These observations bring us to the development of the new non-uniform CA method. In the present work this new concept is applied. The point (instead of cell) automata discretisation is presented which is now based on points and transition rules between the points, where instead of periodic distribution of the cells, the points are distributed randomly in the domain (Figure 3.2). Basic idea of PA discretisation is to distribute nodes randomly which leads to different distances between the nodes and gives different neighbourhood configurations for each of them. The neighbourhood is now different for each point, therefore it must be stored for each node separately. While the new definition of neighbourhood is explained, irregular (also named random) PA cellular transitions rules can be used in exactly the same way as for the regular approach. In this sense the irregular CA model is not much different from the conventional one, despite bringing many advantages.

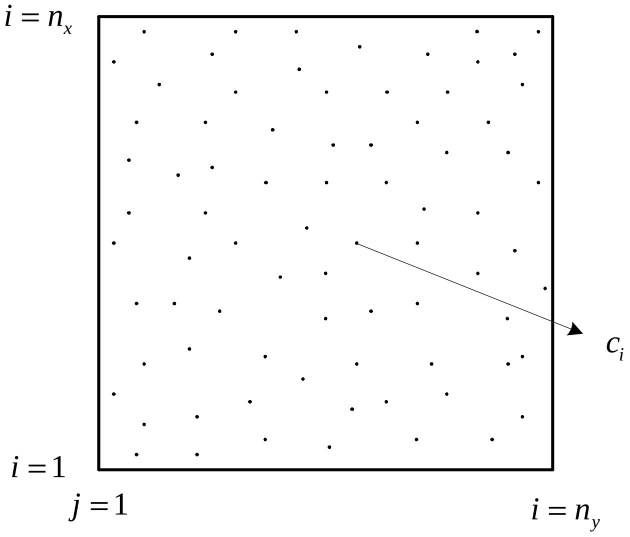

Figure 3.2: Random PA model discretization.

What follows are the basic elements of this novel PA method:

- the starting point is to distribute the PA nodes (not cells) randomly on the n-D computational domain,
- a state is assigned to each PA node,
- the neighbourhood configuration is defined for each node separately with respect to the selected neighbourhood points,
- the neighbourhood of the node includes all random nodes whose positions are located in the domain of a circle in 2D (Figure 3.8) or sphere in 3D (Figure 3.10) with the radius R_H. The number of the neighbours can vary locally. The transition rules are defined and they create a new state of the point as a function of the states(s) of the points(s) consisting the local neighbourhood configuration.

3.3 Typical CA Neighbourhood and PA Neighbourhood Definitions

The basic element of the CA method is the cell. It is a memory element which stores states and supervises the process. These cells are arranged in a static state. To introduce dynamics into the system some rules need to be defined. The 'task' of these rules is to define the state of the cell for the next time as a function of dependence an the neighbouring cells. A basic definition of neighbourhood comes exactly from the classical CA approach which operates on the grid divided into the square cells. In the two dimensional square lattice there are many neighbourhood configurations possible. The most common definitions used for the conventional grid are depicted in Figures 3.3-3.6. For the random node arrangement we propose a definition of PA in which each point has a different neighbourhood configuration in the shape of a circle, during a computation (Figure 3.8). The cells are defined $c_{i,j}$ with i the row number and j the column number of the cell. The definition of the neighbourhood configuration is presented through the location of all neighbouring cells (depicted in the oval brackets under each configuration).

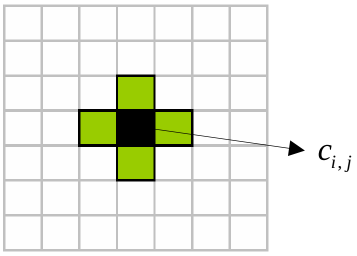

$$c_{i,j} = \left\{ c_{i+1,j}, c_{i,j+1}, c_{i-1,j}, c_{i,j-1} \right\}$$

Figure 3.3: The von Neumann neighbourhood configuration with 4 neighboring cells.

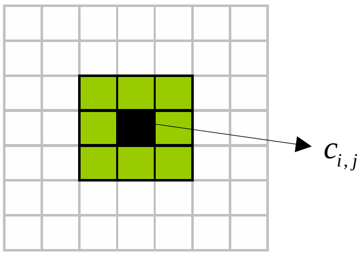

$$c_{i,j} = \left\{ c_{i+1,j-1}, c_{i+1,j}, c_{i+1,j+1}, c_{i,j+1}, c_{i-1,j+1}, c_{i-1,j}, c_{i-1,j-1}, c_{i,j-1} \right\}$$

Figure 3.4: The Moore neighbourhood configuration with 8 neighboring cells.

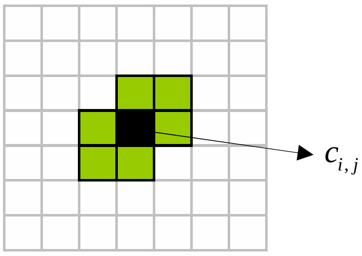

$$c_{i,j} = \left\{ c_{i+1,j}, c_{i+1,j+1}, c_{i,j+1}, c_{i-1,j}, c_{i-1,j-1}, c_{i,j-1} \right\}$$

Figure 3.5: The modified Moore neighbourhood configuration with 6 neighboring cells (variant 1).

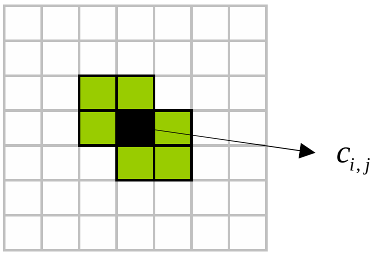

$$c_{i,j} = \left\{ c_{i+1,j}, c_{i,j+1}, c_{i-1,j+1}, c_{i-1,j}, c_{i,j-1}, c_{i+1,j-1} \right\}$$

Figure 3.6: The modified Moore neighbourhood configuration with 6 neighboring cells (variant 2).

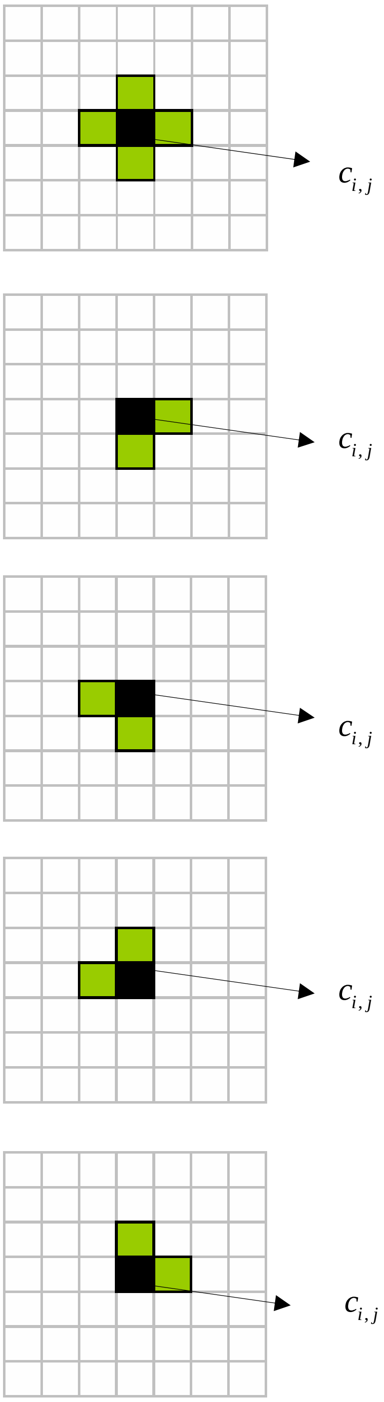

$$c_{i,j} = \left\{ c_{i+1,j}, c_{i,j+1}, c_{i-1,j}, c_{i,j-1} \right\}$$

$$c_{i,j} = \left\{ c_{i,j+1}, c_{i-1,j} \right\}$$

$$c_{i,j} = \left\{ c_{i-1,j}, c_{i,j-1} \right\}$$

$$c_{i,j} = \left\{ c_{i,j-1}, c_{i+1,j} \right\}$$

$$c_{i,j} = \left\{ c_{i+1,j}, c_{i,j+1} \right\}$$

Figure 3.7: A newly introduced neighbourhood configurations to model the grain growth evolution.

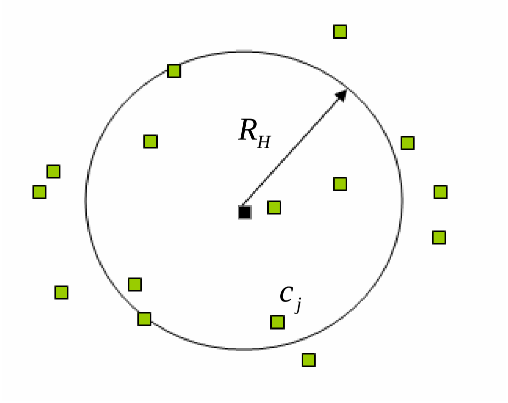

$$c_i = \left\{ c_j ; \left| r_i - r_j \right|_{i \neq j} < R_H \right\}$$

Figure 3.8: Example of 2D PA neighbourhood configuration.

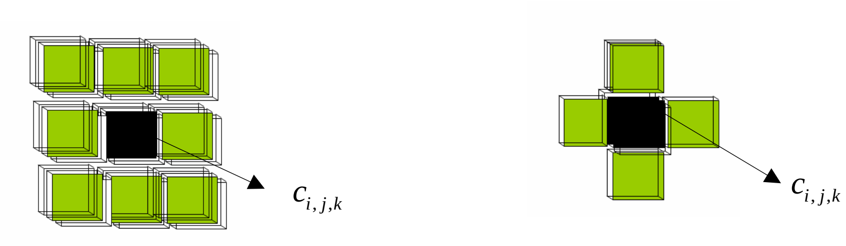

Figure 3.9: Example of 3D CA neighbourhood configurations. Left: Moore, right: von Neumann.

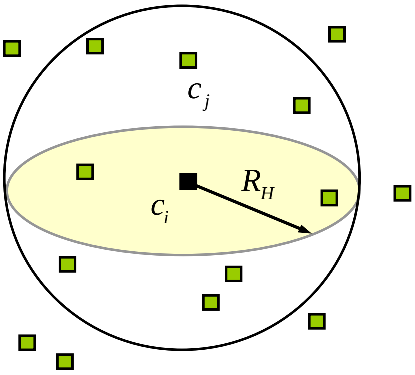

$$c_i = \left\{ c_j ; \left| r_i - r_j \right|_{i \neq j} < R_H \right\}$$

Figure 3.10: Example of 3D PA neighbourhood configuration.

4 Point Automata Advantages

Irregular CA grid structure approach (also named PA method) was first proposed by Janssens [Janssens, 2003] to model the recrystallization process. It is based on the randomly distributed nodes instead of regular CA cells. A detailed definition of this approach has been already presented in the previous section. In this chapter we focus our attention on the reasons for numerical implementation of irregular CA for modelling: recrystallization, ECT/CET and dendritic growth.

Random grid CA model for the simulation of the evolution of a materials microstructure during recrystallization, following the approach proposed by Janssens [Janssens, 2000], is introduced. He focused his attention to the typical problems that might occur when modelling grain boundary displacement. In his publications there are a few numerical results shown. Extended information is given with respect to the definition of the irregular CA.

For modelling ECT/CET transitions and dendritic growth this novel approach represents an original formulation and solution described in Chapters 5 and 6.

In Section 4.2 a simple algorithm for modelling recrystallization process is shown. The basic idea is first presented for the classical CA method and then for the novel PA method following the rules proposed by Janssens. The principal differences in implementations of both methods are explained.

4.1 CA Problems

CAs are attractive as a modelling framework that may provide a better understanding of meso-macro relations. However, many scientists reject the CA approach because the framework is far too simple or - far too idealized, to be an appropriate tool for modelling different involved processes. They argue [Yazdipour *et al.*, 2007; Yazdipour *et al.*, 2008] that the classical CA assumptions like discrete time, regular grid structures, finite sets of states etc. may make the approach so simplistic that it is questionable whether its results can be generalized beyond the particular framework. In CA definitions the discretization of the space is an essential aspect and influences the final results.

The science started to search for a new computational approach to overcome these problems. The novel random grid computing appears to be a promising trend for solving problems that can not be achieved by applying the classical CA definitions. The first publications on irregular CA are by Thieme-Martin [Thieme-Martin, 1999] in technical sciences and by Flache [Flache and Hegselmann, 2001] in general. Other research groups have published similar approaches for modelling recrystallization where the new definition of neighbourhood is used [Yazdipour *et al.*, 2008]. Let us first discuss the objectives with which Janssens introduced the irregular CA's.

Recrystallization. The main reason why the PA method was applied for modelling the recrystallization is the heterogeneous nature of this process. In many cases local variations have a substantial influence on the recrystallization process and at the same time the heterogeneity of these local variations in the microstructure makes it difficult to include them in a statical model. Technique such as CA solves this problem by spatially resolving the microstructure. The main limitations are as follows. Till today the applications of CA have been limited mainly to the qualitative modelling. It is not entirely clear how the computational kinetics of the CA model relates the real world kinetics of recrystallization and grain growth. The conventional CA represent the equidistant cell distribution what is the main reason why the link to the space can not be made, obviously because the distances between the cells are not equal in all spatial directions due to their shape. Consequently, given the same conditions for driving force and mobility, the velocity for the grain boundary is directionally dependent on its relative orientation to the grid. It is also known that the shape of the neighbourhood, which is in the CA approach closely related to the grid, has a major influence on e.g. the way the grain boundaries move in the simulation of recrystallization. It shows that the automata grid directly influences the outcomes of the computation. The main motivation for a new approach was the possibility to break the coupling between the orientation of the periodic discretization grid and the orientation of the grain boundary. A solution to these problems is the use of the PA method. An additional advantage of the random grid is that, when the material is homogeneously deformed, it is still a random grid [Yazdipour *et al.*, 2007]. The deformability of the grid is a necessary requirement to simulate the same as observed evolution of the microstructure.

ECT/CET transitions. During the CC process of steel the three characteristic zones [Lorbiecka *et al.*, 2009] can be distinguished: chill, columnar and equiaxed. The biggest problem which occurs during modelling of this phenomenon is the proper prediction of dimension of these three regions with respect to the industrial measurements. By using different nucleation models only, we are not able to influence directly the grain structure. In additional to the nucleation models many other parameters need to be fit to the experimental results what usually takes a lot of efforts [Lorbiecka and Šarler, 2009].

By the novel PA method we can easily influence on the grain size by changing the density of nucleuses in the domain. Novel PA method offers an attractive alternative to the classical CA method because of the flexibility of node density and neighbourhood definition. The different density of nucleuses across the domain of interest allows us to model the appropriate dimensions of the central region which is usually difficult to predict. Proposed new method gives a more proper modelling of chill, columnar and equiaxed zones, respectively.

In Chapter 5 the solution of the governing stochastic equations is first solved by the conventional CA approach and then by the novel PA approaches. The procedure responsible for generation of random node arrangement is explained as well (see Section 5.6.2.1).

Dendritic growth. During the dendritic growth the crystallographic axes of grains have different orientations. It is commonly known that this process is difficult to simulate by the classical CA method. Mainly, because the configuration of the CA network has a direct influence on the simulated structures. The growth direction of the grain corresponds to the direction of the CA network not to the original crystallographic orientations of the nucleuses. This happens because in the CA growth the principal cell only affects nearest neighbors. This is not the case in the PA method. The first problem with growth on the Cartesian grid is that, despite the specified orientation, it can grow only along the grid axes. For the given rules of the of classical CA model, no other alternative exist. Even if any other orientation will be chosen, the dendrite will always switch to 0° or 45° with the evolution of the process.

In order to solve this problem the novel PA method was for the first time applied for the dendritic growth calculations which are based on the CA rules already described in Chapter 3. A novel method is able to resolve the preferred crystallographic orientation problem. It is shown that when using the random node arrangement the dendrites are able to grow in any direction. In Chapter 6 the solution at the governing stochastic equations is first presented for the CA method and then for the novel PA method. The procedure for generation of random node arrangement is explained as well (see Section 6.5.3).

4.2 An Overview of Modelling the Recrystallization by the CA and PA Methods

In this Section we present a general concept for modelling of recrystallization by the classical CA method. A detailed review of this process is beyond the scope of this dissertation. We discuss only the basic assumptions and method layout. The attention is focused on the important differences of both methods.

Recrystallization is a process through which are the deformed grains replaced by a new set of undeformed grains that nucleate and grow until the original grains have been entirely consumed. Recrystallization is usually accompanied by a reduction in the strength and hardness of a material and a simultaneous increase in the ductility. A precise definition of the process is difficult as the process is strongly related to several other processes, most notably recovery and grain growth. In some cases it is difficult to precisely define the point at which one process begins and another ends [Humphreys and Hatherly, 1996].

4.3 CA Method for Recrystallization

4.3.1 Modelling of the Nucleation Rate

It is well known that recrystallization occurs when the strain or the dislocation density in a deformed matrix reaches a critical level, which depends on the processing parameters such as temperature and strain rate. Two important stages that determine the microstucture of recrystallization are nucleation and grain growth. Both aspects are closely related to the dislocation density represented as the stored energy variation in the deformed grains.

Several models for the rate of nucleation have been proposed. For detailed explanation see Ding and Guo [Ding and Guo, 2001]. In order to simplify the procedures two assumptions are usually proposed:

1. Initial dislocation density is uniform and identical for all grains. When it reaches a critical value the nuclei for recrystallization will form on the grain boundary.
2. Nucleation only occurs on the grain boundaries.

4.3.1.1 Initial Microstructure

In the CA method the calculated domain is divided into the regular square cells.

During the recrystallization two different types of a CA cell are possible: the entire cell which represents a portion of the grain and it is associated with the fixed crystallographic orientation and the grain boundary cell which has a fraction of two grains with their respective orientations. The area of a grain is defined proportional to the number of the CA cells which fall inside the grain (see Figure 4.1).

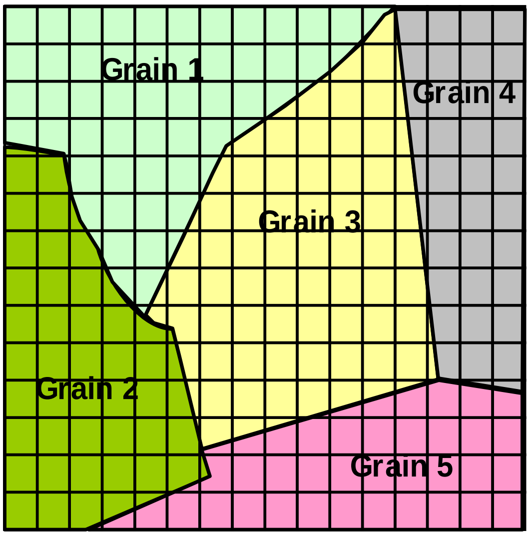

Figure 4.1: Example of a 2D distribution of grains and CA cells. Different colors represent different grains with different orientations, respectively.

4.3.2 Modelling of the Grain Growth Kinetics

4.3.2.1 Neighbourhood Configuration

In the 2D CA model, a von Neumann neighbourhood configuration is usually selected.

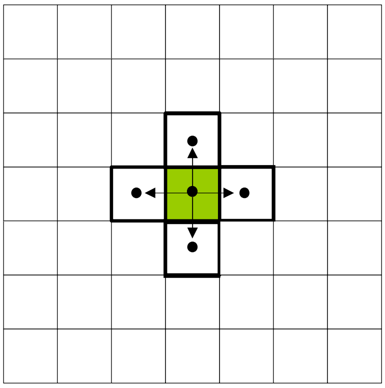

Figure 4.2: A definition of the neighbourhood configuration for the CA method.

4.3.2.2 Grain Boundary Migration

In order to simulate the grain boundary movements the CA cells located at the grain boundary are identified first. The driving force for growth comes from the difference between the dislocation densities of the grain and the matrix. Generally, the growth velocity V can be represented as a function of the grain boundary mobility m_b and the driving force p_d

$$V = m_b p_d. \tag{4.1}$$

In the context of modelling grain growth by the CA approach it is necessary to consider three different grain growth models [Janssens *et al.*, 2004] in general

- Curvature driven grain growth where the energy stored in the grain boundaries drives their motion.
- Non-curvature driven grain growth in which energy is presented in some another form in the microstructure and the energy of the grain boundaries is negligible.
- Mixed mode where the two modes appear simultaneously.

Depending on the grain growth mode a different modification of the CA can be used to construct the algorithm based on the equation (4.1).

For each CA cell located at the grain boundary the displacement is calculated in each time step by the equation [Raghavan and Sahay, 2007]

$$\Delta x_b = m_b\, p_d\, \Delta t. \tag{4.2}$$

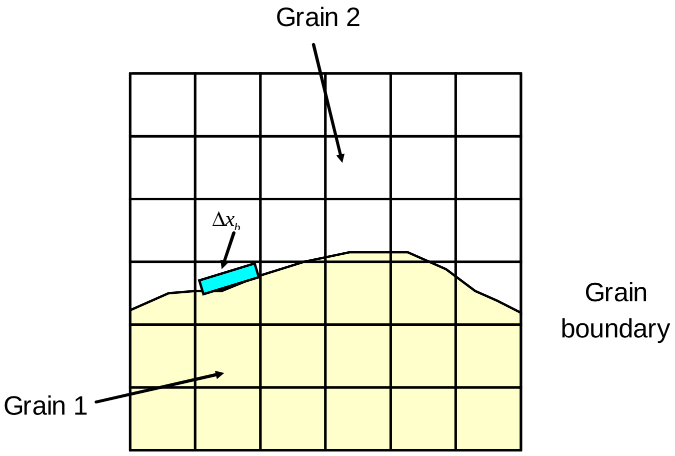

Figure 4.3: Calculation of the grain boundary displacement in the boundary CA cell.

The grain boundary can move forward or backward depending on the sign of Δx_b in equation 4.2 (see Figure 4.3). The area taken by the boundary in a given cell is obtained from Δx_b and the angle of normal at the boundary. The transformation probability for a cell that lies within the growth region is defined with respect to the chosen neighbourhood configuration. When the number of grains decreases with increasing growth time, the grains with the same orientations will frequently connect to each other into a larger grain. A cell is not considered to be recrystallized until completely consumed by a moving boundary. It will change state (orientation and dislocation density) when it is entirely recrystallized.

4.3.3 Transition Rules

The presented algorithm for recrystallization is composed of the lattice of the CA cells that are updated simultaneously according to transition rules. The evolution of a CA cell is controlled by the cells that form the neighbourhood or surrounding of this cell.

Modelling recrystallization can be decomposed into two steps. In the first one, the initial microstructure needs to generated through growth of randomly generated nuclei. The following simple transition rule is applied. A cell under consideration recrystallizes with 50 % probability if at least one of the neighbours from the chosen neighbourhood is recrystallized. Therefore, growing grains reach approximately globular shape [Kroc, 2002].

In the second step, the simulation is done by the sequential realization of the following three steps representing microstructural evolution of each cell during each time step:

- evolution of the dislocation density,
- recrystallization realized by the growth of grains when driving force exceeds a critical value, and
- the nucleation of embryos of new grains.

The transition rules control the cell state transformations between non-recrystallized and recrystallized. Additionally, there are several internal variables describing each cell. These variables are part of the transition rules describing mechanisms leading to the recrystallization.

- orientation which is identical for the whole cells located in each individual grain and determines the grain boundary energy,
- dislocation density that represents the stored energy due to the previous deformation,

- grain boundary energy that would be zero for each two cells not located beside the grain boundaries in the same grain,
- the color variable represents different grains.

A recrystallization event will occur at a cell of interest under consideration of 50% probability when the following conditions are fulfilled simultaneously: the cell of interest is situated at a grain boundary, the difference in dislocation density between the cell of interest and neighbouring cell belonging to different grain is greater than a critical value, the potential new configuration of the grain boundary is not an excluded one, a grain having lower dislocation density grows into a grain having a higher dislocation density.

The mobility of a solid-state grain or phase boundary is determined by the atomistic mechanisms by which the boundary moves. Although uncertainty remains about the exact nature of these mechanisms, it is generally accepted that mobility strongly depends on the crystallographic misorientation between neighbouring grains. Misorientation depends on five independent variables, three to represent the orientation difference between the crystal lattices and two for the grain boundary plane, which represents a substantial parameter space misorientation constant [Janssens *et al.*, 2006]. Mobile boundaries continue moving towards the point that they meet each other and a fully impinged microstructure is obtained.

The above described basic transition rules reflect only the most simple understanding of recrystallization process.

4.4 PA Method for Recrystallization

A novel approach of random CA is not much different from the conventional CA. The two major changes implemented in the recrystallization algorithm connected with the initial distribution of grains and definition of the neighbourhood configuration is required. They are discussed below.

4.4.1 Initial Microstructure

For the PA method the initial microstructure has been generated by using the Voronoi tessellation technique [Watson, 1981], which is widely employed for constructing initial microstructures. The 2D space is randomly nucleated with points conforming to a specific crystal orientation. The space between any two points is bisected with a line, which is equidistant from both the points. Such lines are constructed between all the pairs of points, which eventually form the grain boundaries and the space divided by these lines forms the grains having the

orientation of the corresponding nucleus. In Figure 4.4 grains with different orientation generated by using the Voronoi tessellation have been shown.
The irregular node arrangements with variation in the structure and the size of neighbourhoods between locations in the grid are the input micro-structure to the model. It can be seen that each point represents the cell. Because only points are used in calculations, the shapes of the grain sizes can easily be varied during the time. The recrystallization process starts with constructed initial microstructure, which contains a randomly distributed number of nodes, which are then assumed to grow according to the rules already described below.

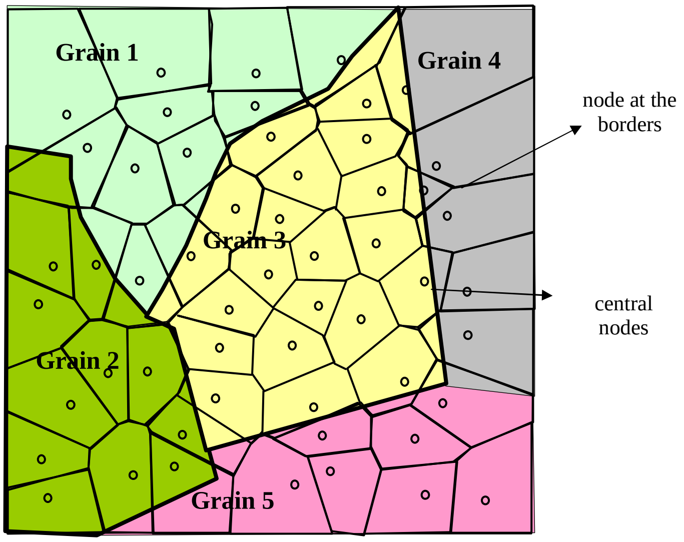

Figure 4.4: Example of irregular CA distribution of cells based on the Voronoi tessellation computed from the random distribution of points. Different colours represent different grains with different orientations.

4.4.2 Neighbourhood Configuration

To obtain even more realistic representation of the grain shape, the random CA neighbourhood was applied to model recrystallization process. As mentioned in the CA method, cells and neighbors are usually equi-distantly distributed over the space while in the random CA, the neighbourhood area depends on the neighbourhood radius. A neighbourhood of a random node includes all random nodes whose positions are contained within the circle with assumed radius (see Figure 3.8). As only random node coordinates are used in the calculations, shapes and size can easily be varied, even locally.

4.4.3 Grain Transition Rules and Grain Boundary Movements

With the new definitions of the neighbourhood configuration and initial grain distribution the irregular CA method can be used exactly in the same way as the conventional CA method. The initial cell structure needs to be created following the Voronoi scheme from the predefined points. The grain boundary movements can be modelled following the same transition rules which are applied for the classical CA. The random nodes located within the new neighbourhood in the shape of circle need to be determined (see Figure 4.4). The transition rules and the general algorithm, already described in Section 4.3.3 for the classical CA method, can be used.

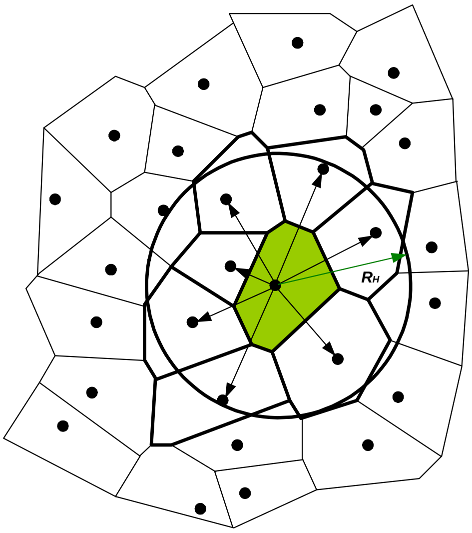

Figure 4.5: A definition of the neighbourhood configuration for the irregular CA method.

5 Mesoscopic Model of ECT/CET

The numerical model described in the present chapter consists of a stochastic mesoscopic model coupled with deterministic macroscopic model to predict the ECT/CET. The two main parts of this model are described in the next sections.

The ECT/CET is frequently observed in the grain structures of cast metals. The phenomena have been investigated both theoretically and experimentally in the past decades [M’Hamdi *et.al.*, 1998; Flood and Hunt, 1987; Flood and Hunt, 1987; Gandin, 2000; Gandin, 2000; Rappaz and Gandin, 1993]. It is assumed that the transition occurs by different mechanisms when equiaxed grains block the growth of columnar grains. Casting of metallic alloys may exhibit either wholly columnar or entirely equiaxed grain structures depending on the alloy composition and the solidification conditions [Wang and Beckermann, 1994]. The prediction of CET [Rappaz and Thevoz, 1987; Kurz *et al.*, 2001] is of great interest for the evolution and design of the mechanical properties of solidified products. First analytical model of CET were proposed by Hunt [Hunt,1984] for unidirectional solidification under steady-state conditions. In this model equiaxed grains nucleate at the temperature less then or equal to the liquidus temperature and grow into the undercooled zone ahead of the growing columnar front. The front is blocked and CET transition takes place. Mathematical models following Hunt can be identified as deterministic either stochastic, when some random parameters are used.

Wang and Beckerman [Wang and Beckerman, 1994] used the concept of the dendritic envelope to represents both the equiaxed and the columnar grains developing a numerical model to predict the CET in unidirectional transient solidification. M’Hamdi [M’Hamdi *et.al.*, 1998; M’Hamdi *et.al.*,1999] modelled the heat transfer and columnar growth in the CC of multicomponent steel billet. Proposed algorithm was able to calculate the position of columnar front at steady state, which was described by the continuous function of the radial distance of the billet. The calculated columnar front shape was the result of strand movement and the growth kinetics of the columnar dendrites. This approach was combined with an equiaxed solidification model to predict the ECT/CET in the CC processes.

Stochastic models of the ECT/CET prediction [Spittle and Brown, 1989; Zhu and Smith, 1992] track the growth of each columnar and equiaxed grain, not only the columnar front alone. They predict the detailed grain structure in two and three dimensional solidification. The highly refined mesh is necessary to resolve all grains, usually demanding larger computational resource. Following the developments of stochastic models for solidification, Gandin and Rappaz [Gandin and Rappaz, 1994] developed CA-FEM which is a combination of the CA method to predict the grain structures and FEM to calculate the temperature field. Their CA-FEM model was extended to three dimensional problems in [Gandin *et al.*, 1999].

Modified CA models that resolve not only the envelope of the grain, as it is in the original CA models, but also the dendritic arms were developed, by increasing the number of the CA sites and the computational resources. Recently, Dong and Lee [Dong and Lee, 2005] proposed such modified CA models of ECT/CET in unidirectional solidification, showing that the equiaxed grains nucleated not ahead but also between the columnar grains.

One of the principal goals of this dissertation represents the development of a new simulation tool for modelling the grain structure in solidification process. The numerical model is designed to outline only the dimension of chill, columnar and equiaxed zones (see Figure 5.1), rather than the detailed structure of each grain separately. The accurate size of the grains is not taken into the consideration because of the chosen calculated domain discretisation, which is too small to predict it in such details.

In this chapter we present the numerical stochastic model which is designed to be able to simulate the positions of the ECT and CET in CC of steel. The governing equations of the macroscopic model are derived by the LRBFCM method and the numerical solution for mesoscopic model by the CA and PA methods is presented.

5.1 Characteristic Zones of CC

In CC three characteristic zones can be distinguished in terms of the size, shape and orientation of the grains, corresponding to the chill layer, columnar growth and equiaxed region, as demonstrated in Figure 5.1. They reveal to the following distinct regions (from the centre to the surface):

- A central region of fine randomly oriented equiaxed grains.
- An outer region of columnar grains, elongated normal to the ingot surface.
- A third zone corresponding to the very fine chill crystals at the surface.

In order to understand the formation of the structures it is necessary to consider various thermal, hydrodynamic and physical-chemical phenomena. The process starts at mould wall where the first solid nuclei form. The sudden cooling produces a very thin layer of extremely fine grains at the surface, no more than a few millimetres thick, called the chill zone. The columnar zone in the middle is composed of the nuclei that nucleate in the chill layer and which grow with respect to the solidification front. Equiaxed crystals in the centre form in the liquid with random orientations and no preferred macroscopic growth direction. This implies that the liquid becomes undercooled, due to the heat conduction through the columnar layer. Growth of the equiaxed grains eventually stop the extension of the columnar zone. The origin of the nuclei that give rise to the equiaxed grains is still a subject of debate. Many authors believe that they can be formed spontaneously in the liquid or by the fragmentation of the dendrites in the columnar zone [Durand-Charre, 2004].

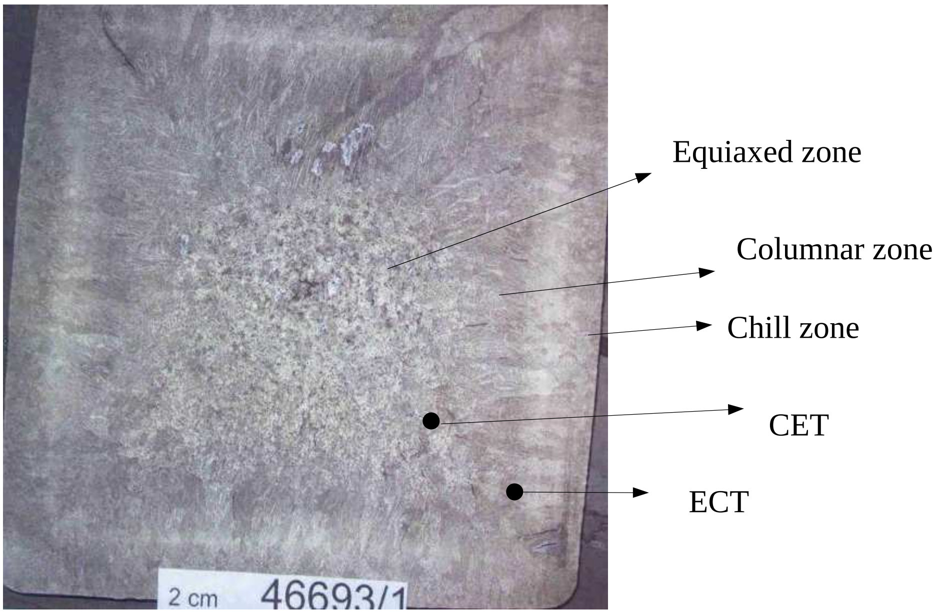

Figure 5.1: Grain structure occurring during CC of steel (Štore Steel company). Billet of dimension 180 mm, 25MoCr4, $T_{cast} = 1545\,\mathrm{K}$ and $V_{cast} = 1.12\,\mathrm{m/min}$.

In case the fragmentation occurs the broken ends of the columnar dendrites can be entrained in the liquid by convection currents and can remain relatively stable if the temperature is not too high. The fragments may remelt in the solute enriched liquid. The respective proportions of the columnar and equiaxed zones depend on numerous factors. The most important is the temperature range between the liquidus and solidus which is determined by the alloy composition. In the industry an extended equiaxed zone in the centre is preferable. This simplifies further rolling and heat treatment operastions.

The developed numerical model is able to predict qualitatively and quantatively the dimension of the three zones with respect to the observed Bauman prints (Figure 5.1). The CA mesostructure model (Section 5.5) is combined with the macroscopic heat transfer calculations described in Section 5.3 and 5.4.

5.2 CC Process

CC process is used to solidify more than million tons of steel produced in the world. This process involves many complex interacting phenomena while molten steel is solidified into a semi-finished billets, blooms, or slabs for subsequent rolling in finishing mills. The scheme of the process is depicted in Figure 5.2.

The ladle with molten steel is placed in a holder. From the ladle, the steel is tapped through a nozzle into the tundish. The tundish is an intermediate vessel designed to maintain a constant melt level and allows for flying ladle changes during the course of casting in a continuous process. CC takes place through a water-cooled mould that is open at the top and bottom. A casting powder is used, so that the steel will slide smoothly through the mould. Intensive water cooling of the mould side plates immediately gives the hot melt a hard shell of solidified steel. The cooled steel shrinks in volume as it is withdrawn from the underside of the mould in a long strand. The strand is continuously cooled on its arc-shaped path down to the cutting station. At this stage, the steel is still hot and glowing, but is sufficiently solid to enable the strand to be cut with movable oxygen lances into pieces of several meters long. The final product of the CC process of the billet is depicted in Figure 5.1. The numerical model developed in the dissertation, was developed in order to investigate the grain structure for different dimensions of billet, different material properties and different casting parameters. In this dissertation all simulations were performed for the square billet of dimension 140 mm (Chapter 7) and 180 mm (Appendix A) and the spring steel grades 51CrMoV4 (Chapter 7) and 52CrMoV4 and 25MoCr4 (Appendix A) typical for the Štore Steel billet cast. The main purpose of this model is to be able to simulate the mesostructure formation which occurs during the CC process. Comparisons between calculated positions of ECT and CET and measured in the industry are analyzed. We verified the numerical model by comparison of the measured transitions with the dimensions of simulated three zones: chill, columnar and equiaxed. The temperature profile can be obtained for any alloy and for different casting parameters (Figure 5.6) through the macro heat transfer model. These macro temperature fields represent the input data to the mesoscopic model. The detailed description of the macro heat transfer model [Vertnik and Šarler, 2002] is described in Sections 5.3 and 5.4 and Appendix A2.

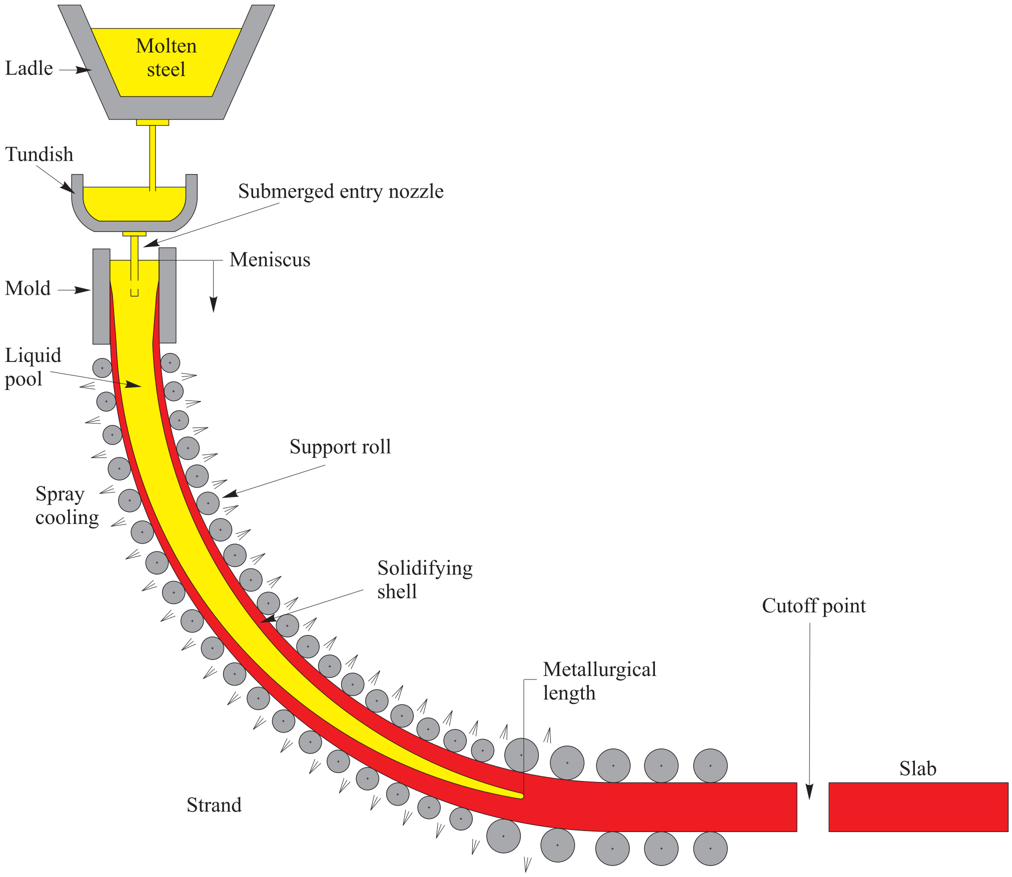

Figure 5.2: Scheme of the CC of steel [Vertnik, 2010].

ECT/CET model is considered in this dissertation. It is physically described by the macroscopic heat transfer model and the mesoscopic model. The temperature field is solved by the LRBFCM and the mesoscopic equations by the stochastic CA and PA methods.

Figure 5.3: CC of steel: the ladle (Štore Steel company).

Figure 5.4: CC of steel: the tundish (Štore Steel company).

Figure 5.5: CC of steel: the billet (Štore Steel company).

5.3 Macroscopic Model

The macroscopic model of the Štore Steel company is designed to be able to calculate the steady temperature distribution in the continuously cast billet as a function of the following process parameters: billet dimension, steel grade, casting temperature, casting velocity, primary, and two secondary cooling systems flows, pressures, temperatures, type and quantity of the casting powder, and the (non)application of the radiation shield and electromagnetic stirring.

The Bennon-Incropera [Bennon and Incropera, 1987] mixture continuum formulation is used for the physical model, solved by the recently developed meshless LRBFCM [Šarler and Vertnik, 2006]. In this novel numerical method, the domain and boundary of interest are divided into overlapping influence areas. On each of them, the fields are represented by the multiquadrics radial basis function collocation on a related sub-set of nodes. Time-stepping is performed in an explicit way. The governing equations are solved in their strong form, i.e. no integrations are performed. The polygonization is not present and the method is practically independent on the problem dimension. The other possibility represents the local approximation by the moving least squares [Šarler *et al.*, 2005] instead of interpolation. The characteristic of the model are represented as follows:

5.3.1 Governing Equations of Macroscopic Model

Consider a connected fixed domain Ω with boundary $\partial\Omega$ occupied by a liquid-solid phase change material described with the temperature dependent density ρ of the phase $\wp$, temperature dependent specific heat at constant pressure c_p, thermal conductivity λ, and the latent heat of the solid-liquid phase change L. The mixture continuum formulation [Bennon and Incropera, 1987] of the enthalpy conservation for the assumed system is

$$\begin{aligned}&\frac{\partial}{\partial t}(\rho h)+\nabla\cdot(\rho\vec{v}h)=\\&\nabla\cdot(\lambda\nabla T)+\nabla\cdot\left(\rho\vec{v}h-f_s^V\rho_s\vec{v}_s h_s-f_l^V\rho_l\vec{v}_l h_l\right)\end{aligned} \tag{5.1}$$

where ρ, h, L, λ, c_p represent the material density, specific enthalpy, specific latent of the solid-liquid phase change, thermal conductivity and specific heat, respectively.

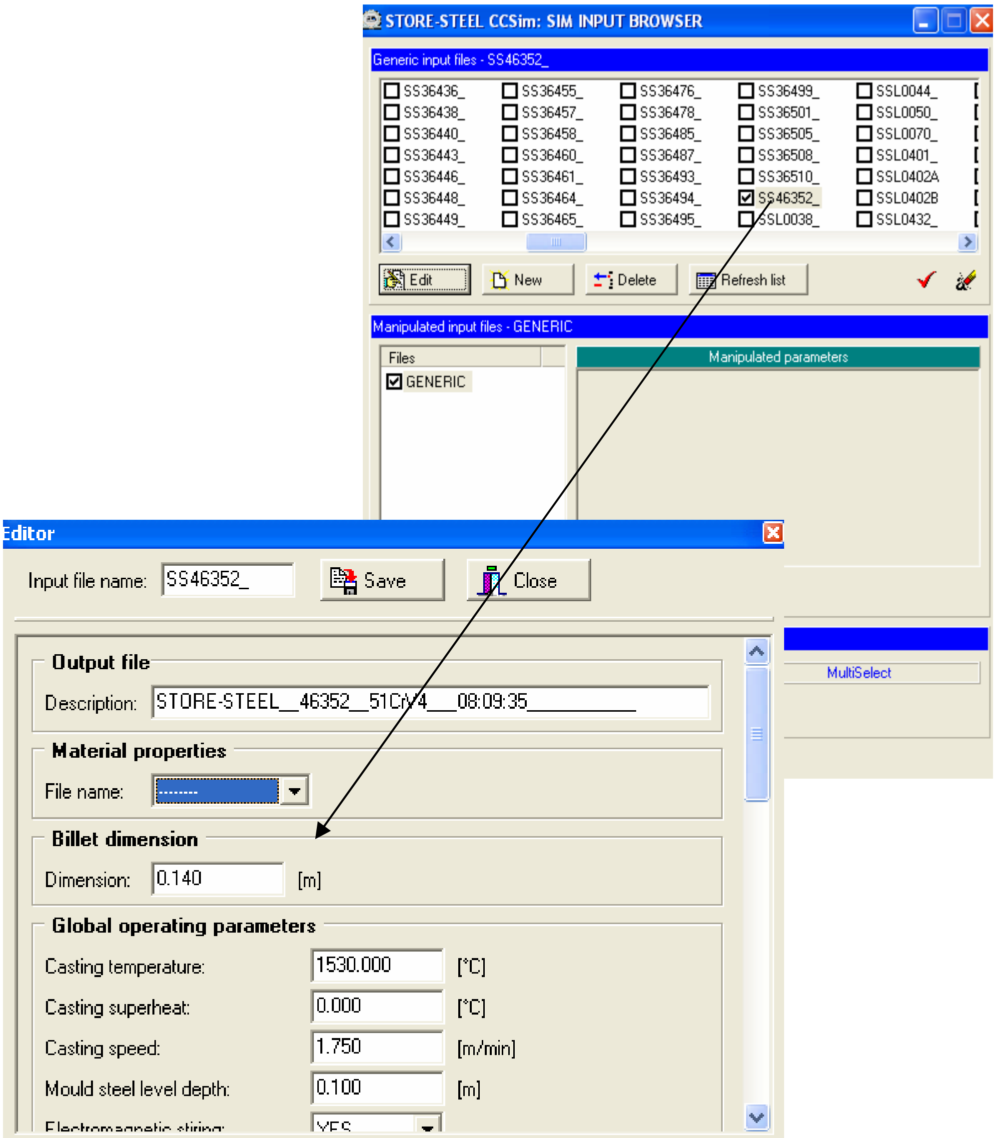

☐ SS36436_
☐ SS36438_
☐ SS36440_
☐ SS36443_
☐ SS36446_
☐ SS36448_
☐ SS36449_
☐ SS36455_
☐ SS36457_
☐ SS36458_
☐ SS36460_
☐ SS36461_
☐ SS36464_
☐ SS36465_
☐ SS36476_
☐ SS36478_
☐ SS36485_
☐ SS36487_
☐ SS36493_
☐ SS36494_
☐ SS36495_
☐ SS36499_
☐ SS36501_
☐ SS36505_
☐ SS36508_
☐ SS36510_
☑ SS46352_
☐ SSL0038_
☐ SSL0044_
☐ SSL0050_
☐ SSL0070_
☐ SSL0401_
☐ SSL0402A
☐ SSL0402B
☐ SSL0432_

☑ GENERIC

Input file name: SS46352_

Description: STORE-STEEL__46352__51CrV4___08:09:35__________

File name: --------

Dimension: 0.140 [m]

Casting temperature: 1530.000 [°C]
Casting superheat: 0.000 [°C]
Casting speed: 1.750 [m/min]
Mould steel level depth: 0.100 [m]
Electromagnetic stiring: YES

Figure 5.6: Macro heat transfer simulator [Vertnik and Šarler, 2002; Šarler *et al*., 2005].

The second term on the right-hand side is a correction term, which needs to accommodate the mixture continuum formulation of the convective term. In continuation we neglect this term. In equation (5.1) the mixture density and the thermal conductivity are defined as

$$\rho = f_s^V \rho_s + f_l^V \rho_l, \tag{5.2}$$

$$\lambda = f_s^V \lambda_s + f_l^V \lambda_l, \tag{5.3}$$

where $f_{\wp}^{V}$, represents the volume fraction of the phase $\wp$, The liquid volume fraction f_l^V might vary from 0 to 1 between solidus T_S and liquidus temperature T_L. Mixture velocity is defined as

$$\vec{v} = \left(f_s^V \rho_s \vec{v}_s + f_l^V \rho_l \vec{v}_l \right) / \rho, \tag{5.4}$$

and mixture enthalpy is defined as

$$h = f_s^V L_s + f_l^V L_l. \tag{5.5}$$

The constitutive temperature-enthalpy relationships are

$$h_s = \int_{T_{ref}}^{T} c_s dT, \tag{5.6}$$

$$h = h(T) + \int_{T_S}^{T} (c_l - c_s) dT + L, \tag{5.7}$$

with T_{ref} standing for the reference temperature. The thermal conductivity and the specific heat of the phases can arbitrarily depend on temperature.

5.3.2 Spatial Discretization

The temperature field of a point in the billet is prescribed by the following three-dimensional vector in the Cartesian coordinate system:

$$\mathbf{p} = x\mathbf{i}_x + y\mathbf{i}_y + z\mathbf{i}_z, \tag{5.8}$$

where x, y, z are the coordinates and $\mathbf{i}_x, \mathbf{i}_y, \mathbf{i}_z$ are base vectors. The z coordinate measures the length of the inner radius of the casting machine. This Cartesian coordinate system represents the flat geometry, which is the geometrical approximation of the real curved casting process (Figure 5.7). The origin of the z coordinate coincides with the top side of the mould, and the base vector $\mathbf{i}_z$ coincides with the casting direction. The x coordinate measures the width (west-east direction) of the billet, perpendicular to the casting direction. Its origin coincides with the centre of the billet. The y coordinate measures the thickness (south-north direction) of the billet, perpendicular to the casting direction. Its origin coincides with the inner (south) side of the billet. According to the heat transfer phenomena of the CC of steel, the heat conduction in the casting direction might be roughly neglected. The z coordinate is then parabolic, while the x and y coordinates are elliptic. The temperature field in the billet at a given time is described by the calculation of the cross-section (called infinite slice) temperature field of the billet. In this way the temperature field at a given z coordinate depends only on the slice history and its cooling intensity as a function of time. The slices form at the z_{start} longitudinal coordinate of casting and travel in the direction of the $\mathbf{i}_z$ base vector with the casting speed v. For calculating the cooling intensity of the slice as a function of time, we need the connection between the z coordinate of the casting machine and the slice history t, which is in general

$$z(t)=\int_{t_i}^{t} v(t')\,dt' + z_{start} \quad v(t)=\vec{v}(t)\cdot\mathbf{i}_z, \tag{5.9}$$

where t_i is the initial time of a slice. In the case when the casting speed and other process parameters are steady, we obtain the following simple connection between the z coordinate of the casting machine and the slice history t

$$t(z)=\frac{z-z_{start}}{v}+t_i. \tag{5.10}$$

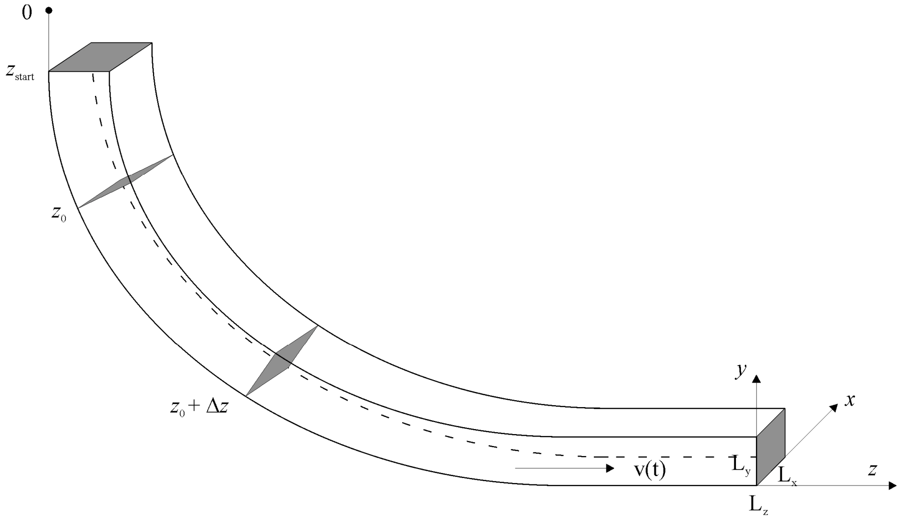

Figure 5.7: Slice traveling schematics of the billet.

In subsequent calculations we use the simple equation (5.10), since we assume the steady-state solution of the casting process. The prescribed simplified spatial discretization also simplifies the equation (5.1) by removing the convective terms. Thus the equation (5.1) transforms into transient equation, defined on x-y plane

$$\frac{\partial}{\partial t}(\rho h)=\nabla\cdot(\lambda\nabla T). \tag{5.11}$$

This simplified model is consistent with the models, introduced by [Louhenkilpi, 1995].

5.3.3 Boundary Conditions

The heat transport mechanisms in the mould take into account the heat transport mechanisms through the casting powder, across the air-gap (if it exists), to the mould surface, in the mould, and from the mould inner surface to the mould cooling water. The heat transport mechanisms in the secondary cooling zone take into account the effects of the casting velocity, strand surface temperature, spray nozzle type, spray water flow, temperature and pressure, radiation and cooling through the rolls contact. Different types of the rolls are considered (driving, passive, centrally cooled, externally cooled, etc.). The mentioned basic heat transfer mechanisms are modified with regard to running water and rolls stagnant water at relevant positions.

Represented model is not in focus of this dissertation. Therefore a more elaborated step by step description and testing of the used LRBFCM solution procedure for temperature field is presented in [Šarler and Vertnik, 2006]. The use of the model in simulation system for CC of steel billets is given in [Šarler, *et al.*, 2006]. The process parameters were taken directly from the process computer, installed on the casting machine. The thermo-physical material properties of the spring steel were calculated by the JMatPro software [Saunders *et al.*, 2003].

5.4 Coupling of the Mesoscopic and the Macroscopic Models

The movement of the solid-liquid interface is governed by the evolution of the temperature field in the computational domain. The ECT/CET is modelled by a stochastic method to track the interface motion coupled to the determinate heat transfer calculations solved by the LRBFCM [Šarler and Vertnik, 2006]. A solution of the mesoscopic model based on the transition rules for the classical CA methods and PA method is described first. The flowchart of the calculations is given in Figure 5.8. Next the coupling scheme for LRBFCM-CA and LRBFCM-PA method is explained.

The flowchart of the numerical solution for the ECT/CET model is presented:

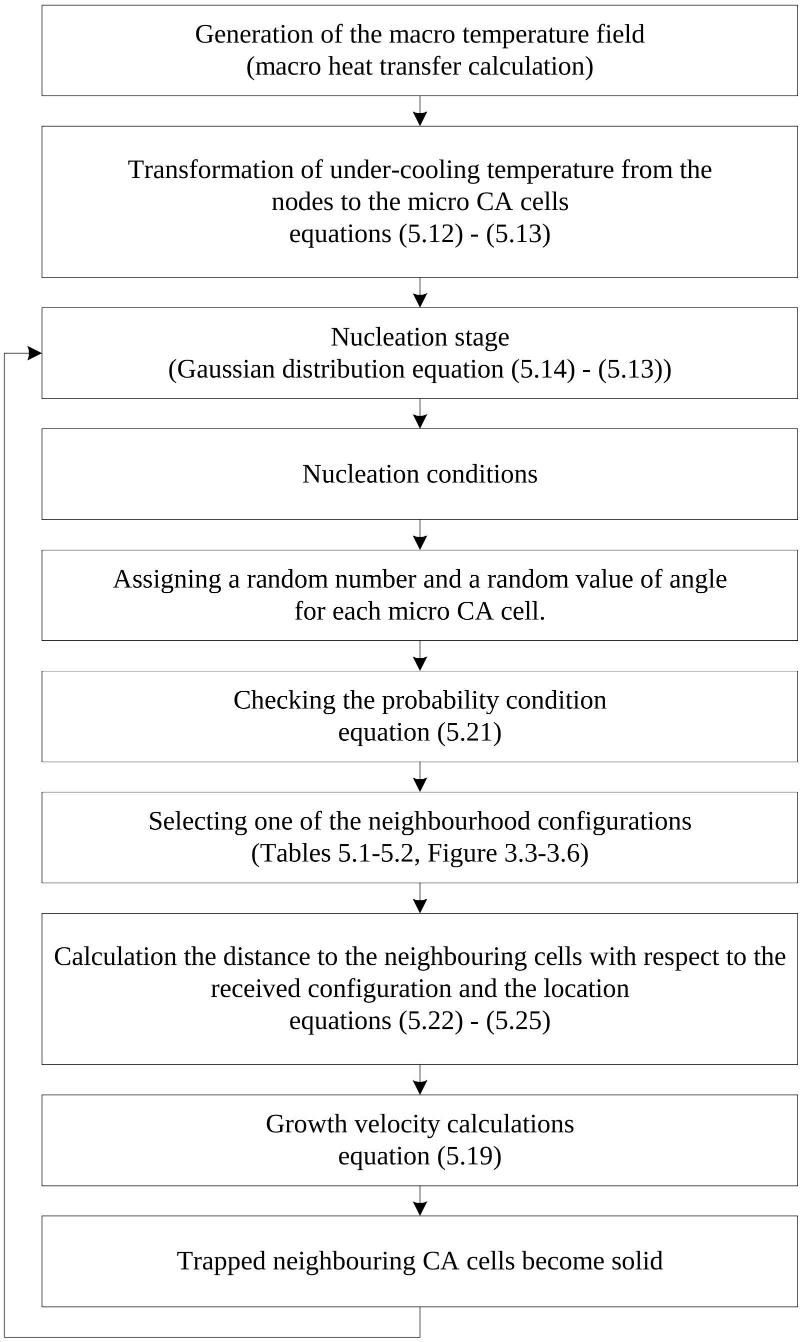

Figure 5.8: Flowchart of the ECT/CET model.

5.4.1 LRBFCM-CA and LRBFCM-PA Transfer of Temperature

The described macroscopic model gives the information on the macroscopic temperature fields (Section 5.3). Temperature values are calculated on the macro nodes so they need to be interpolated for use in the mesoscopic CA and PA model. On the meso level of calculation the temperature of a CA cell (PA node) is influenced by its nearest four neighbouring macro calculation nodes (see Figure 5.9). Obtained values of temperatures are recalculated into the undercooling temperatures by using the following formula $\Delta T_{macro} = T_L - T_{macro}$, where T_{macro} represents the macro node temperature, and then are interpolated for each micro CA cell (PA node) over time. In the present work the following simple interpolation formula is used to find the value of the temperature for each CA cell or PA node

$$\Delta T_{micro} = (\sum_{i=1}^{4} \Delta T_{macro} w_i) / \sum_{i=1}^{4} w_i, \tag{5.12}$$

$$w_i = \exp(l_i^{-1}), \tag{5.13}$$

where ΔT_{micro}, ΔT_{macro}, l_i represent the undercooling temperature of the cell (or PA node), the undercooling temperature for the macro node from the macro heat transfer calculations and the distance to the nearest macro nodes, respectively.

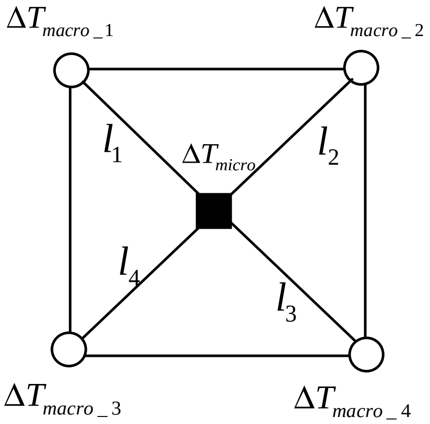

Figure 5.9: Scheme of the transfer of temperature from the macroscopic to mezoscopic discretisation (circles represent the macro nodes, black square represents the CA cell).

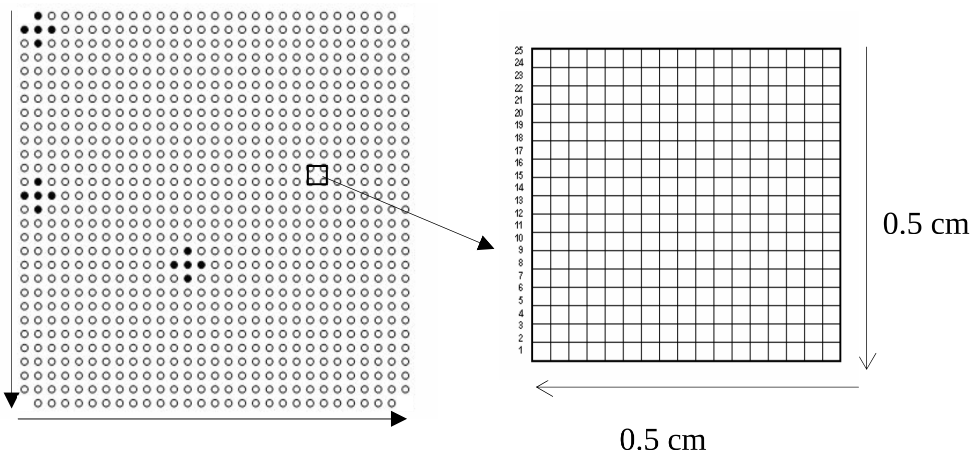

Figure 5.10: Left: Relationship between the macro node arrangement and, right: meso CA mesh. Solid circles in the macro node arrangement represent schematics of the corner, surface and bulk 5-noded domains of influence of the meshless method.

5.5 Mesoscopic Model

The following three processes take place on the mesoscopic level of calculation

- Nucleation process
- Growth process
- Impingement: growth continues until the grains occupy the whole preliminary liquid region.

These stages have been already discussed in details in Chapter 2.

5.5.1 Nucleation Process

The Gaussian nucleation model as defined in [Thevoz *et al.*, 1989] and elaborated in [Lee and Hong, 1997] and already presented in Section 2.1, was applied in the mesoscopic model. If all nuclei of a certain class are active at a certain undercooling, it is natural to relate the nucleus density to the undercooling. Considering this argument, Thévoz *et al.* [Thevoz *et al.*, 1989] proposed a statistical approach (called Gaussian distribution), which indicates a continuous dependency of N on the temperature T. In our work, this heterogeneous continuous nucleation model was adopted in which two different Gaussian distributions were considered at the mould surface and in the bulk (Figure 5.11), respectively.

$$\frac{dN}{d\left(\Delta T\right)_{surface}} = \frac{N_{stot}}{\sqrt{2\pi}\Delta T_{\sigma\_surface}} \exp - \left[\frac{\overline{\Delta T} - \Delta T_{\max\_surface}}{\sqrt{2}\Delta T_{\sigma\_surface}}\right]^2, \qquad (5.14)$$

$$\frac{dN}{d\left(\Delta T\right)_{bulk}} = \frac{N_{stot}}{\sqrt{2\pi}\Delta T_{\sigma\_bulk}} \exp - \left[\frac{\overline{\Delta T} - \Delta T_{\max\_bulk}}{\sqrt{2}\Delta T_{\sigma\_bulk}}\right]^2. \qquad (5.15)$$

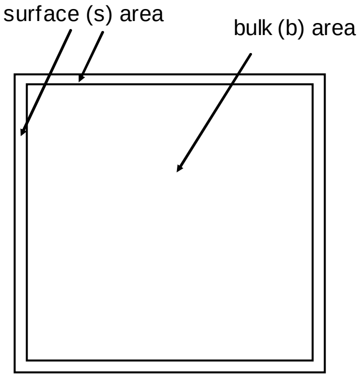

Figure 5.11: Surface and bulk area.

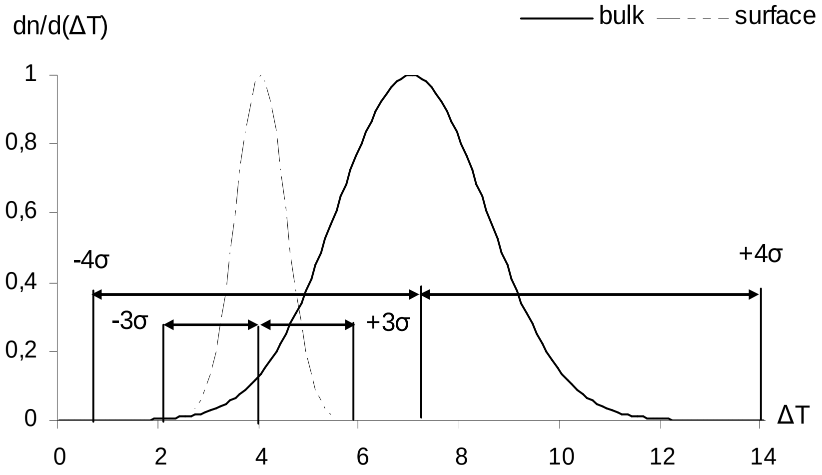

Figure 5.12: Nucleation curves for the surface and bulk area.

Nucleation starts at the surface layer and then moves from the mould with respect to the undercooling temperature. The position of the new grains is chosen randomly according to the equations (5.14) and (5.15) and is related with the value of mean undercooling temperature. It is assumed that the highest occupancy of nucleuses is expected in the range of ($-3\Delta T_\sigma$) to ($+3\Delta T_\sigma$), (Figure 5.12).

5.5.2 Growth Process

The KGT [Kurz, Givoanola and Trivedi, 1986] model was used as the model of the growth kinetics. The description and basic elements of the model have been already presented in Section 2.2.

5.5.2.1 Numerical Treatment of the KGT Model

For assumed Pe values, first the equation (2.21) which represents Ivantsov function and then equation (2.28) which represents the stability parameter, are calculated. Then the coefficients ζ_1 and ζ_2 of the growth velocity are calculated, following the equations (2.33) and (2.34), respectively. The velocity V and the dendritic tip R , can be obtained

$$V = -\zeta_1 / \zeta_2 \tag{5.16}$$

$$R = 2\pi \left(\frac{\Gamma}{m \dfrac{-V(1-k)c_0}{\left[1-(1-k)Iv(\mathrm{Pe})\right]D_l} \varsigma_c - G} \right)^{1/2} . \tag{5.17}$$

Finally the undercooling temperature ΔT is definedw

$$\Delta T = m \left(c_0 - \frac{c_0}{1-(1-k)Iv(\mathrm{Pe})} \right) + \frac{2\Gamma}{R} . \tag{5.18}$$

For each node the value of undercooling temperature ΔT_{macro} from the macro heat transfer calculation, is known. Undercooling temperatures ΔT (equation (5.18)), according to the above scheme, should be related with the interpolated undercooling temperatures ΔT_{micro} (equation (5.12)) in order to find the growth velocity for each node separately. This scheme would take too much time. To reduce the calculation time the following procedure is employed. A range of Peclet numbers from $\mathrm{Pe}_{\min}$ to $\mathrm{Pe}_{\max}$ need to be chosen to be able to compare the recalculated undercooling temperatures with those received from the macro heat transfer calculations. In the present study we assume $\mathrm{Pe}_{\min} = 0.004, \mathrm{Pe}_{\max} = 10$ with step $\Delta\mathrm{Pe} = 0.002$. The values of velocities $V(\mathrm{Pe})_1, ..., V(\mathrm{Pe})_n$ (equation (5.16)) and the undercooling temperatures $\Delta T(\mathrm{Pe})_1, ..., \Delta T(\mathrm{Pe})_n$ (equation (5.18)) are recalculated in advance. The least squares method is used to obtain the coefficients γ_1, γ_2, γ_3 of the growth velocity equation (5.19). The values of three coefficients are determinate through the relation $\left(X^T X\right)^{-1} X^T Y$ using the values of $\Delta T(\mathrm{Pe})$, $\left(\Delta T(\mathrm{Pe})\right)^2$, $\left(\Delta T(\mathrm{Pe})\right)^3$ as matrix X of dimension [3x5000] and $V(\mathrm{Pe})$ as matrix Y of dimension [1x5000].

The growth velocity in each CA cell (or PA node) is then calculated thought the following formula

$$V(\Delta T_{micro}) = \gamma_1(\Delta T_{micro})^3 + \gamma_2(\Delta T_{micro})^2 + \gamma_3(\Delta T_{micro}), \tag{5.19}$$

where

$$\gamma_i = \left(\mathrm{Pe}, V, \Delta T_{micro}\right) \quad \text{for} \quad =1,2,3,... . \tag{5.20}$$

The same solution was proposed by [Yamazaki *et al.*, 2006]. If some of the assumed parameters (material properties of the alloy) change, the coefficients in the relation (5.19) have to be modified as well.

5.5.3 Impingement Process

At the beginning all points are liquid. The nucleation process takes place in the mushy zone where the first grains nucleate and afterwards the growth stage occurs. The process is completed until the whole area is composed of the grains (solid).

5.6 Solution of the Mesoscopic Model by the CA

5.6.1 LRBFCM-CA

Mesoscopic equations are numerically solved by the CA technique [Rappaz *et al.*, 2003]. Conventional CA discretisation is generated first and a set of possible neighbourhood configurations is determined (see Table 5.1). Process starts with nucleation where the following conditions need to be checked: appropriate temperature ΔT in the micro cell and the probability condition (equation (5.21)). During each time step all cells are assigned a random number between

($0 < rand < 1$) and a random computational angle θ from $-45 < \theta < 45$. The transformation from liquid to solid will occur only when $rand < p$

$$p = \frac{1}{\Delta T_\sigma \sqrt{2\pi}} \exp - \left[\left(\Delta T - \Delta T_{\max} \right) / \left(\sqrt{2} \Delta T_\sigma \right) \right]^2 . \tag{5.21}$$

Once a cell is nucleated it grows with a preferential direction corresponding to its assigned orientation and with respect to the heat flow. Depending on the randomly chosen angle θ, the following neighbourhood configurations [Nastac, 2004] are chosen: Neumann, Moore and modified Moore (Section 5.6.1.1), respectively (Figures 3.3-3.6). A new neighbourhood configuration is developed in this dissertation. It is shown in Figure 3.7, see Section 5.6.1.1.

All of new nucleuses which arise from the ‘parent’ grow with different randomly chosen configuration which is fixed for them at the time step when they occur. For all „neighbours” of the treated nucleus, the value *d* is checked by using the formula

$$d = l(t) / a_\theta , \tag{5.22}$$

where

$$l(t) = \int_{t_0}^{t} V(\Delta T) \, dt , \tag{5.23}$$

$$a_\theta = a \sqrt{\tan^2 \theta + 1} , \tag{5.24}$$

where t_o, a, θ represents the initial time, the size of the cell and the crystallographic angle, respectively.

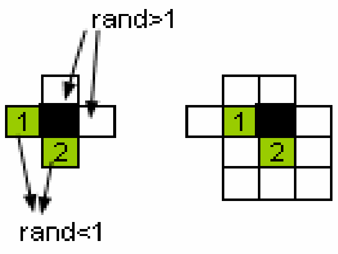

Figure 5.13: The explanation of growth stage, see also Table 5.1.

The $l(t)$ is the length of the moving solid-liquid interface trough the time $t_0, t_0 + \Delta t$. The trapezoidal rule approximation technique was used to calculate the movements of the interface

$$\int_{t_0}^{t} V\left(\Delta T\left(t\right)\right) dt \approx \left(t - t_0\right) \frac{V\left(\Delta T\left(t_0\right)\right) + V\left(\Delta T\left(t\right)\right)}{2}. \tag{5.25}$$

If a neighbour is one of the four nearest east, north, west, south neighbours ($\theta = 0^{\circ}$) then the equation (5.24) is reduced to $a_\theta = a$, but if neighbour is a corner neighbour ($\theta = 45^{\circ}$) then $a_\theta = a\sqrt{2}$.

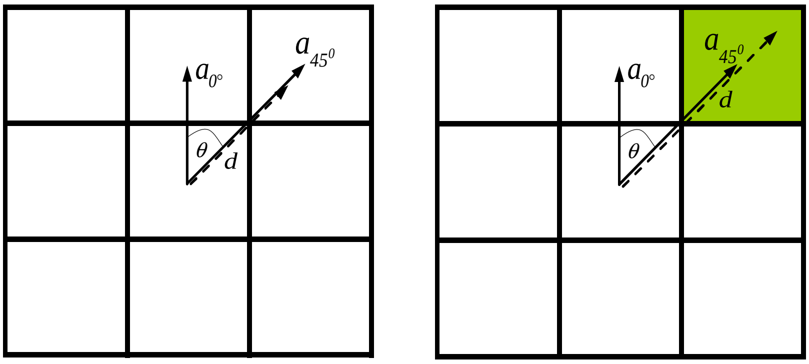

Figure 5.14: Left: growth front will not reach the closest neighbour $c_{i,j} = \{c_{i+1,j+1}\}$ - the cell will not be trapped $d < 1$, right: growth front will reach the closest neighbour $c_{i,j} = \{c_{i+1,j+1}\}$ -the cell will be trapped $d \geq 1$ and becomes solid.

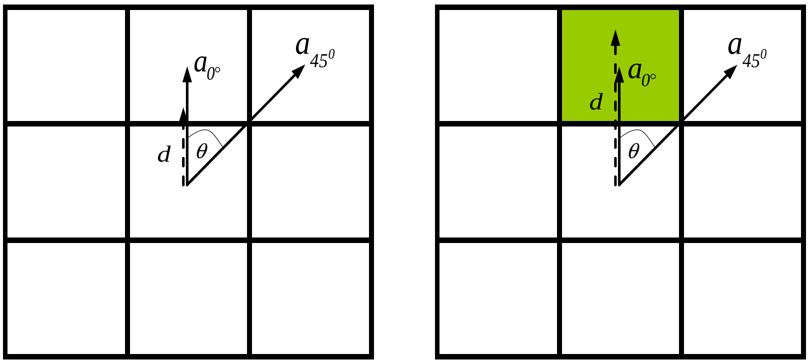

Figure 5.15: Left: growth front will not reach the closest neighbour $c_{i,j} = \{c_{i+1,j}\}$. The cell will not be trapped $d < 1$, right: growth front will reach the closest neighbour $c_{i,j} = \{c_{i+1,j}\}$. The cell will be trapped $d \geq 1$ and becomes solid.

When $d \geq 1$, the growth front of the solid reference cell can touch the centre of the neighbouring cell and then this cell transforms its state from liquid to solid [Zhu and Hong, 2001] (Figure 5.14-5.15). It is assumed that the growth is not allowed to take place for more than a half of CA cell during each meso time step. This is assumed with a sufficient small time step.

5.6.1.1 Neighbourhood Configuration and Mesh in the CA Method

The probabilistic selection of presented neighbourhood configurations is based on the randomly chosen angle θ as shown in Table 5.1. When $-15 < \theta < 30$ modified Moore are selected. Since two types of modified Moore (variant 1 and variant 2) are used in calculations, a further random selection of either one of the two types is chosen. This selection is arbitrary and based on the random number $0 < rand < 1$ that is generated for each CA cell. A schematic of the selection of neighbourhood configuration is seen in Table 5.1 and Table 5.2.

Table 5.1: Selection of neighbourhood configuration based on probabilistic calculation of θ for Nastac configurations.

$\lvert\theta\rvert;\ 0 \le \theta \le 45$	$rand$	Neighbourhood configuration
$30 \le \theta \le 45$	-	Figure 3.4
$0 \le \theta \le 15$	-	Figure 3.5
$15 < \theta \le 30$	$rand \le 0.5$	Figure 3.6
$15 < \theta \le 30$	$rand > 0.5$	Figure 3.3

Table 5.2: Selection of neighbourhood configuration based on probabilistic calculation of i for newly introduced configurations.

i	Neighbourhood configuration
1	Figure 3.7 a
2	Figure 3.7 b
3	Figure 3.7 c
4	Figure 3.7 d
5	Figure 3.7 e

Calculations of the temperature field are done for the regular square gird covered by macro nodes (Figure 5.10 (left)). Each square of four macro nodes includes 625 meso CA cells. Relationship between macro field and meso CA mesh is presented in Figure 5.10.

5.6.2 LRBFCM-PA

The procedures are the same as for the CA method (Section 5.6.1). Nucleation takes place. Once a point nucleates it grows with respect to the heat flow and with respect to the ‘neighbourhood’ configuration which is now associated with the position of the neighbouring points which fall into a circle [Janssens, 2003;

Janssens, 2000] with radius R_H (see Figure 3.8). It means that each point can contain different number and position of the neighbours, which gives various possibilities of neighbourhoods. The growth velocity is calculated according to the KGT model. For all neighbours of the treated point, general criterion d is checked

$$d = l(t) / a_i, \tag{5.26}$$

where a_i ($a_i < R_H$) represent different lengths from the central to the random points in the circular neighbourhood. When $d \geq 1$, the growing solid touches the centre of the neighbouring point and this point transforms its state from liquid to solid (Figures 5.16 - 5.17).

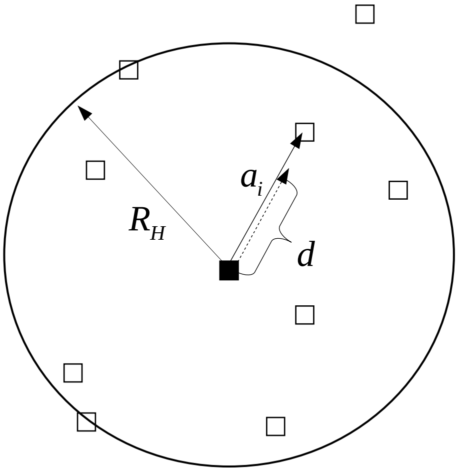

Figure 5.16: Growth front will not reach the closest neighbour. The point will not be trapped $d < 1$.

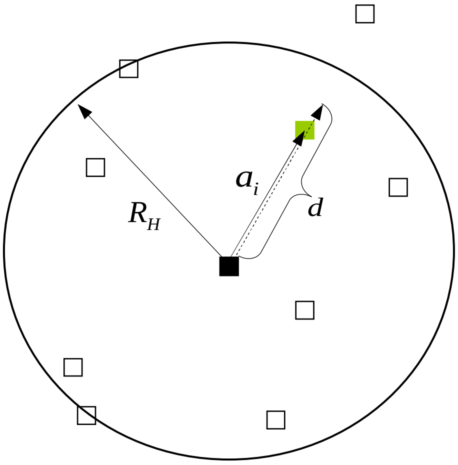

Figure 5.17: Growth front will reach the closest neighbour. The point will be trapped $d \geq 1$ and becomes solid.

5.6.2.1 Neighbourhood Configuration and Node Arrangement in the PA Method

The novel neighbourhood configuration of the PA method has been chosen (see Figure 3.8) which contains points within circle with radius R_H centred on the reference point. Different dimensions of radius of neighbourhood can be chosen. Random PA discretization is always generated first.

Calculations of the temperature field are done for the regular square node arrangements covered by the macro nodes (Figure 5.18 left). The irregular node arrangement is achieved in practice as a random selection of points from the centres of CA cells. It is constructed from the regular CA cell size by randomly taking away certain percentage of the points (Figure 5.18 right).

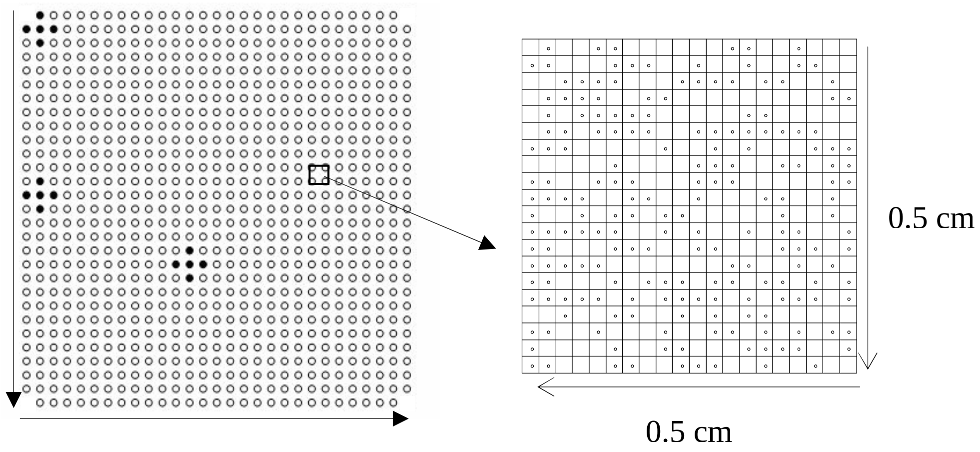

Figure 5.18: Left: Relationship between macro field and, right: PA node arrangement. Solid circles in the macro field represent schematics of the corner, surface and bulk 5-noded domains of influence of the meshless method.

6 Dendritic Growth Model

This chapter represents a simple numerical model which can simulate the dendritic forms [Zhu and Hong, 2001; Nastac, 2004; Feng *et al.*, 2002; Beltran-Sanchez and Stefanescu, 2003] during the solidification of a pure substance from its supercooled melt. The developed algorithm can simulate dendritic growth with the predetermined position of nucleuses, i.e. the nucleation model is not presented. The solution is structured by the classical CA and a novel PA technique, already described in Chapters 3 and 4. In order to predict the dendritic structure, the stochastic CA or PA methods are combined with the heat transfer calculations to obtain the temperature and solid fraction fields [Lorbiecka and Šarler, 2010b; Lorbiecka and Šarler, 2010c]. The governing thermal equation was solved by the explicit FDM.

6.1 Governing Equations

Thermally induced dendritic growth is considered in this dissertation. It is physically described by the heat conduction and phase change kinetics. The stochastic model includes calculations of the interface temperature, curvature, Gibbs-Thomson coefficient. This coefficient takes into account the thermodynamic anisotropy related to the crystal orientation and crystal growth velocity which accounts for the kinetic anisotropy by taking into the consideration the crystal growth direction θ and the preferential orientation θ_{def}. The stochastic model receives temperatures from the deterministic model and the deterministic model receives the solid fraction from the stochastic model. The heat transfer model is solved by the FDM on the regular nodes. The solid fraction calculations are done for the classical CA method and PA method with random node arrangement.

6.1.1 Temperature Field

Consider a two dimensional domain Ω with boundary $\partial\Omega$ filled with a phase change material which consists of at least two phases, solid and liquid, separated by an interfacial region, which is usually very thin in pure substances. The thermal field in such a system is governed by the following equation [Xu *et al.*, 2008]

$$\frac{\partial}{\partial t}(\rho h) = \nabla \cdot (\lambda \nabla T). \tag{6.1}$$

The specific enthalpy is constituted as

$$h = c_p T + f_l L, \tag{6.2}$$

where f_l represents the liquid fraction, respectively. All material properties are assumed constant for simulation simplicity. The solid and liquid fractions are defined as a function of temperature

$$f_s + f_l = 1, \tag{6.3}$$

$$f_s(T) = \begin{cases} 1 & ; \quad T \le T_S \\ \dfrac{T_L - T}{T_L - T_S} & ; \quad T_S < T < T_L \\ 0 & ; \quad T \ge T_L \end{cases}, \tag{6.4}$$

where f_s represents solid fraction. In case of pure substance are the solidus and the liquidus temperatures equal to the melting temperature T_M. However, for the computational purposes a narrow melting interval is always present $T_L > T_M > T_S$. The melting temperature T_M is defined as $T_M = \frac{1}{2}(T_S + T_L)$.
We search for the temperature at time $t_0 + \Delta t$ by assuming the initial conditions

$$T(\mathbf{p}, t_0) = T_o(\mathbf{p});\ \mathbf{p} \in \Omega, \tag{6.5}$$

$$f_s(\mathbf{p}, t_0) = f_{s0}(\mathbf{p});\ \mathbf{p} \in \Omega, \tag{6.6}$$

(where $\mathbf{p}$ represents the position vector) and Neumann boundary conditions

$$\frac{\partial T}{\partial n}(\mathbf{p}, t) = F(\mathbf{p}, t);\ \mathbf{p} \in \partial\Omega,\ t_0 < t \le t_0 + \Delta t, \tag{6.7}$$

where $\mathbf{n}$ represents the normal on $\partial\Omega$ and T_0, f_{s0}, F represent known functions.

6.2 Phase Change Kinetics

6.2.1 Interface Undercooling

The phase change situation can be achieved by undercooling a liquid below its melting or liquidus temperature. When a solid seed is placed in such an undercooled melt, solidification will be initiated. Due to crystal anisotropy and perturbations in the system, the growth of the solid from the seed will not be uniform and an equiaxed dendritic crystal will form. Solid-liquid interface is undercooled to the temperature T_f defined as [Gibbs, 1928; Saito *et al.*, 1988; Nakagawa *et al.*, 2006]

$$T_f = T_M - \Gamma K, \tag{6.8}$$

where K is the interface curvature.

6.2.2 Dendritic Growth Kinetics

The growth process is driven by the local undercooling. The interface growth velocity is given by the classical sharp model [Shin and Hong, 2002]

$$V_g^* = \mu_K \left[T_f - T\left(\mathbf{p}, t\right) \right]; \; \mathbf{p} \in \Gamma_{s,l}, \tag{6.9}$$

where μ_K, $\Gamma_{s,l}$ are the interface kinetics coefficient and the solid-liquid interface, respectively.

Dendrites always grow in the specific orientations. Therefore, it is necessary to consider anisotropy in either the interfacial kinetics or surface energy (or both). The present model accounts for the anisotropy in both kinetics.

6.2.3 Thermodynamic Anisotropy

The Gibbs-Thomson coefficient can be evaluated [Krane *et al.*, 2009] by taking into account the thermodynamic anisotropy related to the crystal orientation and type as follows

$$\Gamma = \overline{\Gamma} \left[1 - \delta_t \cos\left[S\left(\theta - \theta_{def} \right) \right] \right], \tag{6.10}$$

where S, θ, θ_{def}, δ_t, $\bar{\Gamma}$ represent factors which control the number of preferential directions of the material's anisotropy ($S = 0$ for the isotropic case, $S = 4$ for four fold anisotropy and so on), growth angle (angle between the y coordinate and the line that connects the center of the mass of the dendrite and point at $\Gamma_{s,l}$, see Figure 6.1, the preferential orientation, thermodynamic anisotropy coefficient and the average Gibbs - Thomson coefficient, respectively.

6.2.4 Kinetic Anisotropy

The crystal growth velocity is calculated according to the crystal orientation by taking into the consideration the crystal growth direction θ and the preferred orientation θ_{def}. The crystal growth velocity follows the equation [Shin and Hong, 2002]

$$V = V_g^{*}(\mathbf{p},t)\left[1+\delta_k \cos\left(S\left(\theta-\theta_{def}\right)\right)\right];\mathbf{p}\in\Gamma_{s,l}, \tag{6.11}$$

where δ_k represents the degree of the kinetic anisotropy, respectively.

6.3 Coupling Scheme

The movement of the solid-liquid interface is governed by the evolution of the temperature field in the computational domain (Figure 6.3) and the phase change kinetics.

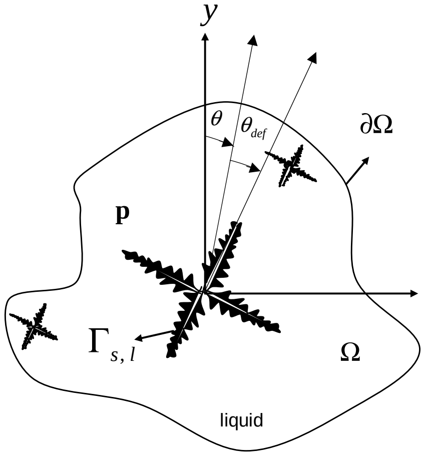

Figure 6.1: Calculation domain of the dendritic growth.

The dendritic structures are modelled by the stochastic method to track the interface motion coupled to the deterministic heat transfer calculations. We first describe the solution of the temperature field based on the FDM and subsequently the transition rules for the CA (PA) methods for calculation of the solid fraction field. The flowchart of the calculations is given in Figure 6.2.

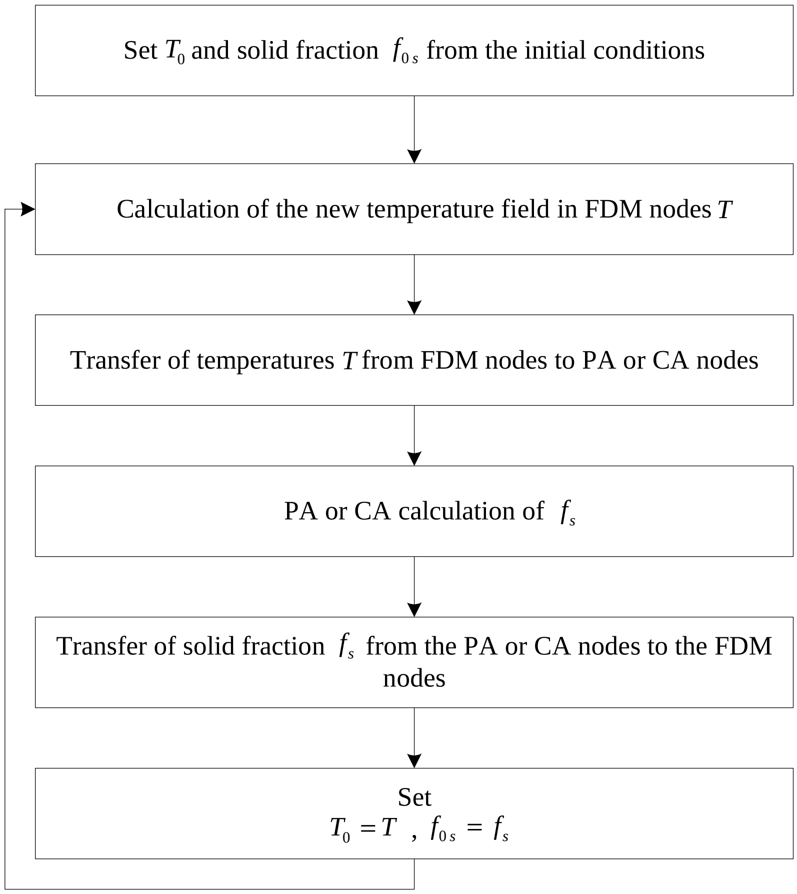

Figure 6.2: Flowchart of the thermal field and solid fraction calculations.

6.4 Solution of the Temperature Field

A square domain with a side l is considered. The solution for the temperature field is performed by the simple explicit FDM. The number of points in FDM mesh in x and y directions is N_{xy}. The total number of FDM grid points is N_{xy}^2 - 4, since the four corner nodes are not considered. A uniform FDM discretization is made with mesh distance $\Delta x = \Delta y = a = l / \left(N_{xy} - 1\right)$ as seen in Figure 6.3 (top). Solution of the temperature field in the domain nodes is thus

$$T_{i,j} = T_{0\,i,j} + \frac{\Delta t \lambda}{\rho c_p}(\left[\left(T_{0\,i-1,j} - 2T_{0\,i,j} + T_{0\,i+1,j}\right) / \left(\Delta x^2\right)\right] + \left[\left(T_{0\,i,j-1} - 2T_{0\,i,j} + T_{0\,i,j+1}\right) / \left(\Delta y\right)^2\right]) + \frac{L}{c_p}\left(f_{s\,i,j} - f_{0s\,i,j}\right), \tag{6.12}$$

for $i = 2,3,...,N_{xy} - 1$ and $j = 2,3,...,N_{xy} - 1$.

The boundary nodes are calculated (the Neumann boundary conditions are set to $F = 0$ W/m^2) as: west side: $T_{1,j} = T_{2,j}$ for $j = 2,...,N_{xy} - 1$. East side: $T_{N_{xy},j} = T_{N_{xy}-1,j}$ for $j = 2,...,N_{xy} - 1$. North side: $T_{i,N} = T_{i,N-1}$ for $i = 2,...,N_{xy} - 1$. South side: $T_{i,1} = T_{i,2}$ for $i = 2,...,N_{xy} - 1$ where $f_{0s\,i,j}$, $T_{0\,i,j}$, $T_{0\,i+1,j}$, $T_{0\,i-1,j}$, $T_{0\,i,j+1}$, $T_{0\,i,j-1}$ are initial solid fraction, initial temperature in the FDM central, east, west, north and south nodes, respectively.

6.5 Solution of the Solid Fraction Field

We now define and discuss the elements of the classical CA and the novel PA solutions in details.

6.5.1 Definition of Mesh and Neighbourhood Configuration

Square cells with length $\Delta x = \Delta y = a = l / n_{xy}$ where $n_{xy} = N_{xy} - 1$ represents the number of cells in x and y directions are considered in the CA approach. In the PA approach the square is divided in uniformly or nonuniformly distributed nodes and the cells are not defined.

6.5.2 Mesh and Neighbourhood in the CA Method

The conventional square mesh structure is applied in CA calculations. It represents a square domain covered by the CA cells $x_{CA\,i,j}$, $y_{CA\,i,j}$ located exactly in the middle of four FDM nodes, as it is depicted in Figure 6.3 (middle).

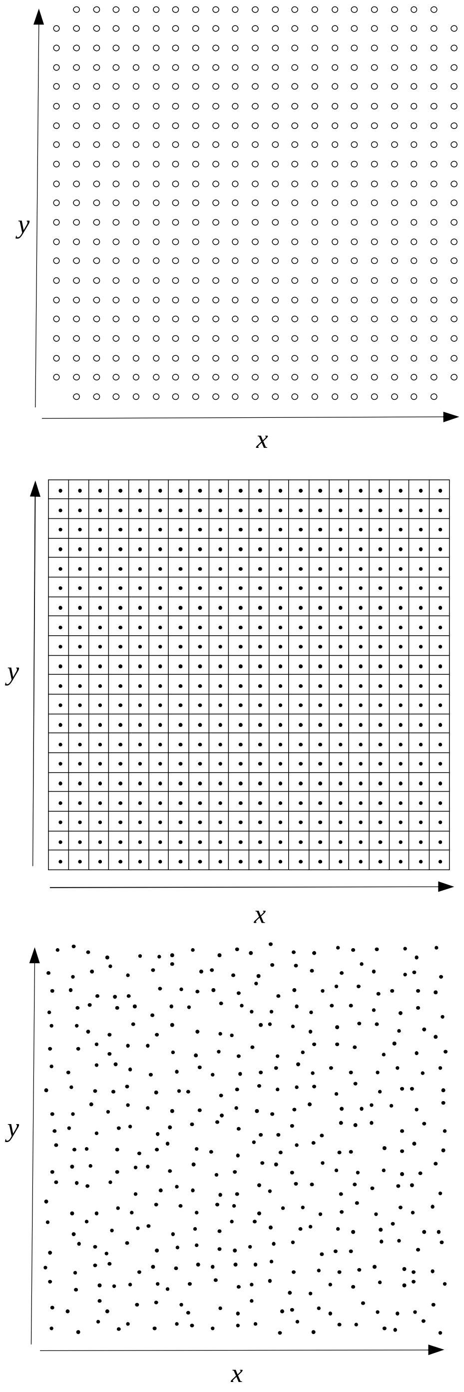

Figure 6.3: Schematics of space discretization. Top: FDM nodes with $N_{xy} = 21$, middle: CA cells with $n_{xy} = 20$, bottom: PA nodes for $n_{xy} = 20$.

$$x_{CA\,i,j} = \frac{1}{2}\left[x_{FDM\ i,j} + x_{FDM\ i+1,j}\right], \tag{6.13}$$

$$y_{CA\,i,j} = \frac{1}{2}\left[y_{FDM\ i,j} + y_{FDM\ i,j+1}\right]. \tag{6.14}$$

The von Neumann neighbourhood (Figure 3.3) that takes into account only the closest neighbours is used in the regular cell structures.

6.5.3 Mesh and Neighbourhood in the PA Method

For the novel PA method the random node arrangement is in the dissertation generated from the regular CA mesh. To construct the random node arrangement the CA cell centres are displaced to randomly quasi positions $x_{PA\,i,j}$, $y_{PA\,i,j}$ on the computational domain (see Figure 6.3, bottom).

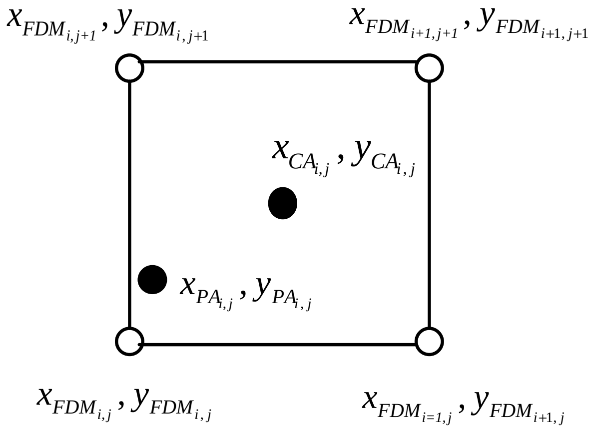

Figure 6.4: Schematic representation of the relationship between FDM nodes (4 corners), CA cell (centre) and the random PA node.

The displacement of each CA centre is assumed to be possible only in the square area defined by the four FDM nodes. The following procedure is applied

$$x_{PAi,j} = x_{CAi,j} + \varepsilon\left[2rand - 1\right], \tag{6.15}$$

$$y_{PAi,j} = y_{CAi,j} + \varepsilon\left[2rand - 1\right], \tag{6.16}$$

where $x_{PA_{i,j}}$, $y_{PA_{i,j}}$, ε represent coordinates of PA nodes and the scaling value $0 \le \varepsilon \le 0.49$, respectively. It must be emphasized that the PA procedure is established on the random nodes in general. The heat transfer calculations are performed on the regular FDM nodes, which are explained in Section 6.8.

The PA node grows with respect to the heat flow and with respect to the 'neighbourhood' configuration which is now associated with the position of the neighbouring PA nodes which fall into a circle [Janssens, 2000; Janssens, 2003] with radius R_H in 2D or a sphere in 3D. It means that each PA node can in case of the random node arrangement contain different number and position of the neighbours, which give various possibilities of neighbourhood configurations for each node.

6.6 Curvature Calculations

The interface curvature is approximated by the counting cell procedure developed by Sasikumar and Sreenivasan [Sasikumar and Sreenivasan, 1994].

6.6.1 Calculation of Curvature in the CA Method

The expression for curvature K is given by the formula [Krane *et al.*, 2009]

$$K = \frac{1}{a}\left(1 - \frac{2N_{s\,CA}}{N_{t\,CA}}\right), \tag{6.17}$$

where $N_{s\,CA}$ and $N_{t\,CA}$ are the number of solid CA cells whose centres fall inside the circle of assumed radius R_c and the total number of CA cells whose centres fall inside the circle, respectively (see Figure 6.5).

6.6.2 Calculation of Curvature in the PA Method

The expression for curvature in PA is derived from the expression of curvature in CA method by assuming the average node distance $\overline{a}$ instead of a.

$$K = \frac{1}{\overline{a}}\left(1 - \frac{2N_{s\,PA}}{N_{t\,PA}}\right), \tag{6.18}$$

where $N_{s\,PA}$, $N_{t\,PA}$ are the number of solid PA nodes inside the circle of assumed radius R_c and the total number of PA nodes inside the circle, respectively (see Figure 6.6).

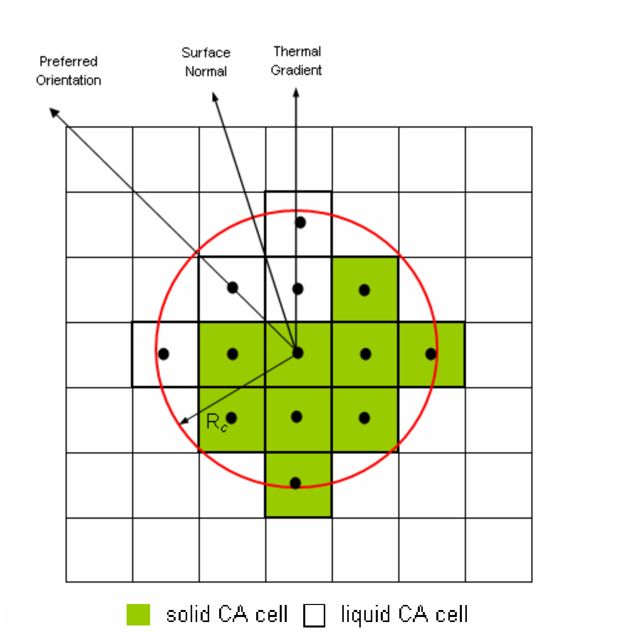

Figure 6.5: Scheme showing a circle sample with $R_c = 2a$ for calculating the curvature in the conventional CA method (example: $N_{s\ CA} = 8$ and $N_{t\ CA} = 12$).

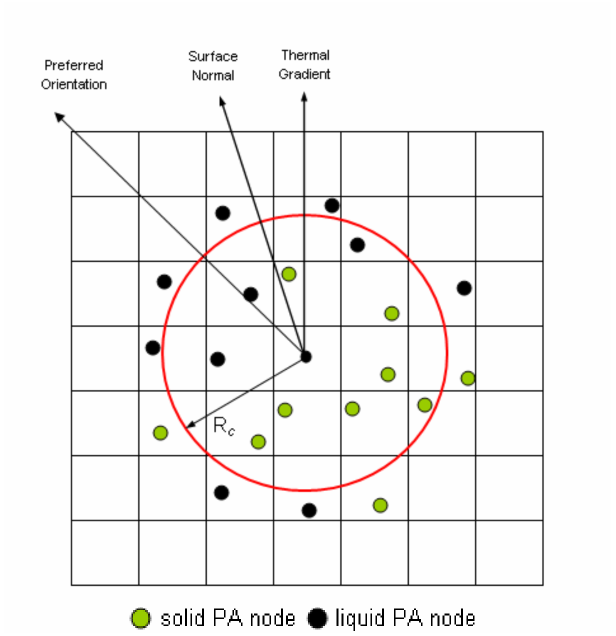

Figure 6.6: Scheme showing a circle sample with $R_c = 2a$ for calculating the curvature in the random PA method (example: $N_{s\ PA} = 7$ and $N_{t\ PA} = 11$).

The curvature of both methods has been calculated and compared on a circular solid fraction arrangement with radius $R = 10$ μm, depicted in Figure 6.7. Two different types of R_c have been chosen ($R_c = 1$ μm and $R_c = 5$ μm). It can be concluded that with the higher radius R_c the value of K becomes almost the same as in the conventional CA approach. This was depicted in Figure 6.8 and Figure 6.9, respectively.

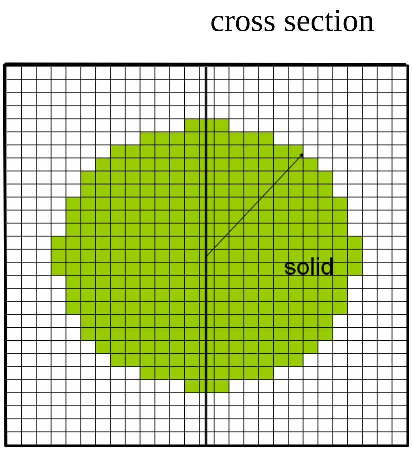

Figure 6.7: Scheme of the area used to compare the curvature calculations by the CA and PA methods. $R = 10$ μm and $a = 1$ μm. Green area represents solid, white area represents liquid.

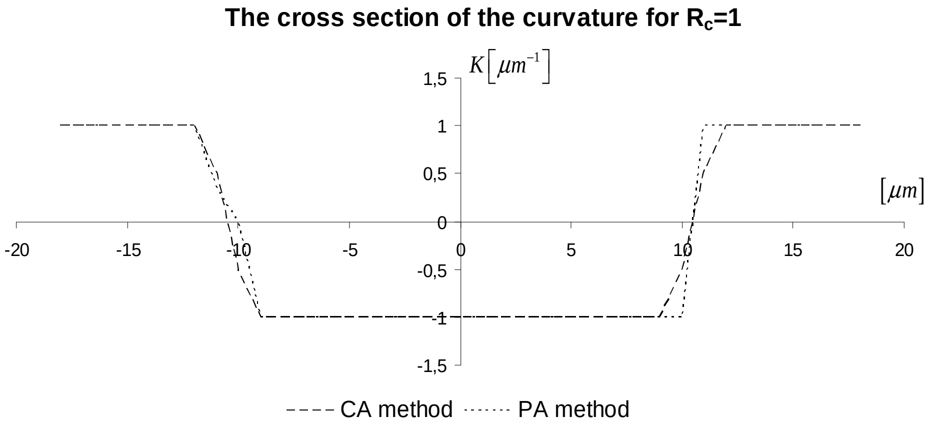

Figure 6.8: Calculated curvature with the CA method and PA-(A) method $(\varepsilon = 0.49)$ for $R_c = 1$ μm and $a = \overline{a} = 1$ μm with respect to the data depicted in Figure 6.7. The node arrangement of CA and PA is given in Table 7.6.

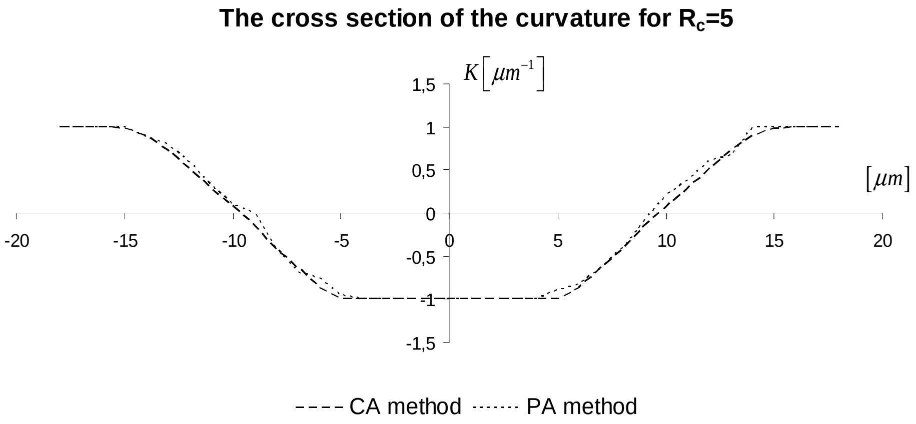

Figure 6.9: Calculated curvature with the CA method and PA-(A) method $(\varepsilon = 0.49)$ for $R_c = 5$ µm and $a = \bar{a} = 1$ µm with respect to the data depicted in Figure 6.7. The node arrangement of CA and PA is given in Table 7.6.

6.7 Phase Change

The crystal growth velocity is calculated according to the crystal orientation. The envelope of the grain can be expressed by the equation (6.11) which is depicted in Figure 6.10. Once a CA cell (or PA node) becomes solid it starts to grow with respect to the 'neighbourhood' configuration. Each of the CA cell (or the random node) can have two possible states: liquid or solid. The CA cell (or PA node) becomes solid through the growth process. The change of solid fraction of the CA cell or PA node is calculated from the crystal growth velocity.

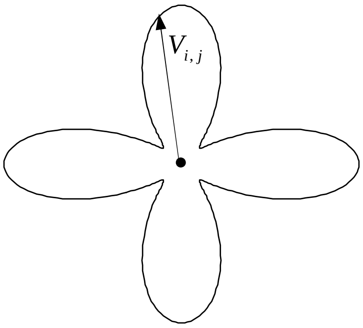

Figure 6.10: Schematic representation of the shape function (parameters see Table 7.3).

For all neighbours of treated solid CA cell (or solid PA node), general criterion d is checked which is represented by the equations (5.22) and (5.25).

For the dendritic growth the Neumann neighbourhood configuration is used. If a neighbour is one of the four nearest east, north, west, south neighbours then in the CA method this distance becomes $a_i = a$ (Figure 5.15). In the PA method $a_i \left(a_i < R_H\right)$ represents the different distances to the neighbouring PA nodes which fall into the circle with radius R_H. When $d \geq a$ or $d \geq a_i$ (Figure 5.14 (left), Figure 5.15 (left) and Figure 5.17) the growing solid touches the centre of the neighbouring CA cell or PA node and this cell/node transforms its state from liquid $f_{sCA} = 0 \left(f_{sPA} = 0\right)$ to solid $f_{sCA} = 1 \left(f_{sPA} = 1\right)$.

6.8 FDM-PA-FDM Transfer of Temperature and Solid Fraction

6.8.1 FDM-CA/PA Transfer of Temperature

The obtained values of temperature on regular FDM grid (equation (6.12)) are in each time step transferred to the CA mesh (random PA grid arrangement) according to scheme in Figure 6.2. The following simple interpolation formula is used in the present calculations

$$T_{PAi,j} = \left(T_{i,j+1}\, l_1 + T_{i+1,j+1}\, l_2 + T_{i+1,j}\, l_3 + T_{i,j}\, l_4\right) / \sum_{j=1}^{4} l_i . \tag{6.19}$$

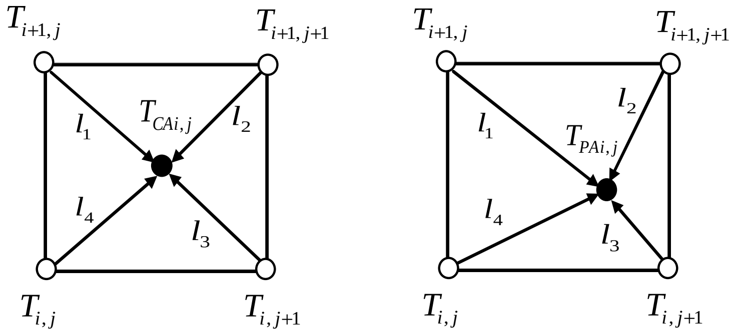

Figure 6.11: Relationship between four FDM nodes and a CA cell (left) and PA node (right) for calculation of the temperature.

In case of FDM-CA the equation (6.19) reduces to

$$T_{CAi,j} = \left(T_{i,j+1} + T_{i+1,j+1} + T_{i+1,j} + T_{i,j}\right)/4, \tag{6.20}$$

where $T_{PA\,i,j}$, $T_{CA\,i,j}$ and l_i represent the temperature of the PA node, the temperature for the center CA cell and the distances to the nearest four FDM nodes, respectively. The calculation is repeated in each time step (see Figure 6.2).

6.8.2 CA/PA-FDM Transfer of Solid Fraction

The temperature field at time $t_0 + \Delta t$ is calculated from the regular FDM mesh. Then these values are recalculated to all CA cells according to the equation (6.20) or PA nodes equation (6.19). Afterwards the PA procedures take place (see Section 6.2). The output information from this level of calculation is the value of solid fraction for all CA cells $f_{s\,CAi,j}$ or random PA nodes $f_{s\,PAi,j}$ which have to be transferred to the FDM nodes to be able to calculate the new values of temperature (Figure 6.12).

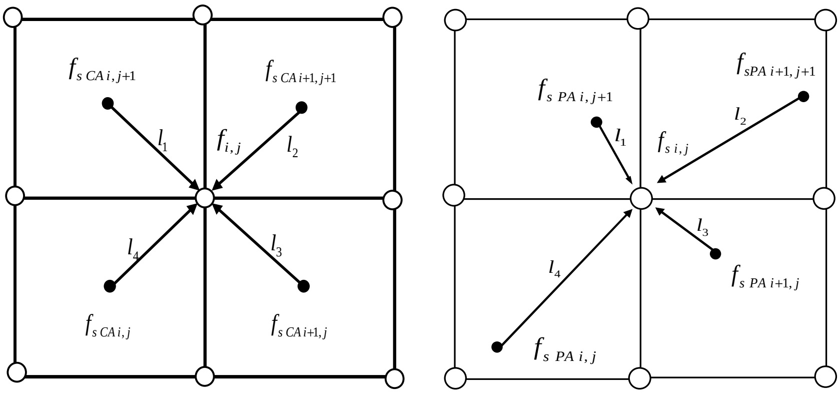

Figure 6.12: Relationship between FDM node and four neighbouring PA nodes or CA cells for transfer of the solid fraction.

The following equation is applied

$$f_{s\,i,j} = (f_{s\,PAi,j+1}\,l_1 + f_{s\,PAi+1,j+1}\,l_2 + f_{s\,PAi+1,j}\,l_3 + f_{s\,PAi,j}\,l_4) / \sum_{i=1}^{4} l_i . \tag{6.21}$$

In case of FDM-CA the equation (6.21) reduces to

$$f_{s\,i,j} = (f_{s\,CAi,j+1} + f_{s\,CAi+1,j+1} + f_{s\,CAi+1,j} + f_{s\,CAi,j})/4, \tag{6.22}$$

where $f_{s\,i,j}$ and $f_{s\,PA}$ represent the solid fraction for the FDM nodes and for the PA nodes, respectively.

7 Numerical Results

In this chapter the numerical results of modelling the grain structures and dendritic growth are obtained by the solution procedures presented in Chapters 5 and 6. The accuracy of presented algorithms is being first tested for the conventional grid structures where the problem is solved by the classical CA technique. These solutions of the governing equations are replaced by the novel PA method where the node arrangement is generated randomly for both models. The definitions of both approaches have been already given in Chapter 3 and 4. Here the numerical results of the two models are presented and discussed.

7.1 Numerical Results of the ECT/CET by the CA Method

The numerical examples are solved by the LRBFCM on the macroscopic level and CA/PA methods on the mesoscopic level. The sensitivity study for the input parameters is prepared on both levels of calculations what is detailed presented in next part of this section.

Initial conditions. Mesoscopic model is combined with the macro heat transfer calculations, which are already described in Sections 5.3 and 5.4.1. Macroscopic model gives the temperature information in 4120 axial positions as the input data to the meso model. On the macro level of calculations the only parameter which influences the mesoscopic model is the value of local undercooling ΔT_{macro} which is interpolated to CA cells or PA nodes. All input data to the ECT/CET model are presented in Figure 7.3. Material properties for heat 46352 from štore Steel company are calculated from the JMatPro software [Saunders *et al.*, 2003], see Table 7.1. Fixed nucleation parameters are presented in Table 7.2.

LRBFCM-CA/PA distretization. Each axial position has a billet dimension 140 mm x 140 mm (or 180 mm x 180 mm) and the size of each macro cell is 0.5 cm. There are 841 macro nodes at each axial position in 140 mm x 140 mm (Figure 7.1-7.2) and 1369 in 180 mm x 180 mm. One macro node includes 625 CA cells.

Time step. Two time-step loops are used in the program: macro loop with time step 0.3 s and meso loop with time step 1.5 µs.

Numerical implementation. Macroscopic simulator takes about 3 minutes to prepare the macro temperature fields, while the microscopic simulation takes approximately 6 hours on a standard PC with 3 GHz and 1024 RAM. The information connected with one CA cell (position in the domain, angle, CA configuration, time of generation) and all cells (amount of nucleuses, generated at the surface and in the bulk areas) are stored in a file for each micro time step. During the simulation the results can be observed on the screen, and afterwards post-processed. The described multiscale model was coupled only in the direction from macro to meso calculations. This means that the meso calculations do not effect the macro calculations.

Table 7.1: Growth model parameters (heat 46352).

Symbol	Unit	Value
Steel grade parameters		
k	1	0.370
Γ	Km	1.9x10^{-7}
D_l	m^2/s	2.0x10^{-8}
c_0	%	0.51
m	1	–30
T_L	K	1755.01

From the measurement data prepared by the Štore Steel company, the 51CrMoV4 heat (Reference case) spring steel was chosen for the basis for analysis of the influence of the input parameters on the meso and macro part of the model. Simulations with different values show that changing some of the parameters can strongly affect the final appearance of the mesostructure.

The following cases have been prepared:

- On the meso level a nucleation parameter (mean nucleation undercooling, standard deviation) and neighbourhood configurations (Nastac's neighbourhood and simplified neighbourhood configuration) sensitivity study is prepared for the heat 46352 (T_{cast} = 1530 K, V_{cast} = 1.75 m/min, dimension 140 mm x 140 mm), see Figures 7.8-7.9 and Figure 7.10.
- The model parameters are adjusted in order to obtain the experimentally determined actual billet ECT and CET positions for the chosen 46352 heat. A systematic procedure is outlined for adjustment of the model data with the Baumann print (Figure 7.11).
- On the macro level the influence of changeable macro parameters are checked. The simulations are prepared for the Reference case with lower

casting temperature T_{cast} = 1500 K and lower casting velocity V_{cast} = 1 m/min, see Figure 7.12.

- Finally, the calculations are prepared for different casting speeds and casting temperatures for heats 48695 3/1 (T_{cast} = 1524 K, V_{cast} = 0.95 m/min, dimension 180 mm), 48695 3/1 (T_{cast} = 1529 K, V_{cast} = 1.15 m/min, dimension 180 mm) and 46693/1 (T_{cast} = 1555 K, V_{cast} = 1.10m/min, dimension 180 mm), see Figures 7.13-7.15.

7.1.1 Mesoscopic Model Input Parameters

The input data to the mesoscopic model (Figure 7.7) have a tremendous influence on the final grain distribution. A sensitivity study has been performed [Lorbiecka and Šarler, 2008], to study this influence and to adjust the model parameters to the experimental values accordingly.

7.1.1.1 Nucleation Parameters Sensitivity Study

It is shown in Figures 7.8 and 7.9 that the parameters of nucleation model most strongly influence the final grain structure results. They determine the number of the possible generated nucleuses in the surface and bulk areas. Increasing the range of $\Delta T_{\max}$ parameter for the bulk the calculated area is widen and the number of new grains drastically arise. Variations of the ΔT_{σ}, brings to the opposite situation what is represented in the examples. It was shown that the best results, with respect to experimental data, are received in the range of value ΔT_{σ} from 1.25 K to 2.25 K for the bulk and around 0.2 K for the surface area. The smaller values of surface nucleation parameters as well as the thickness of surface area bring a smaller number of grains generated at the borders and finally the thinner chill zone. In presented examples 0.5 cm was assumed for the surface area what fits to the observed case.

7.1.1.2 Neighbourhood Configuration Sensitivity Study

To check the influence of the neighbourhood configuration, an analysis of an alternative simplified approach to the Nastac’s neighbourhood configuration was made (Figures 3.3-3.6). Simulations were prepared with the same nucleation parameters as for the Nastac’s neighbourhood configurations and for the simplified one. New approach reduces the time of calculations from four hours to only two. It results in a smaller central zone, because a lower number of grains arise. The simplified neighbourhood is more sensitive to the variations of ΔT_{σ} for the surface area, what results in longer columnar forms, which could not be noticed using the Nastac's configuration (Figure 7.8). From this study one can conclude that the model is also very sensitive to the choice of the neighbourhood configuration. It means that the nucleation parameters need to be adjusted to the experimental data and neighbourhood configuration.

Mesh size and time step sensitivity study. It was deduced also that the mesh size should be 200 μm as it brings the stable results which fit to the experimental observations. The same conclusion was made according to the meso time step, because many variations did not have positive influence on the final structure. The optimal value of 1.5 μs was chosen to combine well with the macro heat transfer calculations and to receive the more precise grain morphology.

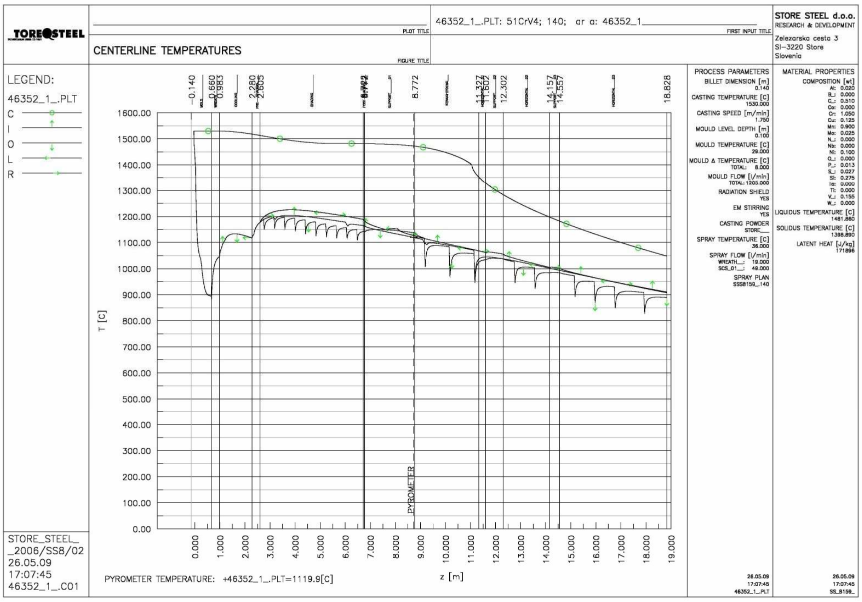

Figure 7.1: Centerline temperatures along the casting direction (reference case).

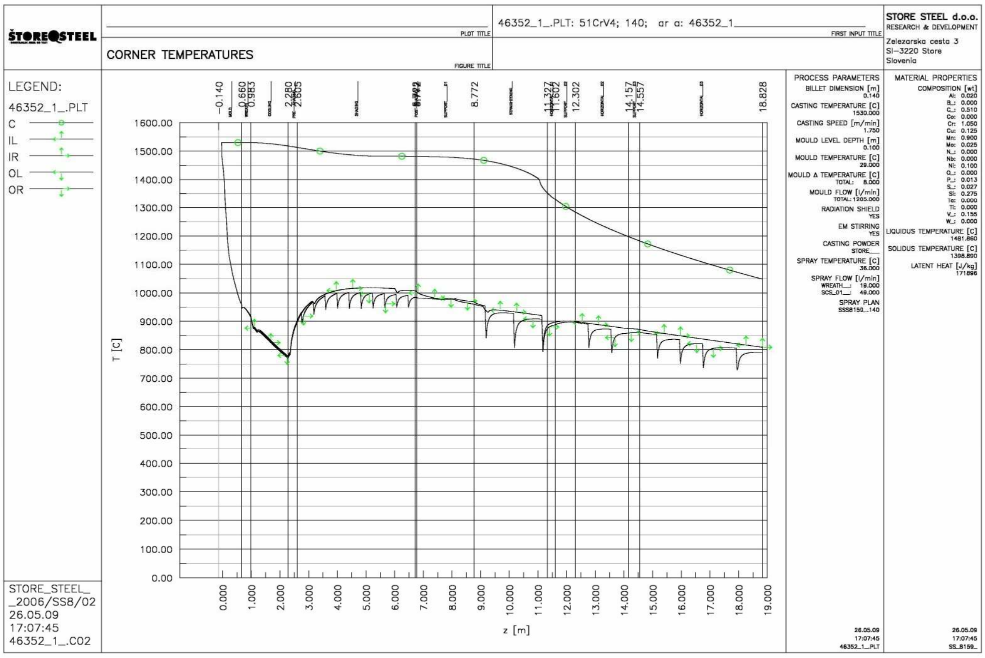

Figure 7.2: Corner temperatures along the casting direction (reference case).

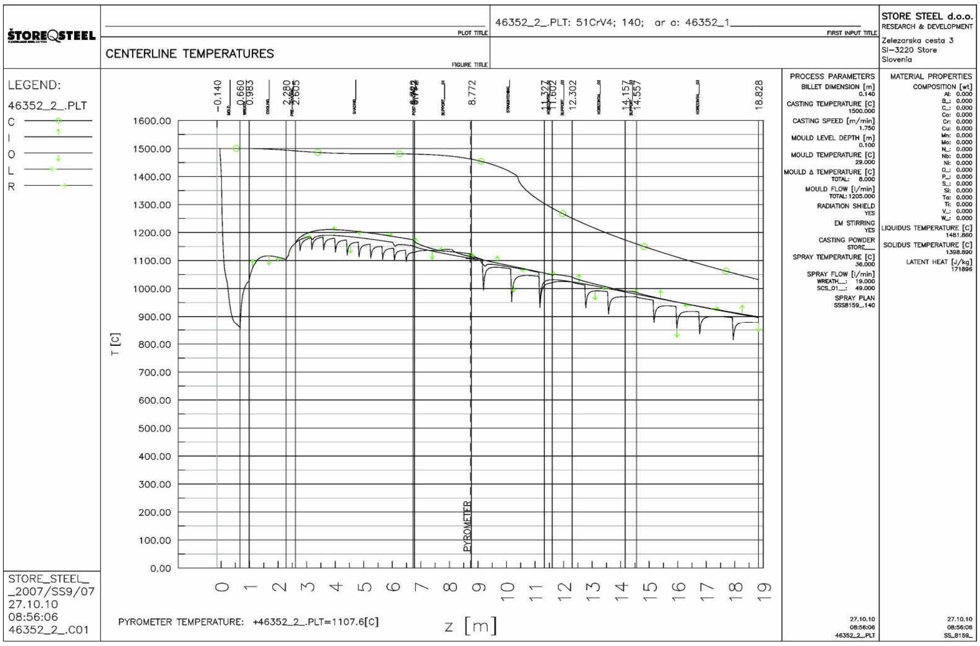

Figure 7.3: Centerline temperatures along the casting direction (reduced casting temperature)

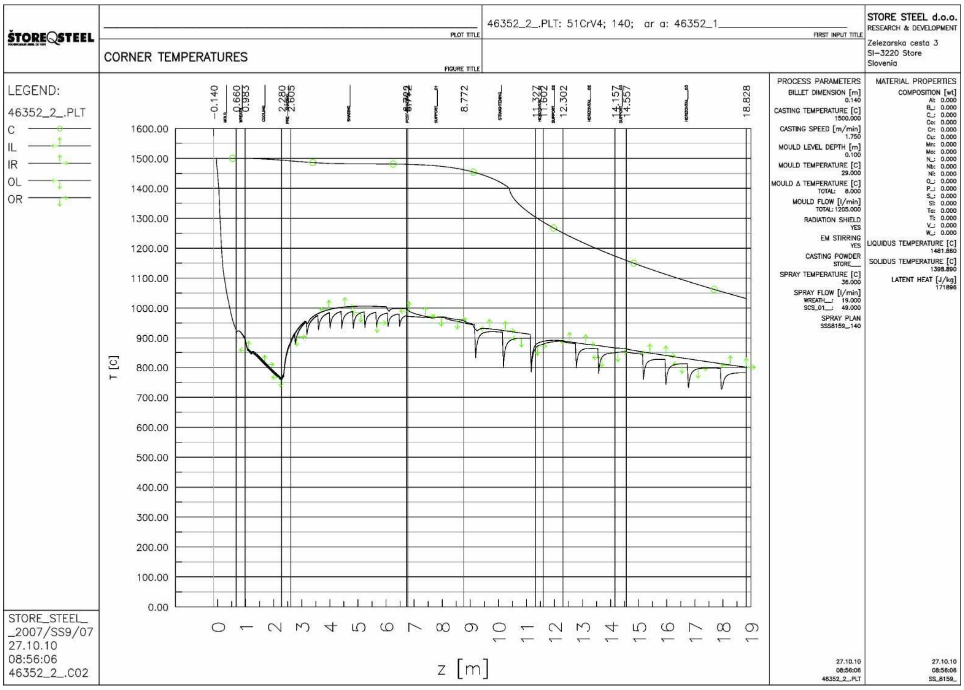

Figure 7.4: Corner temperatures along the casting direction (reduced casting temperature).

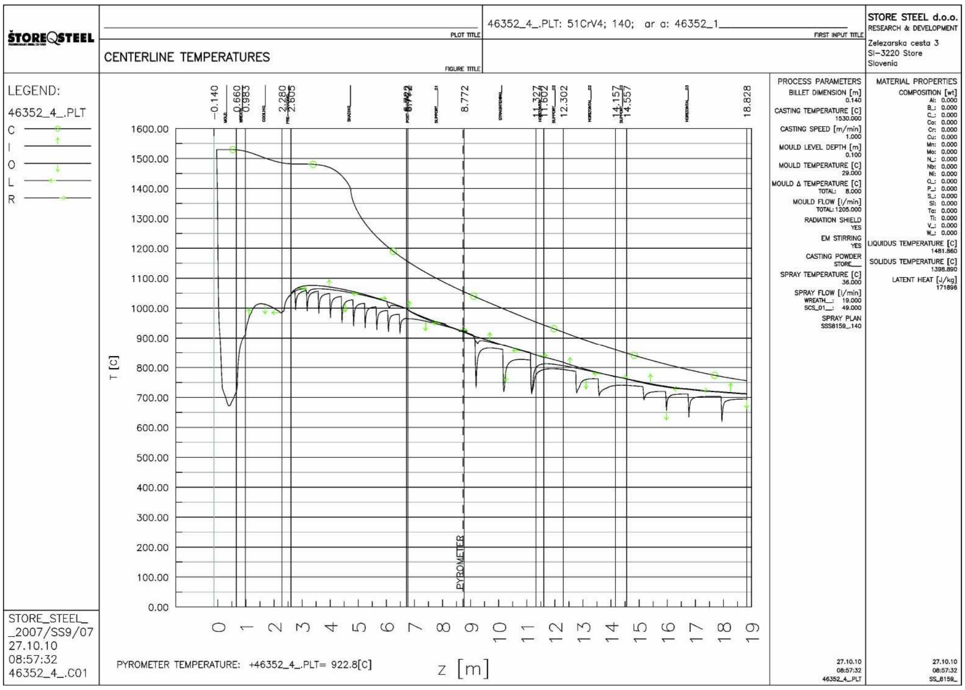

Figure 7.5: Centerline temperatures along the casting direction (reduced casting speed).

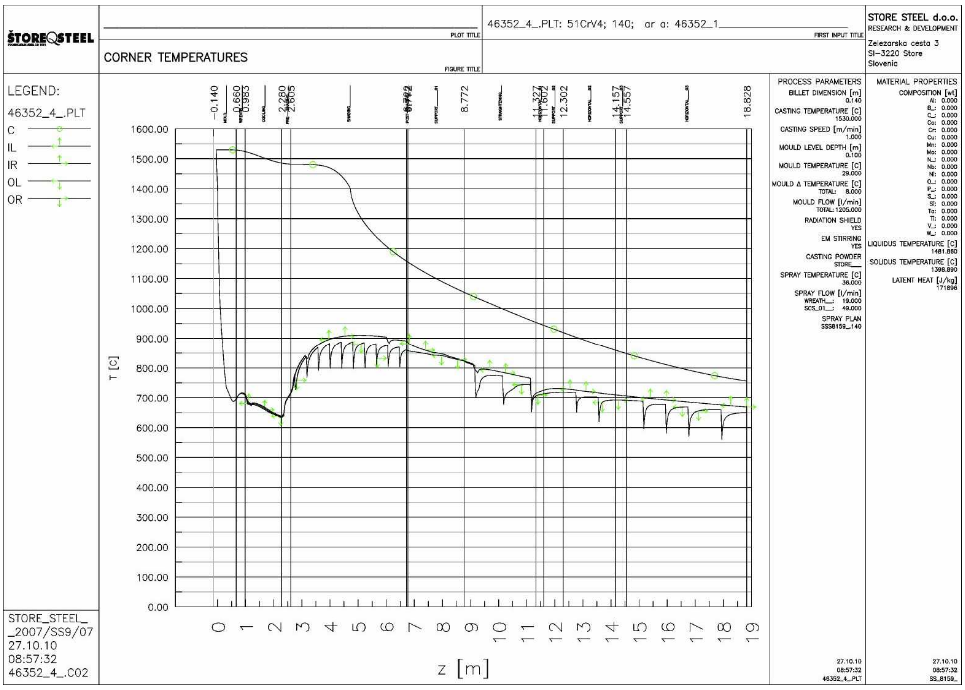

Figure 7.6: Corner temperatures along the casting direction (reduced casting speed).

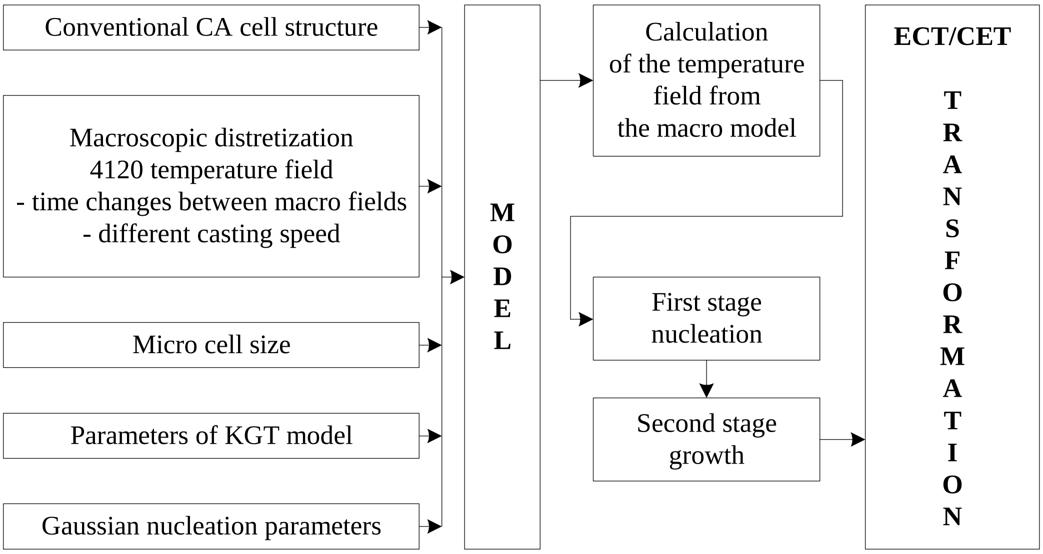

Figure 7.7: Input data to the ECT/CET model.

Table 7.2: Variable parameters of Gaussian distribution for the Nastac's configuration and simplified configuration of the meso model (Figures 7.8 and 7.9).

SYMBOL	UNIT	CASE I	CASE II	CASE III	CASE IV	CASE V	CASE VI
Varied parameters							
For the bulk area							
$\Delta T_{\max}$	K	30	30	30	7.00	15	30
ΔT_{σ}	K	1.25	1.75	2.25	1.75	1.75	1.75
Fixed parameters							
For the surface area							
$\Delta T_{\max}$	K	0.60	0.60	0.60	0.60	0.60	0.60
ΔT_{σ}	K	0.20	0.20	0.20	0.20	0.20	0.20
meso cell size	μm	200	200	200	200	200	200
meso time step	μs	1.50	1.50	1.50	1.50	1.50	1.50

7.1.2 Macroscopic Model Input Parameters

The sensitivity study of casting parameters was analyzed according to the experimental Baumann prints received from the Štore Steel Company from Slovenia. Experimental tests were analyzed to be able to estimate the dimensions of three zones (chill, columnar and equiaxed) for the different value of casting speed and temperature (see Appendix A1). Several experimental results were chosen for the analysis. They prove that even small changes of casting speed (from 0.95 m/min to 1.15 m/min) strongly influence on the extension of the central zone (Figure 7.13). For the higher speed the columnar forms become shorter and start to break which gives bigger equiaxed zone (Figure 7.12 and 7.15). On the Baumann print, the fragmentation can be easily observed. The same situations can be noticed for the strong changes of casting temperature (from 1500 K to 1550 K). The simulated results fit to the experimental samples and indicate exactly the same trend (Figure 7.12). Several examples for different billet dimensions and casting parameters are presented in Appendix 1. Measured Baumann prints are compared with the simulated results.

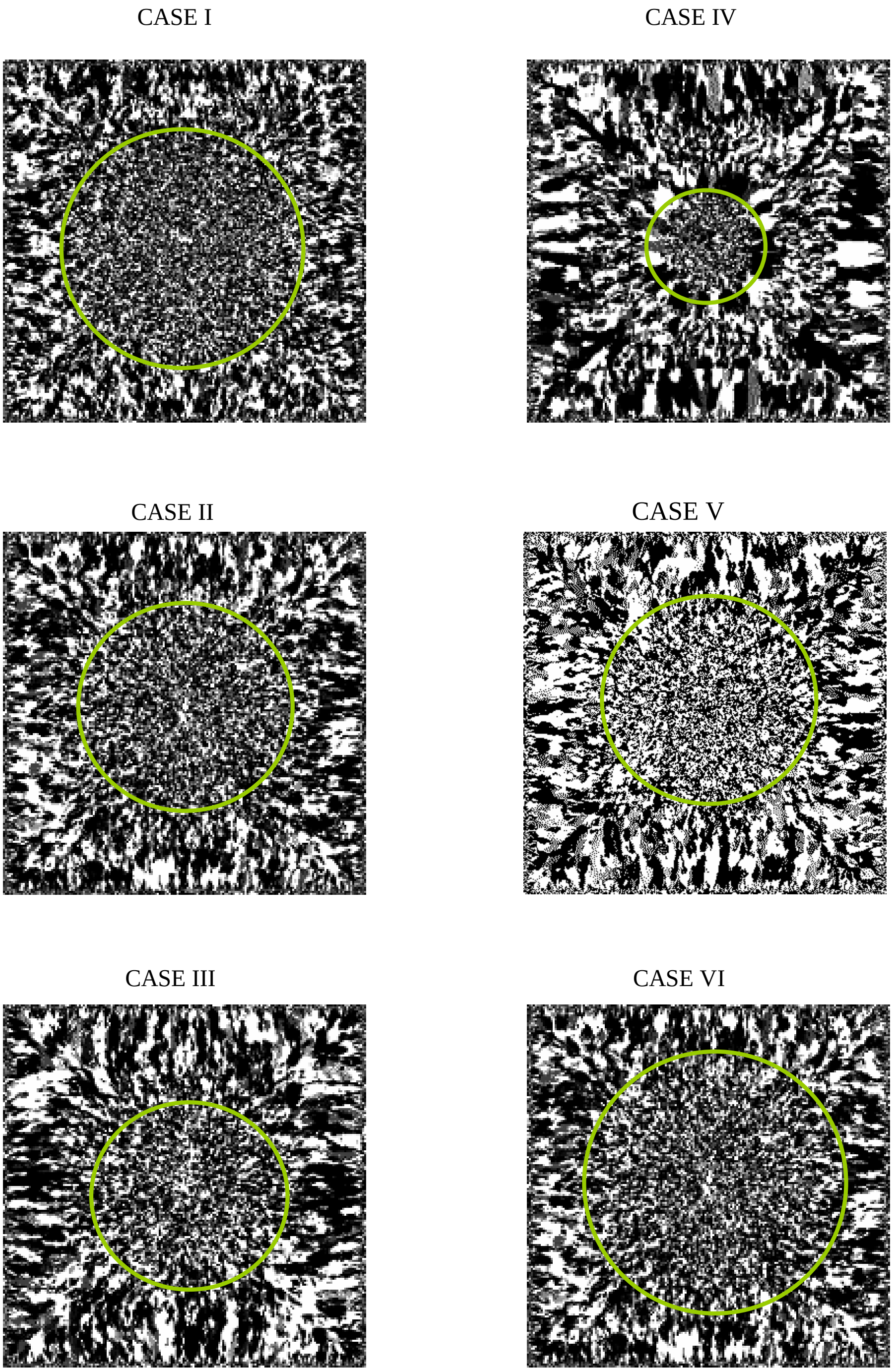

CASE I

CASE IV

CASE II

CASE V

CASE III

CASE VI

Figure 7.8: Calculated billet microstructures as a function of the changeable micro parameters (see Table 7.1 and 7.2) for the Nastac's neighbourhood configuration (see Figures 3.3-3.6), heat 46352 with dimension 140 mm x 140 mm.

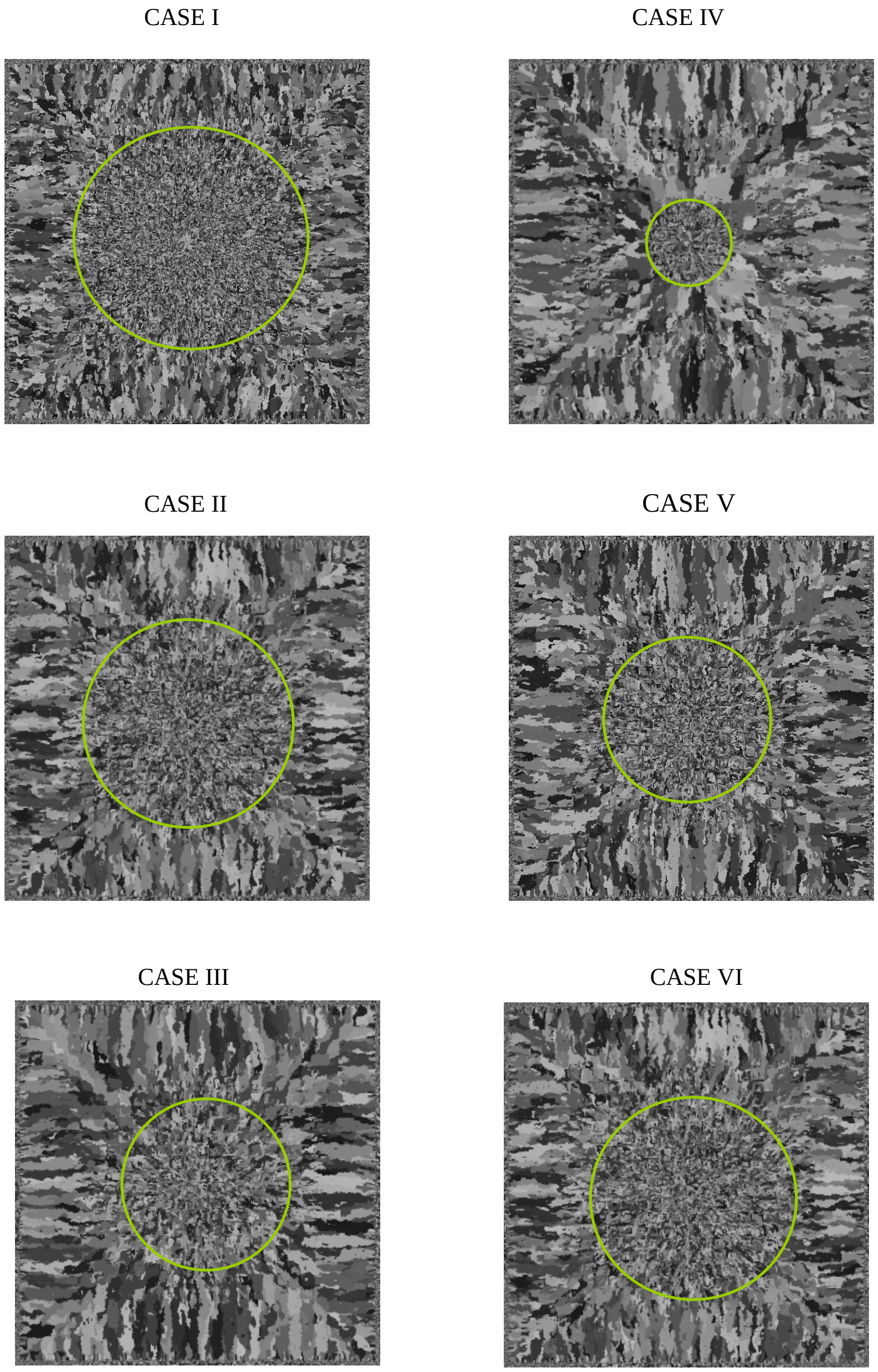

Figure 7.9: Calculated billet microstructures as a function of the changeable micro parameters for the simplified neighbourhood configuration (see Figure 3.7), heat 46352 with dimension 140 mm x 140 mm.

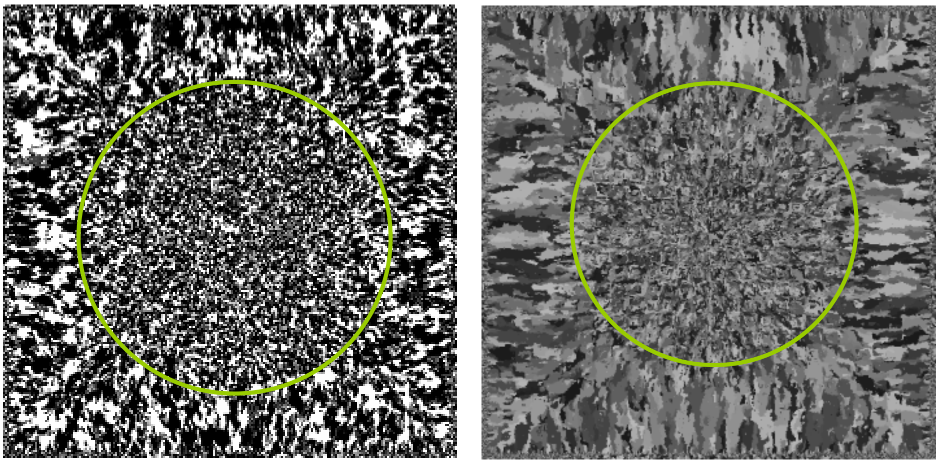

Figure 7.10: Comparison of two different neighbourhood configurations. Left: Nastac's neighbourhood, right: simplified one for the same nucleation and growth parameters (CASE VI).

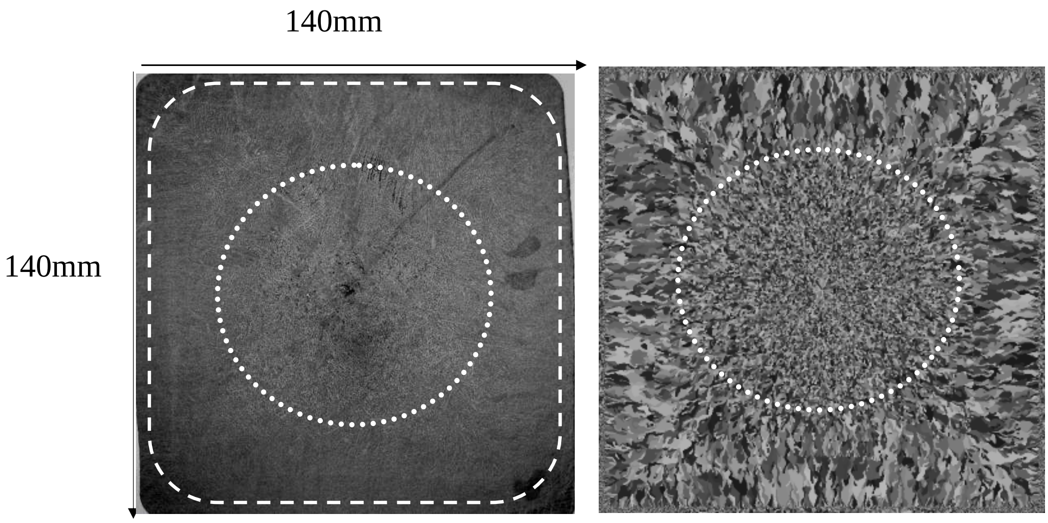

Figure 7.11: Baumann print of the 51CrMoV4 spring steel (see Table A.2), ECT between chill and columnar (dashed line) and CET transition between columnar and central zone (dotted line).

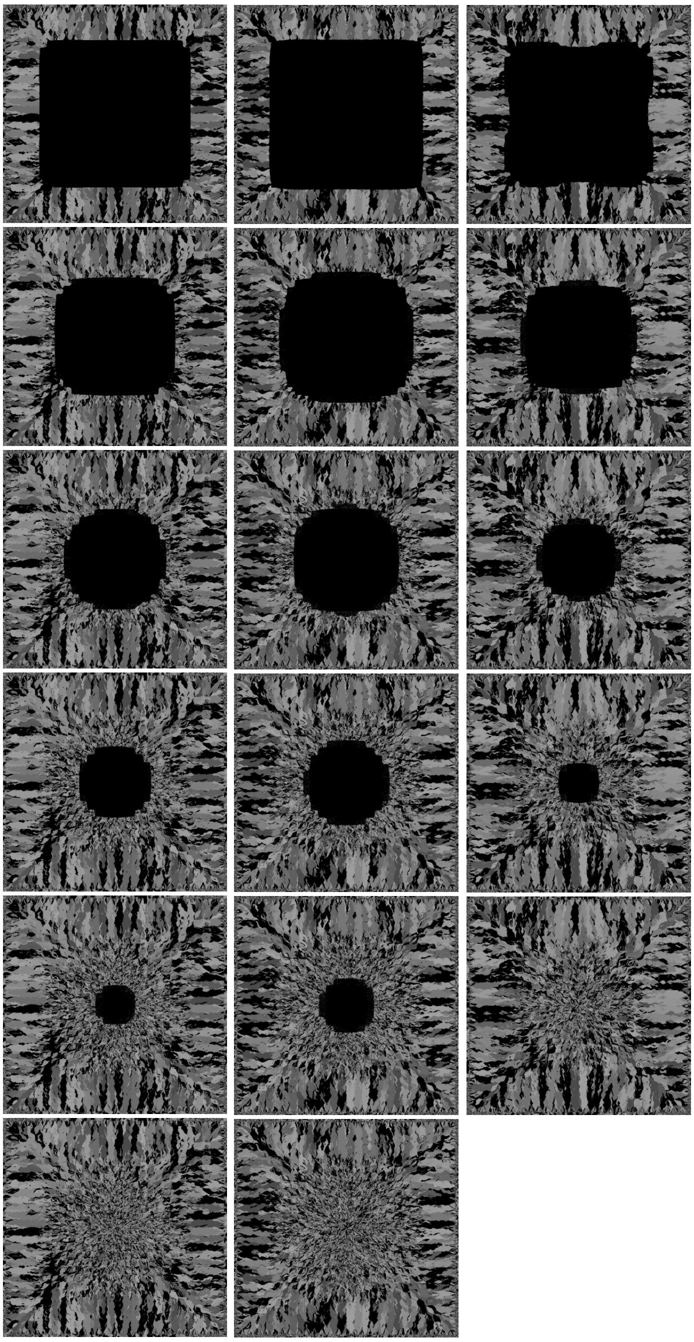

Figure 7.12: Characteristic mesostructure of the heat 46352 after some periods of time for the following casting parameters. Left: T_{cast} = 1500 K, V_{cast} = 1.75 m/min (periods of time: 1 min, 2 min, 3 min, 4 min, 5 min, 5 min 33 s from the top to the bottom), middle: T_{cast} =1530 °C, V_{cast} = 1.75 m/min (periods of time: 1 min, 2 min, 3 min, 4 min, 5 min, 5 min 55 s from the top to the bottom), right: T_{cast} = 1530 °C, V_{cast} = 1.00 m/min (periods of time: 1 min, 2 min, 3 min, 4 min, 4 min 36 s from the top to the bottom).

7.1.2.1 Simulated Results for Variable Casting Parameters

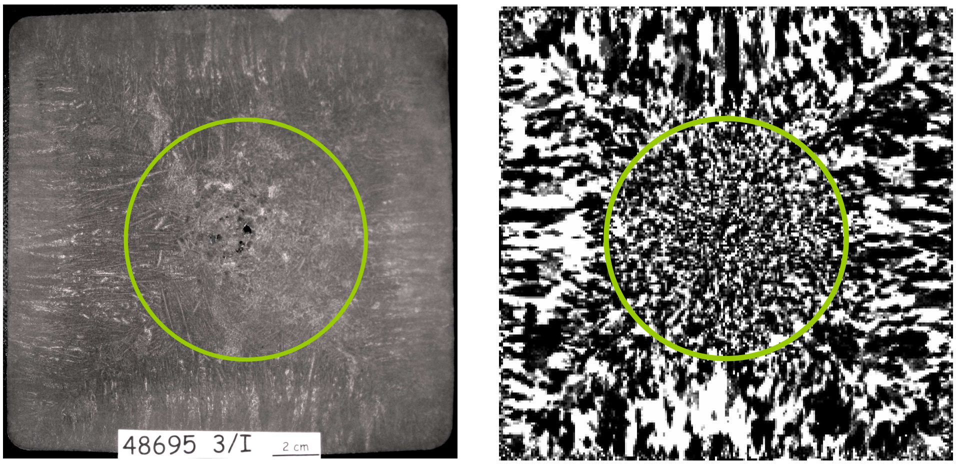

chill zone 2%,
columnar zone 50 %,
equiaxed zone 48 %

chill zone 2%,
columnar zone 44 %,
equiaxed zone 56 %

Figure 7.13: Left: Baumann print of the 51CrMoV4 spring steel (see Table A.2), T_{cast} = 1525 K, V_{cast} = 0.95 m/min, dimension 180 mm, right: simulated result.

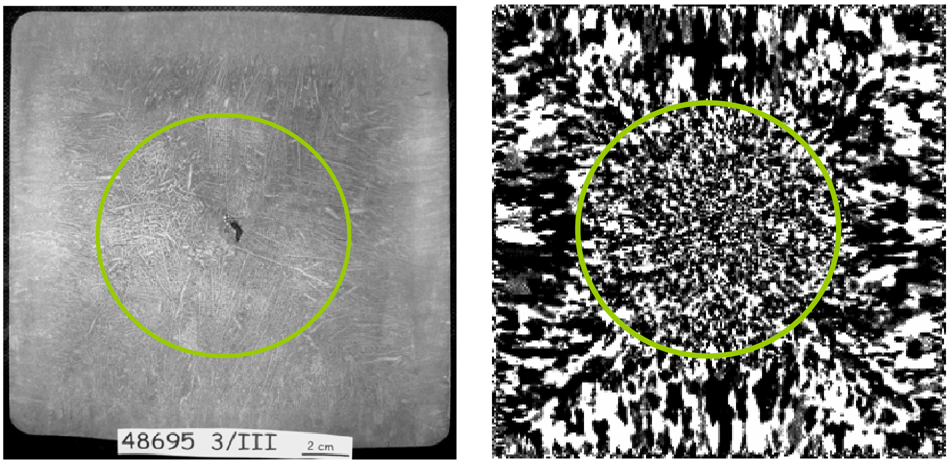

chill zone 2%,
columnar zone 63 %,
equiaxed zone 37%

chill zone 2%
columnar zone 62 %,
equiaxed zone 37%

Figure 7.14: Left: Baumann print of the 51CrMoV4 spring steel (see Table A.2), T_{cast} = 1529 K, V_{cast} = 1.15 m/min, dimension 180 mm, right: simulated example.

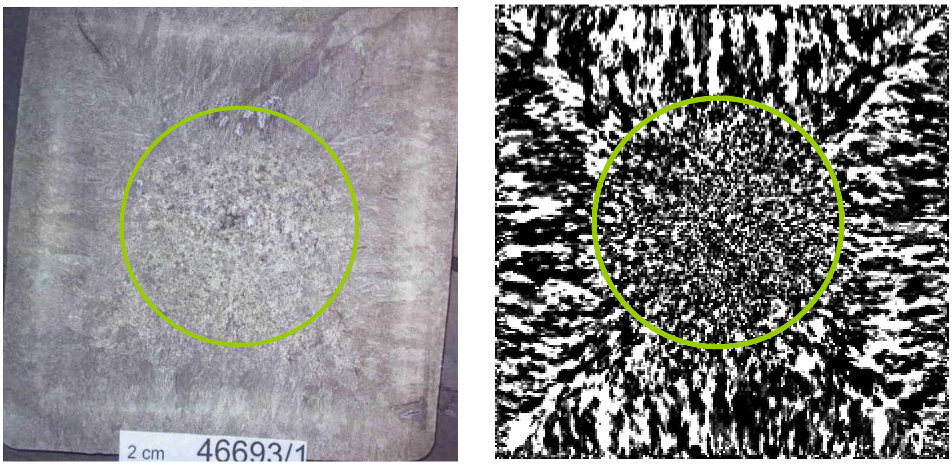

chill zone 2%,
columnar zone 47 %,
equiaxed zone 51 %

chill zone 2%,
columnar zone 47 %,
equiaxed zone 51 %

Figure 7.15: Left: Baumann print of the 51CrMoV4 spring steel (see Table A.2), T_{cast} = 1550 K, V_{cast} = 1.10 m/min, dimension 180 mm, right: simulated example.

7.2 Numerical Results of the ECT/CET by the PA Method

In this chapter the results obtained with the PA method are presented. This apporach was implemented for modelling the position of ECT/CET. The mesostructure equations are solved according to the procedures described in Chapter 4. As for the CA method the same heat 46352 (Figure 7.11 left) was chosen to analyze the influence of the changeable input data for the meso and macro parameters. Simulations of PA demonstrated in Figures 7.16-7.21, are prepared for exactly the same physical input parameters as for the conventional CA method (see Table 7.1). They are finally compared with the CA result.
The following cases have been simulated:

- On the meso level the calculations with different node arrangements and curvature calculation radius R_c are presented for the heat 46352 (T_{cast} = 1530 K, V_{cast} = 1.75 m/min, dimension 140 mm), see Figures 7.16 -7.21.
- The model parameters are adjusted in order to obtain the experimentally determined actual billet ECT and CET positions for chosen 46352 heat.

A systematic procedure is outlined for adjustment of the model data with the Baumann print (Figure 7.16).

- Finally the CA and PA results are compared, see Figure 7.21.

7.2.1 A Sensitivity Study of Meso Input Parameters

The regular CA cell size is 200 µm. The irregular grid includes 490.000 CA cells. Random grid is generated from the regular CA cell size 600 µm by randomly taking away certain percentage (90 % or 70 %) of the regularly positioned points. According to that the number of 490000 micro CA cells is reduced to 54756 points on the computational domain.

The neighbourhood configuration of the PA method has been chosen to contain points within circle with radius R_H ($1.2 \text{x} 10^{-3}$ m or $3.0 \text{x} 10^{-3}$ m) centred around the reference point. Several cases for different radius and node arrangements are shown are depicted in Figures 7.17-7.20. It is noticed that the reduction of the number of micro cells which take part in the calculations, the central (equiaxed) zone becomes larger, while the columnar zone is seen only slightly. This can be modified by changing the radius of the neighbourhood. Larger the value of R_H is chosen the wider columnar forms can be observed (Figure 7.18).

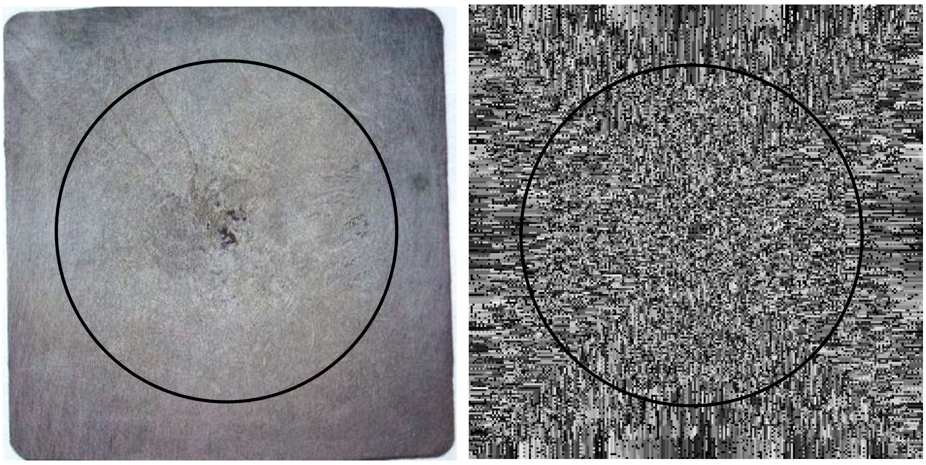

Figure 7.16: Left: Baumann print, right: simulated result with the PA method. Black circle represents approximate position of CET (51CrMoV4).

The maximum radius should be kept around $R_H = 3.6 \text{x} 10^{-3}$ m, otherwise the columnar structures become distorted (waved). The calculation time grows with smaller radius. Process always starts with nucleation first, followed by a growth stage. Each new grain can start to grow only if the two conditions (temperature and probability) are satisfied. Neighbourhoods with a larger number of points have higher probability that at least one of the points will nucleate as well as a higher probability that in the growth process not only one of the neighbouring points will be converted to solid.

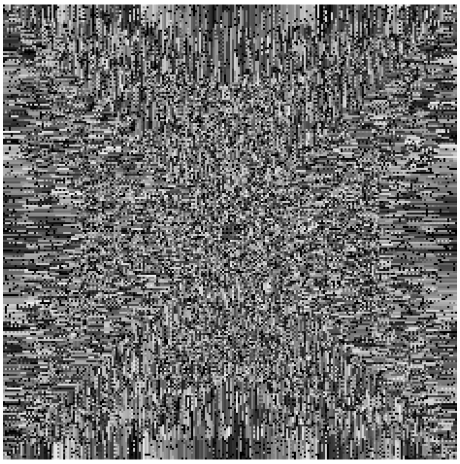

Figure 7.17: Simulated grain structure ECT and CET of the billet by PA method, $R_H = 1.2\text{x}10^{-3}$ m, node density 90 % of CA grid.

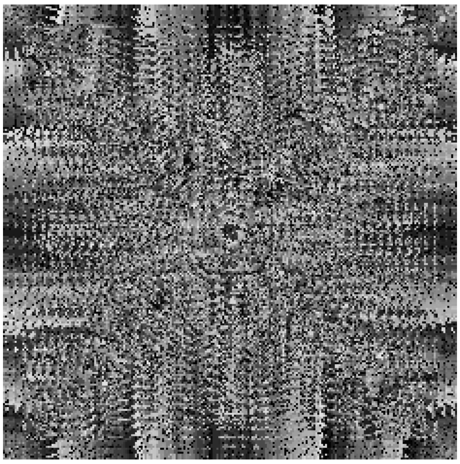

Figure 7.18: Simulated grain structure ECT and CET of the billet by PA method, $R_H = 3.0\text{x}10^{-3}$ m, node density 90 % of CA grid.

It turns out that by using PA some points might not take part in the process. To avoid this problem, an extra procedure is added, which checks the position of the possible ‘left-out’ nodes which are after identification converted to solid. In our previous work [Lorbiecka and Šarler, 2009], where the conventional CA approach was employed, a sensitivity study of the input parameters was discussed. As a result of this study (Figure 7.11-right), a perfect fit of the CA parameters to the experimentally observed microstructure (Figure 7.11-left) of a billet of dimension 140 mm x 140 mm and steel grade 51CrMoV4 was found. We add the PA results in this study as well (see Figure 7.16-right). The input parameters are for both cases the same as in Figure 7.7. It can be seen that the two different methods give similar results.

In this chapter, a new PA approach has been demonstrated for prediction of the grain structure which occurs during the CC of steel. PA method offers a simple and powerful approach of cellular simulations. It was shown that both methods are able to qualitatively and quantitatively model a diverse range of solidification phenomena in almost the same calculation time.

PA method offers an attractive alternative to classical CA method, because of its flexibility of node density and neighbourhood definition. The density of the nodes can in principle vary across the domain of interest and the neighbourhood can be defined in a flexible way. The new approach has thus theoretical advantages of allowing a more proper and versatile modelling of ECT and CET transformations. Very promising and interesting results according to the various neighbourhood configurations and density of points have been shown. It was also shown that the PA method gives compatible results with the conventional CA method when using the same nucleation and growth physics (Figure 7.21).

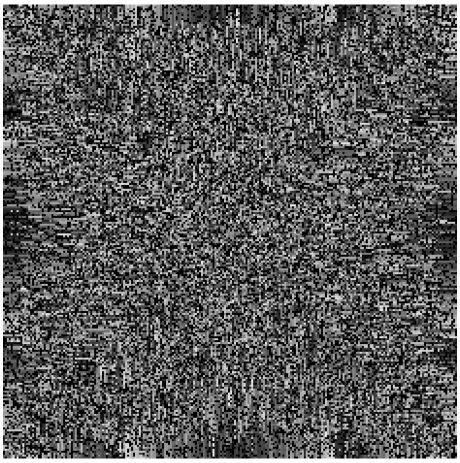

Figure 7.19: Simulated grain structure ECT and CET of the billet by PA method, $R_H = 1.2\text{x}10^{-3}$ m, node density 70 % of the CA grid**.**

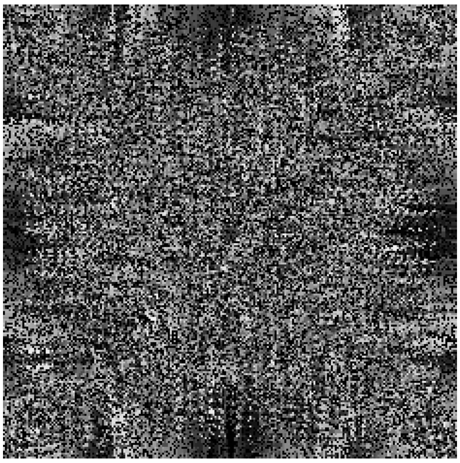

Figure 7.20: Simulated grain structure ECT and CET of the billet by PA method, $R_H = 3.0\text{x}10^{-3}$ m, node density 70 % of CA grid.

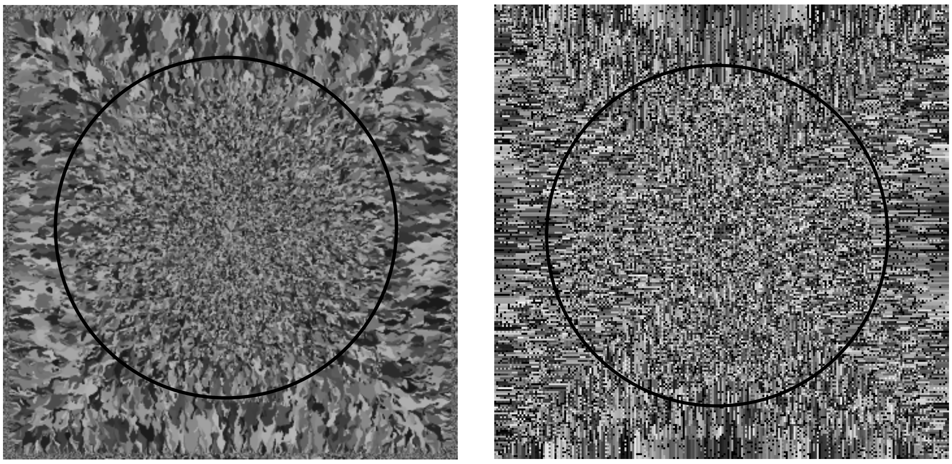

Figure 7.21: Simulated results. Left: conventional CA method, right: PA method. Black circle represents approximate position of CET.

7.3 Numerical Results of the Dendritic Growth

In this chapter the results of the numerical model that was developed for modelling the dendritic growth are presented. The dendritic growth is modelled by the classical CA method and PA method based on algorithms described in Chapter 6. The problem definition and discretization are given in Section 7.3.2.

The numerical results of the CA method are prepared for the following set of input parameters: thermal fluctuations, curvature calculation radius and Gibbs-Thomson coefficient. Finally, the growth process for several dendrites growing simultaneously at orientations 0° and 45° is presented. The results are presented in Section 7.3.2.

In Section 7.3.3 the dendritic growth is simulated by the PA method with the same PA-(A) and different types of random node arrangements PA-(A), PA-(B), PA-(C), PA-(D) that differ in the initial seed for generation of the random numbers that is used in the node arrangement generator (see equations (6.15) and (6.16)). Calculations are prepared for different orientations and with different randomness of the node arrangement $\varepsilon = 0.1$, $\varepsilon = 0.25$ and $\varepsilon = 0.49$.

Next, dendritic growth is simulated by including the randomness growth correction factor responsible for the correction in lengths of the primary branches as compared with the CA method. Finally, we present the growth process simulated by the PA method for seven dendrites growing simultaneously at the same orientations as for the CA model and at random orientations.

7.3.1 Problem Definition and Discretization

The numerical examples are solved by the FDM based temperature calculations and CA or PA based solid fraction calculations.

Initial conditions. Simplified material properties for pure aluminium [Kammer, 1999] are used in all numerical examples. They are summarized in Table 7.3. The process starts from the predetermined solid seed position in one or multiple CA cells (or PA nodes) with the following initial conditions of temperature $933.45\,\mathrm{K} - 1.5\,\mathrm{K}$ and solid fraction $f_s = 1$. All other CA cells or PA nodes are assumed to be liquid $f_s = 0$. All FDM nodes have initial temperature $770.23\,\mathrm{K}$. The initial and boundary conditions $F = 0$ W/m^2 are the same in all simulations.

FDM and CA/PA distretization. The computational domain of the square with $l = 350\,\mu\mathrm{m}$ and uniform discretization $N_{xy} = 701$ is used. FDM and CA methods are always constructed on a regular node arrangement in the present study (Section 7.3.2). In the PA approach the random node arrangement needs to be constructed. The PA approach was first tested with the predetermined node arrangement PA-(A), and then with different types of random node arrangements: PA-(B), PA-(C), PA-(D), respectively (Section 7.3.3).

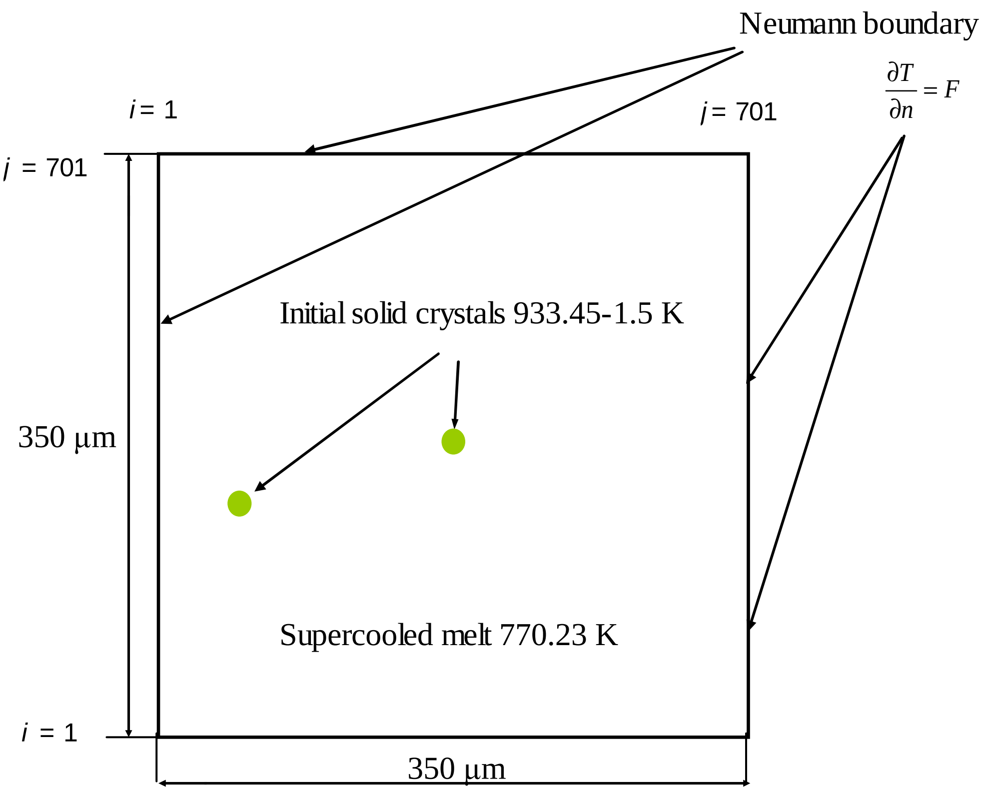

Figure 7.22: Geometry and initial conditions.

Time step. The time step used in FDM calculation of the temperature field is limited by the formula [Zhu and Hong, 2001]

$$\Delta t_{FDM} = \frac{a^2}{4.5\alpha}; \ \alpha = \frac{\lambda}{\rho c_p}, \tag{7.1}$$

where α represents the thermal diffusivity. For the calculations of the solid fraction field by the CA and PA method the following relation is used [Daming *et al.*, 2004] for assuming stability

$$\Delta t_{CA} = \eta \min\left(\frac{a}{V_{max}}, \frac{a^2}{\alpha}\right), \tag{7.2}$$

where η and V_{max} represent the positive constant less then 1 and the maximum growth velocity of all interface cells, respectively.

Numerical implementation. The model was coded in Fortran. The CPU time of the simulations presented in dendritic growth varies form 10 to 15 minutes. The solid CA cell or PA node are graphically presented by coloured pixels which can be observed on the screen during the simulation.

The dendritic morphologies were first calculated by the classical CA method based on the numerical model described in Sections 6.2 and 6.5.

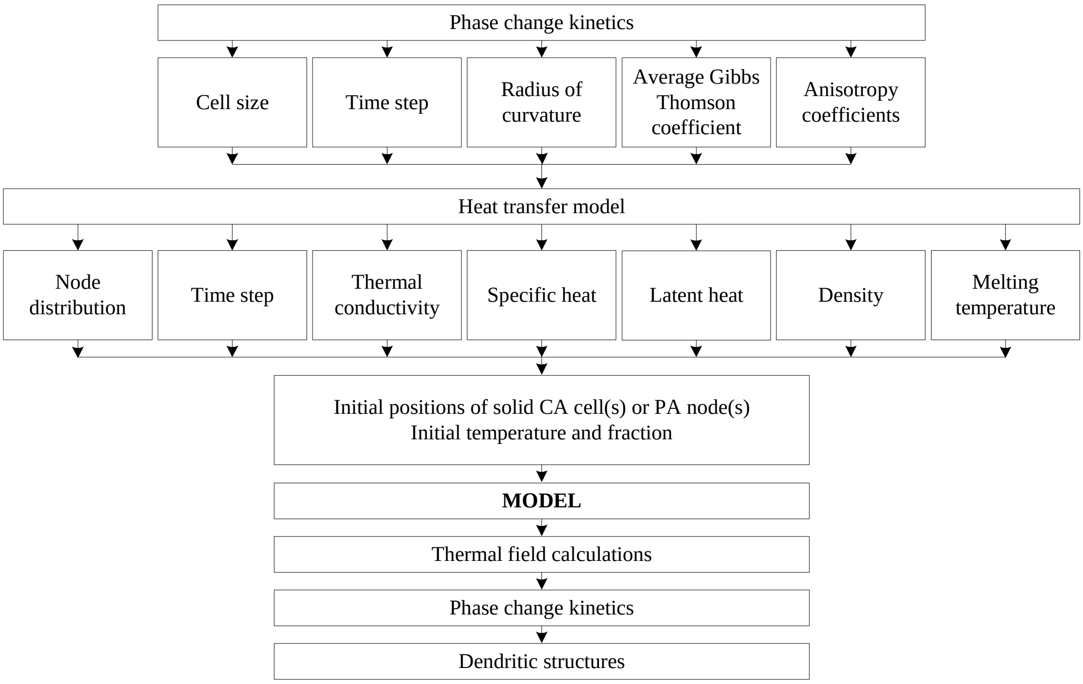

Figure 7.23: Structure of the dendritic growth model.

7.3.2 Simulated Results by the CA Method

In this section many cases corresponding to variation of input parameters are shown. Important input data to the model are analyzed below. We analyse the response of the FDM-CA method with respect to the varied of λ^*, R_c, $\overline{\Gamma}$ and θ_{def} in this section. It can be assumed that these parameters strongly influence the solutions. The respective figures are 7.24-7.28.

- From CASE 1 to CASE 3 the dendritic growth was simulated by the CA method without and with random fluctuations.
- CASE 4 represents the dendritic growth simulated by the CA method at orientation 45°.

- From CASE 5 to CASE 6 the dendritic growth was simulated by the CA method for different values of curvature radius R_c.
- From CASE 7 to CASE 8 the dendritic growth was simulated by the CA method for different values of the average Gibbs-Thomson coefficient.
- Finally, Figure 7.29 represents seven dendrites growing simultaneously at orientations 0° and 45° as the CA grid in constructed. Their exact orientation and position are given in Table 7.5.

Table 7.3: Nominal parameters used in simulations.

Symbol	Value	Unit
ρ	2700	kg/m^3
T_M	933.45	K
T_S	933.45-1.5	K
T_L	933.45+1.5	K
λ	210	W/mK
c_p	955.56	J/kgK
L	259259.26	J/kg
η	0.222	1
$\overline{\Gamma}$	$1.6\text{x}10^{-7}$	Km
δ_t	0.3	1
δ_k	0.75	1
S	4	1
R_c	1.5	μm
R_H	2	μm
μ_k	2	m/sK
Δt_{FDM}	$6.82\text{x}10^{-10}$	s
l	350	μm
n_{xy}	700	PA nodes/ CA cells
N_{xy}	701	FDM nodes

Table 7.4: Parameters varied in the calculations with FDM-CA method**.**

CASE	λ^* [-]	R_c [cell]	$\overline{\Gamma}$ [Km]	θ_{def} [°]	method
CASE 1	0	1	$1.6\text{x}10^{-7}$	0°	CA
CASE 2	0.05	1	$1.6\text{x}10^{-7}$	0°	CA
CASE 3	0.5	1	$1.6\text{x}10^{-7}$	0°	CA
CASE 4	0.05	1	$1.6\text{x}10^{-7}$	45°	CA
CASE 5	0.05	4	$1.6\text{x}10^{-7}$	0°	CA
CASE 6	0.05	12	$1.6\text{x}10^{-7}$	0°	CA
CASE 7	0.05	1	$1.6\text{x}10^{-5}$	0°	CA
CASE 8	0.05	1	$1.6\text{x}10^{-5}$	0°	CA

Table 7.5: Initial positions and orientations of nucleuses for simulation with the FDM-CA method (see Figure 7.29).

nucleus	x, y position [μm]	orientation [deg]
1	120, 290	45
2	150, 550	0
3	300, 100	0
4	350, 350	0
5	410, 550	45
6	500, 150	0
7	570, 380	45

7.3.2.1 Discussion of the Results

Grid size and time step. The grid size of the square domain should be 0.5 μm as it is fine enough to resolve the dendritic tip radius. The same conclusion was made according to the time step. For the stability of the coupled FDM-CA/PA procedure a minimum of Δt_{CA} and Δt_{FDM} was used. For the CA method all depicted results of simulations are shown for 0° and 45° (one example) orientations after 1500 time steps of the length $\Delta t_{FDM} = 6.82\text{x}10^{-10}$ s, i.e after $1.02\text{x}10^{-6}$ s. The example where several dendrities are growing simultaneously at orientations 0° and 45° is presented after 350, 700, 1500 and 2500 time steps, i.e. after $2.39\text{x}10^{-7}$ s, $4.77\text{x}10^{-7}$ s, $1.02\text{x}10^{-6}$ s and $1.71\text{x}10^{-6}$ s, respectively.

Thermal fluctuations. In order to avoid the symmetric shape of the dendrite in the conventional CA approach some fluctuations need to be introduced into the calculations. The following equation is commonly applied $\psi = 1 + \lambda^* rand$.

Thermal noises are usually presented by putting the random fluctuations ψ into the calculations of latent heat, undercooling temperature or velocity [Voller, 2008]. It this work we use them in the velocity calculations $V = V \text{x} \psi$. The effect of increased random fluctuations was studied. Figure 7.24 represents the morphologies of dendrites for different values of λ^*. The number of secondary dendritic branches grow with growing λ^* as seen in Figure 7.24.

Curvature calculation radius. To analyze the influence of the calculation curvature radius the several different values of R_c (Figure 6.3) have been attended. For R_c=3 the results are similar to R_c=4. Smaller values of curvature calculation radius brings more branches. The analyses of curvature calculation radius are presented in Figure 7.27.

Average Gibbs Thomson coefficient. The effect of the variation in the average Gibbs-Thomson coefficient on the evolution of dendritic structure during the growth stage is shown on Figure 7.24. The value of coefficient which is used in the calculations, is the normal value for aluminium ($\overline{\Gamma} = 1.6\text{x}10^{-7}\,\text{Km}$). Insignificant branching takes place for the case of higher $\overline{\Gamma}$(Figure 7.28 (bottom)).

Anisotropy calculations. In the basic approach of CA the grid anisotropy is always a problem in the sense that whatever orientation is assigned first to a dendrite, the final dendritic growth orientation always shifts towards $0°$ or $45°$ as solidification proceeds, due to division of the computational domain into horizontal and vertical mesh structure. In our calculations the orientation of the dendrite is aligned with grid direction by two preferential growth orientations: $\theta_{def} = 0°$ and $\theta_{def} = 45°$ (Figure 7.26). Simulated results show that this model is able to reproduce most of the dendritic features. The classical FDM-CA mode is converted to FDM-PA model in the next section.

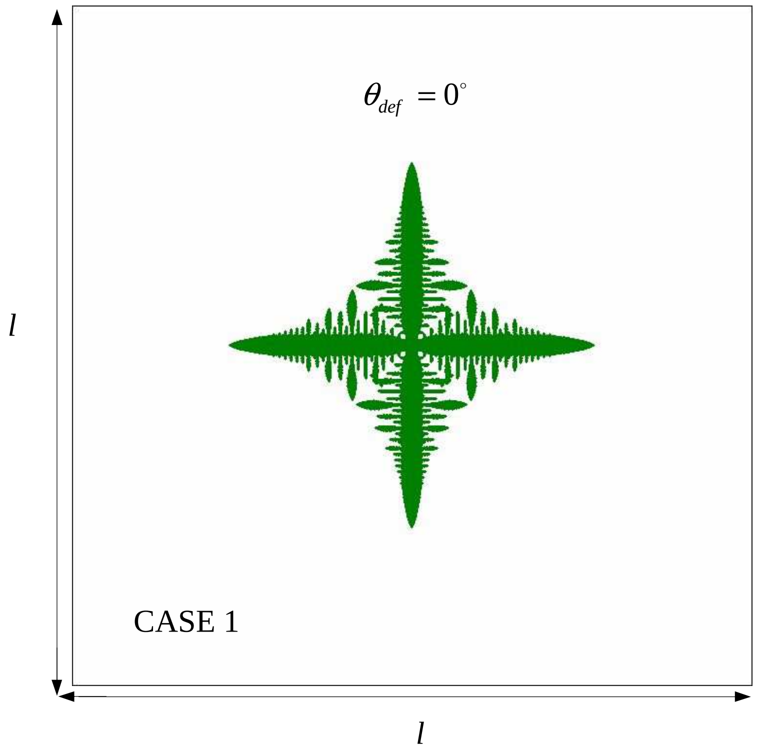
$\theta_{def} = 0^\circ$
CASE 1
l
l

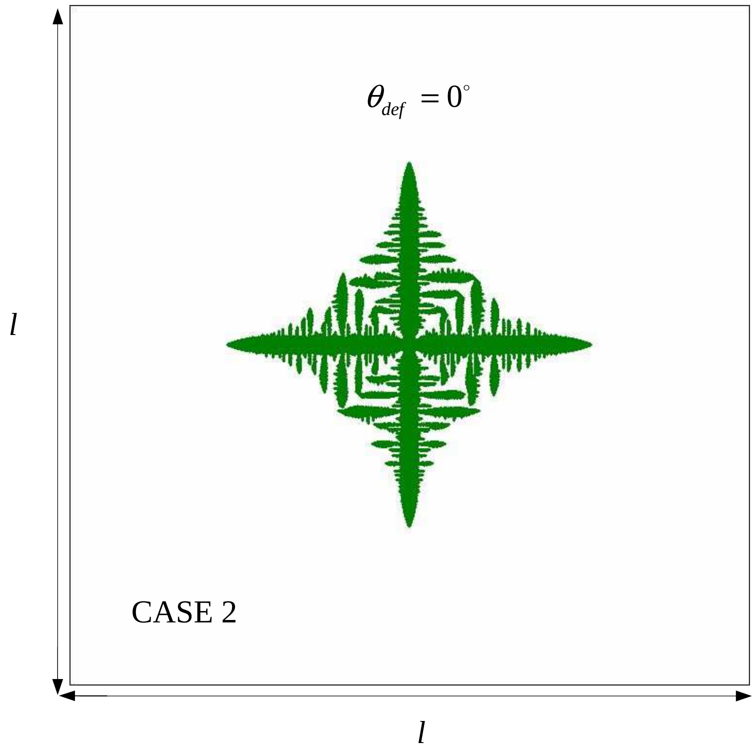
$\theta_{def} = 0^\circ$
CASE 2
l
l

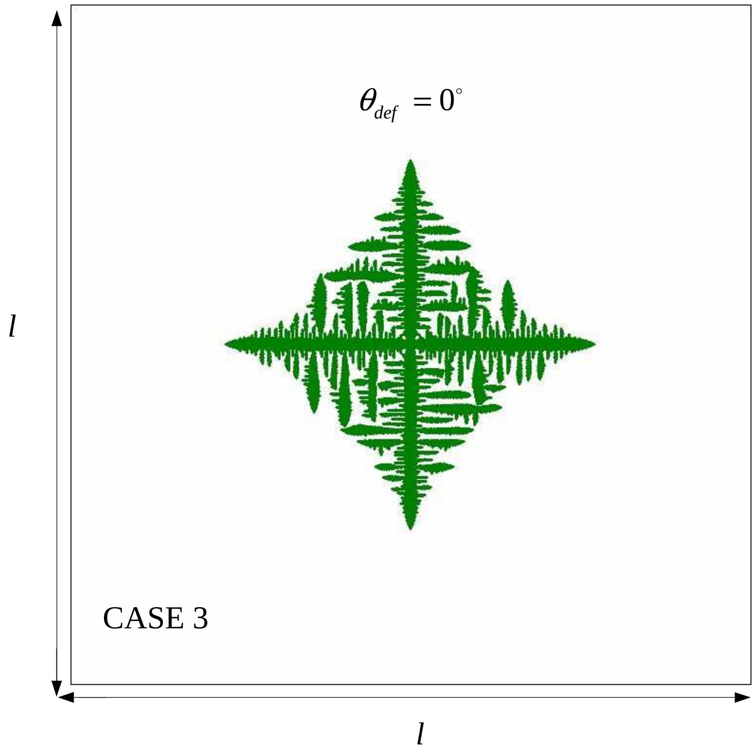

Figure 7.24: Simulated dendritic growth for a single dendrite at orientation $\theta_{def} = 0^\circ$ by the CA method with different fluctuations.

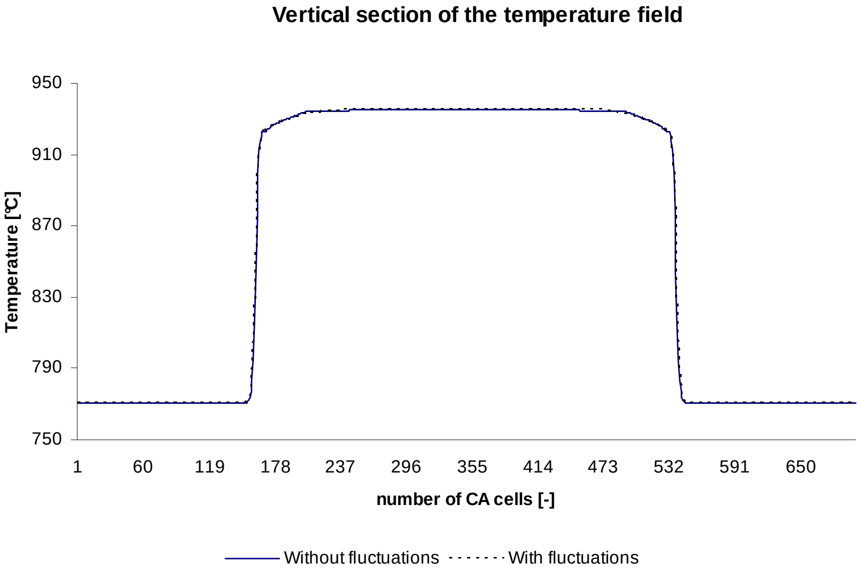

Figure 7.25: Vertical cross section of the temperature field for Case 2 at y =175 μm.

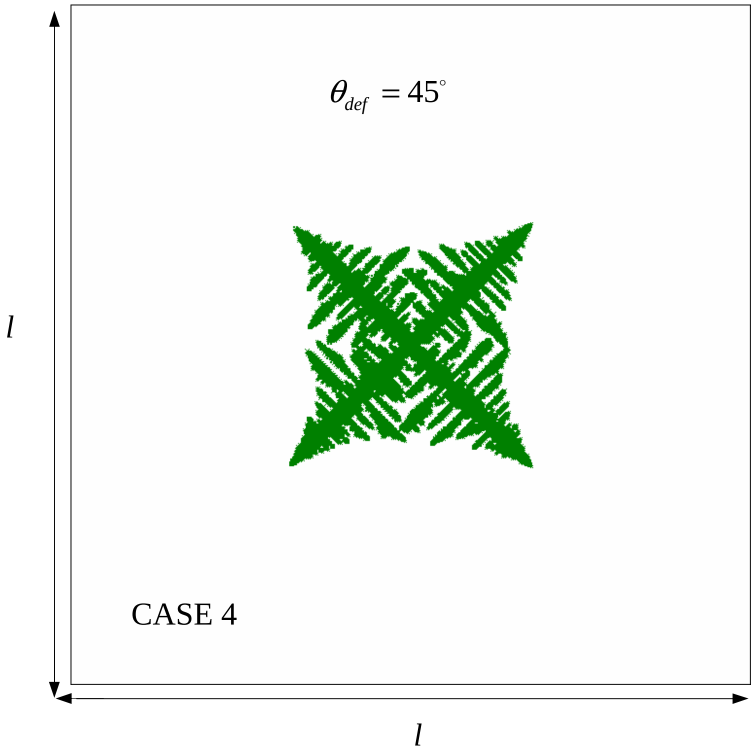

Figure 7.26: Simulated dendritic growth for a single dendrite at orientation $\theta_{def} = 45^\circ$ by the CA method.

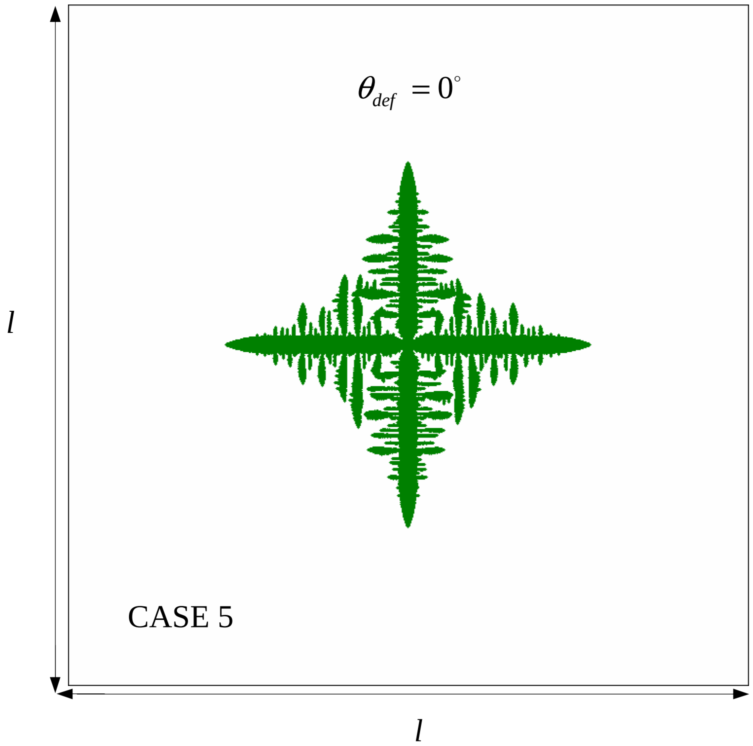

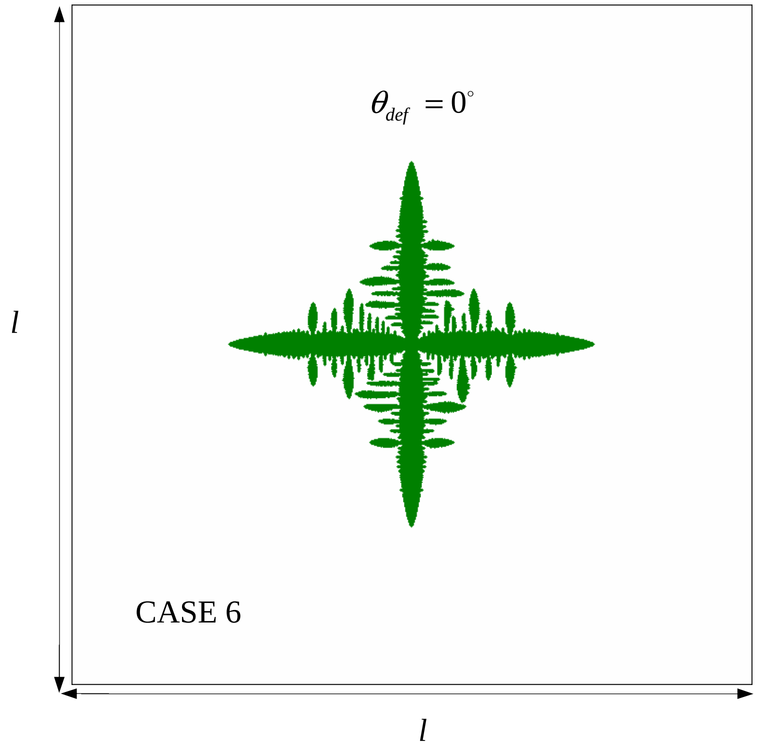

Figure 7.27: Effect of different curvature calculation radius $R_c = 4$ and $R_c = 12$ cell size (from the top to the bottom).

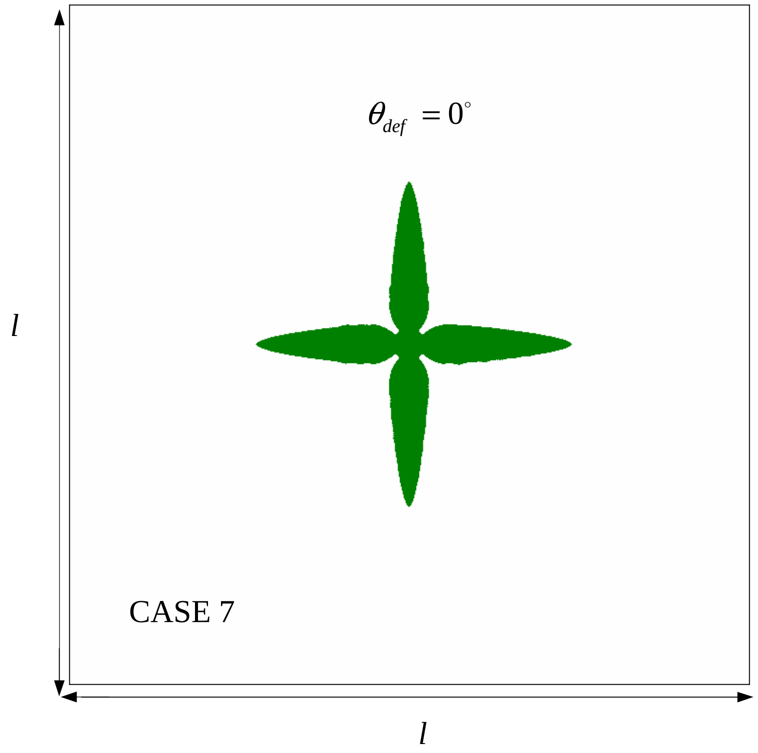

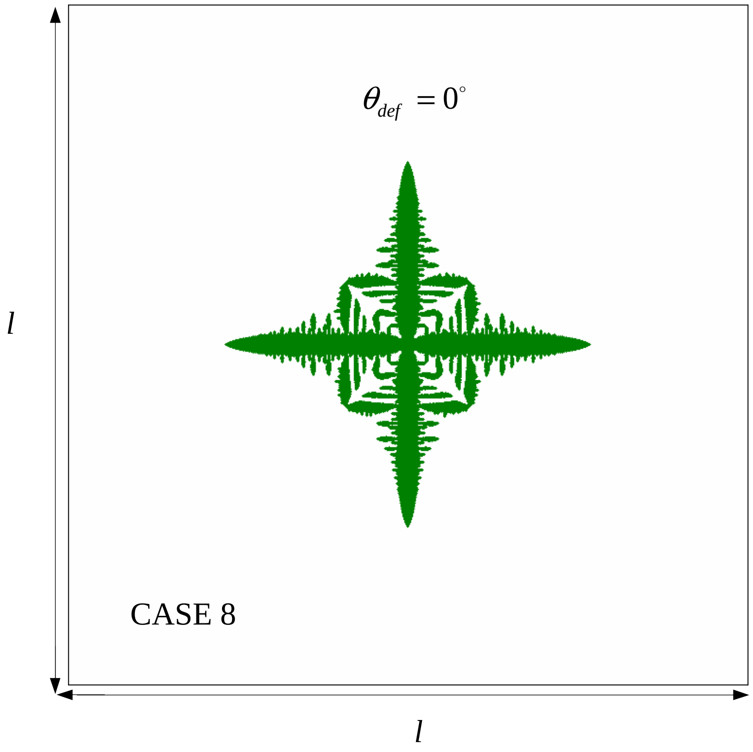

Figure 7.28: Effect of different values of the average Gibbs-Thomson coefficient $\overline{\Gamma} = 1.6\text{x}10^{-5}$ Km and $\overline{\Gamma} = 1.6\text{x}10^{-6}$ Km (from the top to the bottom).

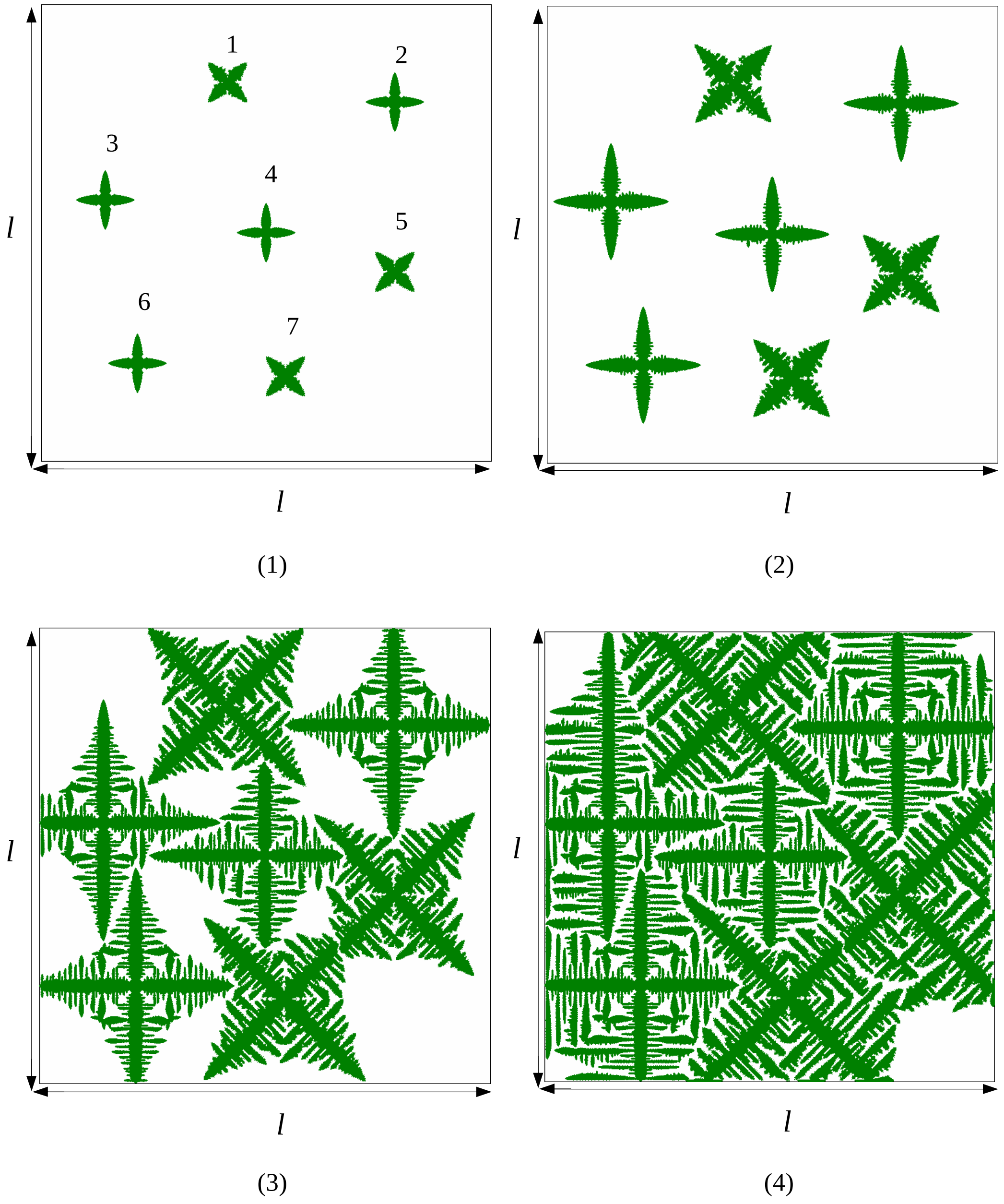

(1)

(2)

(3)

(4)

Figure 7.29: Seven dendrites growing simultaneously at orientations 0° and 45° after (1) 350, (2) 700, (3) 1500 and (4) 2500 time steps of the length $6.82\text{x}10^{-10}$ s. FDM-CA solution procedure, see Table 7.5.

7.3.3 Simulated Results by the PA Method

The dendritic morphologies were in this section calculated by the FDM-PA approach. The simulations have been performed by issues the data presented in Table 7.6.

- From CASE 9 to CASE 18 the dendritic growth process is simulated by the PA method with the same random node arrangement denoted (PA-(A)) for the following ten orientations

$\theta_{def} = 0^\circ, \theta_{def} = 5^\circ, \theta_{def} = 10^\circ, \theta_{def} = 15^\circ, \theta_{def} = 20^\circ, \theta_{def} = 25^\circ, \theta_{def} = 30^\circ,$

$\theta_{def} = 35^\circ, \theta_{def} = 40^\circ, \theta_{def} = 45^\circ.$

- From CASE 19 to CASE 27 the dendritic growth is simulated by the FDM-PA method with different random node arrangements (PA-(B), PA-(C), PA-(D)) for the following orientations

$\theta_{def} = 5^\circ,\ \theta_{def} = 15^\circ,\ \theta_{def} = 30^\circ.$

- From CASE 28 to CASE 33 the dendritic growth process is simulated by the FDM-PA method with different randomness of the node arrangement $\varepsilon = 0.10, \varepsilon = 0.25$ and $\varepsilon = 0.49$, for the following $\theta_{def} = 5^\circ$ and $\theta_{def} = 30^\circ$ orientations.

- From CASE 34 to CASE 36 the dendritic growth is simulated by the FDM-PA method including the randomness growth correction factor responsible for the correction in the lengths of the x and y branches for different random node arrangements (PA-(B)-F, PA-(C)-F, PA-(D)-F).

- CASE 2 where the dendritic growth is simulated by the conventional FDM-CA method with random fluctuations is compared to the CASE 9 and 34 where the dendritic growth process is simulated by the PA method with and without correction randomness growth correction factor.

- Finally, Figures 7.40 and 7.41 represent seven dendrites growing simultaneously at orientations 0°, 45° and orientations 5°, 10°, 12°, 22°, 27°, 31°, 40°. The randomness growth criteria factor has been included.

The results have been arranged and represented in the following way. The FDM-PA calculations with different orientations are depicted in Figure 7.30 based on the same node arrangements. The lengths of the dendritic branches of these calculations are depicted in Figure 7.31. Then Figures 7.33-7.35 show the FDM-PA results with the varied random node arrangement for a single dendrite with $\theta_{def} = 5°$, $\theta_{def} = 15°$ and $\theta_{def} = 30°$, respectively. The length of the dendritic branches of theses calculations are depicted in Figure 7.32. Figure 7.36 and Figure 7.37 represent dendritic growth for a single dendrite with $\theta_{def} = 5°$ and $\theta_{def} = 30°$ for different node arrangement randomness. Finally, the simulations are shown for the conventional CA approach with random fluctuations in Figure 7.39 (top) and for the same input data for the PA method, with and without randomness growth correction factor, Figure 7.39 (middle and bottom) (see discussion in the next paragraph).

Table 7.6: Parameters varied in the calculations with PA method.

CASE	θ_{def} [°]	λ^* [-]	ε [-]	method
CASE 9	0°	0	0.49	PA-(A)
CASE 10	5°	0	0.49	PA-(A)
CASE 11	10°	0	0.49	PA-(A)
CASE 12	15°	0	0.49	PA-(A)
CASE 13	20°	0	0.49	PA-(A)
CASE 14	25°	0	0.49	PA-(A)
CASE 15	30°	0	0.49	PA-(A)
CASE 16	35°	0	0.49	PA-(A)
CASE 17	40°	0	0.49	PA-(A)
CASE 18	45°	0	0.49	PA-(A)
CASE 19	5°	0	0.49	PA-(B)
CASE 20	5°	0	0.49	PA-(C)
CASE 21	5°	0	0.49	PA-(D)
CASE 22	15°	0	0.49	PA-(B)
CASE 23	15°	0	0.49	PA-(C)
CASE 24	15°	0	0.49	PA-(D)
CASE 25	30°	0	0.49	PA-(B)
CASE 26	30°	0	0.49	PA-(C)
CASE 27	30°	0	0.49	PA-(D)
CASE 28	5°	0	0.10	PA-(A)
CASE 29	5°	0	0.25	PA-(A)
CASE 30	5°	0	0.49	PA-(A)
CASE 31	30°	0	0.10	PA-(A)
CASE 32	30°	0	0.25	PA-(A)
CASE 33	30°	0	0.49	PA-(A)
CASE 34	0°	0.05	0.49	CA
CASE 35	0°	0	0.49	PA-(A)
CASE 36	0°	0	0.49	PA-(A)-F

Table 7.7: Initial positions and orientations of nucleuses for simulation with the FDM-PA method (see Figure 7.40).

nucleus	x, y position [μm]	orientation [deg]
1	120, 290	45
2	150, 550	0
3	300, 100	0
4	350, 350	0
5	410, 550	45
6	500, 150	0
7	570, 380	45

Table 7.8: Initial positions and orientations of nucleuses for simulation with the FDM-PA method (see Figure 7.41).

nucleus	x, y position [μm]	orientation [deg]
1	120, 290	12
2	150, 550	27
3	300, 100	22
4	350, 350	5
5	410, 550	31
6	500, 150	40
7	570, 380	10

7.3.3.1 Discussion of the Results

Grid size and time step. Exactly the same assumptions as for the CA method concerning the grid size and the time step were applied. For the PA method all depicted results of simulations are shown for different orientations after 1500 time steps of the length $\Delta t_{FDM} = 6.82\text{x}10^{-10}$ s, so after $1.02\text{x}10^{-6}$ s. The examples with several dendrites growing simultaneously at orientations $0^\circ, 45^\circ$ and with different orientations are presented after 350, 700, 1500 and 2500 time steps, so after $2.39\text{x}10^{-7}$ s, $4.77\text{x}10^{-7}$ s, $1.02\text{x}10^{-6}$ s and $1.71\text{x}10^{-6}$ s, respectively.

Thermal fluctuations. In the PA approach it is not necessary to involve any fluctuations. In the novel method, the calculations are done on the random node arrangement. This substitutes the random fluctuations what can be observed on all of the performed simulations.

Radius of neighbourhood. In the two dimensional square lattice there are many neighbourhood configurations possible. For the random node arrangement the new configuration of the PA method has been chosen which contain points within circle with radius R_H cantered from the reference point. Larger the value of R_H is chosen more dendritic and irregular structures can be seen. Here opposite to the CA approach, where the closest neighbourhood configuration is being analyzed a more extended area of neighbours needs to be taken into the consideration. The radius of neighbourhood should be kept at a minimum of 1.5 μm in case of $a = 0.5\,\mu\text{m}$.

Generation of random node arrangement. The orientations of crystallographic branches of different dendrites have different orientations in general. It is commonly recognized that this process is difficult to simulate by the classical CA method since the dendrite will always switch to 0° or 45° direction during the growth. Our testing is thus primarily focused on the growth of the dendrite at different orientations by the novel PA method. Simulated examples are for the random node arrangements PA-(A),…, PA-(F) presented in Figures 7.33-7.35, respectively. They show that when employing the PA method any of the orientations can easily be achieved. Results show that the proper growth direction is always observed with increasingly random ($\varepsilon \to 0.49$) node arrangement, see equations (6.15) and (6.16).

Randomness growth correction factor. For the same input parameters the dendritic growth process was simulated by the CA method with random fluctuations and by the PA method with and without randomness growth correction factor for the orientation $\theta_{def} = 0^\circ$ (see CASE 2 and CASE 9). The lengths of x and y branches were different in both methods. This is due to the influence of the random node arrangement and subsequent variable distances between the nodes. In the CA method the same value of a is taken while for the PA method this distances are different and might vary between maximum $\Delta x = \Delta y = 2\varepsilon a$ and minimum $\Delta x = \Delta y = 2(1-\varepsilon)a$. It can be concluded that the differences in the length between x and y directions with respect to the random node arrangement are almost constant and kept below $\approx 5\%$. The standard deviation was calculated for the x and y lengths of the dendritic arms and for the ratio between them (see Figures 7.31 and 7.32). The following features can be summarized from Table 7.9. The average length of the dendrite at ten different orientations and some random node arrangement with $\varepsilon = 0.49$ is 152.8 ± 5.18 μm. The average length of the dendrite is calculated with four different random node arrangement for the fixed angles 5°, 15° and 30° is 153.37 ± 5.39 μm, 156.12 ± 6.44 μm and 151.75 ± 5.36 μm, respectively. From this data one can conclude that the errors caused by the rotation of the dendrite are at the same order as the errors cussed by different random node arrangements. Figure 7.36 and Figure 7.37 demonstrate that when reducing ε from 0.49 to 0.1 the PA starts to behave like the CA and the proper simulation of the dendrite is not possible. We are too close to the classical node structure in such case and CA limitations appear. To achieve the same dendrite length in PA method as in the CA method, an empirical factor, which multiplies the calculated velocity in the PA method, was added in the code. It can be shown that putting randomness growth correction factor 1.25, (for the random node arrangement ε = 0.49) in the PA calculations, the primary branches will have the same length in both methods (see Figure 7.38). The factor was included into the calculations of the movements of interface in equations (5.23) and (5.25).

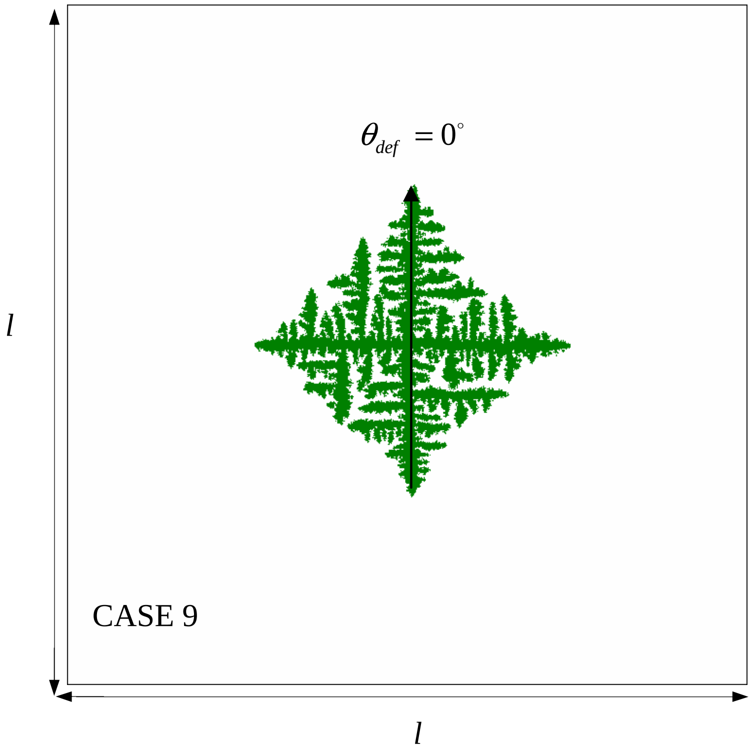
$\theta_{def} = 0^\circ$
CASE 9
l
l

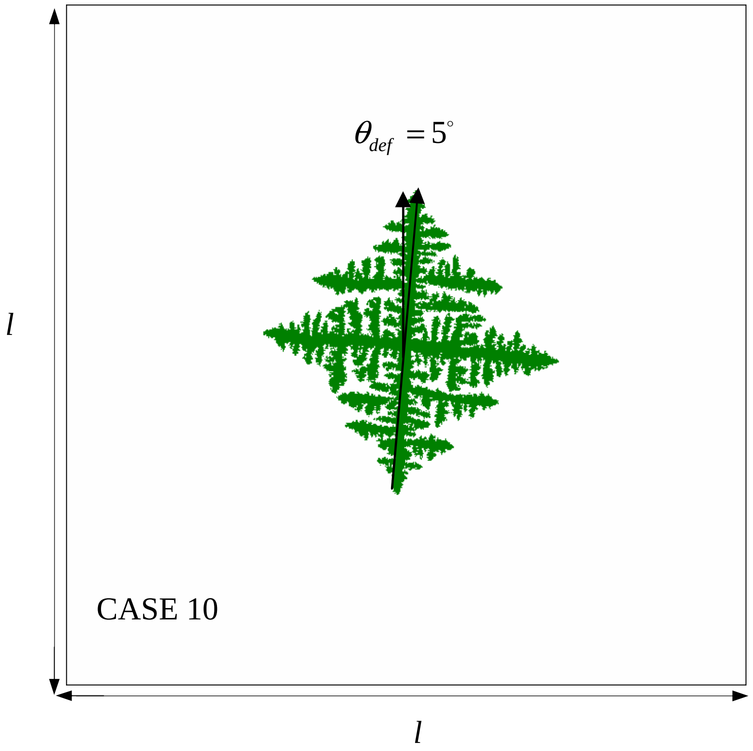
$\theta_{def} = 5^\circ$
CASE 10
l
l

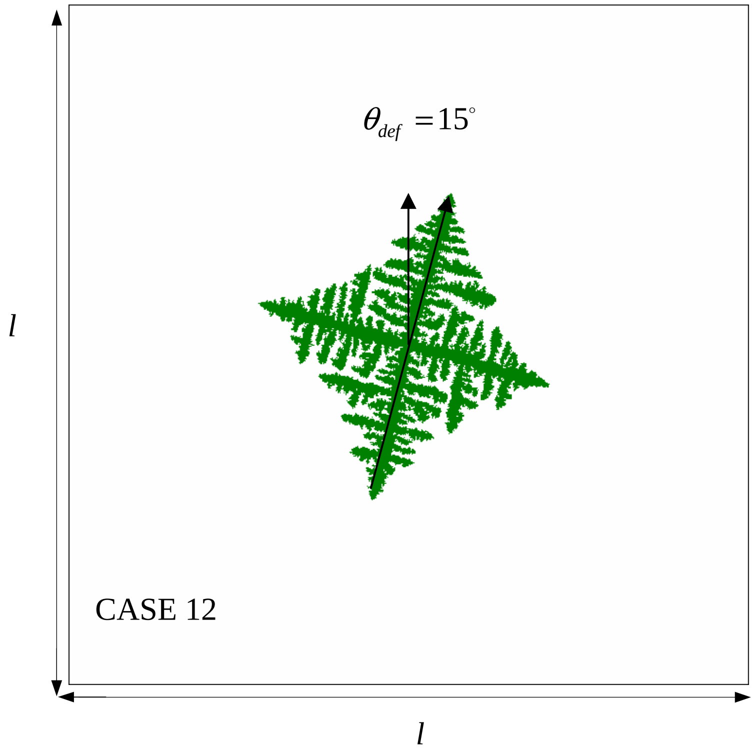
$\theta_{def} = 15^\circ$
l
CASE 12
l

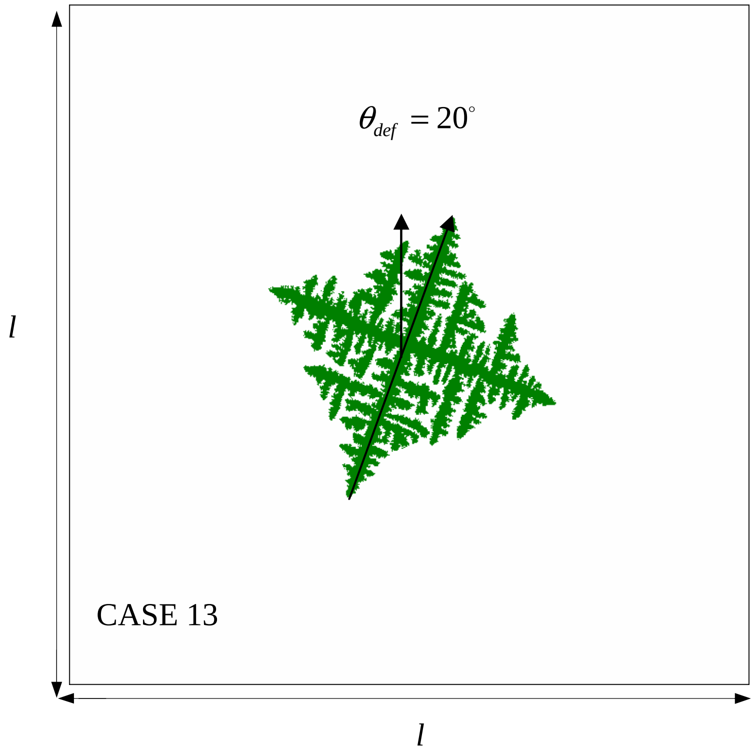
$\theta_{def} = 20^\circ$
l
CASE 13
l

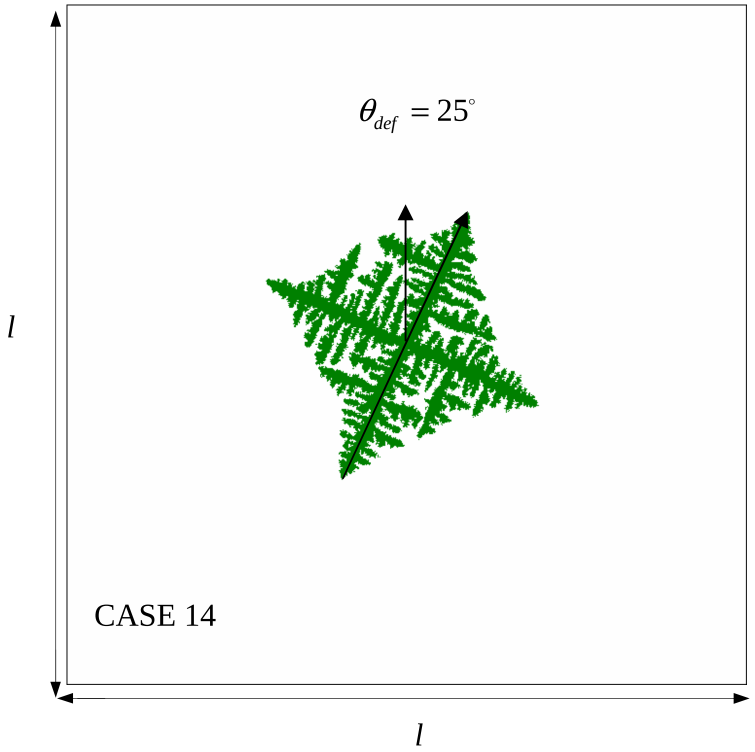
$\theta_{def} = 25^\circ$
CASE 14
l
l

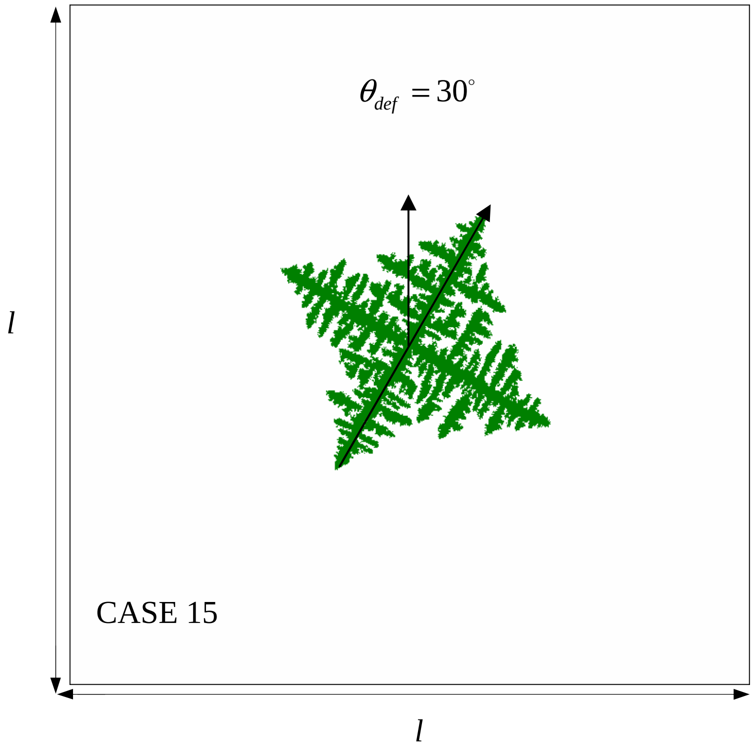
$\theta_{def} = 30^\circ$
CASE 15
l
l

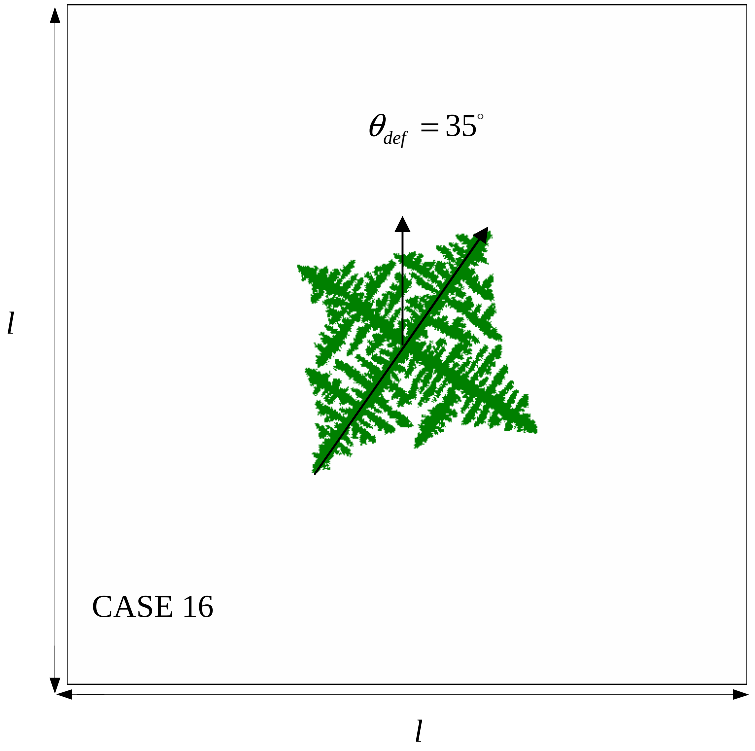
$\theta_{def} = 35^{\circ}$
l
CASE 16
l

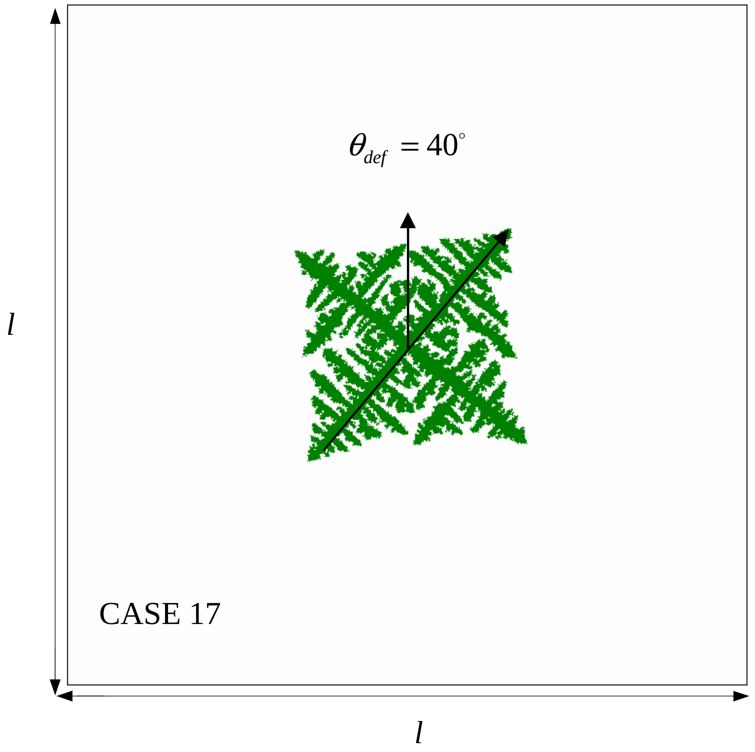
$\theta_{def} = 40^{\circ}$
l
CASE 17
l

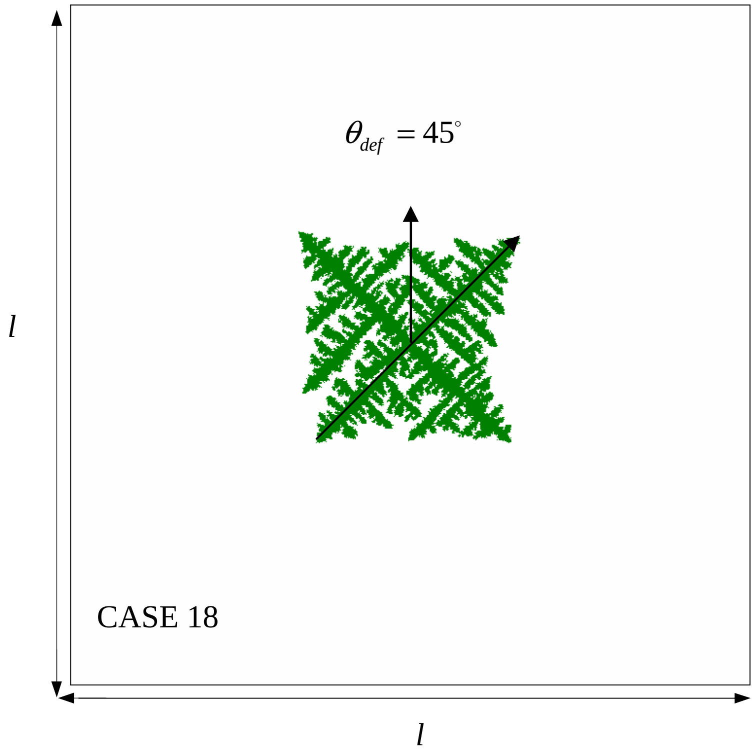

Figure 7.30: Simulated dendrites with different orientations by the PA method for the same PA-(A) random node arrangement.

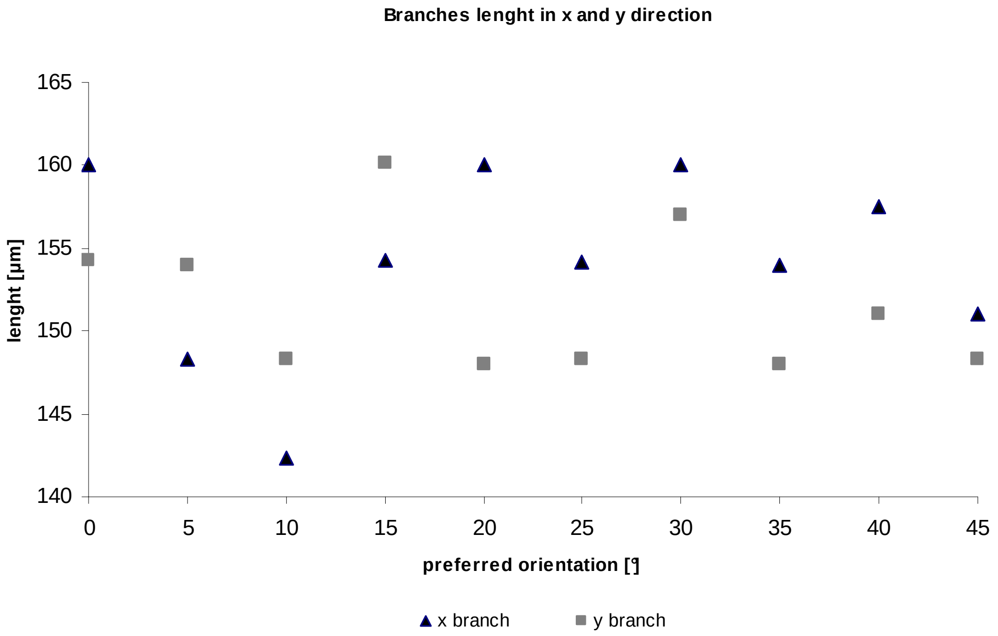

Figure 7.31: The lengths of the dendritic branches in x and y directions for ten orientations, random node arrangement PA-(A), (see Figure 7.30).

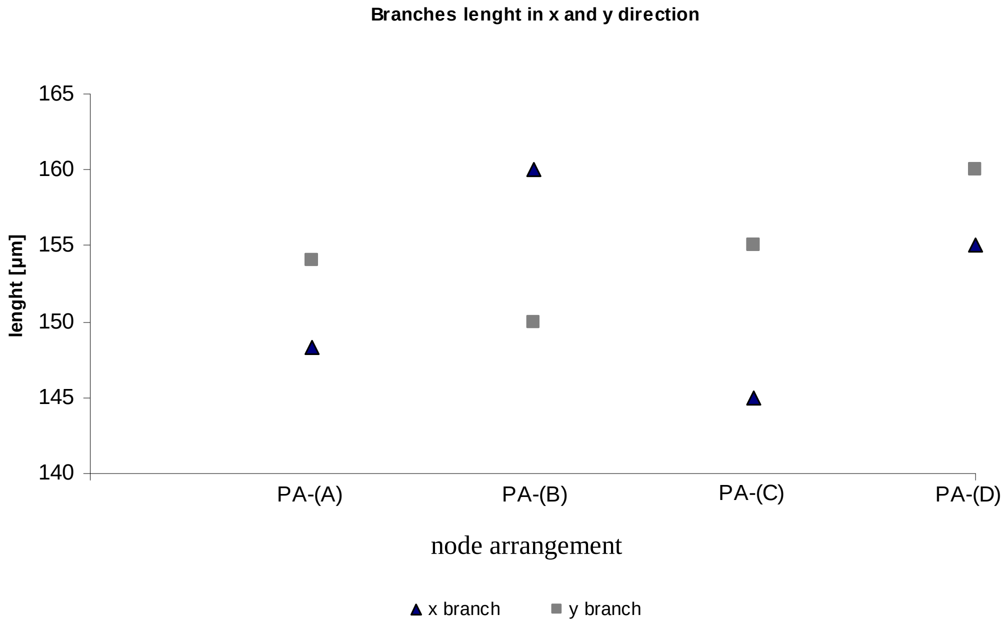

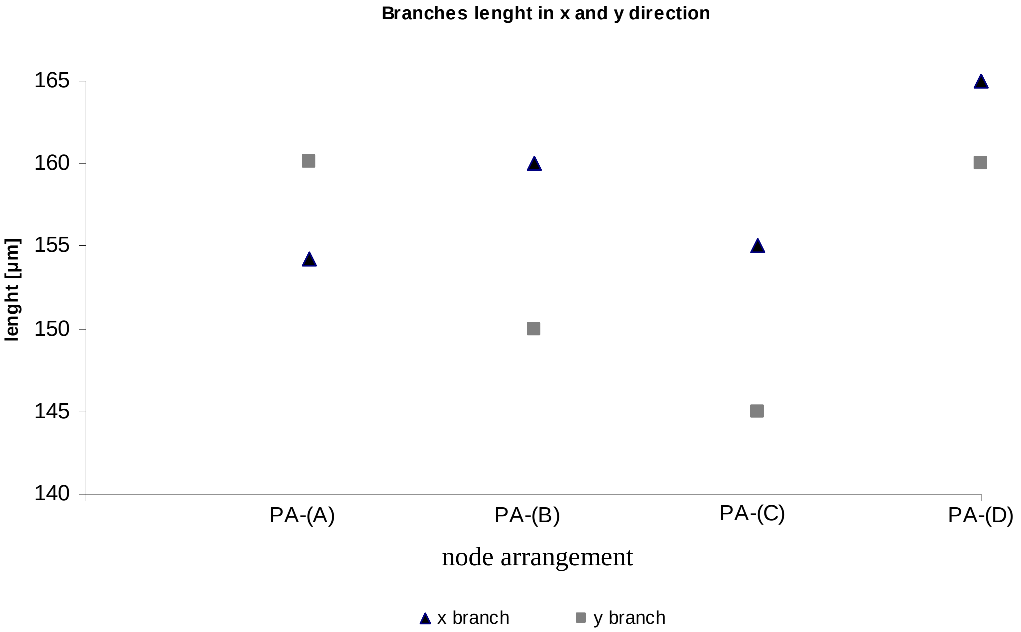

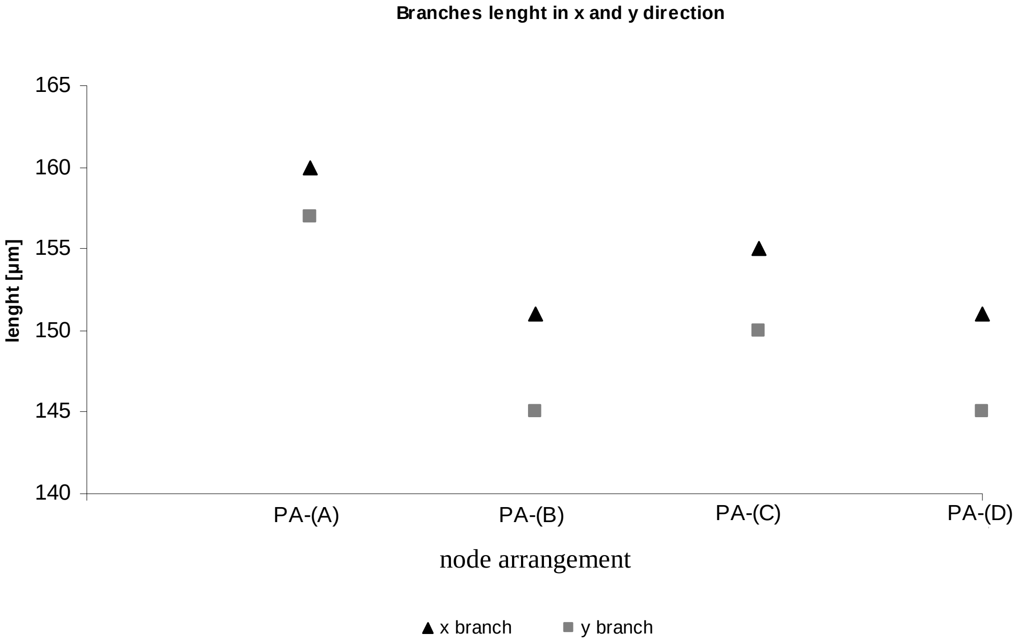

Figure 7.32: The lengths of the dendrite branches in x and y directions at different orientations $\theta_{def} = 5^\circ$, $\theta_{def} = 15^\circ$ and $\theta_{def} = 30^\circ$ (from the top to the bottom), for the random node arrangements (see Figures 7.33-7.35).

Table 7.9: The lengths of dendritic branches in x and y directions with respect to the random node arrangements.

RESULTS	method	x branch length [μm]	y branch length [μm]	ratio of primary dendrite arms x/y [-]	$\overline{x/y}$ average length ratio [-]	σ standard deviation of x/y [-]
					average length of x and y [μm]	σ standard deviation of lenght [μm]
5°	PA-(A)	148.0	154.0	0.961		
5°	PA-(B)	160.0	150.0	1.066	0.982	0.057
5°	PA-(C)	145.0	155.0	0.935	153.37	5.39
5°	PA-(D)	155.0	160.0	0.968		
15°	PA-(A)	154.0	160.0	0.962		
15°	PA-(B)	160.0	150.0	1.066	1.032	0.049
15°	PA-(C)	155.0	145.0	1.068	156.12	6.44
15°	PA-(D)	165.0	160.0	1.031		
30°	PA-(A)	160.0	157.0	1.019		
30°	PA-(B)	151.0	145.0	1.041	1.033	0.010
30°	PA-(C)	155.0	150.0	1.033	151.75	5.36
30°	PA-(D)	151.0	145.0	1.041		
0°	PA-(A)	160.0	154.0	1.038		
5°	PA-(A)	148.0	154.0	0.961		
10°	PA-(A)	142.0	148.0	0.959		
15°	PA-(A)	154.0	160.0	0.962		
20°	PA-(A)	160.0	148.0	1.081	0.980	0.041
25°	PA-(A)	154.0	148.0	1.040	152.8	5.18
30°	PA-(A)	160.0	157.0	1.019		
35°	PA-(A)	154.0	148.0	1.040		
40°	PA-(A)	157.0	151.0	1.039		
45°	PA-(A)	151.0	148.0	1.020		

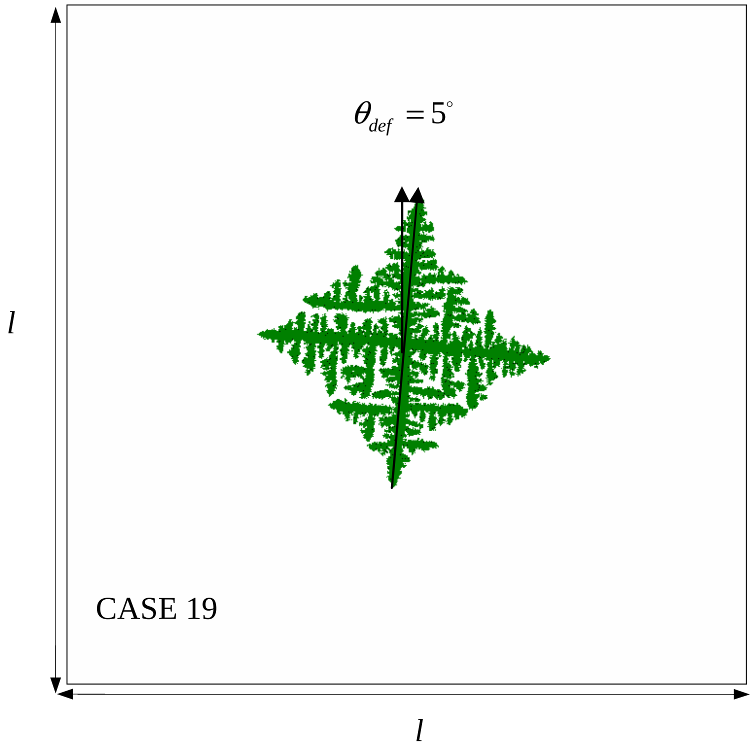
$\theta_{def} = 5^\circ$
l
CASE 19
l

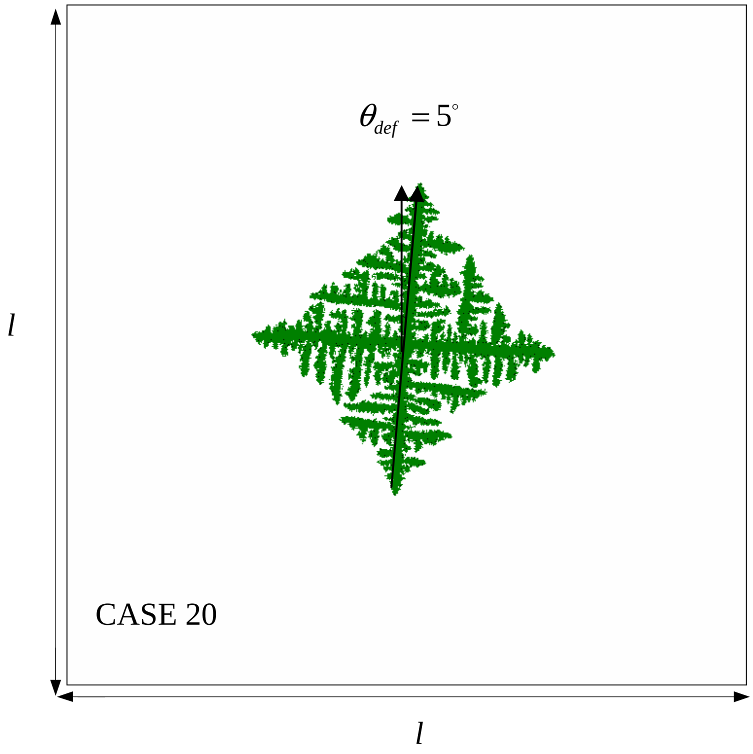
$\theta_{def} = 5^\circ$
l
CASE 20
l

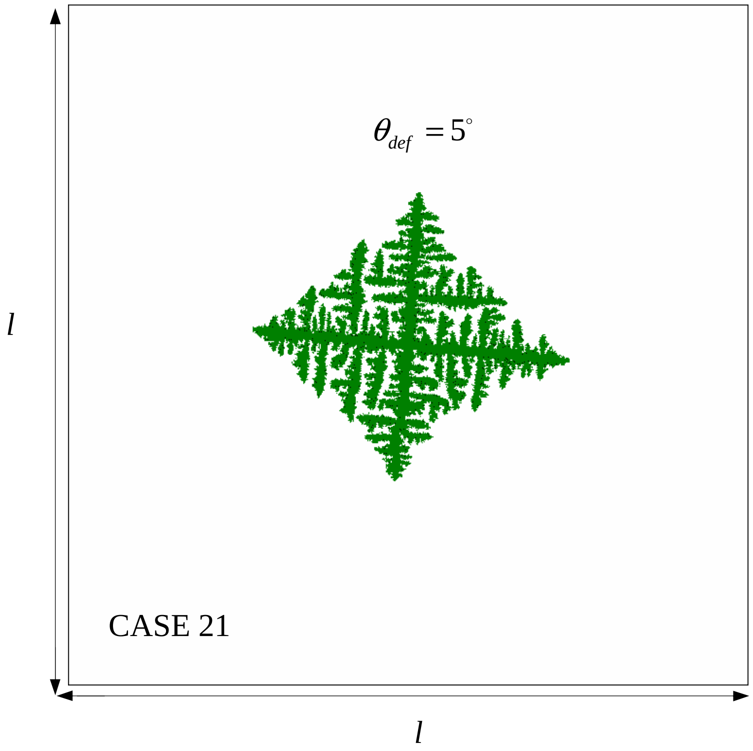

Figure 7.33: Simulated dendritic growth at orientation 5° with different random node arrangements: PA-(B), PA-(C), PA-(D).

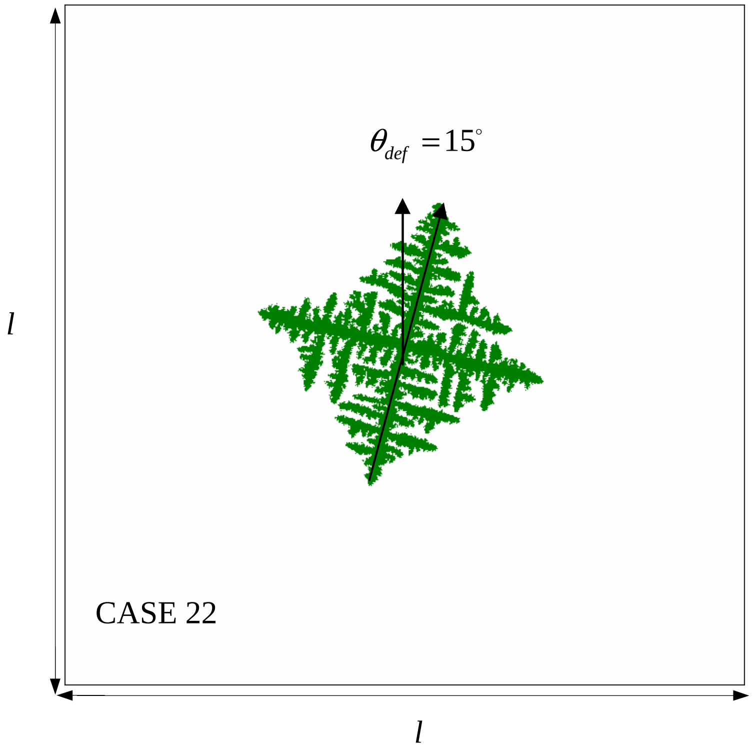

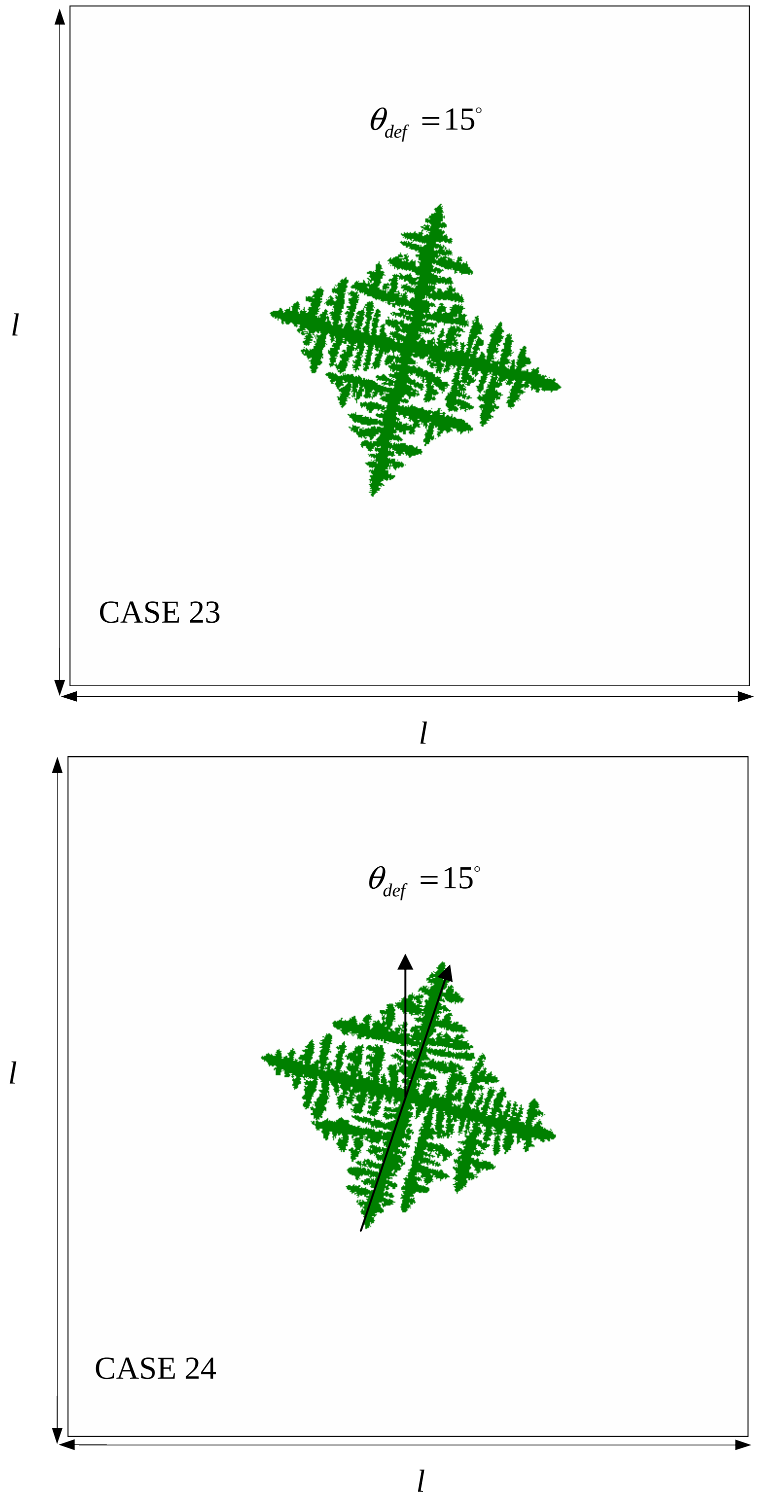

Figure 7.34: Simulated dendritic growth at orientation 15° with different random node arrangements: PA-(B), PA-(C), PA-(D).

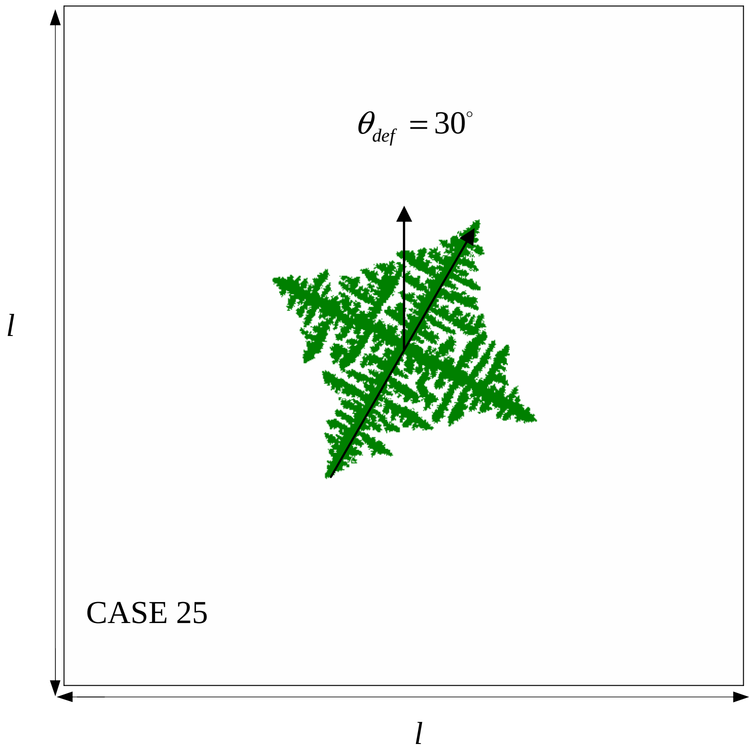
$\theta_{def} = 30^{\circ}$
l
CASE 25
l

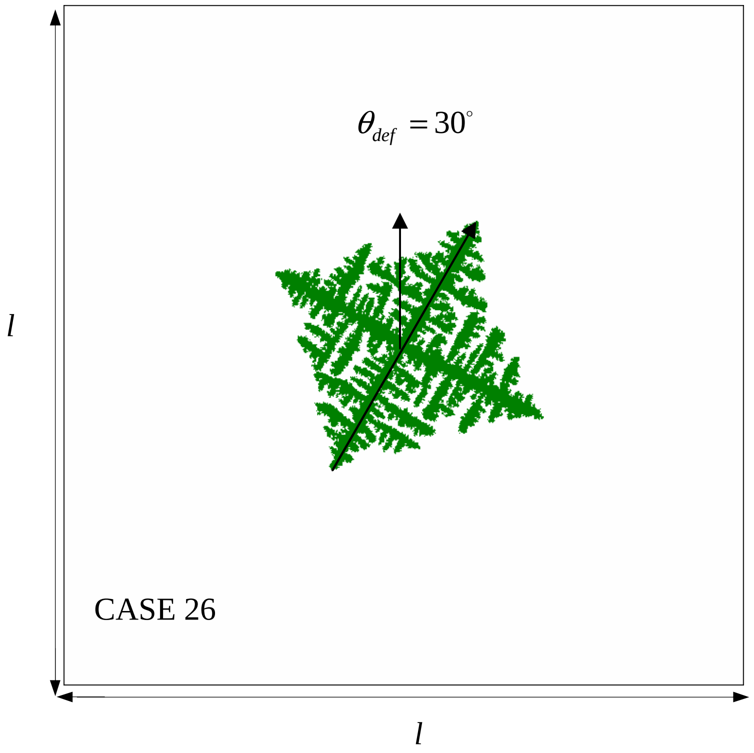
$\theta_{def} = 30^{\circ}$
l
CASE 26
l

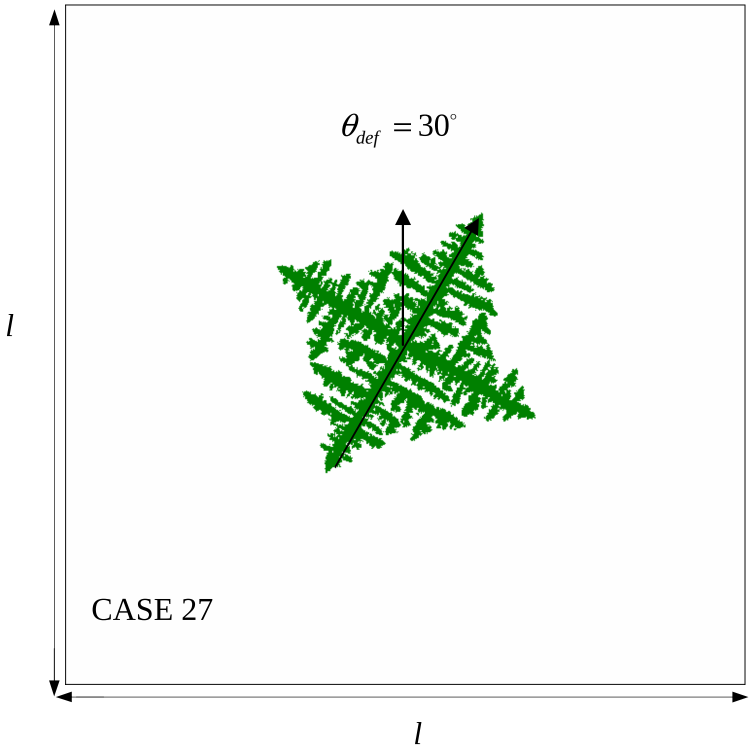

Figure 7.35: Simulated dendritic growth at orientation 30° with different random node arrangements: PA-(B), PA-(C), PA-(D).

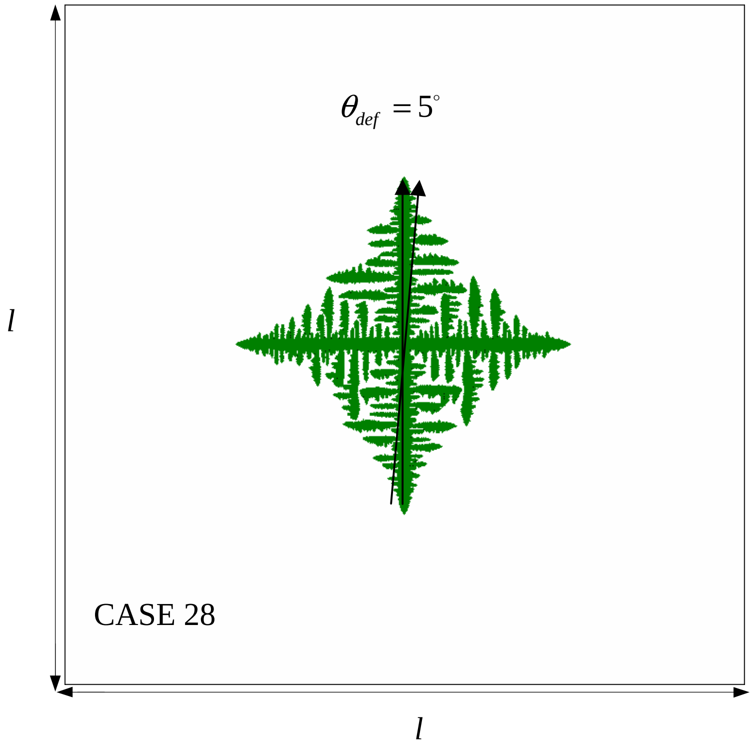
$\theta_{def} = 5^\circ$
CASE 28
l
l

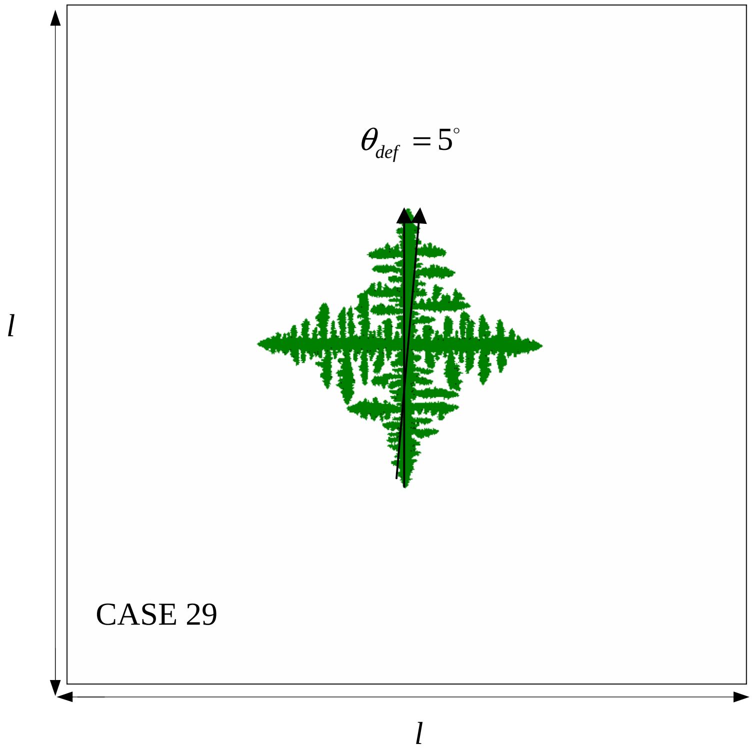
$\theta_{def} = 5^\circ$
CASE 29
l
l

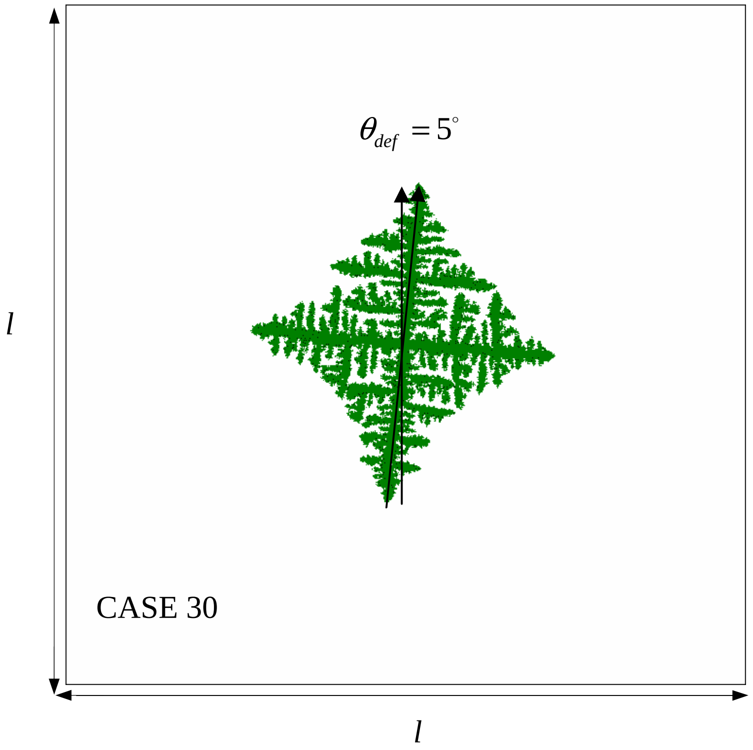

Figure 7.36: Simulated dendritic growth at orientation $\theta_{def} = 5^{\circ}$ for the different node arrangements randomness $\varepsilon = 0.1$, $\varepsilon = 0.25$, $\varepsilon = 0.49$.

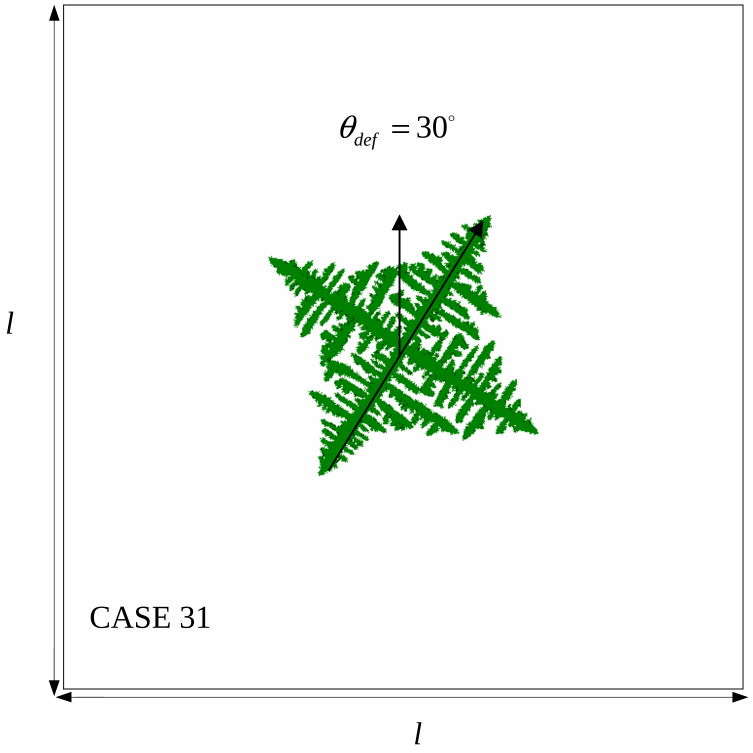

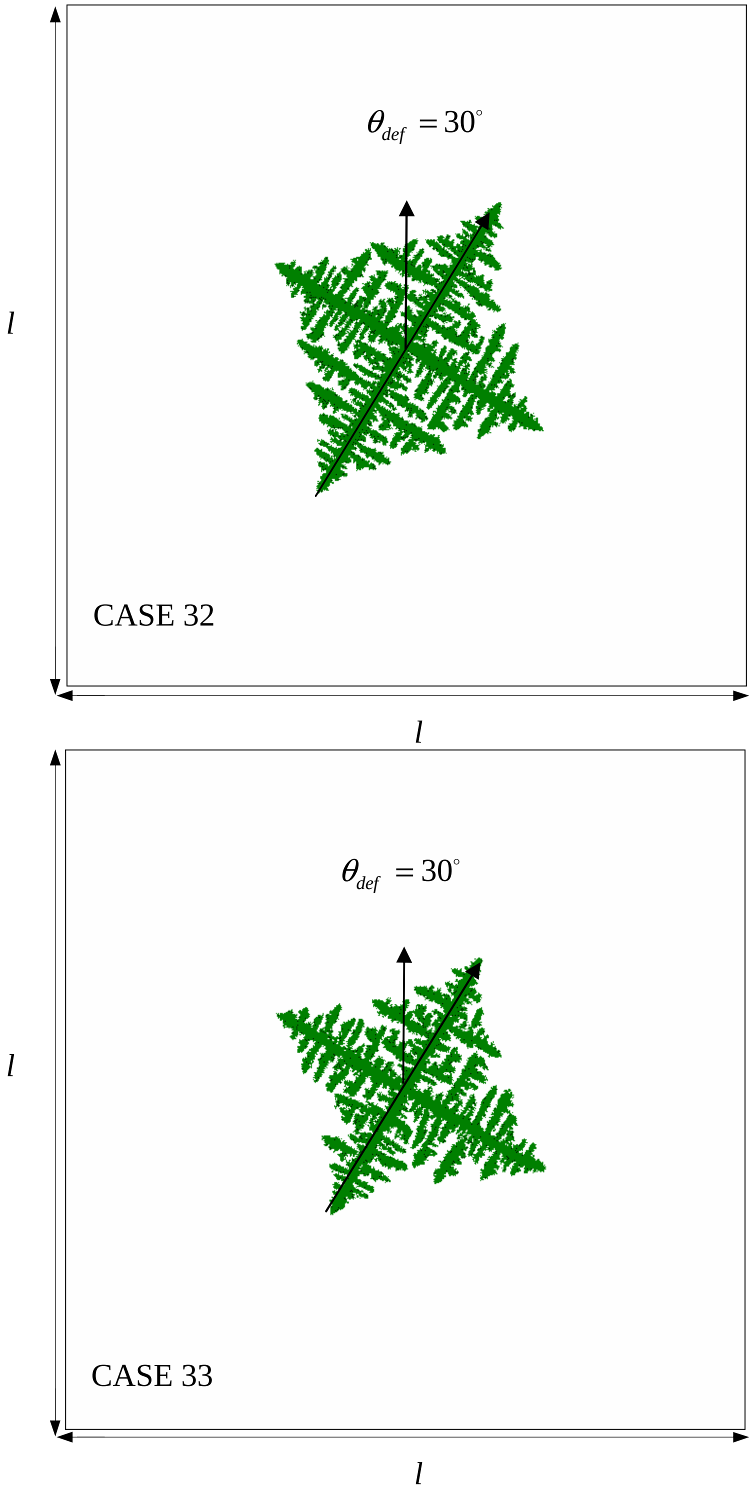

Figure 7.37: Simulated dendritic growth at orientation $\theta_{def} = 30°$ for different node arrangement randomness $\varepsilon = 0.1$, $\varepsilon = 0.25$, $\varepsilon = 0.49$.

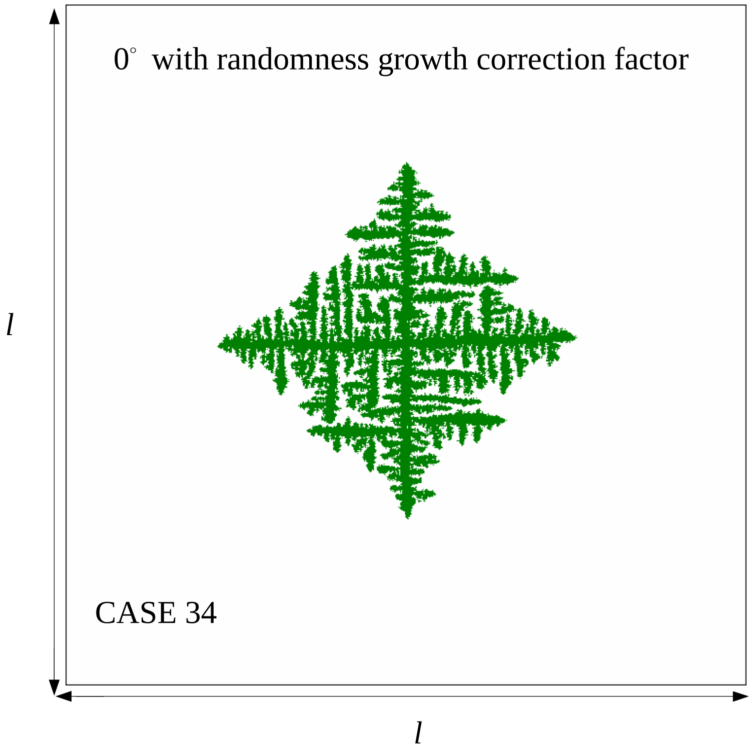
0° with randomness growth correction factor
CASE 34
l
l

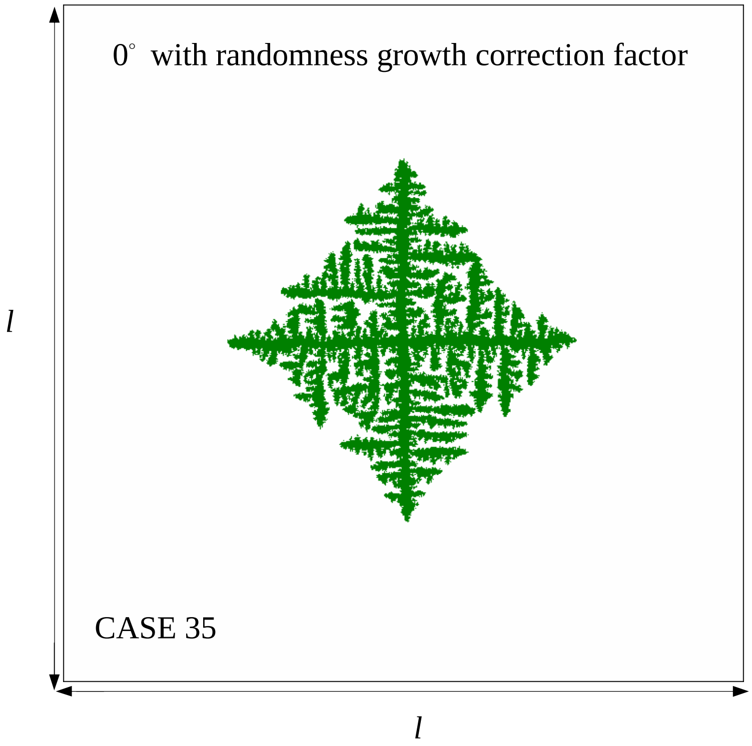
0° with randomness growth correction factor
CASE 35
l
l

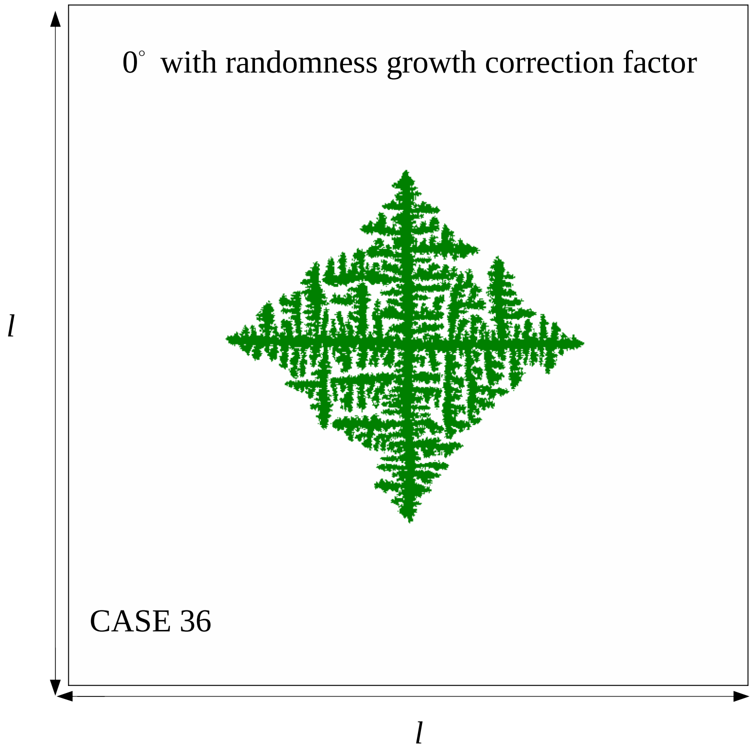

Figure 7.38: Simulated dendritic growth by the PA method with randomness growth correction factor 1.25 for PA-(B)-F, PA-(C)-F, PA-(D)-F node arrangements (from the top to the bottom).

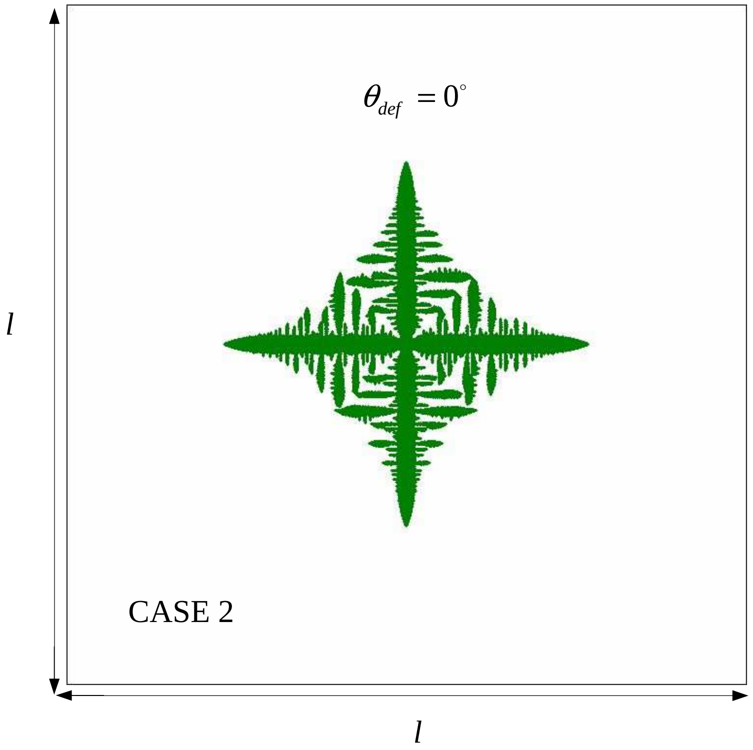
$\theta_{def} = 0^\circ$
l
CASE 2
l

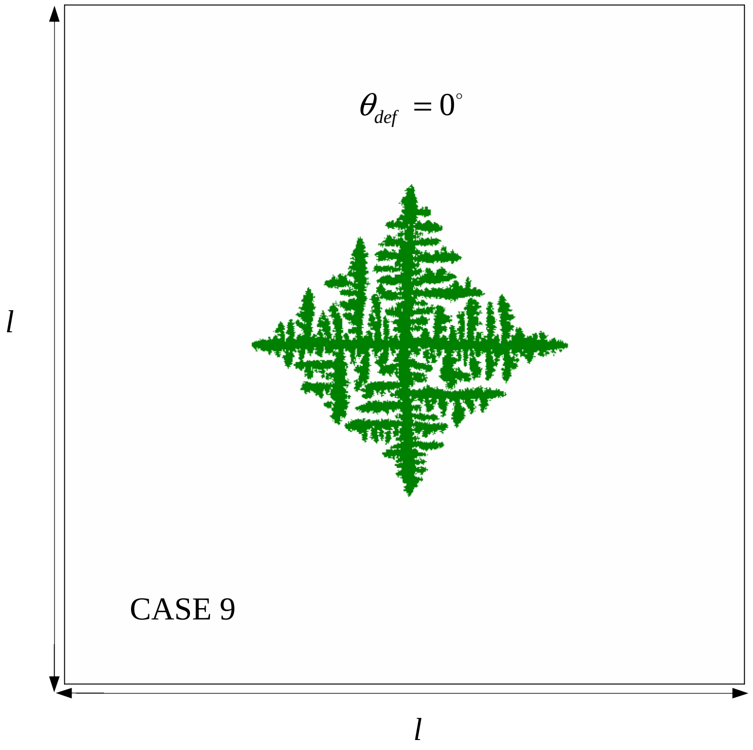
$\theta_{def} = 0^\circ$
l
CASE 9
l

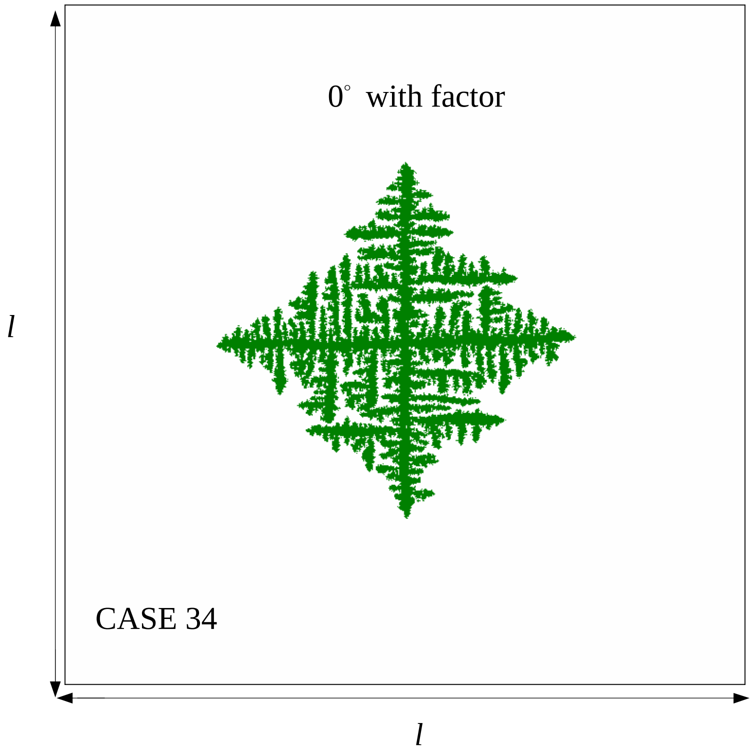

Figure 7.39: Simulated dendritic growth by the CA method, PA method and PA method with randomness growth correction factor (from the top to the bottom).

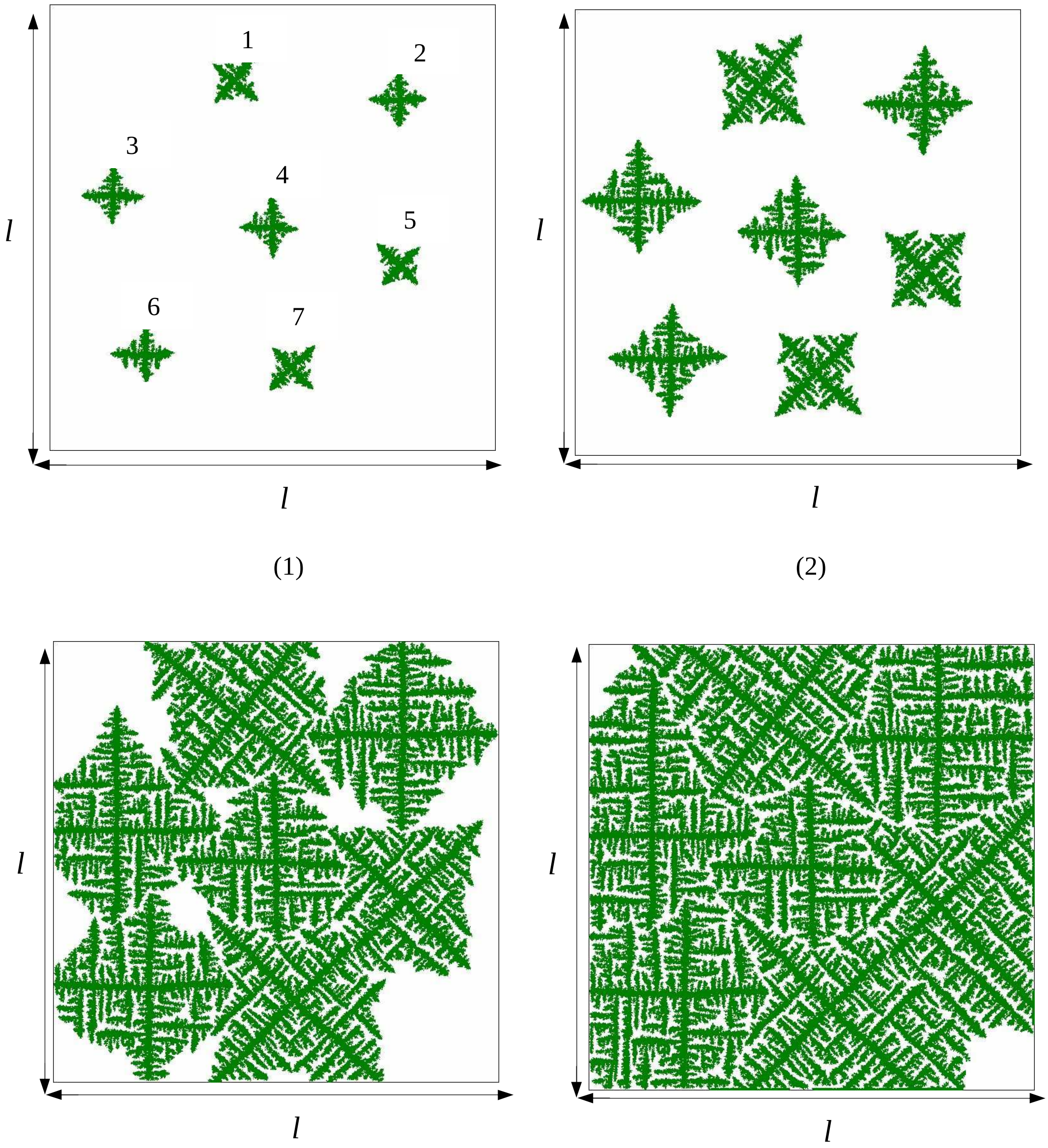

(1) (2)

(3) (4)

Figure 7.40: Seven dendrites growing simultaneously at orientations 0° and 45° (see Tables 7.3 and 7.8) after (1) 350, (2) 700, (3) 1500 and (4) 2500 time steps of the length $6.82\text{x}10^{-10}$ s by the FDM-PA method (such a simulation is not possible with the FDM-CA method).

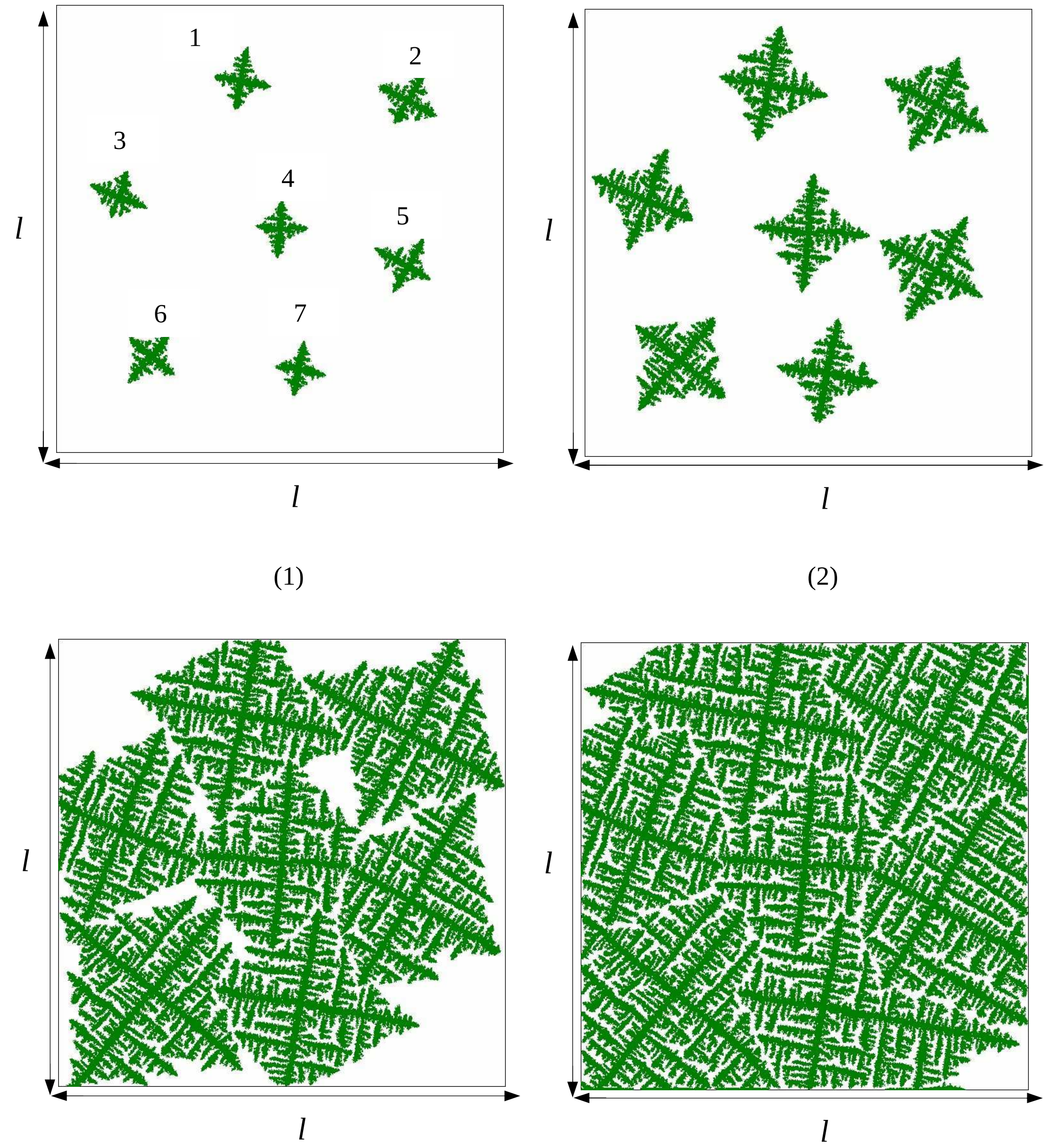

(1) (2)

(3) (4)

Figure 7.41: Seven dendrites growing simultaneously at different orientations (see Table 7.7) after (1) 350, (2) 700, (3) 1500 and (4) 2500 time steps of the length $6.82 \mathrm{x} 10^{-10}$ s by the FDM-PA method.

8 Summary and Conclusions

8.1 Summary of the Main Contributions

The principal goal of the present dissertation was to develop a simulation tool for modelling the grain structure in solidification by using the coupled mesoscopic and macroscopic models and validation by the experimental results as well as to be able to simulate the dendritic growth on the micro level of calculations. Two numerical models were developed to be able to simulate the solidification structure at different levels. The calculations were in both cases done by the conventional CA method with rectangular polygon mesh structure and by the newly developed PA approach, based on the irregular positions of the nodes. The differences in numerical implementation of the classical CA, and the new PA microstructure models were discussed. Usefulness of the novel approach has been demonstrated. The present dissertation can be summarized by the following contributions:

8.1.1 ECT/CET Macro-Mesoscopic Model

- A coupled multiscale model was developed first to predict the nucleation, growth and final grain structure (ECT and CET) of the CC steel billets. The physical model is composed of the macroscopic heat transfer model of the CC process solved by the meshless LRBFCM method and the mesoscopic model solved by the CA and PA methods. The undercooling temperatures received from the macroscopic heat transfer simulator for chosen alloy, are interpolated to the mesoscopic level for the regular CA cells (or random PA nodes) before the calculations start. On the meso level the processes of nucleation, growth and impingement of the grains are modelled as follows: (I) the nucleation is modelled through a continuous dependency of the nucleation density on temperature by the Gaussian distribution. Different nucleation parameters are used at the boundary and in the bulk region. (II) The growth and impingement are modelled by the KGT model. The CA method is based on the Nastac's and simplified neighbourhoods, while for the PA method the neighbourhood in the shape of circle is used. The governing numerical equations were first solved by the LRBFCM-CA method and then converted to the novel LRBFCM-PA method.

- Numerical examples are done for square billets of the dimension 140 mm and 180 mm. Several related industrial examples are collected in Appendix 1. Fixed input parameter of the model represents the macroscopic temperature field obtained from the Štore Steel billet simulation system. All other grain structure physical model parameters are varied, such as: the surface and the bulk area, mean nucleation undercooling, standard deviation of undercooling, maximum density of nuclei. The sensitivity study of these parameters were presented through the numerical results. The influence of the variation of the principal macroscopic heat transfer parameters (casting temperature and casting speed) on calculated grain structure is shown as well.
  In the dissertation the ECT/CET model parameters were adjusted in order to obtain the experimentally determined actual billet ECT and CET positions of the heat 46352 for the alloy properties 51CrMoV4 (Al: 0.02, Cr: 1.05, Cu: 0.125, Mn: 0.9, Mo: 0.025, Ni: 0.1, Si: 0.275, V: 0.155, C: 0.51, P: 0.0125, S: 0.0275 wt%). A systematic procedure is outlined for adjusting of the model data with the experiment.
  Many measurements from the Štore Steel alloyed for different alloys and casting temperatures and casting speeds were analysed (see Appendix1). The dimensions of the three characteristic zones: chill, columnar and equiaxed were compared to the simulated examples. The following heats for different casting parameters are analyzed. Different casting temperatures:
    - heat 48695 3/I for the alloy properties 51CrMoV4 (Al: 0.02, Cr: 1.05, Cu: 0.125, Mn: 0.9, Mo: 0.025, Ni: 0.1, Si: 0.275, V: 0.155, C: 0.51, P: 0.013, S: 0.027 wt%).
    - heat 48695 3/III for the alloy properties 51CrMoV4 (Al: 0.02, Cr: 1.05, Cu: 0.125, Mn: 0.9, Mo: 0.025, Ni: 0.1, Si: 0.275, V: 0.155, C: 0.51, P: 0.013, S: 0.027 wt%).
    - heat 48807 3/II for the alloy properties 51CrMoV4 (Al: 0.027, Cr: 1.05, Cu: 0.125, Mn: 0.9, Mo: 0.200, Ni: 0.125, Si: 0.275, V: 0.095, C: 0.00, P: 0.015, S: 0.013 wt%).

- 48807 3/IV for the alloy properties 51CrMoV4 (Al: 0.027, Cr: 1.05, Cu: 0.125, Mn: 0.9, Mo: 0.200, Ni: 0.125, Si: 0.275, V: 0.095, C: 0.00, P: 0.015, S: 0.013 wt%).

and different casting speeds:

- 46484/1 for the alloy properties 52 CrMoV4 (Al: 0.027, Cr: 1.05, Cu: 0.125, Mn: 0.9, Mo: 0.200, Ni: 0.125, Si: 0.275, V: 0.095, C: 0.00, P: 0.015, S: 0.013 wt%).
- 46693/1 for the alloy properties 25MoCrV4 (Al: 0.027, Cr: 1.05, Cu: 0.125, Mn: 0.750, Mo: 0.225, Ni: 0.100, Si: 0.180, V: 0.025, C: 0.00, P: 0.015, S: 0.013 wt%).
- 46693/3 for the alloy properties 25MoCrV4 (Al: 0.027, Cr: 1.05, Cu: 0.125, Mn: 0.750, Mo: 0.225, Ni: 0.100, Si: 0.180, V: 0.025, C: 0.00, P: 0.015, S: 0.013 wt%).

8.1.2 Dendritic Growth Model

- The aim of the dendritic growth model is the simulation of thermally induced liquid-solid dendritic growth in two dimensions by a coupled deterministic continuum mechanics heat transfer model and a stochastic localized phase change kinetics model that takes into account the undercooling, curvature, kinetic and thermodynamic anisotropy. The stochastic model receives temperature information from the deterministic model and the deterministic model receives the solid fraction information from the stochastic model. The heat transfer model is solved on a regular grid by the standard explicit FDM. The phase-change kinetics model is solved by the classical CA approach and a novel PA approach. The CA approach is established on quadratic cells and the Neumann neighbourhood. The PA approach is established on randomly distributed points and neighbourhood configuration, similar as appears in meshless methods. Both methods provide same results in case of regular PA node arrangements and neighbourhood configuration with five points.
- Numerical examples are done for square domain of dimension 350 µm with Neumann boundary conditions. Fixed input parameter of the dendritic model represent the material properties for the pure aluminium, cell size, average Gibbs-Thomson coefficient and anisotropy coefficients for the CA/PA methods. In the CA method the numerical results are prepared for the following varied input parameters: thermal fluctuations, curvature calculation radius and Gibbs-Thomson coefficient. Finally, the growth process was simulated by the CA method for seven four branched

dendrites growing simultaneously at orientations $0^\circ, 45^\circ$ and by the PA method at the same orientations as for the CA model and additionally at random orientations.

8.2 Technological Relevance

The developed numerical model for simulating grain growth structures during the CC of steel is found to be a very important tool for extending the technologically relevant capabilities of the already developed simulation system [Šarler and Vertnik, 2002] in the Štore Steel company and steel industry in general. These models are appropriate for optimizing the process parameters. Despite the powerful futures of the already developed thermal model, approved in practise, the developed meso-macro model can be used for simulation of the grain growth process which seems to be a technologically relevant problem. The main scientific achievement of the dissertation is a development of an entirely new generation of PA methods. This method can be used in grain growth and dendritic growth modelling. The main characteristic of the new approach are:

- No need for mesh generation or polygonisation. Only the node arrangement has to be generated, but without any geometrical connection between the nodes.
- In the new PA method the governing equations are solved with respect to the location of points (not polygons) on the computational domain.
- PA method offers a simple and powerful approach of CA type simulations. It was shown that both methods are able to qualitatively simulate a diverse range of solidification phenomena at approximately the same CPU time.
- Straightforward node refinement possibility.
- Straightforward extension to 3D.

8.3 Conclusions and Future Work

The computational modelling is one of the tools which increasingly helps the engineers to better understand the influence of different process parameters on the details of microstructure. With the help of computational modelling it is able to dissect the microstructure in space and in its evolution in time, and can, for example, perform different parameter studies to decide how to ameliorate the manufacturing process.

We construct two numerical models defining the underlying physics of the different sub-processes that influence on microstructure evolution. Our models are capable of simulating the evolution of the grain growth formation using the underlaying laws of physics as the input data.

The following conclusions can be summarized:

- The developed numerical model for prediction of grain strictures is capable to predict the position of ECT/CET transitions with a very good agreement to the experimental data from the Štore Steel company. It is shown that the measurements are very important aspect during the verification of the numerical model. The novel PA approach is successfully implemented to the ECT/CET model. The advantage of the PA method is its simplicity, simple transitions and straightforward applicability in non-uniform mesh structure.

- In this dissertation, a new PA approach is the first time demonstrated for prediction of the grain structure which occurs during the CC of steel. It is shown that the PA method offers a simple and powerful approach of cellular simulations. It is shown that both methods used are able to qualitatively and quantitatively model a diverse range of solidification phenomena in almost the same calculation time. PA method offers an attractive alternative to the classical CA method, because of its flexibility of node density and neighbourhood definition. The density of the nodes can in principle vary across the domain of interest and the neighbourhood can be defined in a flexible way what establish a very promising CA computational environment.

- The new approach always brings some disadvantages. For the ECT/CET model we need to be careful when choosing the dimension of radius of the neighbourhood. To small or too high value will bring distorted forms of the columnar grains. A sensitivity study needs to be done. Any of the newly developed neighbourhood configurations for the CA and PA methods has been subject to comprehensive verification tests. The reason for this is that there is a high probability that some of the nucleuses will not take part in the growth stage. There will be to many left cells (points) on the domain what will not give a reliable sight of microstructure. There is also a possibility that the code might never complete calculations.

- It is shown that the novel PA method can also be successfully used for calculation of the dendrites in any preferential direction. The novel approach is developed and introduced in this work to circumvent the mesh anisotropy problem, associated with the classical CA method.

Dendritic structures are in the CA approach sensitive on the relative angle between the cell structure and the preferential crystal growth direction which is not physical. The use of FDM-PA method instead of FDM-CA method implies transfer of the results from the regular FDM mesh to the irregular PA node arrangements and vice versa. This is not the case in the classical FDM-CA method. A replacement of the FDM method with a meshless [Atluri, 2004; Liu and Gu, 2005; Šarler *et al.*, 2005; Šarler and Vertnik, 2006] method that is able to directly cope with irregular node arrangement is underway.

- The radius of neighbourhood has to be chosen carefully. To small or too high value will bring distorted dendritic forms. The second important aspect is the generation of the random node arrangement. The randomness of PA nodes is required in order to be able to rotate the dendrites, otherwise we are too close to the conventional CA approach.

- The efforts of the future work should be focused on:
    - Inclusion of the species diffusion.
    - The thermal and the solutal dendritic growth should be coupled.
    - Deformation of grains due to mechanical forces.
    - Calculating of the recrystallization processes in addition to the solidification.
    - The ECT/CET model should be upgraded by including the concentration field received from the measurements from the industry. The influence of the concentration to the formation of equiaxed and columnar grains should be analyzed.

Appendix A

A.1 Database of Measurements from Štore Steel Company

Four Technical Reports from the Slovenian Štore Steel company were received.

1. Influence of casting speed on the grain structure [Manojlović, 2008].
2. Influence of casting speed on the grain structure [Manojlović, 2007].
3. Research on grain morphology (casting temperature and casting speed) [Manojlović, 2008].
4. Influence of EMS on the grain structure [Manojlović, 2008].

From these measurements, the positions of ECE/CET transformations for the different casting parameters were determined. The results were divided into four groups according to the received reports. From all the measurements we choose only few examples which are believed to be of the good quality. First one 46352_1 represents the example from the Chapter 7, where the sensitivity. The following alloys were analyzed: 48807 3/II, 48807 3/IV, 48695 3/II, 48695 3/IV, and for the different casting speeds and 46484/1, 46693/1 and 46693/3 for the different casting temperatures. For all Baumann prints the centre and corner cross sections of the temperature fields are prepared.

Finally the chosen measurements were compared with the simulated result prepared for the conventional grid structure using Nastac's neighbourhood configuration (following procedures from Chapter 5).

Mesoscopic CA model was studied and refined in order to obtain a good agreement with the measurement observations. The simulated positions of ECT/CET transformation fit to the industrial examples.

Table A.1: Database of measurements from Štore Steel company.

Alloy	Material	V_{cast} [m/min]	T_{cast} [K]	Dimension [m]	Simulation
48807 3/II	52CrMoV4	0.95	1522	0.180	Figure A2
48807 3/IV	52CrMoV4	1.15	1520	0.180	Figure A3
48695 3/I	51CrMoV4	0.95	1524	0.180	Figure A7
48695 3/III	51CrMoV4	1.15	1529	0.180	Figure A9
48696 3/I	51CrMoV4	0.95	1523	0.180	*
48696 3/II	51CrMoV4	1.05	1521	0.180	*
48696 3/III	51CrMoV4	1.15	1520	0.180	*
48939/1	51CrV4	0.95	1531	0.180	*
48939/2	51CrV4	1.15	1531	0.180	*
48938/1	51CrV4	0.95	1530	0.180	*
48938/2	51CrV4	1.15	1530	0.180	*
Reference Case 46352	**51CrMoV4**	**1.65**	**1530**	**0.140**	Figure A1
46484/1	52CrMoV4	1.05	1522	0.180	Figure A11
46484/3	52CrMoV4	1.05	1520	0.180	*
46693/1	25MoCr4	1.12	1545	0.180	Figure A13
46693/3	25MoCr4	1.12	1550	0.180	Figure A15
46392/1	51CrV4	1.05	1529	0.180	*
46392/3	51CrV4	1.05	1528	0.180	*
46340/1	51CrV4	1.08	1522	0.140	*
46340/3	51CrV4	1.08	1529	0.140	*
46342/1	51CrV4	1.80	1527	0.140	*
46342/3	51CrV4	1.80	1528	0.140	*
46352/3	51CrV4+Mo	1.75	1531	0.140	*
46379/1	52CrMoV4	1.10	1520	0.180	*
46379/3	52CrMoV4	1.10	1517	0.180	*
46381/1	50CrV4	1.10	1516	0.180	*
46381/3	50CrV4	1.10	1519	0.180	*
46391/1	51CrV4	1.07	1527	0.180	*
46391/3	51CrV4	1.07	1528	0.180	*
50644/3-1	51 CrV4			0.180	Figure A17
50644/3-2	51 CrV4			0.180	Figure A18

* bad quality of measurements or entirely unknown casting parameters.

Table A.2: Material properties - compositions

Heat/ compositions	Al	Cr	Cu	Mn	Mo	Ni	Si	V	C	P	S
46352	0.02	1.05	0.125	0.9	0.025	0.1	0.275	0.155	0.51	0.0125	0.0275
48695 3/1	0.02	1.05	0.125	0.9	0.025	0.1	0.275	0.155	0.51	0.013	0.027
48695 3/III	0.02	1.05	0.125	0.9	0.025	0.1	0.275	0.155	0.51	0.013	0.027
48807 3/II	0.027	1.05	0.125	0.9	0.200	0.125	0.275	0.095	0.00	0.015	0.013
48807 3/IV	0.027	1.05	0.125	0.9	0.200	0.125	0.275	0.095	0.00	0.015	0.013
46484/1	0.027	1.05	0.125	0.9	0.200	0.125	0.275	0.095	0.00	0.015	0.013
46693/1	0.027	1.05	0.125	0.750	0.225	0.100	0.180	0.025	0.27	0.015	0.013
46693/3	0.027	1.05	0.125	0.750	0.225	0.100	0.180	0.025	0.27	0.015	0.013

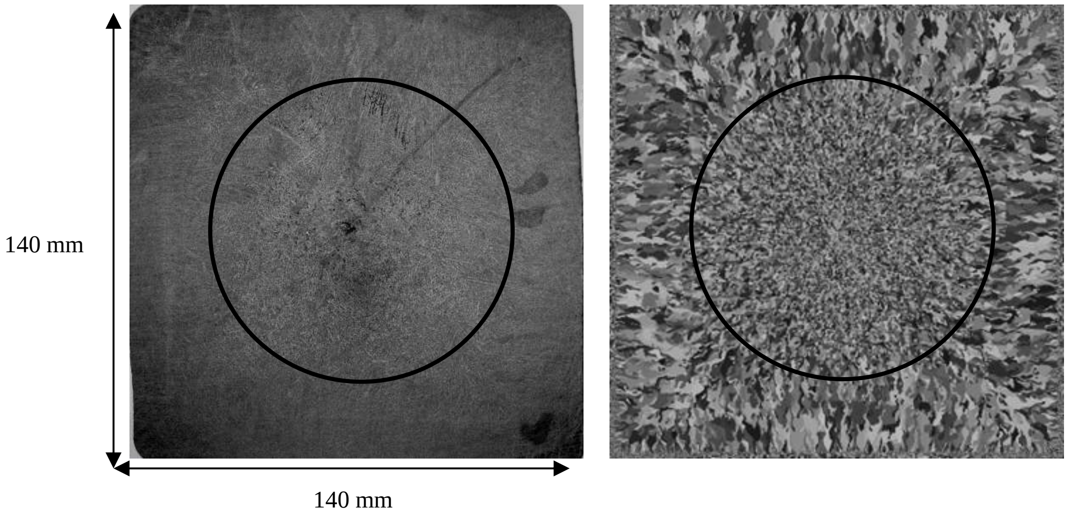

Figure A.1: Left: Baumann print, right: simulated result for steel 51CrMoV4, dimension 140 mm, $T_{cast} = 1530\,\mathrm{K}$ and $V_{cast} = 1.75\,\mathrm{m/min}$ (Reference case, heat 46352).

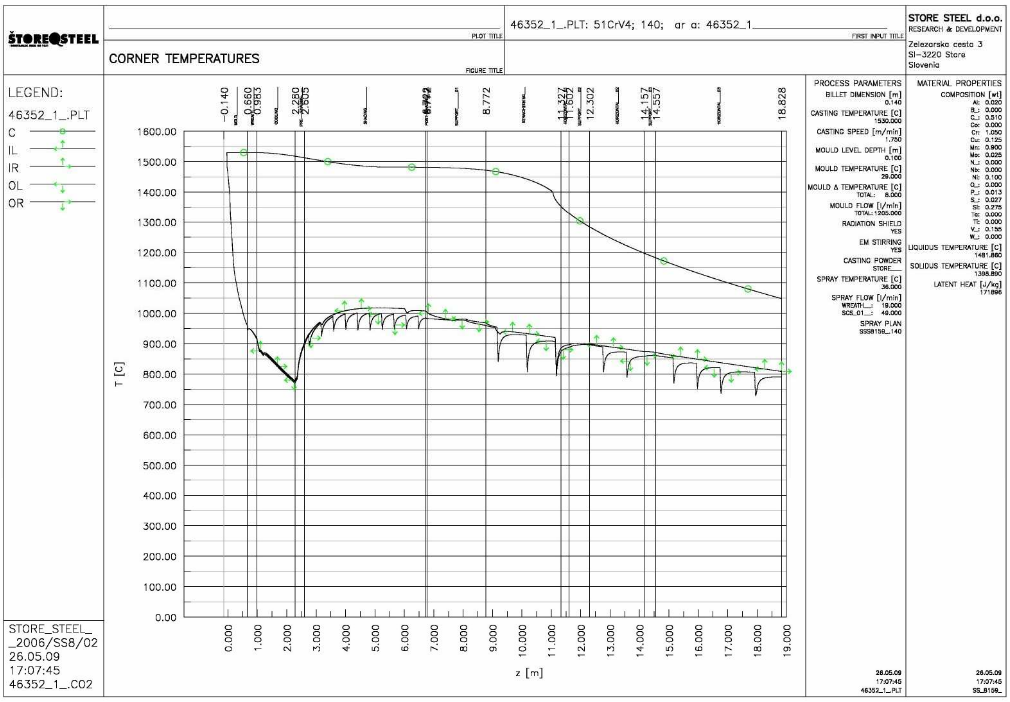

PROCESS PARAMETERS
BILLET DIMENSION [m]
0.140
CASTING TEMPERATURE [C]
1530.000
CASTING SPEED [m/min]
1.750
MOULD LEVEL DEPTH [m]
0.100
MOULD TEMPERATURE [C]
29.000
MOULD Δ TEMPERATURE [C]
TOTAL: 8.000
MOULD FLOW [l/min]
TOTAL: 1205.000
RADIATION SHIELD
YES
EM STIRRING
YES
CASTING POWDER
STORE___
SPRAY TEMPERATURE [C]
36.000
SPRAY FLOW [l/min]
WREATH__: 19.000
SCS_01__: 49.000
SPRAY PLAN
SSS8159_.140

MATERIAL PROPERTIES
COMPOSITION [wt]
Al: 0.020
B_: 0.000
C_: 0.510
Co: 0.000
Cr: 1.050
Cu: 0.125
Mn: 0.900
Mo: 0.025
N_: 0.000
Nb: 0.000
Ni: 0.100
O_: 0.000
P_: 0.013
S_: 0.027
Si: 0.275
Ta: 0.000
Ti: 0.000
V_: 0.155
W_: 0.000
LIQUIDUS TEMPERATURE [C]
1481.860
SOLIDUS TEMPERATURE [C]
1398.890
LATENT HEAT [J/kg]
171896

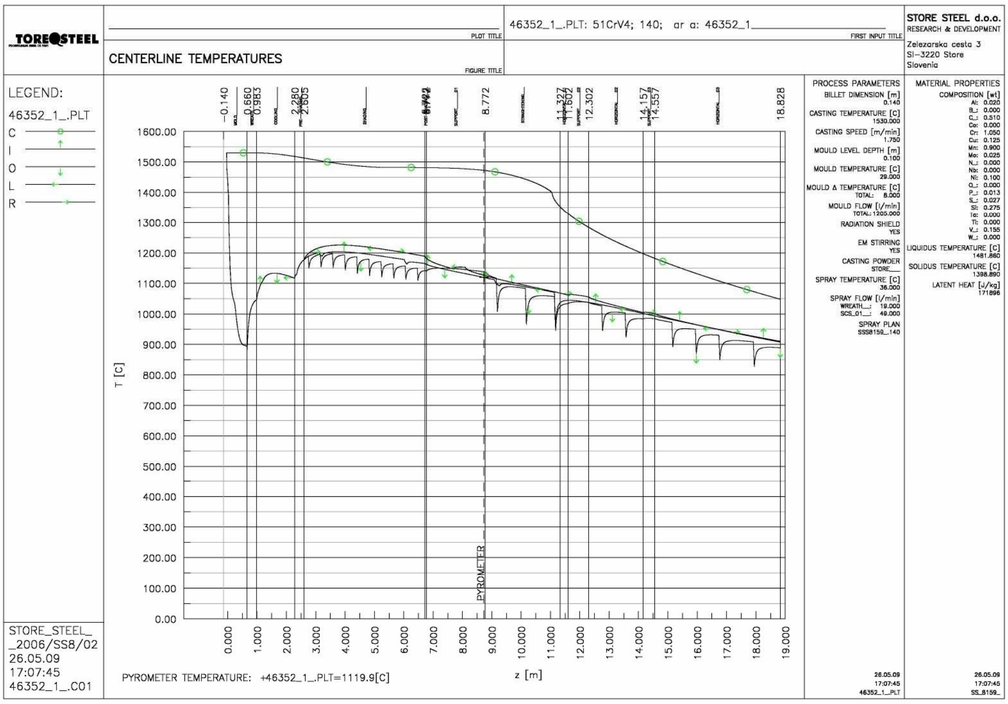

CENTERLINE TEMPERATURES

46352_1_.PLT: 51CrV4; 140; ar a: 46352_1

STORE STEEL d.o.o.
RESEARCH & DEVELOPMENT
Zelezarska cesta 3
SI–3220 Store
Slovenia

PROCESS PARAMETERS
BILLET DIMENSION [m] 0.140
CASTING TEMPERATURE [C] 1530.000
CASTING SPEED [m/min] 1.750
MOULD LEVEL DEPTH [m] 0.100
MOULD TEMPERATURE [C] 29.000
MOULD Δ TEMPERATURE [C] TOTAL: 8.000
MOULD FLOW [l/min] TOTAL: 1205.000
RADIATION SHIELD YES
EM STIRRING YES
CASTING POWDER STORE___
SPRAY TEMPERATURE [C] 36.000
SPRAY FLOW [l/min]
WREATH__: 19.000
SCS_01__: 49.000
SPRAY PLAN SSS8159_.140

MATERIAL PROPERTIES
COMPOSITION [wt]
Al: 0.020
B_: 0.000
C_: 0.510
Co: 0.000
Cr: 1.050
Cu: 0.125
Mn: 0.900
Mo: 0.025
N_: 0.000
Nb: 0.000
Ni: 0.100
O_: 0.000
P_: 0.013
S_: 0.027
Si: 0.275
Ta: 0.000
Ti: 0.000
V_: 0.155
W_: 0.000
LIQUIDUS TEMPERATURE [C] 1481.860
SOLIDUS TEMPERATURE [C] 1398.890
LATENT HEAT [J/kg] 171896

PYROMETER TEMPERATURE: +46352_1_.PLT=1119.9[C]

STORE_STEEL_
_2006/SS8/02
26.05.09
17:07:45
46352_1_.C01

26.05.09
17:07:45
46352_1_.PLT

26.05.09
17:07:45
SS_8159_

Figure A.2: Centerline and corner temperatures along the casting direction (heat 46352).

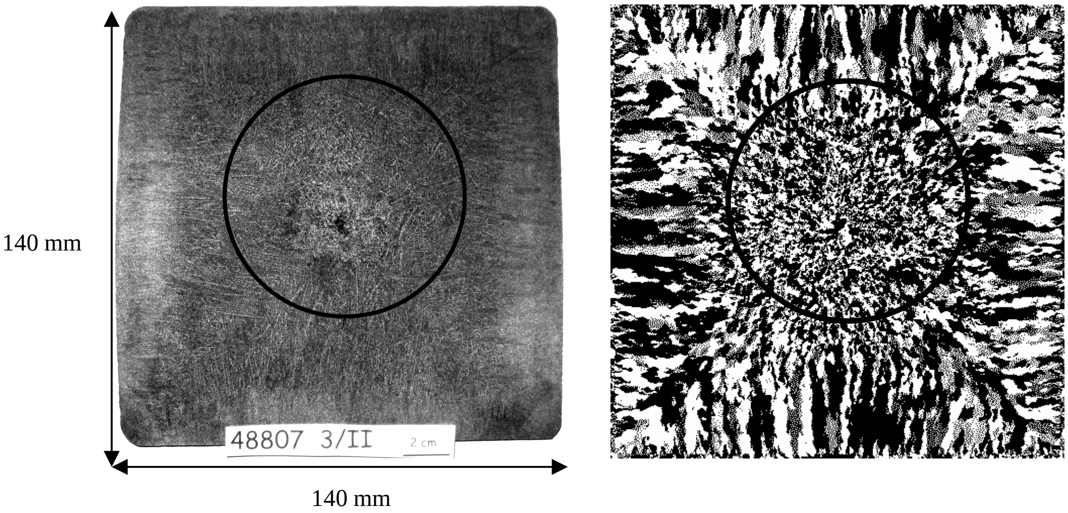

Figure A.3: Left: Baumann print, right: simulated result for steel 51CrV4+Mo, dimension 180 mm, T_{cast} = 1522 K and V_{cast} = 0.95 m/min.

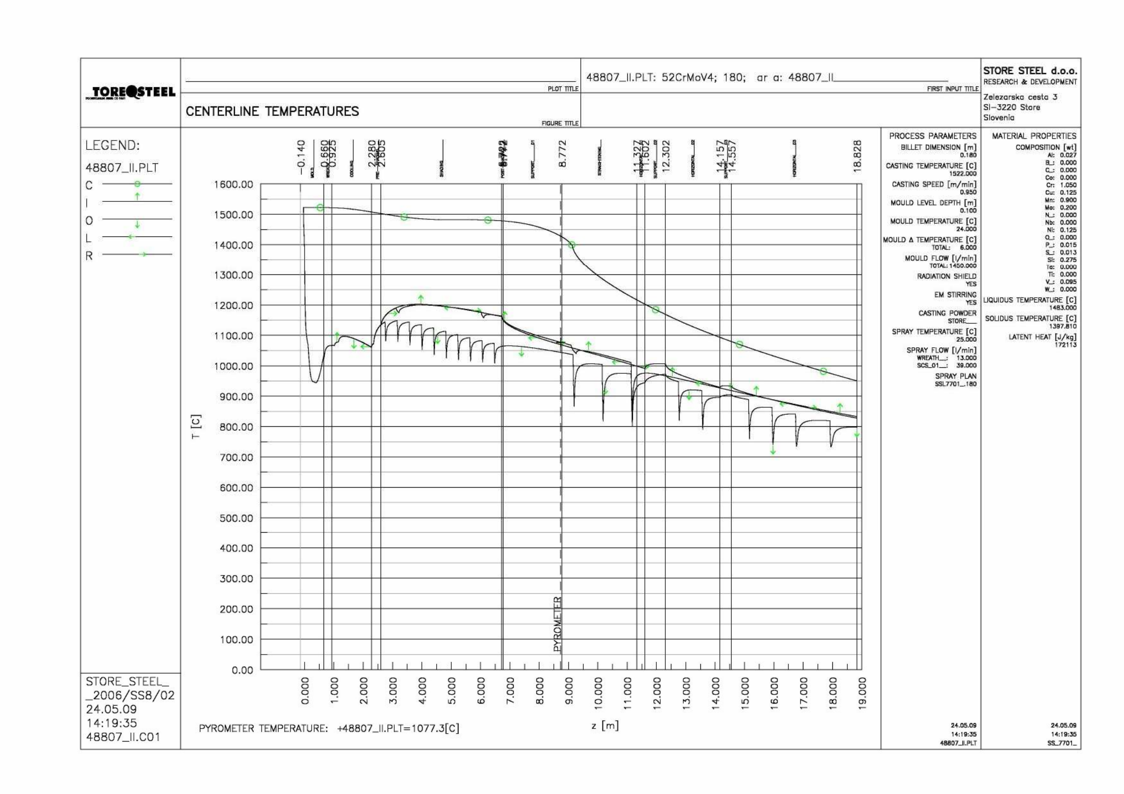

CENTERLINE TEMPERATURES

48807_II.PLT: 52CrMoV4; 180; ar a: 48807_II

STORE STEEL d.o.o.
RESEARCH & DEVELOPMENT
Zelezarska cesta 3
SI–3220 Store
Slovenia

48807_II.PLT

PROCESS PARAMETERS
BILLET DIMENSION [m] 0.180
CASTING TEMPERATURE [C] 1522.000
CASTING SPEED [m/min] 0.950
MOULD LEVEL DEPTH [m] 0.100
MOULD TEMPERATURE [C] 24.000
MOULD Δ TEMPERATURE [C] TOTAL: 6.000
MOULD FLOW [l/min] TOTAL: 1450.000
RADIATION SHIELD YES
EM STIRRING YES
CASTING POWDER STORE___
SPRAY TEMPERATURE [C] 25.000
SPRAY FLOW [l/min]
WREATH__: 13.000
SCS_01__: 39.000
SPRAY PLAN SSL7701_.180

MATERIAL PROPERTIES
COMPOSITION [wt]
Al: 0.027
B_: 0.000
C_: 0.000
Co: 0.000
Cr: 1.050
Cu: 0.125
Mn: 0.900
Mo: 0.200
N_: 0.000
Nb: 0.000
Ni: 0.125
O_: 0.000
P_: 0.015
S_: 0.013
Si: 0.275
Ta: 0.000
Ti: 0.000
V_: 0.095
W_: 0.000
LIQUIDUS TEMPERATURE [C] 1483.000
SOLIDUS TEMPERATURE [C] 1397.810
LATENT HEAT [J/kg] 172113

STORE_STEEL_
_2006/SS8/02
24.05.09
14:19:35
48807_II.C01

PYROMETER TEMPERATURE: +48807_II.PLT=1077.3[C]

24.05.09
14:19:35
48807_II.PLT

24.05.09
14:19:35
SS_7701_

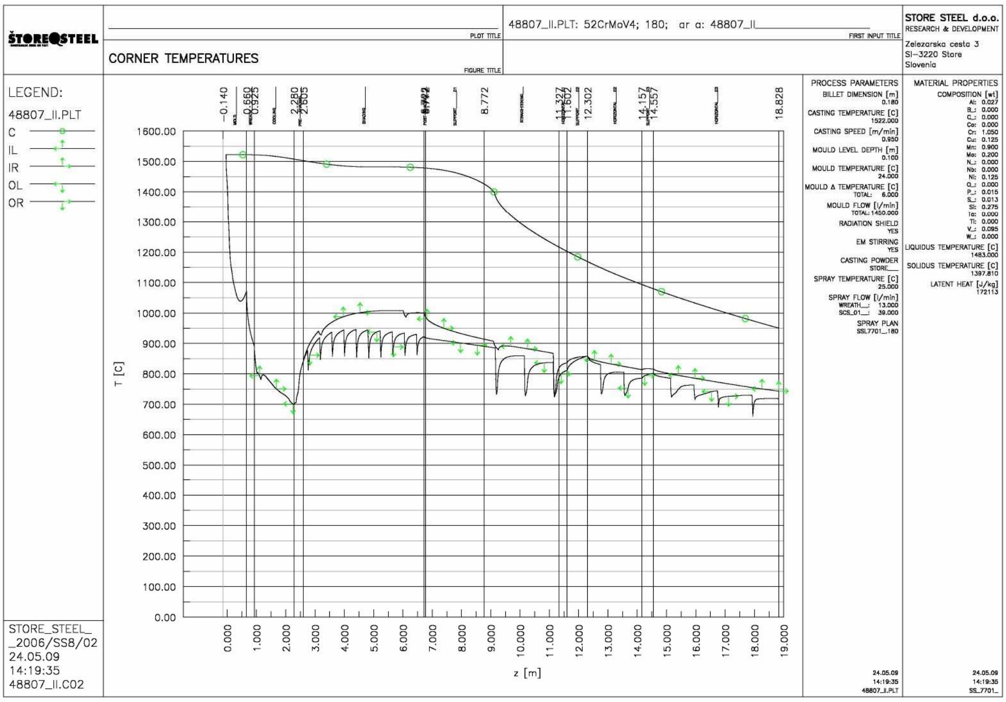

Figure A.4: Centerline and corner temperatures along the casting direction (heat 48807 3/II).

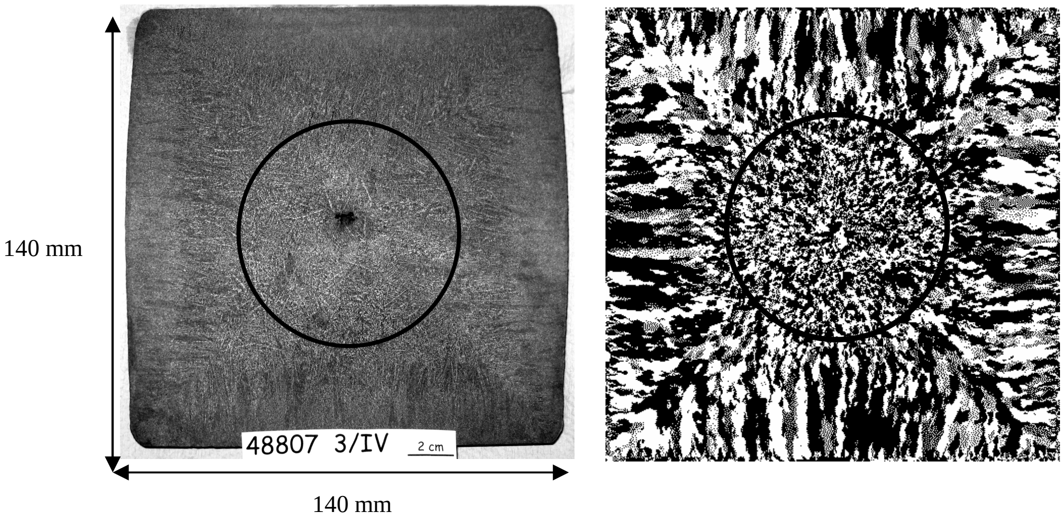

Figure A.5: Left: Baumann print, right: simulated result for steel 51CrV4+Mo, dimension 180 mm, T_{cast} = 1520 K and V_{cast} = 1.15 m/min .

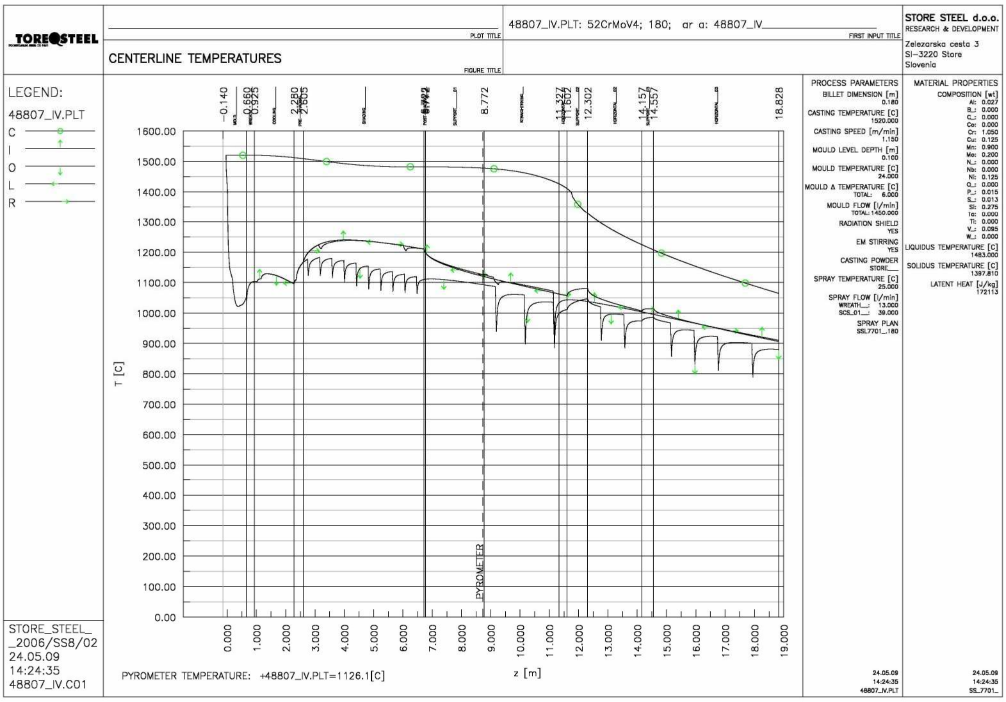

48807_IV.PLT: 52CrMoV4; 180; ar a: 48807_IV________
FIRST INPUT TITLE

PLOT TITLE

CENTERLINE TEMPERATURES
FIGURE TITLE

STORE STEEL d.o.o.
RESEARCH & DEVELOPMENT
Zelezarska cesta 3
SI–3220 Store
Slovenia

LEGEND:
48807_IV.PLT
C
I
O
L
R

PROCESS PARAMETERS
BILLET DIMENSION [m] 0.180
CASTING TEMPERATURE [C] 1520.000
CASTING SPEED [m/min] 1.150
MOULD LEVEL DEPTH [m] 0.100
MOULD TEMPERATURE [C] 24.000
MOULD Δ TEMPERATURE [C] TOTAL: 6.000
MOULD FLOW [l/min] TOTAL: 1450.000
RADIATION SHIELD YES
EM STIRRING YES
CASTING POWDER STORE___
SPRAY TEMPERATURE [C] 25.000
SPRAY FLOW [l/min]
WREATH__: 13.000
SCS_01__: 39.000
SPRAY PLAN SSL7701_.180

MATERIAL PROPERTIES
COMPOSITION [wt]
Al: 0.027
B_: 0.000
C_: 0.000
Co: 0.000
Cr: 1.050
Cu: 0.125
Mn: 0.900
Mo: 0.200
N_: 0.000
Nb: 0.000
Ni: 0.125
O_: 0.000
P_: 0.015
S_: 0.013
Si: 0.275
Ta: 0.000
Ti: 0.000
V_: 0.095
W_: 0.000
LIQUIDUS TEMPERATURE [C] 1483.000
SOLIDUS TEMPERATURE [C] 1397.810
LATENT HEAT [J/kg] 172113

STORE_STEEL_
_2006/SS8/02
24.05.09
14:24:35
48807_IV.C01

PYROMETER TEMPERATURE: +48807_IV.PLT=1126.1[C]

24.05.09
14:24:35
48807_IV.PLT

24.05.09
14:24:35
SS_7701_

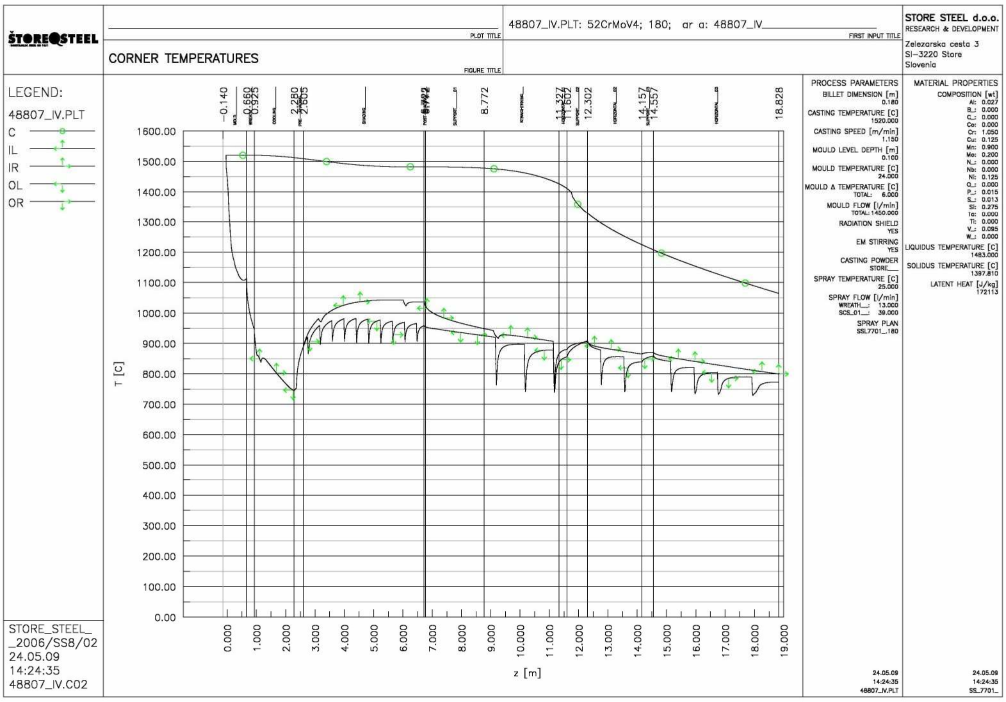

Figure A.6: Centerline and corner temperatures along the casting direction (heat 48807 3/IV).

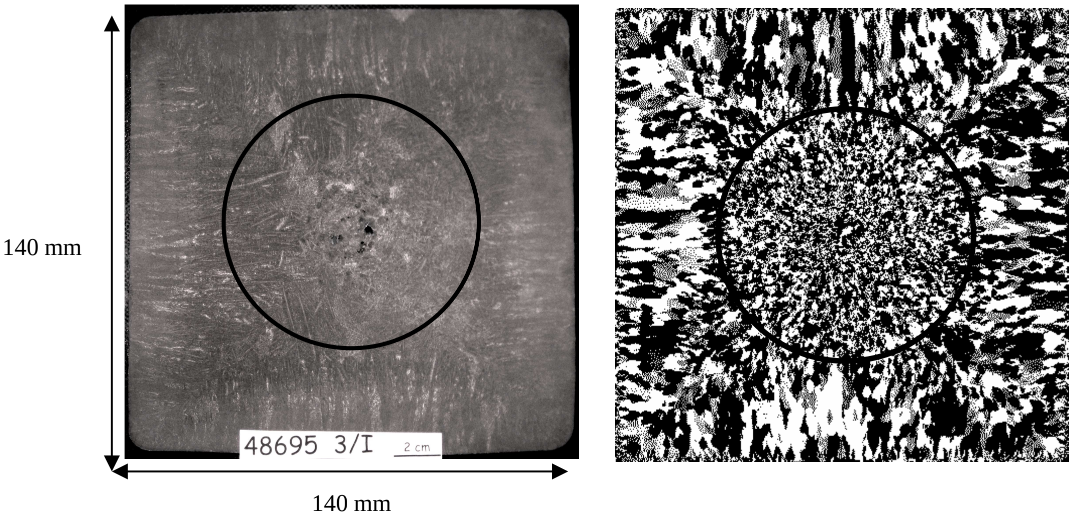

Figure A.7: Left: Baumann print, right: simulated result for steel 51CrV4+Mo, dimension 180 mm, $T_{cast} = 1524\,\mathrm{K}$ and $V_{cast} = 0.95\,\mathrm{m/min}$.

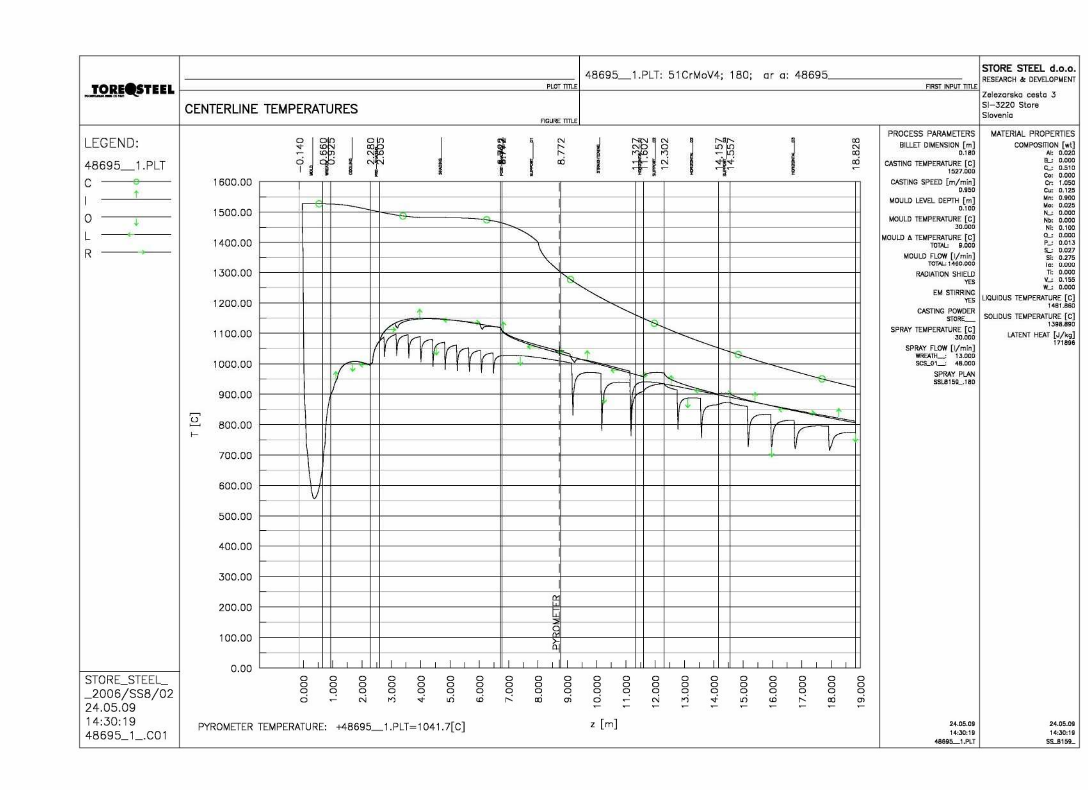

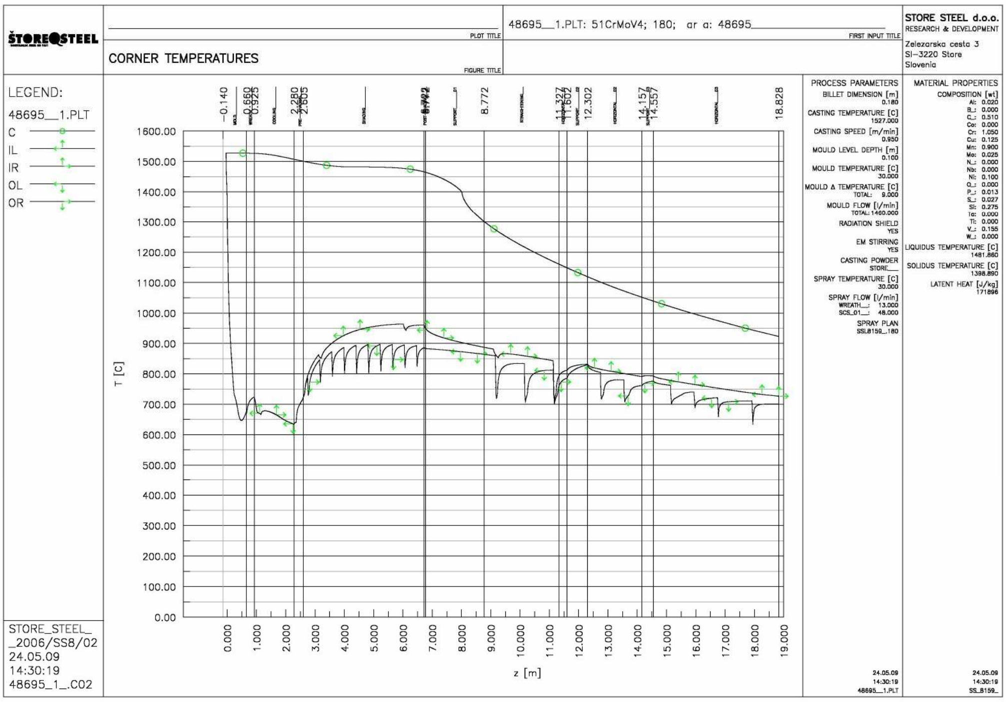

Figure A.8: Centerline and corner temperatures along the casting direction (heat of 48695 3/I).

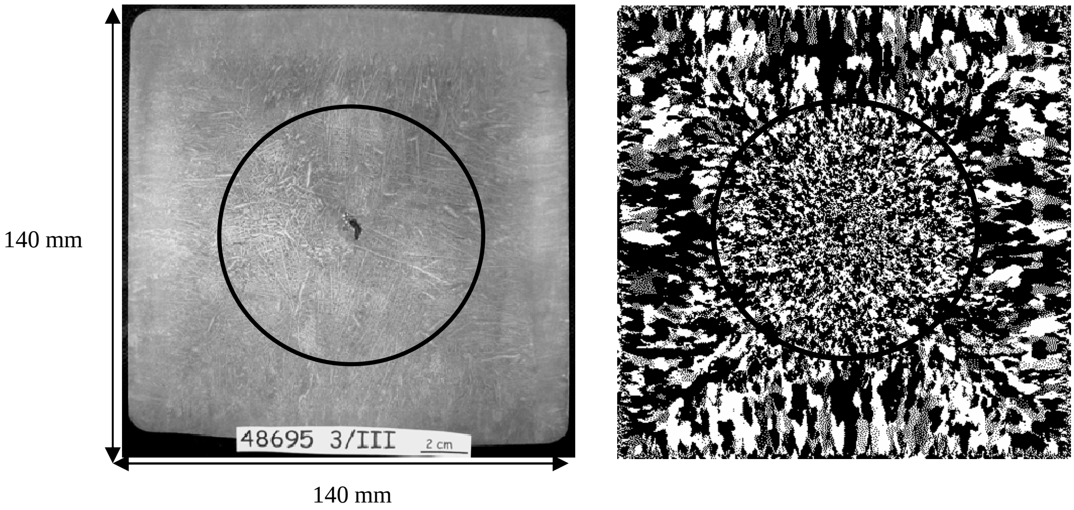

Figure A.9: Left: Baumann print, right: simulated result for steel 51CrV4+Mo, dimension 180 mm, T_{cast} = 1525 K and V_{cast} = 1.15 m/min.

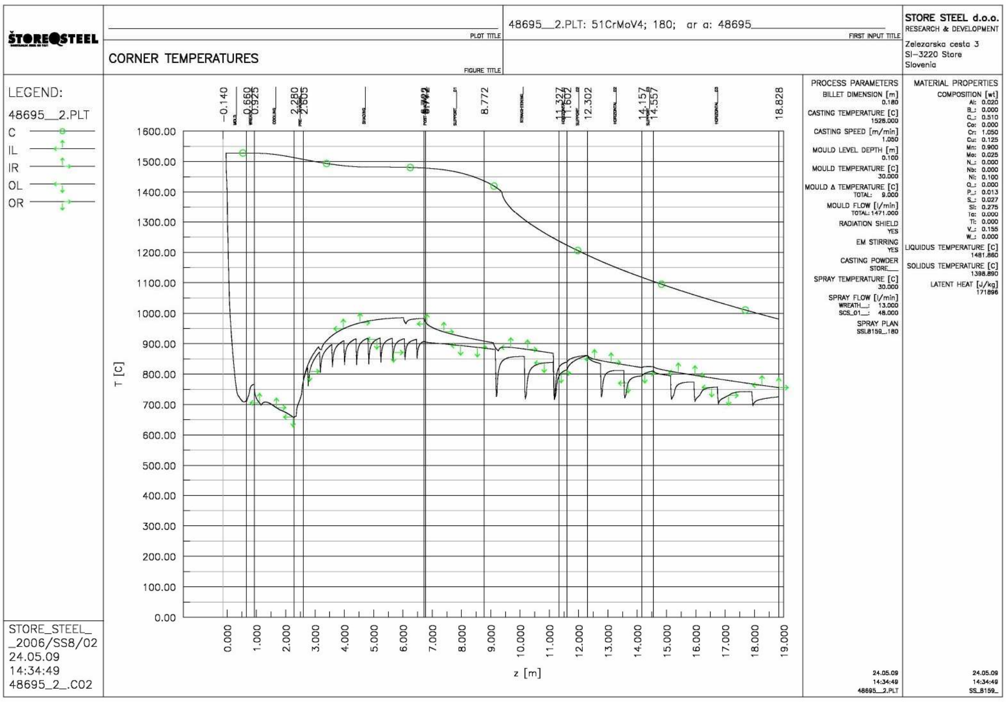

STORE STEEL d.o.o.
RESEARCH & DEVELOPMENT
Zelezarska cesta 3
SI–3220 Store
Slovenia

PROCESS PARAMETERS
BILLET DIMENSION [m] 0.180
CASTING TEMPERATURE [C] 1528.000
CASTING SPEED [m/min] 1.050
MOULD LEVEL DEPTH [m] 0.100
MOULD TEMPERATURE [C] 30.000
MOULD Δ TEMPERATURE [C] TOTAL: 9.000
MOULD FLOW [l/min] TOTAL: 1471.000
RADIATION SHIELD YES
EM STIRRING YES
CASTING POWDER STORE___
SPRAY TEMPERATURE [C] 30.000
SPRAY FLOW [l/min]
WREATH__: 13.000
SCS_01__: 48.000
SPRAY PLAN SSL8159_.180

MATERIAL PROPERTIES
COMPOSITION [wt]
Al: 0.020
B_: 0.000
C_: 0.510
Co: 0.000
Cr: 1.050
Cu: 0.125
Mn: 0.900
Mo: 0.025
N_: 0.000
Nb: 0.000
Ni: 0.100
O_: 0.000
P_: 0.013
S_: 0.027
Si: 0.275
Ta: 0.000
Ti: 0.000
V_: 0.155
W_: 0.000
LIQUIDUS TEMPERATURE [C] 1481.860
SOLIDUS TEMPERATURE [C] 1398.890
LATENT HEAT [J/kg] 171896

STORE_STEEL_
_2006/SS8/02
24.05.09
14:34:49
48695_2_.C02

24.05.09
14:34:49
48695__2.PLT

24.05.09
14:34:49
SS_8159_

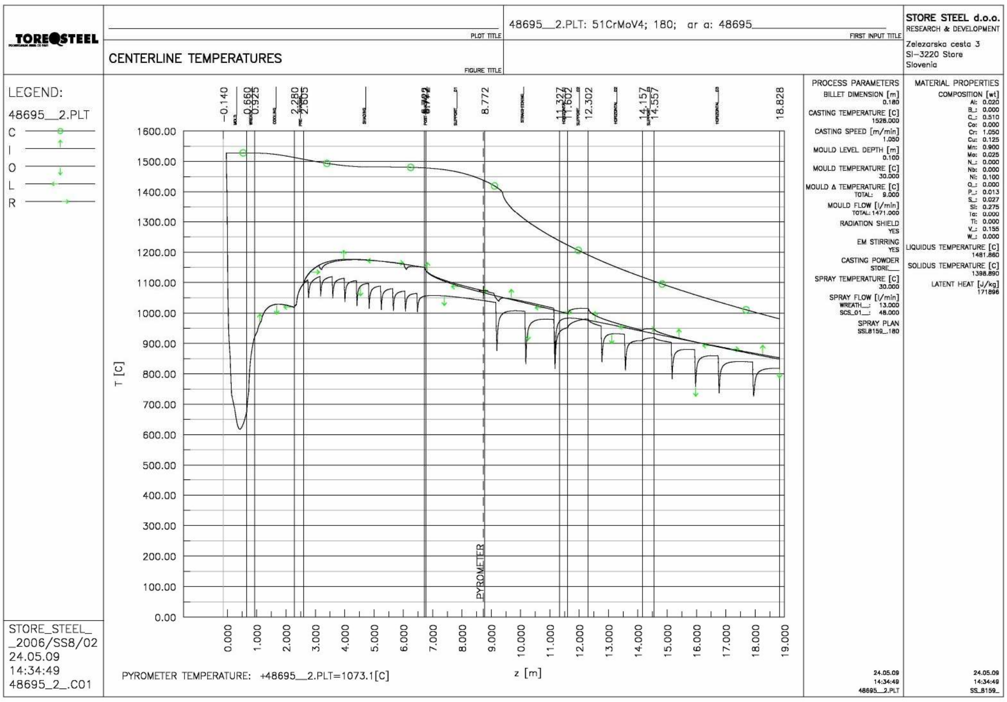

Figure A.10: Centerline and corner temperatures along the casting direction (heat 48695 3/III).

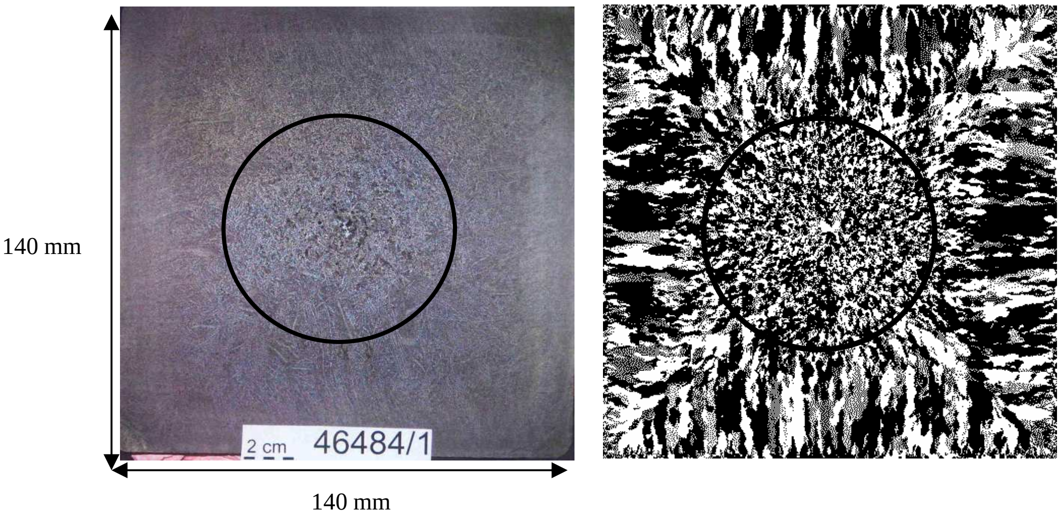

Figure A.11: Left: Baumann print, right: simulated result for steel 52CrMoV4o, dimension 180 mm, T_{cast} = 1522 K and V_{cast} = 1.05 m/min.

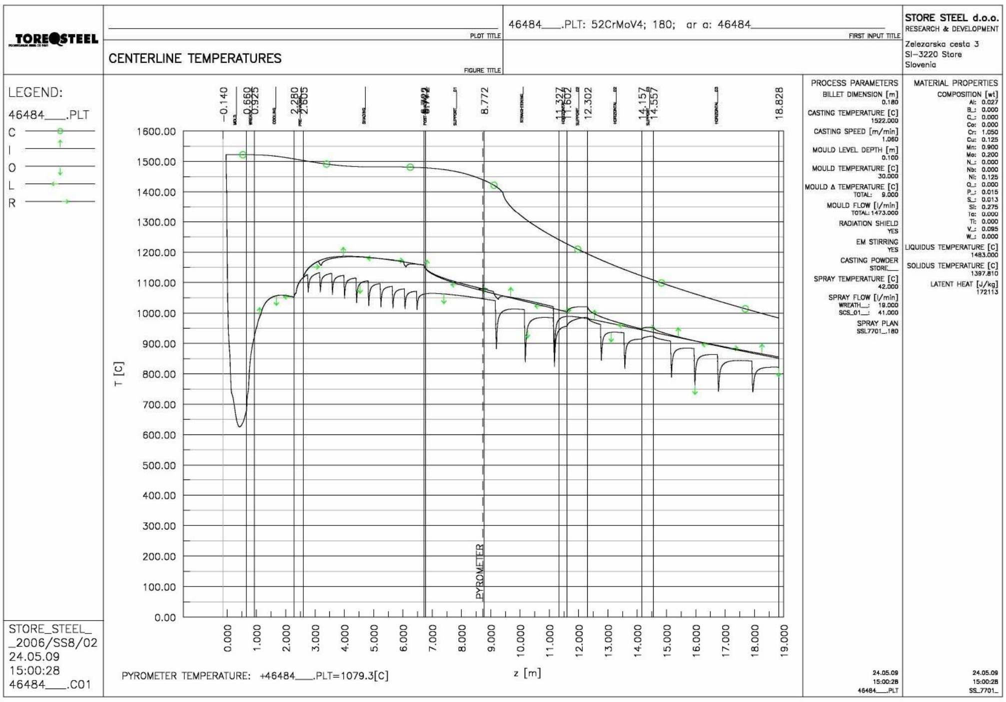

CENTERLINE TEMPERATURES

46484___.PLT: 52CrMoV4; 180; ar a: 46484___

STORE STEEL d.o.o.
RESEARCH & DEVELOPMENT
Zelezarska cesta 3
SI–3220 Store
Slovenia

46484___.PLT

PROCESS PARAMETERS
BILLET DIMENSION [m] 0.180
CASTING TEMPERATURE [C] 1522.000
CASTING SPEED [m/min] 1.060
MOULD LEVEL DEPTH [m] 0.100
MOULD TEMPERATURE [C] 30.000
MOULD Δ TEMPERATURE [C] TOTAL: 9.000
MOULD FLOW [l/min] TOTAL: 1473.000
RADIATION SHIELD YES
EM STIRRING YES
CASTING POWDER STORE___
SPRAY TEMPERATURE [C] 42.000
SPRAY FLOW [l/min]
WREATH__: 19.000
SCS_01__: 41.000
SPRAY PLAN SSL7701_.180

MATERIAL PROPERTIES
COMPOSITION [wt]
Al: 0.027
B_: 0.000
C_: 0.000
Co: 0.000
Cr: 1.050
Cu: 0.125
Mn: 0.900
Mo: 0.200
N_: 0.000
Nb: 0.000
Ni: 0.125
O_: 0.000
P_: 0.015
S_: 0.013
Si: 0.275
Ta: 0.000
Ti: 0.000
V_: 0.095
W_: 0.000
LIQUIDUS TEMPERATURE [C] 1483.000
SOLIDUS TEMPERATURE [C] 1397.810
LATENT HEAT [J/kg] 172113

STORE_STEEL_
_2006/SS8/02
24.05.09
15:00:28
46484___.C01

PYROMETER TEMPERATURE: +46484___.PLT=1079.3[C]

24.05.09
15:00:28
46484___.PLT

24.05.09
15:00:28
SS_7701_

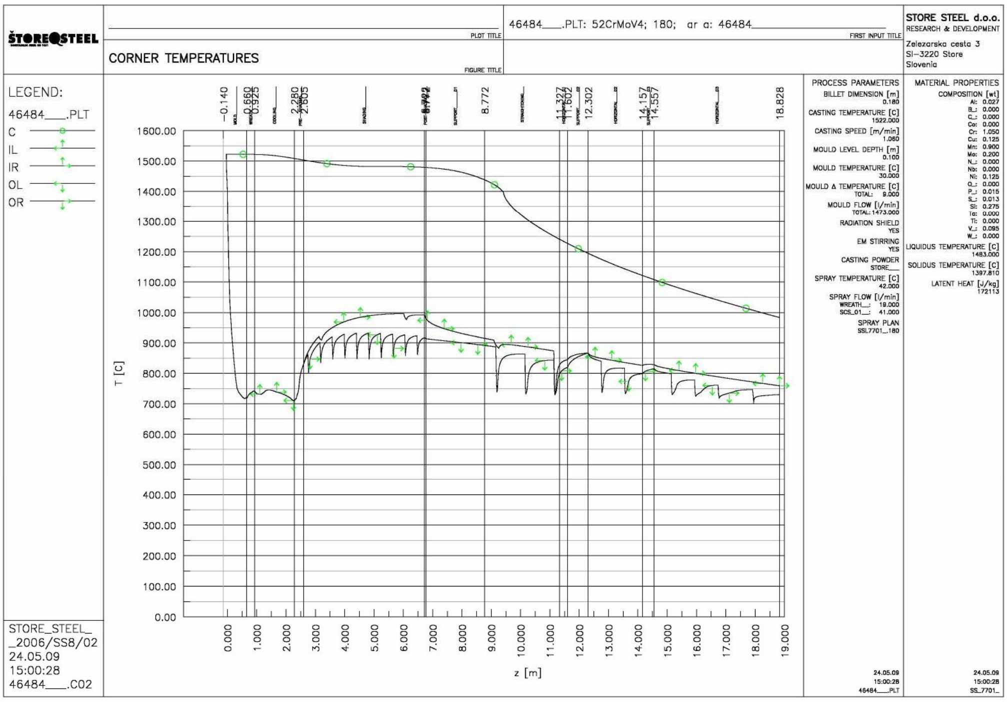

Figure A.12: Centerline and corner temperatures along the casting direction (heat 46484/1).

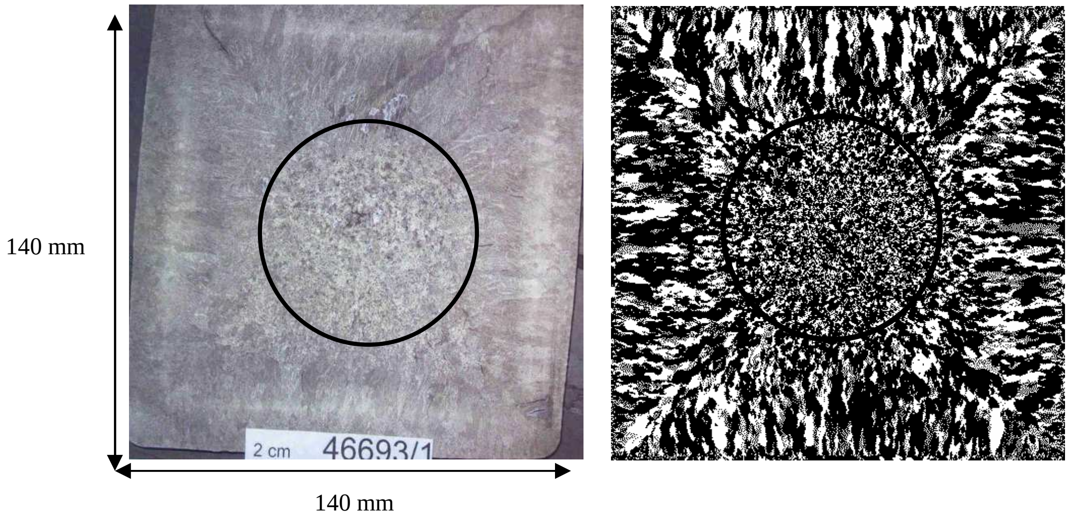

Figure A.13: Left: Baumann print, right: simulated result for steel 25MoCr4, dimension 180 mm, T_{cast} = 1545 K and V_{cast} = 1.12 m/min.

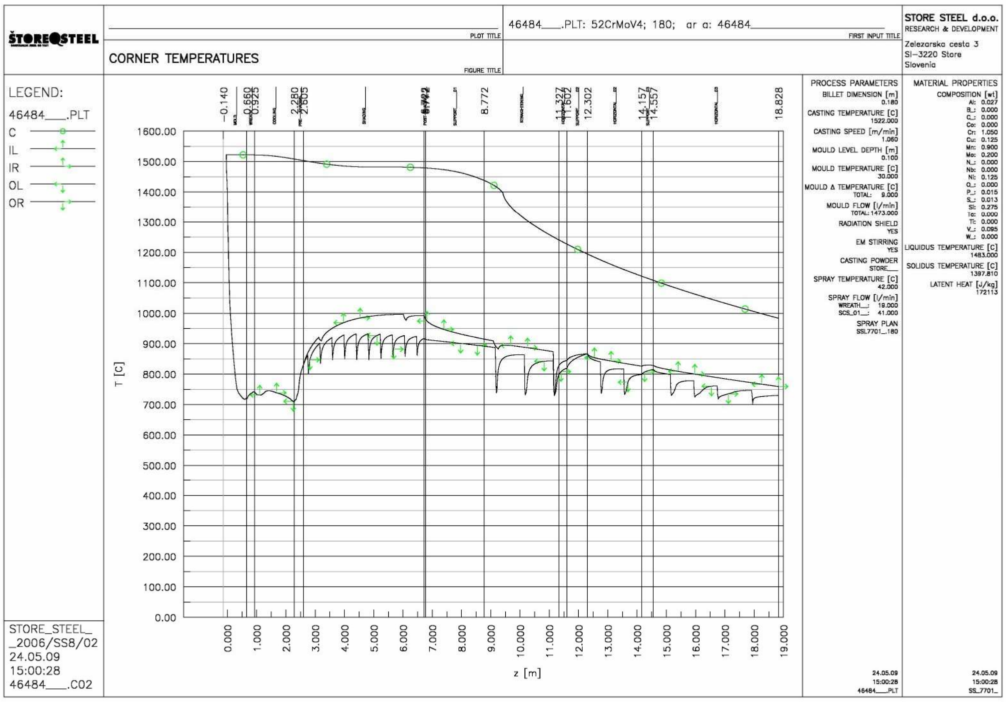

CORNER TEMPERATURES

46484___.PLT: 52CrMoV4; 180; ar a: 46484___

STORE STEEL d.o.o.
RESEARCH & DEVELOPMENT
Zelezarska cesta 3
SI-3220 Store
Slovenia

LEGEND:
46484___.PLT

PROCESS PARAMETERS
BILLET DIMENSION [m] 0.180
CASTING TEMPERATURE [C] 1522.000
CASTING SPEED [m/min] 1.060
MOULD LEVEL DEPTH [m] 0.100
MOULD TEMPERATURE [C] 30.000
MOULD Δ TEMPERATURE [C] TOTAL: 9.000
MOULD FLOW [l/min] TOTAL: 1473.000
RADIATION SHIELD YES
EM STIRRING YES
CASTING POWDER STORE___
SPRAY TEMPERATURE [C] 42.000
SPRAY FLOW [l/min]
WREATH__: 19.000
SCS_01__: 41.000
SPRAY PLAN SSL7701_.180

MATERIAL PROPERTIES
COMPOSITION [wt]
Al: 0.027
B_: 0.000
C_: 0.000
Co: 0.000
Cr: 1.050
Cu: 0.125
Mn: 0.900
Mo: 0.200
N_: 0.000
Nb: 0.000
Ni: 0.125
O_: 0.000
P_: 0.015
S_: 0.013
Si: 0.275
Ta: 0.000
Ti: 0.000
V_: 0.095
W_: 0.000
LIQUIDUS TEMPERATURE [C] 1483.000
SOLIDUS TEMPERATURE [C] 1397.810
LATENT HEAT [J/kg] 172113

STORE_STEEL_
_2006/SS8/02
24.05.09
15:00:28
46484___.C02

24.05.09
15:00:28
46484___.PLT

24.05.09
15:00:28
SSL7701_

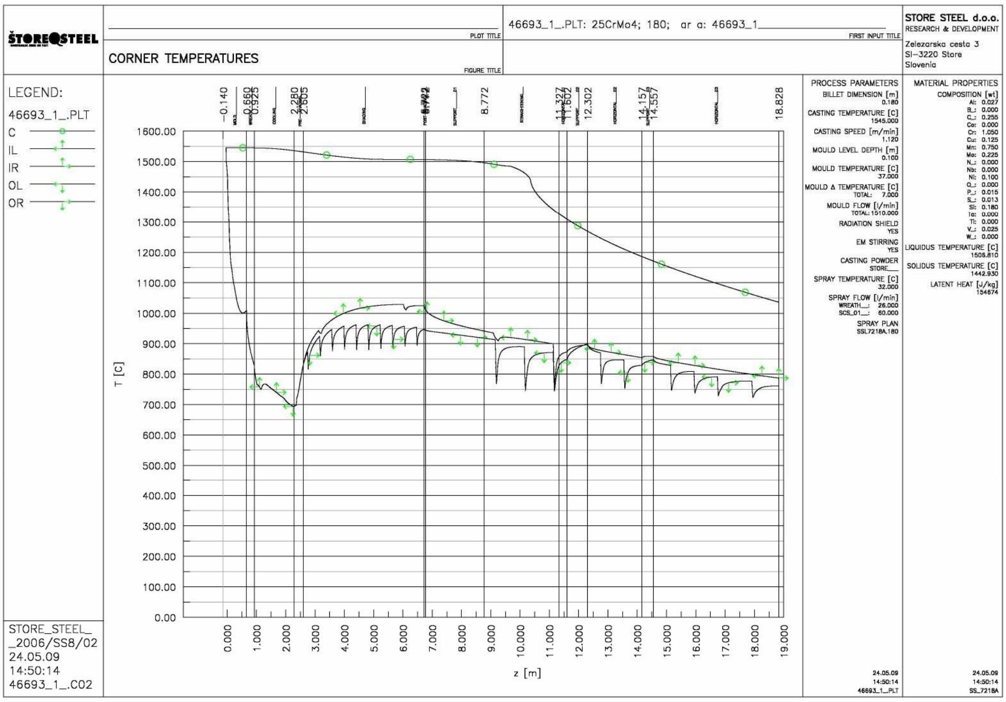

PLOT TITLE

46693_1_.PLT: 25CrMo4; 180; ar a: 46693_1

FIRST INPUT TITLE

CORNER TEMPERATURES

FIGURE TITLE

STORE STEEL d.o.o.
RESEARCH & DEVELOPMENT
Zelezarska cesta 3
SI–3220 Store
Slovenia

PROCESS PARAMETERS
BILLET DIMENSION [m] 0.180
CASTING TEMPERATURE [C] 1545.000
CASTING SPEED [m/min] 1.120
MOULD LEVEL DEPTH [m] 0.100
MOULD TEMPERATURE [C] 37.000
MOULD Δ TEMPERATURE [C] TOTAL: 7.000
MOULD FLOW [l/min] TOTAL: 1510.000
RADIATION SHIELD YES
EM STIRRING YES
CASTING POWDER STORE___
SPRAY TEMPERATURE [C] 32.000
SPRAY FLOW [l/min] WREATH__: 26.000
SCS_01__: 60.000
SPRAY PLAN SSL7218A.180

MATERIAL PROPERTIES
COMPOSITION [wt]
Al: 0.027
B_: 0.000
C_: 0.255
Co: 0.000
Cr: 1.050
Cu: 0.125
Mn: 0.750
Mo: 0.225
N_: 0.000
Nb: 0.000
Ni: 0.100
O_: 0.000
P_: 0.015
S_: 0.013
Si: 0.180
Ta: 0.000
Ti: 0.000
V_: 0.025
W_: 0.000
LIQUIDUS TEMPERATURE [C] 1506.810
SOLIDUS TEMPERATURE [C] 1442.930
LATENT HEAT [J/kg] 154674

STORE_STEEL_
_2006/SS8/02
24.05.09
14:50:14
46693_1_.C02

24.05.09
14:50:14
46693_1_.PLT

24.05.09
14:50:14
SS_7218A

Figure A.14: Centerline and corner temperatures along the casting direction (heat 46693/1).

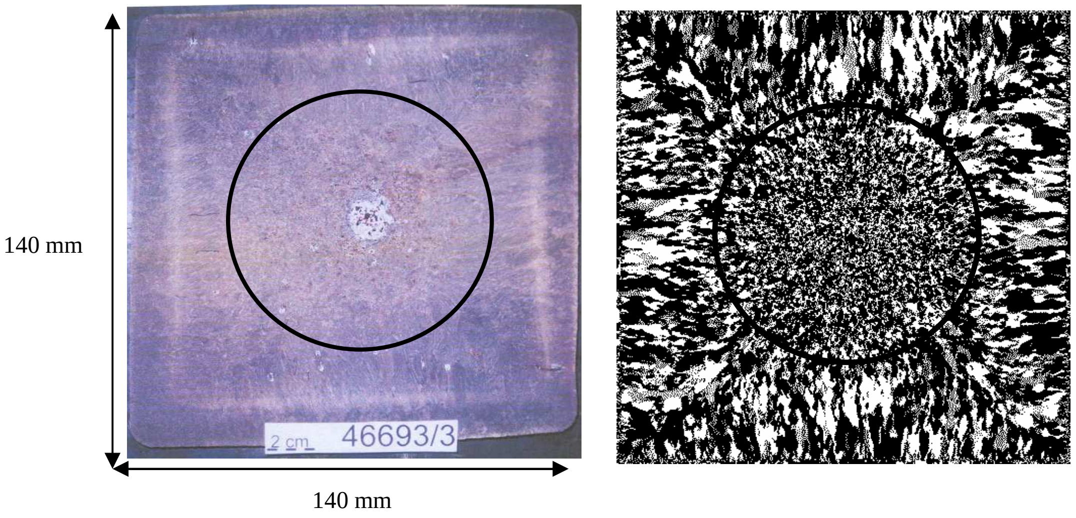

Figure A.15: Left: Baumann print, right: simulated result for steel 25MoCr4, dimension 180 mm, T_{cast} = 1550 K and V_{cast} = 1.12 m/min.

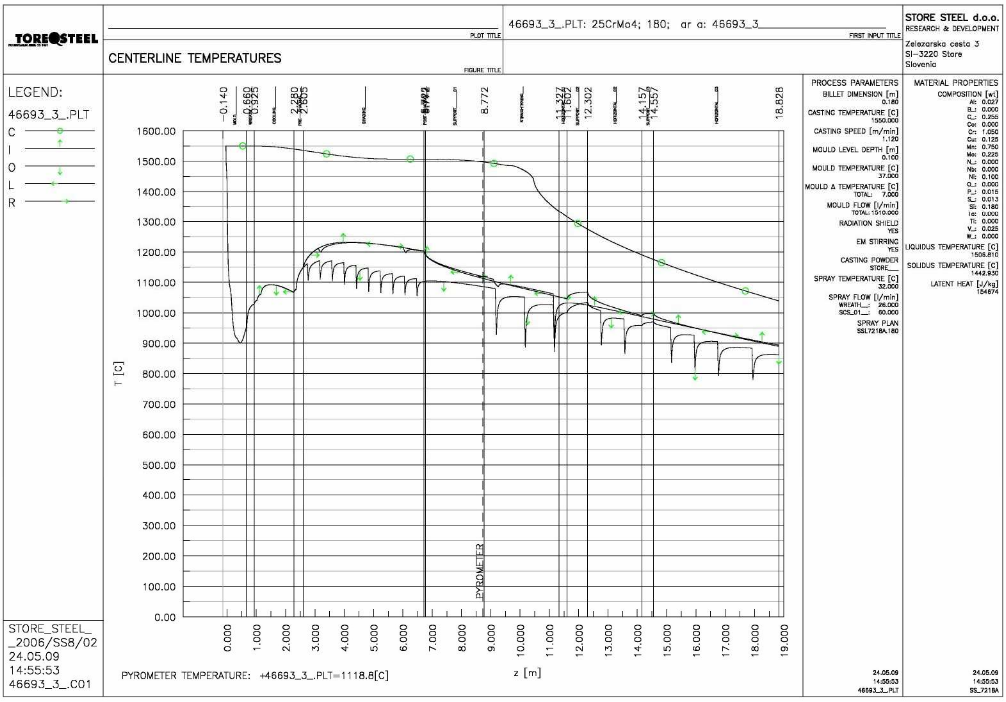

STORE STEEL d.o.o.
RESEARCH & DEVELOPMENT
Zelezarska cesta 3
SI–3220 Store
Slovenia

PROCESS PARAMETERS
BILLET DIMENSION [m] 0.180
CASTING TEMPERATURE [C] 1550.000
CASTING SPEED [m/min] 1.120
MOULD LEVEL DEPTH [m] 0.100
MOULD TEMPERATURE [C] 37.000
MOULD Δ TEMPERATURE [C] TOTAL: 7.000
MOULD FLOW [l/min] TOTAL: 1510.000
RADIATION SHIELD YES
EM STIRRING YES
CASTING POWDER STORE___
SPRAY TEMPERATURE [C] 32.000
SPRAY FLOW [l/min]
WREATH__: 26.000
SCS_01__: 60.000
SPRAY PLAN SSL7218A.180

MATERIAL PROPERTIES
COMPOSITION [wt]
Al: 0.027
B_: 0.000
C_: 0.255
Co: 0.000
Cr: 1.050
Cu: 0.125
Mn: 0.750
Mo: 0.225
N_: 0.000
Nb: 0.000
Ni: 0.100
O_: 0.000
P_: 0.015
S_: 0.013
Si: 0.180
Ta: 0.000
Ti: 0.000
V_: 0.025
W_: 0.000
LIQUIDUS TEMPERATURE [C] 1506.810
SOLIDUS TEMPERATURE [C] 1442.930
LATENT HEAT [J/kg] 154674

STORE_STEEL_
_2006/SS8/02
24.05.09
14:55:53
46693_3_.C01

PYROMETER TEMPERATURE: +46693_3_.PLT=1118.8[C]

24.05.09
14:55:53
46693_3_.PLT

24.05.09
14:55:53
SS_7218A

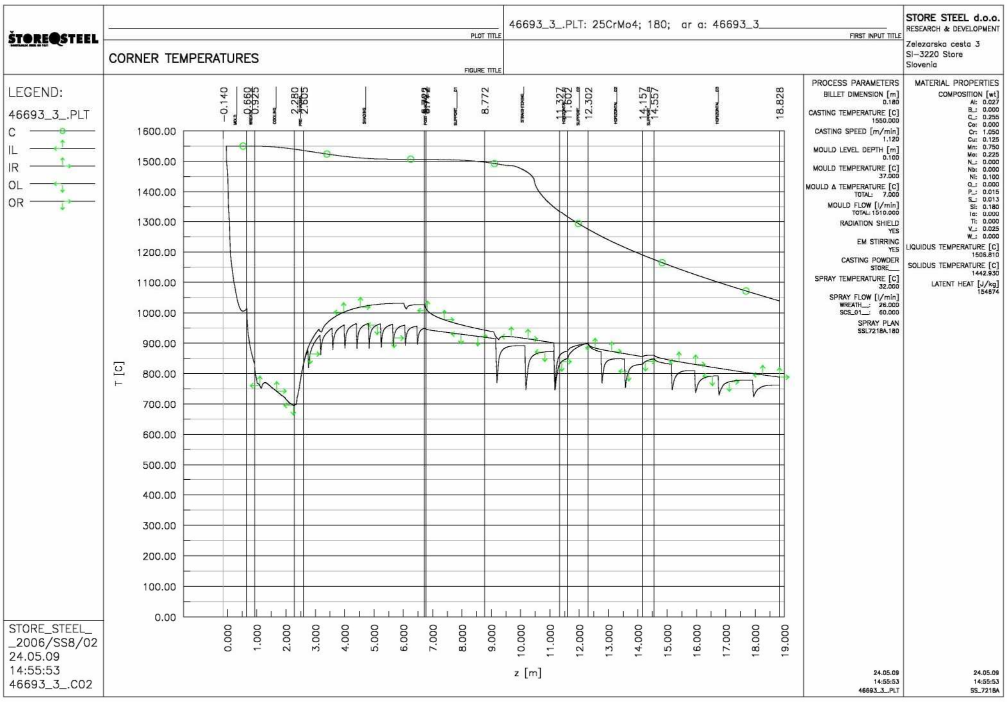

Figure A.16: Centerline and corner temperatures along the casting direction (heat 46693/3).

Influance of EMS on the final microstructure (report Štore, 19.12.2008)

Figure A.17: Baumann print for steel 51CrV4, dimension 180 mm, with EMS**.**

Figure A.18: Baumann pront for steel 51CrV4, dimension 180 mm, without EMS.

A.2 Meshless Solution Procedure of the Macroscopic Heat Transfer Model

The solution procedure follows developments in publications [Šarler and Vertnik, 2006] and [Lorbiecka *et al.*, 2009] We seek for mixture temperature at time $t_0 + \Delta t$ by assuming known initial temperature, velocity field, and boundary conditions at time t_0. The initial value of the temperature $T(\mathbf{p},t)$ at a point with position vector $\mathbf{p}$ and time t_0 is de fined through the known function T_0

$$T(\mathbf{p},t) = T_0(\mathbf{p});\ \mathbf{p} \in \Omega + \partial\Omega. \tag{A1}$$

The boundary $\partial\Omega$ is divided into not necessarily connected parts $\partial\Omega = \partial\Omega^D \cup \partial\Omega^N \cup \partial\Omega^R$ with Dirichlet, Neumann and Robin type boundary conditions, respectively. At the boundary point $\mathbf{p}$ with normal $\mathbf{n}_{\partial\Omega}$ and time $t_0 \le t \le t_0 + \Delta t$, these boundary conditions are defined through known functions $T_{\partial\Omega}^D$, $T_{\partial\Omega}^N$, $T_{\partial\Omega}^R$, $T_{\partial\Omega ref}^R$

$$T = T_{\partial\Omega}^D;\ \mathbf{p} \in \partial\Omega^D, \tag{A2}$$

$$\frac{\partial}{\partial n_\Gamma} T = T_{\partial\Omega}^N;\ \mathbf{p} \in \partial\Omega^N, \tag{A3}$$

$$\frac{\partial}{\partial n_\Gamma} T = T_{\partial\Omega}^R\left(T - T_{\Gamma ref}^R\right);\ \mathbf{p} \in \partial\Omega^R, \tag{A4}$$

The numerical discretization of equation (A1), using explicit (Euler) time discretization has the form

$$\frac{\partial(\rho h)}{\partial t} \approx \frac{\rho h - \rho_0 h_0}{\Delta t} = \nabla \cdot \left(\lambda_0 \nabla T_0\right) \tag{A5}$$

From equation (A1) the unknown function value h_l in domain node $\mathbf{p}_l$ can be calculated as

$$h_l = h_{0l} + \frac{\Delta t}{\rho_0 c_0}\left(\nabla\lambda_{0l} \cdot \nabla T_{0l} + k_{0l} \cdot \nabla^2 T_{0l}\right), \tag{A6}$$

The spatial derivatives in equation (A5) are approximated by the LRBFCM. In the LRBFCM, the representation of unknown function value over a set of ${}_lN$ (in general) non-equally spaced nodes ${}_l\mathbf{p}_n;\ n = 1, 2, ..., {}_lN$ is made in the following way

$$\phi(\mathbf{p}) \approx \sum_{k=1}^{{}_lK} {}_l\psi_k(\mathbf{p})\, {}_l\alpha_k, \tag{A7}$$

where ${}_l\psi_k$ stands for the shape functions, ${}_l\alpha_k$ for the coefficients of the shape functions, and ${}_lK$ represents the number of the shape functions. The left lower index on entries of equation (4.18) represents the influence domain (subdomain or support) ${}_l\omega$ on which the coefficients ${}_l\alpha_k$ are determined. The influence domains ${}_l\omega$ can in general be contiguous (overlapping) or non-contiguous (non-overlapping). Each of the influence domains ${}_l\omega$ includes ${}_lN$ nodes of which ${}_lN_\Omega$ can in general be in the domain and ${}_lN_\Gamma$ on the boundary, i.e. ${}_lN = {}_lN_\Omega + {}_lN_{\partial\Omega}$. The total number of all nodes $\mathbf{p}_n$ is equal $N = N_\Omega + N_{\partial\Omega}$ of which N_Γ are located on the boundary and N_Ω are located in the domain. The influence domain of the node ${}_l\mathbf{p}$ is defined with the nodes having the nearest ${}_lN - 1$ distances to the node ${}_l\mathbf{p}$. The five nodded ${}_lN = 5$ influence domains are used in this paper. The coefficients are calculated by the collocation (interpolation).

Let us assume the known function values ${}_l\phi_n$ in the nodes ${}_l\mathbf{p}_n$ of the influence domain ${}_l\omega$. The collocation implies

$$\phi({}_l\mathbf{p}_n) = \sum_{k=1}^{{}_lN} {}_l\psi_k({}_l\mathbf{p}_n)\, {}_l\alpha_k. \tag{A8}$$

For the coefficients to be computable, the number of the shape functions has to match the number of the collocation points ${}_lK = {}_lN$, and the collocation matrix has to be non-singular. The system of equation (4.19) can be written in a matrix-vector notation

$$ {}_l\underline{\boldsymbol{\psi}}\, {}_l\boldsymbol{\alpha} = {}_l\boldsymbol{\Phi};\ {}_l\underline{\psi}_{kn} = {}_l\psi_k({}_l\mathbf{p}_n),\ {}_l\phi_n = \phi({}_l\mathbf{p}_n). \tag{A9}$$

The coefficients ${}_l\boldsymbol{\alpha}$ can be computed by inverting the system

$$ {}_l\boldsymbol{\alpha} = {}_l\underline{\boldsymbol{\psi}}^{-1}\, {}_l\boldsymbol{\Phi}. \tag{A10}$$

By taking into account the expressions for the calculation of the coefficients ${}_l\boldsymbol{\alpha}$, the collocation representation of temperature $\phi(\mathbf{p})$ on subdomain ${}_l\omega$ can be expressed as

$$\phi(\mathbf{p}) \approx \sum_{k=1}^{{}_lN} {}_l\psi_k(\mathbf{p}) \sum_{n=1}^{{}_lN} {}_l\underline{\Psi}_{\mathrm{kn}}^{-1}\, {}_l\phi_n . \tag{A11}$$

The first partial spatial derivatives of $\phi(\mathbf{p})$ on subdomain ${}_l\omega$ can be expressed as

$$\frac{\partial}{\partial p_\varsigma}\phi(\mathbf{p}) \approx \sum_{k=1}^{{}_lN} \frac{\partial}{\partial p_\varsigma} {}_l\psi_k(\mathbf{p}) \sum_{n=1}^{{}_lN} {}_l\underline{\Psi}_{\mathrm{kn}}^{-1}\, {}_l\phi_n ;\ \varsigma = x, y . \tag{A12}$$

The second partial spatial derivatives of $\phi(\mathbf{p})$ on subdomain ${}_l\omega$ can be expressed as

$$\begin{gathered}\frac{\partial^2}{\partial p_\varsigma p_\xi}\phi(\mathbf{p}) \approx \sum_{k=1}^{{}_lN} \frac{\partial^2}{\partial p_\varsigma p_\xi} {}_l\psi_k(\mathbf{p}) \sum_{n=1}^{{}_lN} {}_l\underline{\Psi}_{\mathrm{kn}}^{-1}\, {}_l\phi_n ; \\ \varsigma, \xi = x, y.\end{gathered} \tag{A13}$$

The radial basis functions, such as multiquadrics, can be used for the shape functions

$${}_l\psi_k(\mathbf{p}) = \left[{}_lr_k^2(\mathbf{p}) + c^2 \right]^{1/2}, \tag{A14}$$

where c represents the shape parameter. The explicit values of the involved first and second derivatives of $\psi_k(\mathbf{p})$ are

$$\frac{\partial}{\partial p_\varsigma} {}_l\psi_k(\mathbf{p}) = \frac{p_\varsigma - {}_lp_{k\varsigma}}{\left({}_lr_k^2 + c^2 \right)^{1/2}}, \varsigma = x, y, \tag{A15}$$

$$\frac{\partial^2}{\partial p_\varsigma^2} {}_l\psi_k(\mathbf{p}) = \frac{{}_lr_k^2 - \left(p_\varsigma - {}_lp_{k\varsigma} \right)^2 + c^2}{\left({}_lr_k^2 + c^2 \right)^{3/2}}, \varsigma = x, y, \tag{A16}$$

Bibliography

Anderson, M.P., Srolovitz, D.J., Grest, G.S. and Sahni, P.S. (1984). Computer simulation of grain growth - I part. Kinetics. *Acta Metallurgica*, 32:783-792.

Anderson, M.P., Srolovitz, D.J., Grest, G.S. and Sahni, P.S. (1984). Computer simulation of grain growth - II part. Grain size distribution, topology and local dynamics. *Acta Metallurgica*, 32:793-801.

Asta, M.D., Beckermann, C., Karma, A., Kurz, W., Napolitano, R., Plapp, M., Purdy, G., Rappaz, M. and Trivedi, R. (2009). Solidification microstructures and solid-state parallels: recent developments, future directions. *Acta Materialia*, 57:941-71.

Atamanenko, T.V., Eskin, D.G. and Katgerman, L. (2007). Experimental study of grain growth in aluminium melts under the influence of ultrasonic melt treatment. *Material Science Forum*, 561-565:987-990.

Atluri, S.N. (2004). *The Meshless Method (MLPG) for Domain and BIE Discretization*. Tech Science Press, Forsyth.

Atwood, R.C. and Lee, P.D. (2003). Simulation of the three dimensional morphology of solidification porosity in an aluminum-silicon alloy. *Acta Materialia*, 51:5447-5466.

Beckermann, C. (2002). Modelling of microsegregation: Applications and future needs. *International Materials Reviews*, 47:243-261.

Beltran-Sanchez, L. and Stefanescu, D.M. (2003). Growth of solutal dendrites: a cellular automaton model and its quantitative capabilities. *Metallurgical and Materials Transactions,* A34:367-382.

Bennon, W. D. and Incropera, F. P. (1987). A continuum model for momentum, heat and species transport in binary solid-liquid phase change systems - I. Model formulation. *International Journal of Heat and Mass Transfer,* 30:2161-2170.

Boettinger, W.J., Coriell, S.R., Greer, A.L., Karma, A., Kurz, A., Rappaz, M. and Trivedi, R. (2000). Solidification microstructure recent developments, future directions. *Acta Metallurgica*, 48:43-70.

Brown, S.G.R. (1998). Simulation of diffusional composite growth using the cellular automata finite difference (CAFD) method. *Journal of Materials Science*, 33:4769-4773.

Brown, S.G.R., Williams, T. and Spittle, J.A. (1994). A cellular automation model of the steady-state “free” growth of a non-isothermal dendrite. *Acta Metallurgica,* 42:2893-2898.

Bruncko, M. and Anzel, I. and Krizman, A. (2003). Monitoring of directional solidification with simultaneous measurements of electrical resistance and temperature. *Materials Characterization*, 51: 185-199.

Chen, L.Q. (2002). Phase-field models for microstructure evolution. *Annual Review of Materials Research*, 32:113-140.

Chen, L.Q., Wolverton, C., Vaithyanathan, V. and Liu, Z. (2001). Modelling solid-state phase transformations and microstructure evolution. *Materials Research Society Bulletin,*26:197-202.

Cho, S. and Hong, C.P. (1997). Modelling of microstructure evolution in squeeze casting of an Al-4.5 mass% C Alloy. *ISIJ International*, 37:1098-1106.

Chorin, A.J. (1973). Numerical study of slightly viscous flow. *Journal of Fluid Mechanics*, 57:785-796.

Daming, L., Ruo, L. and Zhang, P. (2004). A new coupled model for alloy solidification. *In China Series A-Mathematics*, 47:41-52.

Dantzig, J.A. and Rappaz, M. (2009). *Solidification*. EPEL Press, Switzerland.

Ding, R. and Guo, Z.X. (2001). Coupled quantitative simulation of microstructure evolution and plastic flow during dynamic recrystallization. *Acta Materialia.*, 49:3163-3175.

Dong, H.B. and Lee, P.D. (2005). Simulation of the columnar to equiaxed transitions in directionally solidified Al-Cu alloys. *Acta Materialia*, 53:659-668.

Durrand-Charre, M. (2004). *Microstructure of Steels and Cast Irons*. Springer Editor, New York.

Fan, D. and Chen, L.Q. (1997). Computer simulation of grain growth using a continuum field model. *Acta Materialia*, 45:611-622.

Feng, W., Xu, Q. and Liu, B. (2002). Microstructure simulation of aluminium alloy using parallel computing technique. *ISIJ International*, 42:702-707.

Flache, A. and Hegselmann, R. (2001). Do irregular grids make a difference? Relaxing the spatial regularity assumption in cellular models of social dynamics. *Journal of Artificial Societies and Social Simulation*, vol.4.

Flemings, M.C. (1974). *Solidification Processing*. McGraw-Hill Press, New York.

Flood, C.S. and Hunt, J.D. (1987). A model of a casting. *Applied Scientific Research,* 44:27-42.

Flood, C.S. and Hunt, J.D. (1987). Columnar and equiaxed growth. Equiaxed growth ahead of columnar front. *Journal of Crystal Growth,* 82:552-560.

Flood, C.S. and Hunt, J.D. (1987). Columnar and equiaxed growth. I. A model of a columnar front with temperature dependent velocity. *Journal of Crystal Growth,* 82:543-551.

Fredriksson, H. and Akerlind, U. (2010). *Materials Processing During Casting.* John Wiley & Sons Ltd Press, West Sussex, England.

Fullman, R.L. (1952). Metal interface. *American Society for Metals*, 179-259

Gandin, Ch.A. (2000). From constrained to unconstrained growth during directional solidification. *Acta Materialia,* 48:2483-2501.

Gandin, Ch.A. (2000). Experimental study of the transition from constrained to unconstrained growth during directional solidification. *ISIJ International,* 40:971-979.

Gandin, Ch.A. (2001). Stochastic modelling of dendritic grain structures. *Materials Science and Technology*, 17:786-789.

Gandin, Ch.A., Charbon, Ch. and Rappaz, M. (1995). Stochastic modelling of solidification grain structures. *ISIJ International*, 35:651-657.

Gandin, Ch.A., Desbiolles, M., Rappaz, M. and Thevoz, Ph. (1999). A three-dimensional cellular automaton-finite element model for the prediction of solidification grain structures. *Metallurgical and Materials Transactions*, A30:3153-3165.

Gandin, Ch.A. and Rappaz, M. (1994). A coupled finite element-cellular automata model for the prediction of dendritic grain structures in solidification processes. *Acta Metallurgica*, 42:2233-2246.

Gandin, Ch.A. and Rappaz, M. (1997). A 3D cellular automata algorithm for the prediction of dendritic grain growth *Acta Metallurgica*, 45:2187-2195.

Gandin, Ch.A., Schaefer, R.J. and Rappaz, M. (1996). Analytical and numerical prediction of dendritic grain envelopes. *Acta Materialia*, 44:3339-3347.

Gibbs, J.W. (1928). On the equilibrium of heterogeneous substances, in *The collected works of J. W. Gibbs*, New York: Longmans, pp. 55-353.

Goettsch, D.D. and Dantzig, J.A. (1990). Modelling microstructure development in gray iron castings. In: M. Rappaz, M.R. Ozgu and K.W. Mahin (ed), *International Conference on Modelling of Casting, Welding and Advanced Solidification Processes V*, Minerals, Metals and Materials Society, Warrendale, 377-385.

Gosalvez, M.A., Xing, Y., Sato, K. and Nieminen, R.M. (2008). Atomistic methods for the simulation of evolving surfaces. *Journal of Micromechanics and Microengineering*, 18:1-17.

Haghighat, S.M.H. and Taheri, A.K. (2007). An analytical and experimental investigation on the normal grain growth in metals using monte carlo method. *Materials & Design*, 28:2533-2539.

Hesselbarth, H.W. and Gobel, I.R. (1991). Simulation of recrystallization by cellular automata. *Acta Metallurgica*, 39:2135-2144.

Humphreys, F.J. and Hatherly, M. (1996). *Recrystallization and related annealing phenomena*. Elsevier Science Press, Oxford, UK.

Hunt, J.D. (1979). *Solidification and Casting of Metals*. The Metal Society Press, London.

Hunt, J.D. (1984). Steady state columnar and equiaxed growth of dendrites and eutectic. *Materials Science and Engineering,* 65:75-83.

Hurley, P.J. and Humphreys, F.J. (2003). Modelling the recrystallization of single-phase aluminium. *Acta Materialia,* 51:3779-3793.

Ivantsov, G.P. (1947). Dokl. Akad. Nauk. SSR, 58:567-569.

Janssens, K.G.F. (2000). *Irregular Cellular Automata Modelling of Grain Growth.* Continuum Scale Simulation of Engineering Materials, Germany.

Janssens, K.G.F. (2003). Three dimensional, space-time coupled cellular automata for the simulation of recrystallization and grain growth. *Modelling and Simulation in Materials Science and Engineering*, 11:157-171.

Janssens, K.G.F. (2010). An introductory review of cellular automata modelling of moving grain boundaries in polycrystalline materials. *Mathematics and Computers in Simulations,* 80:1361-1381.

Janssens, K.G.F, Holm, E.A. and Foiles, S.M. (2004). Introducing solute drag in irregular cellular automata modelling of grain growth. In: Proceedings of the 2nd International Conference on Recrystallization and Grain Growth, Annecy, Recrystallization and Grain Growth, *Trans Tech Publications*, 2:1045-1050.

Janssens, K.G.F., Olmsted, D., Holm, E.A., Foiles, S.M, Plimpton, S.J and Derlet, P.M. (2006). Computing the mobility of grain boundaries. *Nature Materials*, 5:124-127.

Janssens, K.G.H., Raabe, D., Kozeschnik, E., Miodownik, M.A. and Nestler, B. (2007). *Computational Materials Engineering*. Elsevier Academic Press, Great Britain.

Jarvis, D.J., Brown, S,G.R. and Spittle, J.A. (2000). Modelling of non-equilibrium solidification in ternary alloys: comparison of 1D, 2D, and 3D cellular automata-finite difference simulations. *Materials Science and Technology*, 16:1420-1424.

Kammer, K. (1999). *Aluminium Handbook 1.* Aluminium-Verlag Marketing & Kommunikation GmbH.

Kawasaki, K., Nagai, T. and Nakashima, K. (1989). Vertex models for two-dimensional grain growth. *Philosophical Magazine B*, 60:399-421.

Krane, M.J.M., Johnson, D.R. and Raghavan, S. (2009). The development of a cellular automata-finite volume model for dendritic growth. *Applied Mathematical Modelling*, 33:2234-2247.

Kroc, J. (2002). Applicataion of cellular automata simulations to modelling of dynamic recrystallization. In: Sloot, P.M.a, Hoekstra, A.G., Kenneth Tan, C.J. and Dongarra, J.J., editors, *Computational Science-ICCS 2002*, International Conference, Springer-Verlag Press, The Netherlands, 773-782.

Kugler, G. and Turk, R. (2006). Study of the influence of initial microstructure topology on the kinetics of static recrystallization using a cellular automata model. *Computational Materials Science*, 37:284-291.

Kumar, M.R., Sasikumar, R. and Kesavan, P. (1998). Competition between nucleation and early growth of ferrite from austenite-studies using cellular automation simulations. *Acta Materialia*, 46:6291-6303.

Kurz, W., Bezencon, M. and Gaumann, M. (2001). Columnar to equiaxed transition in solidification processing. *Science and Technology of Advanced Materials*, 2:185-191.

Kurz, W. and Fisher, D.J. (1981). Dendrite growth at the limit of stability: tip radius and spacing. *Acta Metallurgica*, 29:11-20.

Kurz, W. and Fisher, D.J. (1998). *Fundamentals of Solidification*. Trans Tech Publications Ltd, Zurich.

Kurz, W., Giovanola, B. and Trivedi, R. (1986). Theory of microstructural development during rapid solidification. *Acta Metallurgica*, 34:823-830.

Langer, J. and Muller-Krumbhaar, H. (1987). Theory of dendritic growth-III. Effects of surface tension. *Acta Metallurgica*, 26:1697-1708.

Lee, K.Y. and Hong, C.P. (1997). Stochastic modelling of solidification grain structure of Al-Cu crystalline ribbons in planar flow casting. *ISIJ International*, 37:38-46.

Lipton, J., Glicksman, M.E. and Kurz, W. (1987a). Equiaxed dendritic growth in alloy at small supercooling. *Metallurgical and Materials Transactions*, A18:341-345.

Lipton, J., Kurz, W. and Trivedi, R. K. (1987b). Rapid dendrite growth in undercooled melts. *Acta Metallurgica*, 35:957-964.

Liu, G.R. and Gu, Y.T. (2005). *An Introduction to Meshfree Methods and Their Programming*. Springer Press, Dordrecht.

Lorbiecka, A.Z., Vertnik, R., Gjerkeš, H., Manojlović, G., Senčič B., Cesar, J. and Šarler, B. (2009). Numerical modelling of grain structure in continuous casting of steel. *CMC: Computers, Materials & Continua*, 8:195-208.

Lorbiecka, A.Z. and Šarler, B. (2009). Point automata method for prediction of grain structure in the continuous casting of steel. In: L. Andreas (ed), *3nd International Conference of Simulation and Modelling of Metallurgical Processes in Steelmaking, Steelsim 2009,* ASMET, Leoben, Austria, 192-197.

Lorbiecka, A.Z. and Šarler, B. (2009). Modelling grain growth processes by the conventional cellular automata and new point automata method. In: G. Tsatsaronis and A. Boyano (ed) *International Conference of Optimization Using Exergy-based Methods and Computational Fluid Dynamics*, Berlin, Germany, 243-252.

Lorbiecka, A.Z. and Šarler, B. (2009). Meshless point automata method for simulation of dendritic growth. In: A.N. Atluri and B.Šarler (ed), *5th ICCES International Symposium on Meshless and Another Novel Computational Methods,* University of Nova Gorica, Bistra, Slovenia.

Lorbiecka, A.Z. and Šarler, B. (2010a). A sensitivity study of grain growth Model for prediction of ECT and CET transformations in continuous casting of steel. *Materials Science Forum,* 649:373-378.

Lorbiecka, A.Z. and Šarler, B. (2010b). Simulation of dendritic growth with different orientation by using the point automata method. *CMC: Computers, Materials & Continua*, 18:69-104.

Lorbiecka, A.Z. and Šarler, B. (2010c). *Cellular Automata*. Point automata method for dendritic growth, in print.
Louhenkilpi, S. (1995). *Simulation and control of heat transfer in continuous casting of steel*. Acta Polytechnica Scandinavica, Chemical Technology Series no. 230, The Finnish Academy of Technology, Finland.

Manojlović, G. (2007). *Preiskave gredic vzmetnega jekla kv.180 mm*. Internal Report, Štore Steel.

Manojlović, G. (2008). *O preiskavah vpliva hitrosti in temperature ulivanja na strjevalno strukturo kontinuirno ulitih gredic kv.800*. Internal Report, Štore Steel company.

Manojlović, G. (2008). *Vpliv EMS (Electro Magnetic Stirring) na strukturo gredic*. Internal Report, Štore Steel company.

Mathiesen, R.H. and Arnberg, L. (2006). X-ray monitoring of solidification phenomena in Al-Cu alloys. *Materials Science Forum,* 508:69-74.

Manojlović, G. (2008). *Preiskava hitrosti odlivanja na strjevalno strukturo gredic*. Internal Report, Štore Steel.

Maxwell, I. and Hellawell, A. (1975). A simple model for refinement during solidification. *Acta Metallurgica*, 23:229-237.

M’Hamdi, M., Bobadilla, M., Lesoult, G. and Combeau, H. (1998). Numerical modeling of the columnar to equiaxed transition in continuous casting of steel. In: B. G.Thomas and C. Beckermann (ed), *Modeling of Casting, Welding and Advanced Solidification Processes*-VIII, San Diego, USA, 375-82.

M’Hamdi, M., Combeau, H. and Lesoult, G. (1999). Modelling of heat transfer coupled with columnar dendritic growth in continuous casting of steel. *International Journal of Numerical Methods for Heat & Fluid Flow,* 9:296-317.

Midownik, M.A. (2002). A review of microstructural computer models used to simulate grain growth and recrystallization in aluminium alloys. *Journal of Light Metals,* 2:125-135.

Nakagawa, M., Narsume, Y. and Ohsasa, K. (2006). Dendrite growth model using front tracking technique with new growth algorithm. *ISIJ International*, 46:909-913.

Nastac, L. (1999). Numerical modelling of solidification morphologies and segregation patterns in cast dendritic alloy. *Acta Materialia*, 47:4253-4262.

Nastac, L. (2004). *Modelling and Simulation of Microstructure Evolution in Solidifying Alloys*. Kluwer Academic Publishers, USA.

Oldfield, W. (1966). A quantitative approach to casting solidification, freezing of cast iron. *ASM Transactions*, 59:945-960.

Papapetrou, A. (1935). Zeitschrift fur Kristallographie 92, 89.

Potts, R.B. (1952). Some generalized order disorder transformations. Mathematical. *Proceedings of the Cambridge Philosophical Society*, 48:106-109.

Qin, R.S. and Wallach, E.R. (2003). A phase-field model coupled with a thermodynamic database. *Acta Materialia*, 51:6199-6210.

Raabe, D. (2001). Mesoscale simulation of recrystallization textures and microstructures. *Advanced Engineering Materials*, 3:745-752.

Raabe, D. (2002). Cellular automata in materials science with particular reference to recrystallization simulation. *Annual Review of Materials Research*, 32:53-76.

Raabe, D. (2004). Mesoscale simulation of spherulite growth during polymer crystallization by use of a cellular automata. *Acta Materialia*, 52:2653-2664.

Raabe, D., Roters, F., Barlat, F. and Chen, L.Q. (2004). *Continuum Scale Simulation of Engineering Materials*. Wiley-vch Verlag GmbH & Co.KgaA Press, Weinbeim.

Raghavan, S. and Sahay, S.S. (2007). Modelling the grain growth kinetics by cellular automata. *Materials Science and Engineering*, A445-446:203-209.

Rappaz, M. (1989). Modelling of microstructure formation in solidification process. *International Materials Reviews*, 34:93-194.

Rappaz, M., Bellet, M. and Deville, M. (2003). *Numerical Modelling in Materials Science and Engineering*. Springer Series in Computational Mechanics, Springer, Berlin.

Rappaz, M. and Gandin, Ch.-A. (1993). Probabilistic modelling of microstructure formation in solidification processes. *Acta Metallurgica,* 41:345-360.

Rappaz, M. and Thevoz, P.H. (1987). Solute diffusion model for equiaxed dendritic growth. *Acta Metallurgica,* 7:1487-1497.

Rettenmayr, M. and Buchmann, M. (2006). Solidification and melting-asymmetries and consequences. *Materials Science Forum*, 508:205-210.

Saito, Y., Goldbeck-Wood, G. and Muller-Krumbhaar, H. (1988). Numerical simulation of dendritic growth. *Physical Review*, 33:2148-2157.

Sasikumar, R. and Sreenivasan, R. (1994). Two-dimensional simulation of dendrite morphology. *Acta Metallurgica*, 42:2381-2386.

Saunders, N., Li, X., Miodownik, P. and Schille, J.Ph. (2003). Using JmatPro to model materials properties and behaviour. *Journal of Metals,* 55:60-65.

Shin, Y.H. and Hong, C.P. (2002). Modelling of dendritic growth with convection using a modified cellular automata model with a diffuse interface. *ISIJ International*, 42:359-367.

Soares, A., Ferro, A. C. and Fortes, M. A. (1985). Computer simulation of grain growth in a bidimensional polycrystal. *Scripta Metallurgica*, 19:1491-1496.

Spittle, J.A. and Brown, S.G.R. (1989). A computer simulation of the influence of processing condition on a as-cast grain structures. *Journal of Materials Science*, 23:1777-1781.

Spittle, J.A. and Brown, S.G.R. (1989). Computer simulation of the effect of alloy variable on the grain structures of castings. *Acta Metallurgica*, 37:1803-1810.

Spittle, J.A. and Brown, S.G.R. (1994). 3D cellular-automata model of coupled growth in 2-component systems. *Acta Metallurgica,* 42:1811-1815.

Spittle, J.A. and Brown, S.G.R. (1995). A cellular automata model of steady state columnar dendritic growth in binary alloys. *Journal of Materials Science,* 30:3989-3994.

Stefanescu, D.M., Upadhya, G. and Bandyopadhyay, D. (1990). Heat transfer-solidification kinetics modeling of solidification of castings. *Metallurgical and Materials Transactions*, A21:997-1005.

Stefanescu, D.M. (2009). *Science and Engineering of Casting Solidification*. Springer Science Business Media, LCC, USA.

Steinbach, I., Kauerauf, B., Beckermann, C. and Guo, J. (1998). Modelling of the growth and interactions of equiaxed dendrites on a mesoscopic scale. In: S. P. Marsh, J. A. Dantzig, R. Trivedi, W. Hofmeister, M.G. Chu, E. J. Lavernia and J. H. Chun (ed), *Solidification 1998*, TMS Publication, Warrendale, USA, 5-14.

Šarler, B., Kosec, G. and Lorbiecka, A. Z. (2008). A meshless approach in solution of multiscale solidification modelling. In: A. Roosz, M. Rettenmayr, Z. Gracsi (ed), *Fifth International Conference on Solidification and Gravity*, University of Miskolc, Material Science Forum, Miskolc-Lillafüred, Hungary, 34.

Šarler, B., Kosec, G., Lorbiecka, A.Z. and Vertnik, R. (2009). Solution of multiphysics and multiscale problems by a novel meshless method. *6th International Congress of Croatian Society of Mechanics*, Dubrovnik, Croatia, 127.

Šarler, B., Vertnik, R. and Perko, J. (2005). Application of diffuse approximate method in convective diffusive solidification problems. *CMC: Computers, Materials & Continua*, 2:77-83.

Šarler, B. and Vertnik, R. (2006). Meshfree local radial basis function collocation method for diffusion problems. *Computers and Mathematics with Application*, 51:1269-1282.

Šarler, B., Vertnik, R., Gjerkeš, H., Lorbiecka, A., Manojlović, G., Cesar, J., Marčič, B., Sabolič-Mijovič, M. (2006). Multiscale integrated numerical simulation approach in Štore - Steel casthouse. *WSEAS Transactions on Systems and Control*, 2:294-299.

Šarler, B., Vertnik, R., Šaletić, R., Manojlović, G. and Cesar, J. (2005). Application of contiunuous casting simulation at Štore steel, *Berg-und Huttenmannische Monatchefte*, 9:300-306.

Thévoz, Ph., Desbiolles, J.L. and Rappaz, M. (1989). Modelling of equiaxed microstructure formation in castings. *Metallurgical and Materials Transactions*, A20:311-322.

Thieme-Martin, S. (1999a). *Dynamische zellulaere atomaten*. Internal Note, IfU, ETH Zurich.

Vertnik, R. (2010). *Heat and Flow Simulation of the Continuous Casting of Steel by a Meshless Method*. Doctoral Dissertation, Univeristy of Nova Gorica, Slovenia.

Vertnik, R. and Šarler, B. (2002). *Graphical user interface of the simulation system for the continuous casting of billets in the Inexa-Štore d.o.o.,* version 2002/IS4/09, University of Nova Gorica, Laboratory for Multiphase Processes, Nova Gorica, CD-ROM (in Slovenian).

Vertnik, R. and Šarler, B. (2006). Meshless local radial basis function collocation method for convective-diffusive solid-liquid phase change problems. *International Journal of Numerical Methods for Heat & Fluid Flow*, 16:617-640.

Voller, V.R. (2008). An enthalpy method for modelling dendritic growth in a binary alloy. *International Journal of Heat and Mass Transfer*, 52: 823-834.

von Neumann, J. (1951). The general and logical theory of automata. Edited by L. A. Jeffress: *Cerebral Mechanisms in Behaviour*, New York, Wiley, pp.1-41.

von Neumann, J. (1966). *Theory of Self-Reproducing Automata*. Edited by A. W. Burks (University of Illinois, Urbana), Urbana IL, pp. 91-381.

Wainwright, R. T. (1974). *Life is universal*. Proceedings of the Winter Simulation Conference, Washington, D.C., ACM, 448.

Waldrop, M. (1993). *Complexity: the emerging science at the edge of order and chaos*. Simon&Schuster Editor, New York.

Wang, C,Y. and Beckermann, C. (1994). Prediction of columnar to equiaxed transition during diffusion-controlled dendritic alloy solidification. *Metallurgical and Materials Transactions*, A25:1081-1093.

Wang, W., Lee, P.D. and McLean, M. (2003). A model of solidification microstructures in nickel-based superalloys: predicting primary dendrite spacing selection. *Acta Materialia,* 51:2971-2987.

Wolfram, S. (2002). *A New Kind of Science.* Wolfram Media, Inc., USA.

Watson, D.F. (1981). Computing the n-dimensional Delaunay tessellation with application to Voronoi polytopes. *The Computer Journal,* 2:167-172.

Weaire, D. and Kermode, J.P. (1983). Computer simulation of a two dimensional soap froth. Method and motivation. *Philosophical Magazine Part B,* 48:245-259.

Xu, Q., Li, B., Liu, Y. and Liu, B. (2008). Numerical modelling of microstructure evolution and dendrite growth in alloy solidification process. *International Journal of Materials and Product Technology,* 33:37-49.

Yamazaki, M., Natsume, Y., Harada, H. and Ohsasa, K. (2006). Numerical simulation of solidification structure formation during continuous casting in Fe-0.7mass%C alloy using cellular automata method. *ISIJ International*, 46:903-908.

Yazdipour, N., Davies, C.H.J. and Hodgson, P.D. (2008). Microstructural modelling of dynamic recrystallization using irregular cellular automata. *Computational Materials Science,* 44:566-576.

Yazdipour, N., Dehghan-Manshadi, A., Davies, C.H.J. and Hodgson, P.D. (2007). Simulation of dynamic recrystallization using irregular cellular automata. *Materials Forum*, 31:164-176.

Yazdipour, N., Hodgson, P.D., Madej, L. and Rauch, L. (2008). Numerical simulation of the static recrystalization at micro shear bands. *Materials Science and Technology*, Materials Science & Technology Conference, 832-843.

Zhu, M.F. and Hong, C.P. (2001). A modified cellular automata model for the simulation of dendritic growth in solidification of alloys. *ISIJ International,* 41:436-445.

Zhan, Z., Wei, Y. and Dong, D. (2008). Cellular automata simulation of grain growth with different orientation angles during solidification process. *Journal of Materials Processing Technology,* 208:1-8.

Zhu, M.F. and Hong, C.P. (2001). A modified cellular automata model for the simulation of dendritic growth in solidification of alloys. *ISIJ International*, 41:436-445.

Zhu, P. and Smith, R.W. (1992). Dynamic simulation of crystal growth by Monte Carlo method-I. Model description and kinetics. *Acta Metallurgica*, 40:683-692.